ANGLE-RESOLVED PHOTOEMISSION AND FIRST-PRINCIPLES STUDIES OF TOPOLOGICAL THIN FILMS

BY

GUANG BIAN

DISSERTATION

Submitted in partial fulfillment of the requirements
for the degree of Doctor of Philosophy in Physics
in the Graduate College of the
University of Illinois at Urbana-Champaign, 2013

Urbana, Illinois

Doctoral Committee:

Professor S. Lance Cooper, Chair
Professor Tai-Chang Chiang, Director of Research
Professor Michael Stone
Professor Jen-Chieh Peng

Abstract

Topological insulators are electronic materials that have a bulk band gap like an ordinary insulator but have protected conducting states on their edge or surface. The exotic electronic properties of topological materials are of great interest for spin-related electronics and quantum computation. In this thesis research, the combination of angle-resolved photoemission spectroscopy (ARPES) and first principles calculation is used to examine the electronic properties of topological thin films and 2D electronic systems with large spin-orbit splitting. The topological thin films are prepared *in situ* by molecular beam epitaxy (MBE) method and characterized by experimental tools such as reflection high-energy electron diffraction (RHEED) and low energy electron diffraction (LEED). The systems investigated in this thesis include topological Sb, Bi_2Te_3, Be_2Se_3 thin films, Bi films, and Bi/Ag surface alloy.

Topological Sb films have been successfully fabricated on Si(111) substrates. By examining the connection pattern between surface states and the quantum well bulk states, our photoemission spectra show clearly the topological order of the Sb films. When topological films become ultrathin, the quantum tunneling effect breaks the degeneracy at the Dirac point of the topological surface bands, resulting in a gap. Our ARPES mapping of the surface band structure of a 4-BL Sb film reveals no energy gap at the Dirac point. This lack of tunneling gap can be explained by a strong interfacial bonding between the film and the substrate.

The topological order of topological materials is a robust quantity, but the topological surface states themselves can be highly sensitive to the boundary conditions. Specifically, the surface states of Bi_2Se_3 and Bi_2Te_3 form a single Dirac cone at the zone center. Our first-principles calculations based on a slab geometry show that, upon hydrogen termination of either face of the slab, the Dirac cone associated with this face is replaced by three Dirac cones centered at the time-reversal-invariant $\overline{M}$ points at the zone boundary. The critical behavior of the TI film near the quantum critical point is also

studied theoretically. When the strength of the spin-orbit coupling (SOC) is tuned across the critical point, the topological surface states, while protected by symmetry in the bulk limit, can be missing completely in topological films even at large film thicknesses.

We have observed, using angle-resolved photoemission, a structural phase transformation of Bi films deposited on Si(111)-(7×7). Films with thicknesses 20 to ~100 Å, upon annealing, first order into a metastable pseudocubic (PC) phase and then transform into a stable rhombohedral (RH) phase with very different topologies for the quantum well subband structures. The PC phase shows a surface band with a maximum near the Fermi level at $\bar{\Gamma}$, whereas the RH phase shows a Dirac-like subband around $\bar{M}$ along $\bar{K}-\bar{M}-\bar{K}$. The formation of the metastable phase over a wide thickness range can be attributed to a surface nucleation mechanism.

Finally, we have studied the electronic structure of the Bi/Ag surface alloy, a system possessing a huge Rashba splitting in its surface bands. The Bi/Ag surface alloy is prepared by depositing Bi onto ultrathin Ag films followed by annealing. The electronic structure of the system is measured using circular angle resolved photoemission spectroscopy (CARPES). The results reveal two interesting phenomena: the hybridization of spin polarized surface states with Ag bulk quantum well states and the umklapp scattering by the perturbed surface potential. In addition, our CARPES spectra show clearly a unique dichroism pattern which is closely related to the spin texture of this 2D strongly spin-orbit coupled electron system.

Acknowledgements

First and foremost, I would like to thank my advisor, Professor Tai-Chang Chiang, for his guidance, support and encouragement throughout the course of this work. I owe special thanks to Dr. Thomas J. Miller. The data comprising this thesis could not have been taken without his assistance and technical expertise.

I've enjoyed very much working with present and past group members Dr. Ruqing Xu, Dr. Yang Liu, Dr. Matthew Brinkley, Dr. Aaron Gray, Dr. Xiaoxiong Wang, Dr. Huanhua Wang, Dr. Gazzy Weng, Longxiang Zhang, Caizhi Xu, Man-Hong Wong, Jie Ren and Xinyue Fang. I am also grateful to the staff scientists at the SRC for their technical support of my experiments. Thanks to Prof. Simon Brown, Dr. Pawel Kowalczyk and Ojas Mahapatra for the enjoyable collaboration.

I would like to mention my friends Dr. Hefei Hu, Jia Gao, Ching-Kai Chiu, Xianhao Xin, Han Cheng, Gang Ling and Yaxuan Yao, who made the days at Urbana so pleasant and memorable.

In particular, I wish to thank my parents for their support and understanding during all my studies.

The thesis is based on work supported by the U.S. Department of Energy, under Grant No. DE-FG02-07ER46383. I acknowledge partial financial support by the Yee Memorial Fund Fellowship. The Synchrotron Radiation Center, where the ARPES data were taken, is supported by the U.S. National Science Foundation (Grant DMR-05-37588). Acknowledgement is also made to the ACS Petroleum Research Fund and the U.S. National Science Foundation (Grant DMR-09-06444) for partial support of beamline operations.

Table of Contents

List of Symbols and Abbreviations

$h\nu$	Photon energy
E_B	Electron binding energy (relative to the Fermi level)
E_F	Fermi Energy
k	Electron wave vector
Å	Angstrom (10^{-10} m or 0.1 nm)
1D, 2D, 3D	One-, Two-, Three-Dimensional
ARPES	Angle-Resolved Photoemission Spectroscopy
Ag	Silver
Au	Gold
Bi	Bismuth
Sb	Antimony
Si	Silicon
Se	Selenium
Te	Tellurium
ML	Monolayer
BL	Bilayer
SIA	Structural Inversion Asymmetry
UHV	Ultrahigh Vacuum

MBE	Molecular Beam Epitaxy
LEED	Low-Energy Electron Diffraction
RHEED	Reflection High-Energy Electron Diffraction
SRC	Synchrotron Radiation Center
EDC	Energy Distribution Curve
MDC	Momentum Distribution Curve
DOS	Density of States
QWS	Quantum Well State
SS	Surface State
TSS	Topological Surface State
TI	Topological Insulator
TRIM	Time Reversal Invariant Momentum
BZ	Brillouin Zone
SBZ	Surface Brillouin Zone
DFT	Density Functional Theory
LDA	Local Density Approximation
GGA	Generalized Gradient Approximation
FCC	Face-Centered Cubic
PC	Pseudocubic
RH	Rhombohedral
RT	Room Temperature

SA	Surface Alloy
TB	Tight Binding
HP	Horizontally Polarized
VP	Vertically Polarized
LCP	Left-handed Circularly Polarized
RCP	Right-handed Circularly Polarized

1 Introduction

1.1 Topological thin films and quantum size effect

Topological materials present opportunities for realizing new fundamental physics, novel devices for spintronics, and quantum computation [1,2] which may be facilitated through the realization of exotic states such as Majorana fermions [3] and magnetic monopoles [4]. Topological thin films grown on semiconductor substrates have great potential for future device applications. When the thickness of a thin film becomes comparable to the electronic coherence length, quantum size effects can alter greatly physical properties [5,6]. A direct consequence of such effects is the formation of electronic standing waves, i.e., quantum well states (QWS) [7,8]. Quantum size effects have been well known to exert a thickness-dependent modulation on thermal and transport properties of nanoscale systems. For example, the superconducting transition temperature of Pb films oscillates with the increasing film thickness [9]. The thermal stability of metal thin films also critically depends on the film thickness [10]. Quantum size effects have even more profound influences on topological thin films due to the presence of the topological ordering and the protected surface states. Topological insulator thin films show an oscillatory behavior as a function of the layer thickness, alternating between topologically trivial and nontrivial order [11]. Moreover, the quantum tunneling effect, intrinsic to thin films, opens a thickness-dependent energy gap at the Dirac point of the topological surface bands, which opens a door for manipulating the spin current on the surface of topological insulators [12].

Exciting physics can arise from the interplay between quantum size effects and topological ordering. However, up to now, experimental investigations of nanoscale

topological systems have not been well established due to the stringent material engineering requirements. Considerable effort of my thesis research has been put on fabrication of atomically uniform topological thin films on semiconductor substrates by molecular beam epitaxy (MBE) technique. The surface condition of the substrates is crucially important for the structural quality of the epitaxial thin films. The electronic structure of the epitaxial grown thin films is examined by a combined method of angle-resolved photoemission spectroscopy (ARPES) and first-principles calculation. The spectroscopic information of the thin films can provide a deep understanding of the transport properties and a significant guidance for practical device applications. The procedure of the research works reported in this thesis basically consists of three parts:

1. MBE growth of atomically uniform thin films and surface characterization,
2. Synchrotron-based ARPES measurement of the electronic band structure,
3. Theoretical modeling and first-principles calculations.

This dissertation examines the electronic properties of topological Sb, Bi_2Te_3, Be_2Se_3 thin films [13,14,15,16,17]. Besides the topological thin films, Bi films and Bi/Ag surface alloy are the other two systems studied in this thesis [18,19]. Semi-metallic Bi is one of the parent ingredients of the alloy topological insulater $Bi_{1-x}Sb_x$ ($0.07 < x < 0.2$) [20,21]. But, unlike Sb, Bi doesn't share the nontrivial topological order of the alloy insulator. Nevertheless, Bi has attracted intense interest because of its unique combination of physical properties including a strong spin-orbit coupling, a large Fermi wavelength, and a small Fermi surface. The Bi/Ag surface alloy, one third of a monolayer (ML) of Bi alloyed into a Ag(111) surface, possesses a giant Rashba spin splitting in its free-electron-like surface states [22,23]. This unique property is of great interest in connection with device applications of spintronics and quantum computation.

1.2 Thesis Overview

This thesis is organized as follows: Chapter 2 and 3 provide the necessary background information on photoemission and the other experimental methods. Chapter 4 gives the necessary theoretical background for understanding the work in this dissertation. Chapter 5 focuses on our ARPES study of epitaxial Sb films grown on the Si(111) surface. Chapter 6 presents our theoretical work on Bi_2Te_3, Be_2Se_3 thin films. Chapter 7 describes our discovery of the surface-mediated metastability of Bi films. Chapter 8 discusses experiments and calculations targeted to understand the electronic structure and spin texture of the Bi/Ag surface alloy. Finally, Chapter 9 will summarize the results of the thesis and outline some possible directions for future research.

References:

[1] Z. Hasan and C. Kane, Rev. Mod. Phys. **82**, 3045 (2010).

[2] X. Qi and S. Zhang, Rev. Mod. Phys. **83**, 1057 (2011).

[3] L. Fu and C. Kane, Phys. Rev. Lett. **100**, 096407 (2008).

[4] X. Qi et al., Science **323**, 1184 (2009).

[5] T.-C. Chiang, Surf. Sci. Rep. **39**, 181 (2000).

[6] P. Halperin, Rev. Mod. Phys. **58**, 533 (1986).

[7] F. J. Himpsel et al., Adv. Phys. **47**, 511 (1998).

[8] M. Milun, P. Pervan, and D. P. Woodruff, Rep. Prog. Phys. **65**, 99 (2002).

[9] Y. Guo et al., Science **306**, 1915 (2004).

[10] M. Upton et al., Phys. Rev. Lett. **93**.026802 (2004).

[11] C. Liu, Phys. Rev. B **81**, 041307 (2010).

[12] O. V. Yazyev, J. E. Moore, S. G. Louie, Phys. Rev. Lett. **105**, 266806 (2010).

[13] G. Bian et al., Phys. Rev. Lett. **107**, 036802 (2011).

[14] G. Bian et al., Phys. Rev. Lett. **108**, 176401 (2012).

[15] G. Bian et al., Phys. Rev. B **80**, 245407 (2009).

[16] X. Wang, G. Bian et al., Phys. Rev. Lett. **108**, 096404 (2012).

[17] Y. Liu, G. Bian et al., Phys. Rev. B **85**, 195442 (2012)

[18] G. Bian et al., Phys. Rev. B **80**, 245407 (2009).

[19] G. Bian et al., Phys. Rev. Lett. **108**, 186403 (2012).

[20] L. Fu and C. L. Kane, Phys. Rev. B **76**, 045302 (2007).

[21] D. Hsieh et al., Science **323**, 919 (2009).

[22] H. Bentmann et al., Europhys. Lett. **87**, 37003 (2009).

[23] C. Ast et al., Phys. Rev. Lett. **98**, 186807 (2007).

2 Experimental Techniques

2.1 Introduction

This chapter gives some background information on surface reconstruction and film deposition, and describes the various experimental tools used to prepare and characterize the surfaces and films. Angle-resolved photoemission spectroscopy, the primary experimental technique, is discussed in the next chapter.

2.2 Surface reconstruction

The ideal crystal surface is an abrupt termination plane of the bulk crystal and possesses perfect two-dimensional periodicity. In reality, the surface atoms always exhibit relaxation or reconstruction as the crystal periodic potential is broken at the surface. This is because the surface atoms are not fully coordinated, and therefore have higher energy than the fully coordinated bulk atoms [1]. To minimize the surface energy, the surface atoms typically rearrange form their original lattice. This rearrangement can be a simple adjustment in the layer spacing perpendicular to the surface as common in metals. Such relaxations don't change either the periodicity parallel to the surface or the symmetry of the surface. The displacement of the surface atoms can be much more readily observable and form a reconstruction, a complicated superstructure with symmetry different for that of the ideal surface termination [2]. Surface reconstructions occur on many of the less stable metal surfaces such as FCC(110), but are much more prevalent on semiconductor surfaces due to the presence of surface dangling bonds. The 7×7 reconstructed Si(111) surface is the primary substrate for the MBE growth of the thin films studied in this thesis. The 7×7 superstructure as shown in Fig. 2.1 can be readily achieved by flashing a Si(111)

sample cut from a commercial wafer briefly to 1300 K. The Dimer-Adatom-Stacking Fault (DAS) model [3] describes the 7×7 reconstruction as consisting of 12 adatoms arranged with a local 2×2 periodicity in a 7×7 rhombohedral unit cell. Compared with 49 dangling bonds for the bulk-truncated surface (per 7×7 unit cell), the DAS reconstruction has only 19.

Surface reconstruction can also happen when an adsorbate is introduced to the surface. Such adsorbate-induced reconstructions are sensitively dependent on a number of variables: the adsorbate species, adsorbate coverage, chemical reactivity of the adsorbate-substrate interaction, the substrate temperature, size mismatch between the adsorbate-substrate atoms, adsorption geometry, and more. The most natural adsorbate-substrate interaction is to saturate dangling bonds during the formation of a local surface chemical bond [4]. Adsorbate-induced reconstructions usually possess a periodicity different from that of the clean surface. One example is the Bi/Si(111)-$\sqrt{3}\times\sqrt{3}-R30^{\circ}$ surface which facilitates the smooth growth of epitaxial Sb films. The $\sqrt{3}\times\sqrt{3}-R30^{\circ}$ structure can be prepared by depositing 10Å Bi on the surface of a Si(111)-(7×7) substrate at room temperature, and then annealed at 450°C for 15 min to desorb any excess Bi. Previous study [5] has shown that the Bi adatoms form a trimer on the Si(111) surface as illustrated in Fig. 2.2. Bi is a heavy group V element, and a trimer arrangement allows it to form a threefold coordinated configuration, which is consistent with its most stable valence value of three. The final surface structure is fully passivated with no remaining dangling bonds, and all atoms are coordinated in a manner close to their optimum configurations.

2.3 Molecular beam epitaxy

The thin films studied in this thesis research are produced by molecular beam

epitaxy (MBE), a process in which sample layers are deposited epitaxially on a substrate in an ultra-high-vacuum (UHV) chamber. The principle behind the method is simple: a substance such as Bi or Sb is evaporated and the vapor deposited on a substrate such as Si. UHV systems with base pressures in the 10^{-10} Torr range are used to prevent contamination and to ensure good conditions both in the molecular beam and at the surface of the sample. At a pressure of 10^{-10} Torr, it takes a few hours for newly prepared surface to become covered with a monolayer of adsorbates even if every impinging gas molecule sticks to the surface. Attaining and preserving UHV condition in the chamber is also a prerequisite for a successful ARPES experiment because APRES is a well-known surface sensitive probe.

A schematic diagram of our MBE system is shown in Fig. 2.3 [6]. A crucible containing high purity materials to be evaporated is biased at high voltage (typically 200-2000V), and is bombarded by electrons emitted from a hot tungsten filament. The deposition rate is controlled by the total power supplied to the crucible, which is proportional to the product of the high voltage and the emission current associated with this high voltage. To achieve a constant evaporation rate, the emission current is held constant by adjusting the current of the tungsten filament through an external feedback circuit. The actual deposition rate is calibrated by a water-cooled crystal thickness monitor (XTM). XTM calibrates the deposition rate by monitoring the change of the oscillation frequency of a quartz crystal as a result of its mass change from the deposition. The inaccuracy of XTM is typically within ~10% [7].

2.4 Reflection high-energy electron diffraction

The most common technique for surface characterization is electron diffraction, including reflection high-energy electron diffraction (RHEED) and low-energy electron diffraction (LEED). RHEED utilizes a monoenergetic (typical ~10 keV), focused beam of

electrons impinging on the surface at a glazing angle (about 3-4º with respect to the sample surface) as illustrated in Fig. 2.4 [8]. The electrons get diffracted by the sample surface and then illuminate a fluorescent screen. Shining the beam at grazing incidence not only ensures that the penetration depth of the electrons is limited to the top layers, it also allows for real-time monitoring of surface symmetry and morphology during film growth, as the electron gun and phosphor screen do not occlude the sample face. Since RHEED mostly probes the surface structure, the reciprocal lattice is made up of rods that extend along the normal direction of the surface. Every spot on the RHEED screen corresponds to a crossing of a reciprocal rod with the Ewald's sphere. As a result of this diffraction geometry, the RHEED pattern consists of Laue circles. It is straightforward to determine the surface structure from the RHEED pattern given the geometric parameters such as the incidence angle and the sample-to-screen distance. RHEED patterns acquired from the Si(111)-(7×7) surface along the $[1\bar{1}0]$ and $[\bar{1}\bar{1}2]$ directions are shown in Fig. 2.5.

2.5 Low energy electron diffraction

Low-energy electron diffraction (LEED) is a powerful technique for the determination of the surface structure of crystalline materials by bombardment with a collimated beam of low energy electrons (20-200eV) [9] and observation of diffracted electrons as spots on a fluorescent screen. A typical LEED apparatus is schematically depicted in Fig.2.6(a). The basic reason for the high surface sensitivity of LEED is the fact that for low-energy electrons the interaction between the solid and electrons is especially strong. Upon penetrating the crystal, primary electrons will lose kinetic energy due to inelastic scattering processes such as plasmon and phonon excitations as well as electron-electron interactions. Fig. 2.6(b) shows the Ewald's sphere for the case of normal incidence of the primary electron beam, as would be the case in an actual LEED setup. It is apparent that the pattern observed on the fluorescent screen is a direct picture of the

reciprocal lattice of the surface. The size of the Ewald's sphere and hence the number of diffraction spots on the screen is controlled by the incident electron energy. LEED patterns taken from the Si(111)-(7×7) surface with different electron energies are shown in Fig. 2.7.

References:

[1] L. H. Van Vlack, *Elements of Materials Science* (Addison-Wesley, 1964).

[2] C. Kittle, *Introduction to Solid State Physics* (John Wiley & Sons, Inc., New York, 1986).

[3] K. Takayanagi et al., Surf. Sci. **164**, 367 (1985).

[4] A. Zangwill, *Physics at Surfaces* (Cambridge University Press, Cambridge, 1988).

[5] J.M. Roesler et al., Surf. Sci. **417**, L1143 (1998).

[6] M. K. Brinkley, *Angle-resolved photoemission studies of quantum-electronic coherence in metallic thin-film systems,* Ph.D. thesis, University of Illinois at Urbana-Champaign (2010).

[7] Y. Liu, A*ngle-resolved photoemission studies of two-dimensional electron systems,* Ph.D. thesis, University of Illinois at Urbana-Champaign (2010).

[8] Jürgen Klein, *Epitaktische Heterostrukturen aus dotierten Manganaten,* Ph.D. thesis, University of Cologne (2001).

[9] K. Oura, V.G. Lifshifts, A.A. Saranin, A. V. Zotov, M. Katayama, *Surface Science*. (Springer-Verlag, New York, 2003).

Figures:

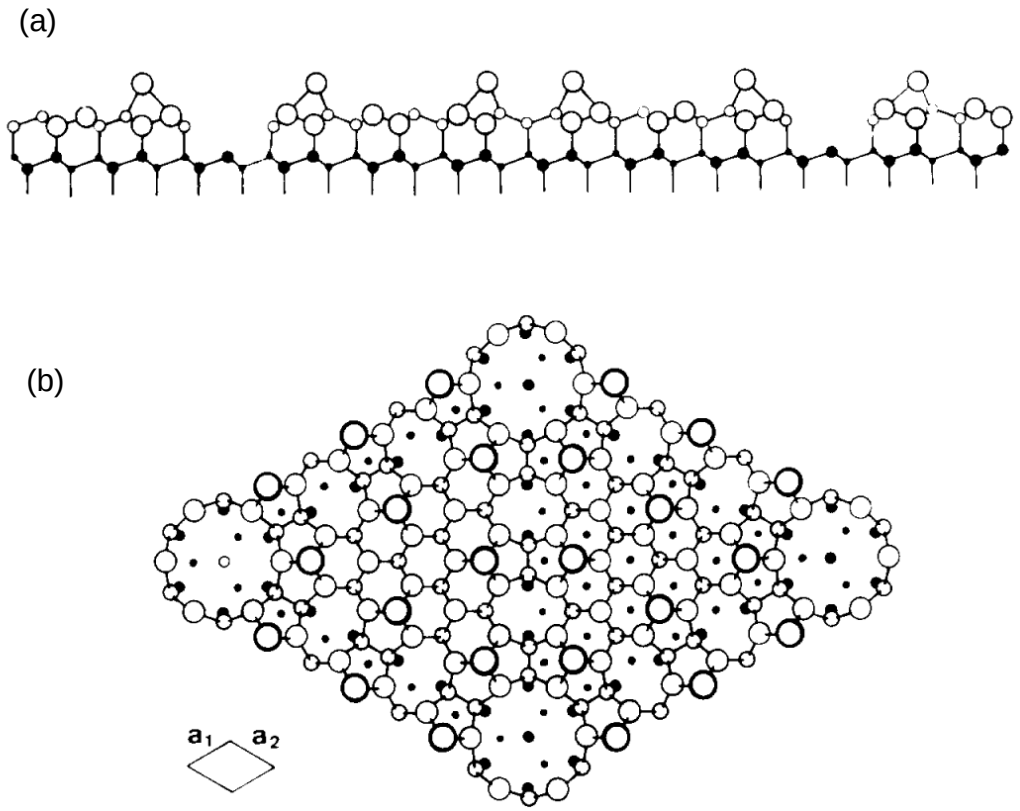

Figure 2.1. DAS model of the Si(111)-7 × 7 surface [3]. (a) Side view. (b) Top view.

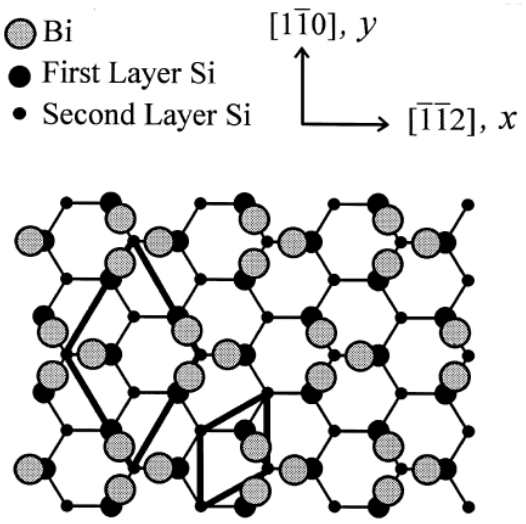

Figure 2.2. Trimer model for Bi/Si(111) system viewed from above. The coordinate system is indicated. The 1×1 and $\sqrt{3} \times \sqrt{3}\,R30°$ unit cells are outlined.

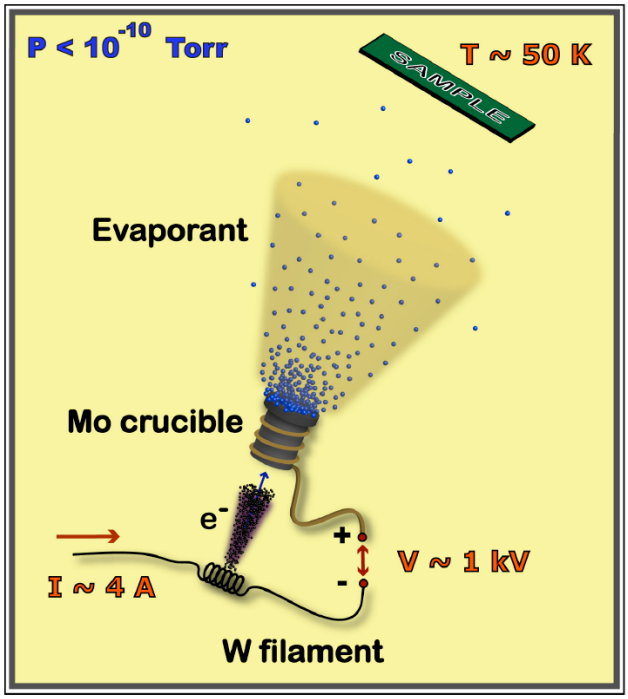

Figure 2.3. A schematic diagram of our MBE system [6].

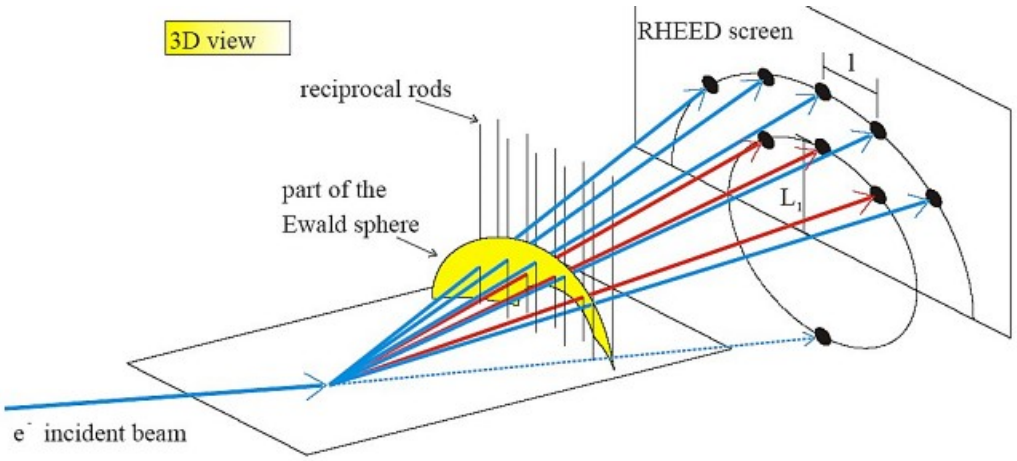

Figure 2.4. A schematic view of the diffraction geometry of RHEED [8]. The diffraction spots on the RHEED screen arise from crossings of the reciprocal rods (of the sample surface) with the Ewald's sphere. The resulting RHEED pattern consists of Laue circles. Red (blue) lines correspond to Laue circle #0 (#1), respectively.

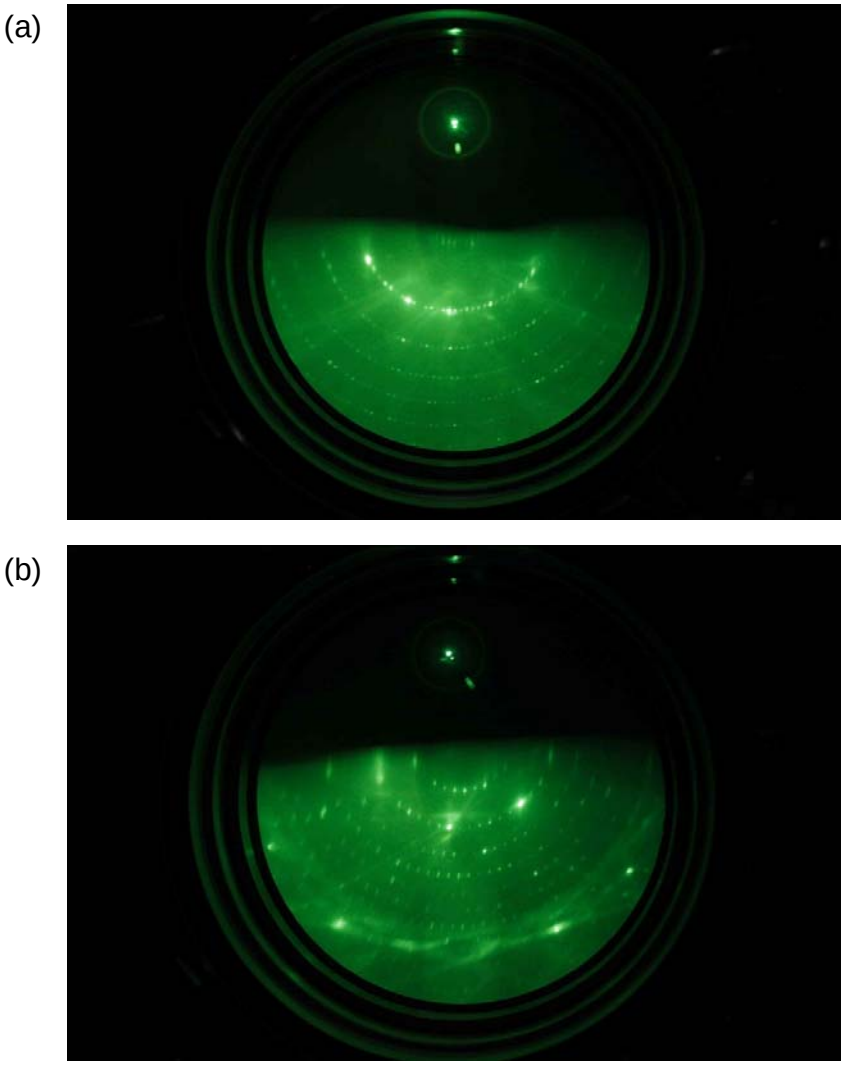

Figure 2.5. Reflection high-energy electron diffraction patterns taken from the Si(111)-(7×7) surface along (a) [$1\bar{1}0$] and (b) [$\bar{1}\bar{1}2$] real space directions.

(a)

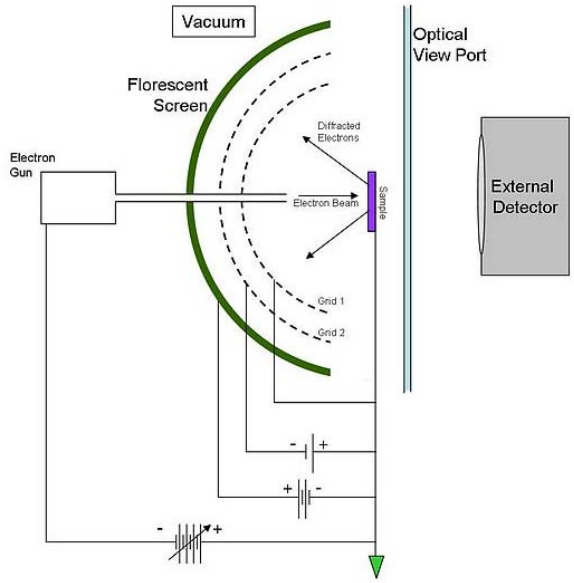

(b)

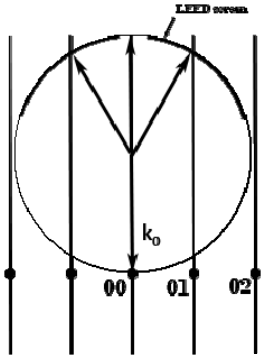

Figure 2.6. (a) Schematic depicting a LEED apparatus. (b) Ewald's sphere construction for the LEED technique. The intersections between Ewald's sphere and reciprocal lattice rods define the allowed diffracted beams.

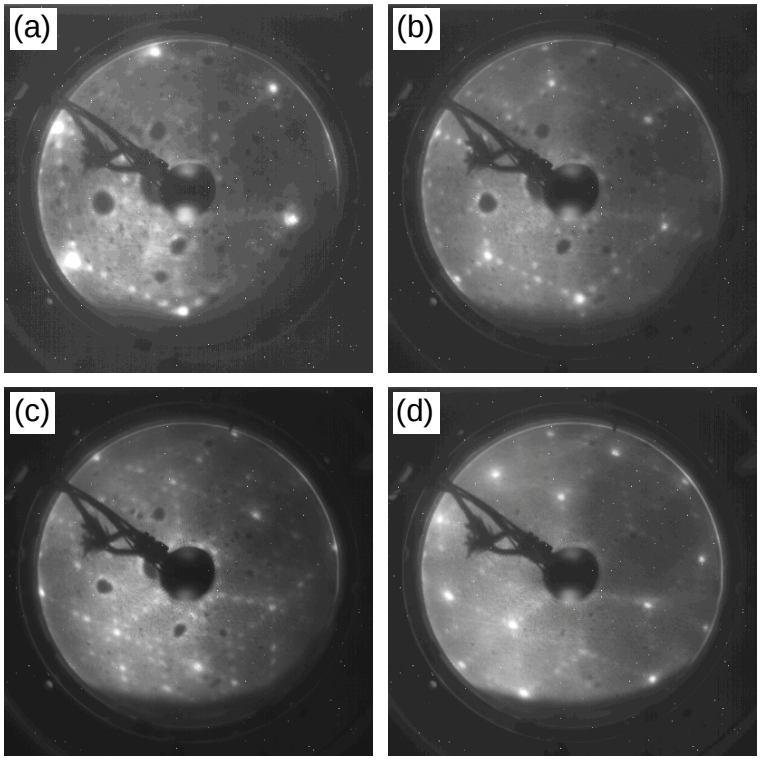

Figure 2.7. LEED patterns taken from the Si(111)-(7×7) surface with (a) 38 eV, (b) 61 eV, (c) 83 eV and (d) 117 eV electron beams

3 Angle-Resolved Photoemission Spectroscopy

3.1 Introduction

Angle-resolved photoemission spectroscopy (ARPES) can directly detect the band structures of solid materials. This unique advantage, together with its broad applicability to various material systems, has made ARPES a technique that is widely used to study solid state materials. This chapter provides an introduction to ARPES that will allow readers to understand the work presented in this thesis. An intuitive physical picture of the ARPES process which is based on a three-step model will be presented in Sec. 3.2. ARPES experimental apparatus will be discussed in detail in Sec. 3.3, respectively. A more rigorous interpretation of the photoemission process will be offered in Sec. 3.4.

3.2 An intuitive view of photoemission process

The photoemission technique is a direct out-growth of the photoelectric effect explained by Einstein in 1905. The typical experimental geometry for an ARPES experiment is shown in Fig. 2.1. Monochromatic photons with energy *hv* impinge on the sample, and electrons are ejected from the sample as a result of photoelectric effect. Both the kinetic energy and the emission angle of the electrons are recorded by a photoelectron analyzer. From this kinetic information the electronic properties inside the solid can be deduced.

The photocurrent produced in a photoemission experiment results from the excitation of electrons for the initial states *i* with wavefunction Ψ_i to the final states

with wavefunction Ψ_f by the photon field having the vector potential **A**. The transition probability can be approximated by Fermi's Golden Rule [1]:

$$w_{f,i} = \frac{2\pi}{\hbar}\left|\left\langle \Psi_f \left| H_{\text{int}} \right| \Psi_i \right\rangle\right|^2 \delta(E_f - E_i - h\nu), \tag{3.1}$$

where E_i and E_f are the initial- and final-state energies of the *N*-particle system. The interaction Hamiltonian is given by

$$H_{\text{int}} = \frac{e}{2mc}(\boldsymbol{A}\cdot\boldsymbol{p} + \boldsymbol{p}\cdot\boldsymbol{A}) = \frac{e}{2mc}(2\boldsymbol{A}\cdot\boldsymbol{p} - i\hbar\nabla\cdot\boldsymbol{A}), \tag{3.2}$$

where $\boldsymbol{p}$ is the momentum operator and $\boldsymbol{A}$ is the electromagnetic vector potential. The $\boldsymbol{A}\cdot\boldsymbol{p}$ term in Eqn. (3.2) is called the direct transition term which normally dominates in the photoemission intensity. It preserves the crystal momentum of the electron during the photoexcitation process. The $\nabla\cdot\boldsymbol{A}$ term is usually ignored by an appropriate choice of gauge. However, at a surface, this term is not negligible and can even be comparable to the direct transition term $\boldsymbol{A}\cdot\boldsymbol{p}$ [2,3]. A detailed discussion of this surface transition term is given in Sec. 3.4. In addition, a spin-orbit coupling term has also important contribution to the total photocurrent when considering the surfaces with large Rashba spin splitting. This spin-dependent term will be discussed in detail in Chapter 8.

In order to calculate the transition probability correctly, the true final state has to be introduced into Eqn. 3.1 in addition to the initial Bloch state. The so-called time reversed LEED wavefunction is a good description for the final state. In LEED an incoming monochromatic beam of electrons is scattered from the ions in the crystal and the scattered waves sum up to yield the LEED diffraction pattern. If one consider the LEED

process backwards in time, one obtains a monochromatic wave of electrons which originates from the ions of the crystal, very similar to the electron wave produced by the photoemission process [1].

The calculation for the exact final states is quite tedious. A more comprehensive model, the three-step model [4,5] has been developed to capture the essential physics of photoemission, and has been widely adopted in the photoemission community [6]. Within this approach, the photoemission process is subdivided into three independent and sequential steps (see Fig. 2.2):

(1) optical excitation of the electron in the bulk,

(2) transport of the excited electron to the surface,

(3) escape of the photoelectron into vacuum.

In step (1), an electron is excited from an occupied Bloch state (initial state) to an unoccupied Bloch state (final state) through photon absorption. Because the photons possess very little momentum compared to the typical crystal momentum of the Bloch state, the momentum of the electron is essentially unchanged. Step (2) can be described in terms of an effective mean free path which is proportional to the probability that the excited electron reaches the surface without scattering. The inelastic scatterings give rise to a continuous background in the photoemission spectra which is usually ignored or subtracted. Once the electron reaches the surface, it overcomes the work function of the material and eventually emits from the surface. The momentum perpendicular to the surface is not conserved in step (3), and the electron is refracted in a similar manner to that of light at the interface between two materials. Nevertheless, the parallel component of the momentum is still conserved analogous to Snell's Law.

In an ARPES experiment, energy conservation requires

$$E_K = h\nu - \Phi_{wf} - \left|E_B\right|, \tag{3.3}$$

where E_K is the kinetic energy of the electron in vacuum, Φ_{wf} is the work function of the material, and E_B is the binding energy of the electron relative to the Fermi level. The conservation of the parallel momentum gives

$$k_{\parallel} = \sqrt{\frac{2m_e}{\hbar^2} E_K} \sin\theta , \tag{3.4}$$

where $k_{\parallel}$ is the parallel wave vector of the initial state, θ is the polar emission angle (Fig. 3.1). E_K, Φ_{wf} and θ can all be measured directly from the experiment. Therefore, the energy and in-plane wave vector of the electronic state before photoemission can be determined from Eqs. 3.4 and 3.5. The results from an ARPES measurement are generally expressed as a three-variable photocurrent function $I(E_B, k_x, k_y)$. Tracing the peaks in the photocurrent function allows us to obtain the in-plane dispersion of the occupied bands. A plot of photocurrent as a function of energy for a fixed (k_x, k_y) is called the energy distribution curve (EDC), while the momentum distribution curve (MDC) refers to the photocurrent as a function of $k_{\parallel}$ at a fixed energy E_B.

The perpendicular momentum of the initial state, $k_{\perp}$, cannot be determined from ARPES in a direct manner. Extracting $k_{\perp}$ requires knowledge of the final state dispersion, which is generally complicated. This is the well-known "$k_{\perp}$ problem" in photoemission. The $k_{\perp}$ problem is not an issue for two-dimensional systems, because there is no dispersion along the z direction. Most of the systems studied in this thesis are in this category.

The three-step model is only a phenomenological model, because the division of the photoemission process into three steps is artificial and unrealistic. A more rigorous theory of photoemission will be presented in Sec. 3.4.

3.3 ARPES experimental apparatus

Photoemission spectroscopy is notable for its surface sensitivity. It allows the technique to probe surface-related electronic states, but it also restricts the method to detecting only the surface part of a general bulk contribution. Photons usually have no trouble penetrating crystal samples, but the short mean-free path of photoelectrons limits the probing depth. Fig. 3.3 shows a plot of the experimental mean free path λ of electrons as a function of the kinetic energy [7]. The dots are the empirically-determined values of λ for many different materials, showing that λ is almost material independent. Due to the constraint from the photoemission cross section, as well as the energy and momentum resolution, ARPES experiments for valence electrons are typically carried out with the kinetic energy of electrons in the range of 10-200 eV. Considering the mean free path, the useful photoemission intensity comes from only the first few atomic layers of the material. The electrons from deeper layers form a continuous secondary electron background as a result of inelastic scatterings. The surface sensitivity of ARPES requires that the sample surface stays clean and free of contamination during the measurement. Therefore an UHV system is essential for a successful APRES experiment.

Modern electron analyzers employ 2D detectors, which allow for the simultaneous acquisition of energy distribution curves (EDC) at a wide angular range. This feature has greatly enhanced the rate of data acquisition. High angle and energy resolutions make ARPES a leading tool in the investigation of the electronic properties of solid state materials.

First let us have a look at how the hemisphere electron energy analyzer works. A schematic diagram of a hemisphere electron energy analyzer is shown in Fig. 3.4. The electrons from the sample are focused and retarded by the lens and enter the analyzer through the entrance aperture. Only electrons that have the right kinetic energy can go

through the hemisphere analyzer and reach the exit aperture without colliding with the inner walls of the analyzer. The kinetic energy of the electron traveling on the central path $R_0 = \frac{R_1 + R_2}{2}$ is given by

$$E_p = \frac{eV}{\frac{R_2}{R_1} - \frac{R_1}{R_2}}. \tag{3.5}$$

This energy is called the pass energy of the analyzer, and it is determined by the radii of both hemispheres and the voltage applied between them. Electrons that have the same kinetic energy but a different entrance angle can still reach the exit aperture, although they undergo slightly different trajectories. The pass energy is normally fixed during an EDC scan for a constant energy resolution. In order to scan different energies, a retarding voltage is applied at the lens to adjust the electrons to the pass energy.

The energy resolution of a hemisphere analyzer is given by

$$\Delta E = E_p\left(\frac{x_1 + x_2}{2R_0} + \alpha^2\right), \tag{3.6}$$

where x_1 and x_2 are the radii of the entrance and exit apertures, α is the maximum angular deviation of the electron trajectories at the entrance and is determined by the lens system [8]. It is obvious from Eq. (3.6) that a large hemisphere is favored because of a better resolution. The pass energy and the aperture sizes are usually set to achieve a good compromise between signal intensity and energy resolution.

The hemisphere electron analyzer shown in Fig. 3.4 can only measure the photoemission spectrum at one emission angle (EDC) per scan. This makes Fermi surface mapping very time-consuming. The invention of the 2D electron analyzer has greatly

increased the rate of data acquisition. Fig. 3.5 shows a schematic diagram of the 2D electron analyzer. The apertures are replaced by slits, which permits electrons with a wide range of emission angles to enter the analyzer simultaneously. The original point detector is now a 2D detector. The position where an electron hit the 2D detector is determined by the electron's kinetic energy and emission angle. The exact conversion between the positions on the detector and the electron's kinetic energy/emission angle is done by the Scienta software. The energy window on the 2D detector is quite small. Therefore, the retarding voltage still has to be scanned (in the swept mode) if a large energy range is needed.

The acquired data after each scan is a 2D matrix, with one axis being the electron's kinetic energy and the other the emission angle along a certain direction (see Fig. 3.6). Besides the rapid data acquisition rate, the photoemission data taken with the 2D electron analyzer can be directly visualized. In Fig 3.6, the quantum well subbands of a 22 monolayer Ag film can be clearly identified even in the original ARPES spectrum.

3.4 Theory of photoemission spectroscopy

The theoretical interpretation of photoemission in this section follows the previous works [1,6,9,10,11] An important concept in the theory of photoemission spectroscopy is the sudden approximation. It means that the response of the system to the photoexcitation is assumed instantaneous and that there is no interaction between the escaping photoelectron and the remaining system [1]. In Eqn. 3.1, the wave function of the initial state can be written in the form of a Slater determinant as,

$$\Psi_i^N = C\phi_i^{\mathbf{k}}\Psi_i^{N-1}, \tag{3.7}$$

where $\phi_i^{\mathbf{k}}$ is the orbital with momentum **k** from which the electron is excited, Ψ_i^{N-1} is

the wave function of the remaining (N-1) electrons and C is the operator that antisymmetrizes the wave function. The wave function of the final state under the sudden approximation can be written as a product of the wavefunction of the photoemitted electron $\phi_f^{\mathbf{k}}$ and that of the remaining (N-1) electrons Ψ_f^{N-1},

$$\Psi_f^N = C\phi_f^{\mathbf{k}}\Psi_f^{N-1}, \tag{3.8}$$

Therefore, the matrix element in Eq. (3.1) is obtained as

$$\left\langle \Psi_f^N \middle| H_{\text{int}} \middle| \Psi_i^N \right\rangle = M_{f,i}^{\mathbf{k}} \left\langle \Psi_f^{N-1} \middle| \Psi_i^{N-1} \right\rangle, \tag{3.9}$$

where $\left\langle \phi_f^{\mathbf{k}} \middle| H_{\text{int}} \middle| \phi_i^{\mathbf{k}} \right\rangle \equiv M_{f,i}^{\mathbf{k}}$ is the one-electron matrix element, and the second term is the (N-1)-electron overlap integral. In the first step of evaluating the overlap integral, one can assume that the remaining orbitals are the same in the final state as they were in the initial state (frozen-orbital approximation), meaning that $\Psi_f^{N-1} = \Psi_i^{N-1}$. This renders the overlap integral unity, and the transition matrix element is just the one-electron matrix element. Under this assumption, the photoemission experiment probes only the one-electron state (from $\phi_i^{\mathbf{k}}$ to $\phi_f^{\mathbf{k}}$) which does not interact with the remainder of the (N-1) electrons. Of course, this cannot be a very good approximation.

In reality this simple picture breaks down because the excitation of an electron from $\phi_i^{\mathbf{k}}$ disturbs the remaining (N-1) electrons. The remaining system will readjust itself in such a way as to minimize its energy (relaxation). We now assume that the final state with (N-1) electrons has many possible excited states (labeled by s) with wave function $\Psi_{f,s}^{N-1}$ and energy E_s^{N-1}. Therefore, the total photoemission intensity measured as a function of electron kinetic energy at a momentum **k** is

$$I(\mathbf{k}, E_{\text{kin}}) = \sum_{f,i} \left| M_{f,i}^{\mathbf{k}} \right|^2 \sum_s \left| c_s \right|^2 \delta(E_K + E_s^{N-1} - E_i^N - h\nu), \tag{3.10}$$

where $\left| c_s \right|^2 = \left| \left\langle \Psi_s^{N-1} \middle| \Psi_i^{N-1} \right\rangle \right|^2$ is the probability that the removal of an electron from the initial state **k** from the *N* electron ground state will leave the (N-1)-electron system in the excited state *s*. For strongly correlated systems, many of the c_s will be nonzero because the removal of the photoelectron results in a strong change of the system's effective potential and, in turn, Ψ_i^{N-1} will overlap with many of the eigenstates Ψ_s^{N-1}. Thus, the ARPES spectrum will not be a single delta function, but will instead show a main line and several satellites according to the number of excited states *s* created in the process.

The term $\sum_s \left| c_s \right|^2 \delta(E_K + E_s^{N-1} - E_i^N - h\nu)$ in Eq. (3.10) is essentially the one-particle spectral function. To see this, the wave function Ψ_i^{N-1} can be expressed as $\Psi_i^{N-1} = c_{\mathbf{k}} \Psi_i^N$, where $c_{\mathbf{k}}$ is the annihilation operator for an electron with wave vector **k**. This term can be rewritten as

$$\sum_s \left| \left\langle \Psi_s^{N-1} \middle| c_{\mathbf{k}} \middle| \Psi_i^N \right\rangle \right|^2 \delta(\omega - E_s^{N-1} + E_i^N). \tag{3.11}$$

This is exactly the spectral function with wave vector **k** and energy $\omega = h\nu - E_K$. For a 2D single-band system, one can write the intensity measured in an ARPES experiment as

$$I(\mathbf{k}, \omega) = I_0(\mathbf{k}, v, \mathbf{A}) f(\omega) A(\mathbf{k}, \omega), \tag{3.12}$$

where $\mathbf{k}=\mathbf{k}_{//}$ is the in-plane electron momentum, ω is the electron energy with respect to

the Fermi level, and $I_0(\mathbf{k}, v, \mathbf{A})$ is proportional to the squared one-electron matrix element $\left|M_{f,i}^{\mathbf{k}}\right|^2$, which depends on electron momentum **k**, and on the energy and polarization of the incoming photon. $f(\omega)$ is the Fermi-Dirac function, which accounts for the fact that photoemission probes only the occupied electronic states. $A(\mathbf{k}, \omega)$ is the spectral function. Therefore, Eq. (3.12) shows that the photoemission intensity is essentially the product of the squared matrix element $I_0(\mathbf{k}, v, \mathbf{A})$ and the spectral function of the electron. For many 2D systems, $I_0(\mathbf{k}, v, \mathbf{A})$ is a slowly varying function of electron momentum and photon energy, and therefore can be viewed as a constant within a small momentum and energy space. In these cases, photoemission directly probes the spectral function.

The spectral function is of crucial importance for understanding many-body physics. The spectral function is directly related to the Green's function as

$$A(\mathbf{k}, \omega) = \frac{\mathrm{Im}\{G(\mathbf{k}, \omega)\}}{\pi}. \tag{3.13}$$

In a correlated electron system, the Green's function is described in terms of the electron self-energy $\Sigma(\mathbf{k}, \omega)$. The real and imaginary parts of the self-energy contain all the information about the energy renormalization and lifetime of an electron with band energy $\varepsilon_{\mathbf{k}}$ and momentum **k**. The Green's function can be expressed as

$$G(\mathbf{k}, \omega) = \frac{1}{\omega - \varepsilon_{\mathbf{k}} - \Sigma(\mathbf{k}, \omega)}. \tag{3.14}$$

The corresponding spectral function is

$$A(\mathbf{k},\omega) = -\frac{1}{\pi}\frac{\mathrm{Im}\,\Sigma(\mathbf{k},\omega)}{[\omega - \varepsilon_{\mathbf{k}} - \mathrm{Re}\,\Sigma(\mathbf{k},\omega)]^2 + [\mathrm{Im}\,\Sigma(\mathbf{k},\omega)]^2}. \tag{3.15}$$

Note that $\varepsilon_{\mathbf{k}}$ is the bare band energy of the electron, assuming there is no electron-electron correlation. It is obvious from Eq. (3.15) that the resulting spectral function is a Lorentzian function.

When there is no interaction between the electrons, i.e., $\Sigma(\mathbf{k},\omega) = 0$, the spectral function is a delta function at $\varepsilon_{\mathbf{k}}$. If the electron-electron correlation is adiabatically switched on, the system remains at equilibrium. However, any electron added into a Bloch state has a certain probability of being scattered out of it by a collision with another electron, leaving the system in an excited state in which additional electron-hole pairs have been created. The result of this electron-electron correlation is that the energy and lifetime of the electrons are changed. The slightly modified electron (with normalized mass), described by Eq. (3.15), is generally called a quasiparticle. One can view this quasiparticle as an electron dressed by virtual excitations that move coherently with the electron through the crystal. In a correlated electron system, the spectral function is a Lorentzian function, with its center and width determined by the energy and lifetime of the quasiparticle, respectively.

Photoemission which probes the spectral function of the electron can be used to study the quasiparticle dynamics in correlated electron systems. The peak positions and linewidths are directly related to the electron self-energy, which makes ARPES a powerful tool for studying many-body physics. It should be noted that the above derivation is generally carried out for 2D electron systems where the spectral function primarily determines the spectrum features. For 3D electron systems, the one-electron matrix element could play the dominant role instead.

Photoemission spectra measured at various photon energies effectively probe the electronic states with different $k_\perp$ s. The reason is as follows: the energy conservation (Eq. (3.1)) requires that the photoexcited electron gains the energy of the incoming photon $h\nu$. In addition, the dipole transition term in (3.2), $\boldsymbol{A}\cdot\boldsymbol{p}$ preserves the crystal momentum of the electron during photoexcitation. Therefore, the photoexcitation caused by the dipole transition term is a direct optical transition [3]. In the case of a three-dimensional crystal, the direct transition can only occur at a specific $k_\perp$ for a given photon energy (See Fig. 3.7(b)). As the photon energy is swept, electronic states with different $k_\perp$ is probed accordingly. This photon energy dependence is demonstrated in Fig. 3.7 (a) as the displacement of the direct transition peak at different photon energies. In order to investigate the dispersion along the k_z direction, photoemission spectra must be taken at various photon energies. If the quasiparticle peak positions do not move when the photon energy is varied, there is no dispersion along the *z* direction.

As mentioned in Sec. 3.2, the contribution from the $\nabla\cdot\boldsymbol{A}$ term is not necessarily small, especially near the surface. The dielectric discontinuity near the surface gives rise to an abrupt change in $A_\perp$, which, upon differentiation, yields a delta function at the surface [3]. As a result, the matrix element between the initial and final states $\left\langle \phi_f^{\mathbf{k}} \middle| \nabla\cdot\boldsymbol{A} \middle| \phi_i^{\mathbf{k}} \right\rangle$ is generally nonzero provided that both states have non-zero amplitude at the surface. The contribution from this surface term to the transition matrix element is proportional to the product of the amplitudes of the wavefunctions at the surface, namely, $C\phi_f^{\mathbf{k}}{}^*(z_0)\phi_i^{\mathbf{k}}(z_0)$, where z_0 denotes the surface position. The coefficient *C* is approximately proportional to the difference between the internal and external fields, namely, $(\varepsilon-1)A$, where ε is the dielectric constant of the material. The resulting

spectral contribution from this surface term generally resembles the one-dimensional joint density of states.

Surface transition has been observed in many cases among which is the normal emission spectrum of the Ag(111) surface as shown in Fig. 3.8. The direct transition peak from the Ag *sp* bulk band exhibits a pronounced asymmetry with a long tail extending to higher energy. This asymmetry arises from the spectral contribution of the surface transition term which resembles the density of valence states. In general, the dipole transition term dominates in photoemission when direct transition is allowed and surface transition gives rise to only a small modification to the lineshape of the direct transition peaks. However, when the direct transition is forbidden by certain selection rules, surface transition will play a dominant role in the photoemission spectrum.

References:

[1] S. Hüfner, *Photoelectron Spectroscopy*, (Springer-Verlag, New York, 1996).

[2] H. J. Levinson, E. W. Plummer and P. J. Feibelman, Phys. Rev. Lett. **43**, 952 (1979).

[3] T. Miller, W. E. McMahon and T.-C. Chiang, Phys. Rev. Lett. **77**, 1167 (1996).

[4] W. Spicer, Phys. Rev. **112**, 114 (1958).

[5] E. Rotenberg, *2001 Berkeley-Stanford Summer School Lecture* (2001).

[6] A. Damascelli, Z. Hussain, and Z.-X. Shen, Rev. Mod. Phys. **75**, 473 (2003).

[7] G. Somorjai, *Chemistry in Two Dimensions: Surfaces* (Cornell University Press, Ithaca, 1981).

[8] H. Lüth, *Solid Surfaces, Interfaces and Thin Films* (Springer, 4ed, 2001).

[9] W. Schattke and M. A. Van Hove, *Solid-State Photoemission and Related Methods: Theory and Experiment* (Wiley-VCH, 2003).

[10] E. W. Plummer and W. Eberhardt, Advances in Chemical Physics **49**, 533 (1982).

[11] Y. Liu, A*ngle-resolved photoemission studies of two-dimensional electron systems,* Ph.D. thesis, University of Illinois at Urbana-Champaign (2010).

Figures:

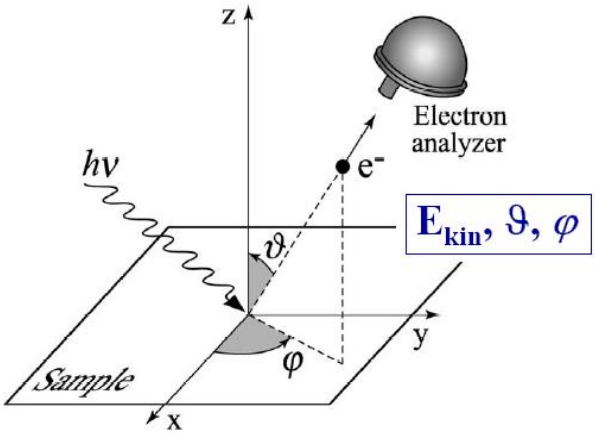

Figure 3.1. A schematic showing the angle-resolved photoemission geometry. *hv* is the incoming photon energy, and θ is the polar emission angle.

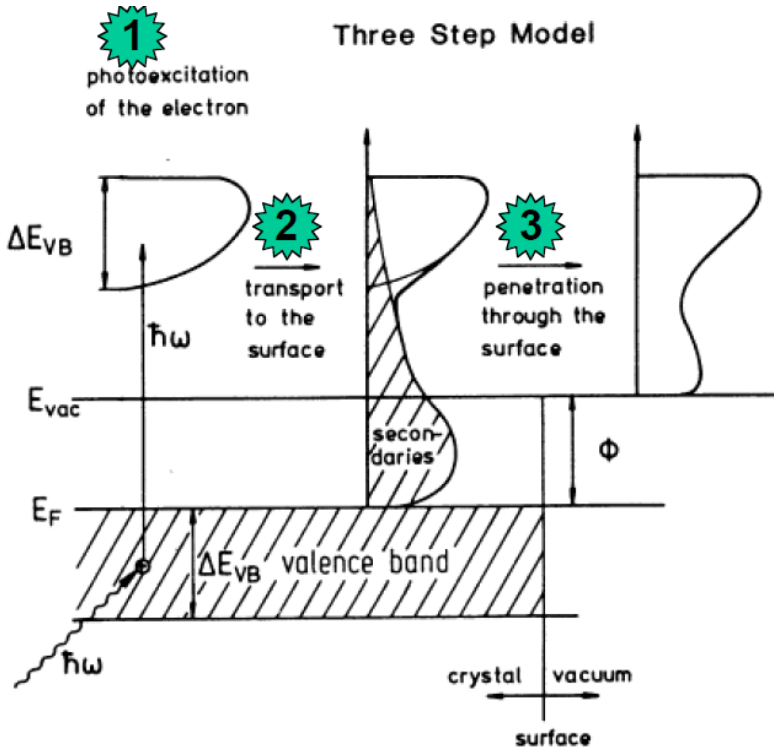

Figure 3.2. The photoemission process based on the three-step model [5].

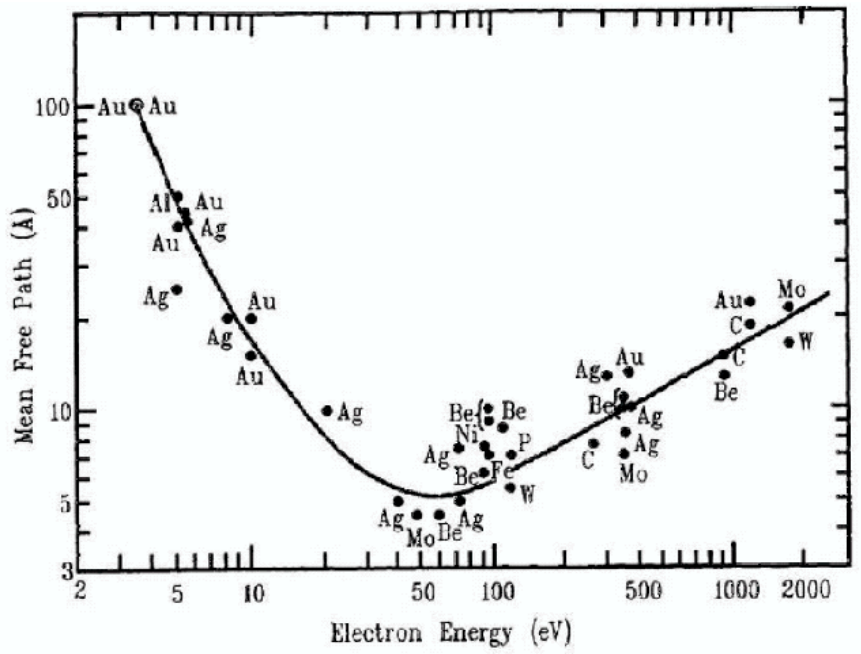

Figure 3.3. Universal curve of the mean free path for inelastic scattering of electrons in a solid [7].

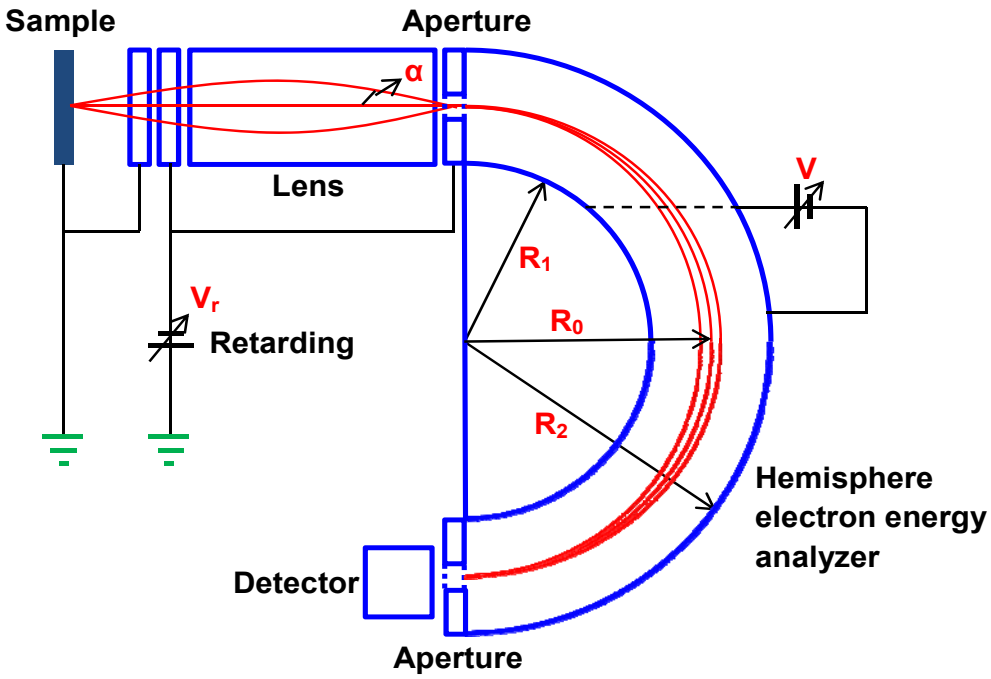

Figure 3.4. Schematic of a hemisphere electron energy analyzer.

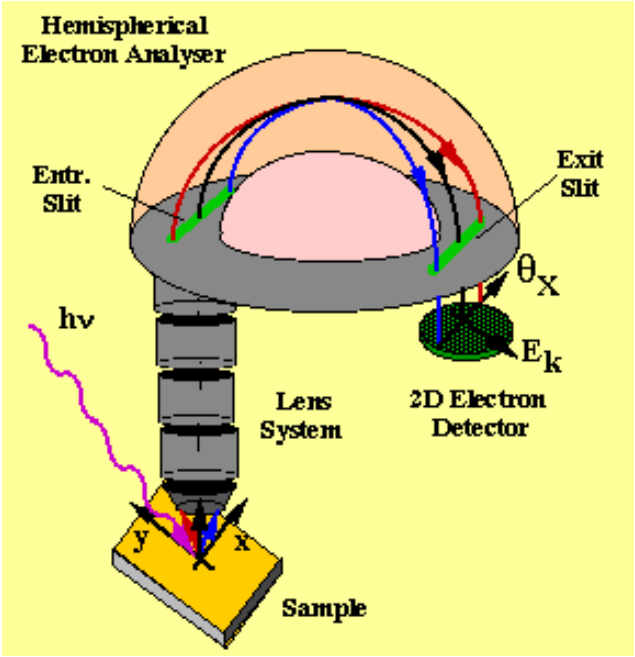

Figure 3.5. Schematic of a 2D electron analyzer.

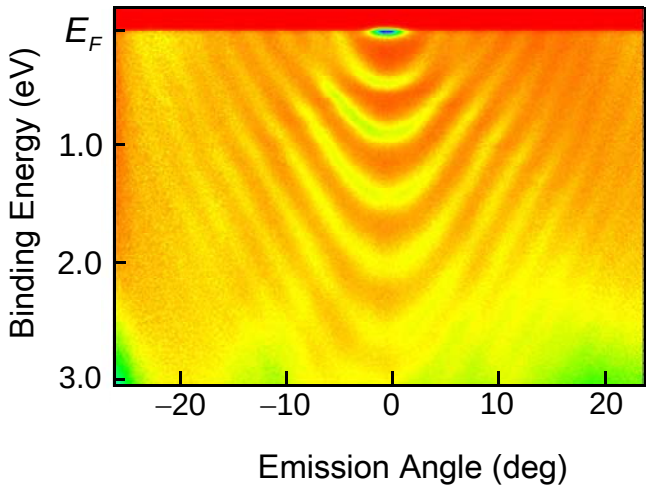

Figure 3.6. Original photoemission spectrum taken from a 22 ML Ag film on Si(111) along $\overline{\Gamma}\overline{\mathrm{M}}$ direction.

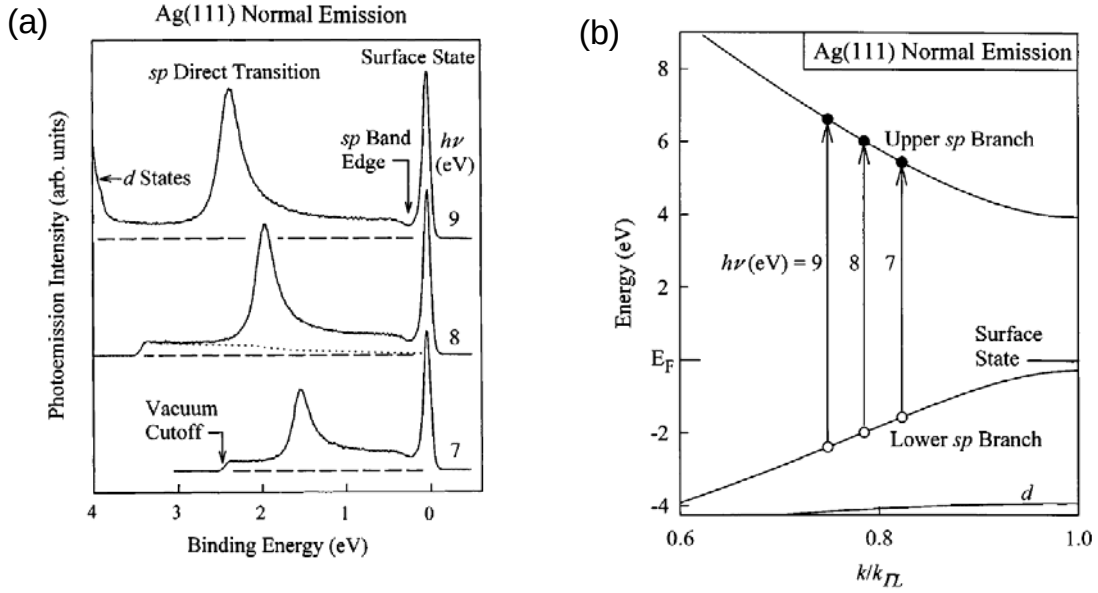

Figure 3.7. (a) Normal emission spectra from Ag(111) taken with photon energies of 7, 8, and 9 eV as indicated. (b) Band structure of Ag along the [111] direction. The horizontal axis is the wave vector normalized to the distance between the zone center and the zone boundary. Direct transitions for photon energies of 7, 8, and 9 eV are indicated by vertical arrows [3].

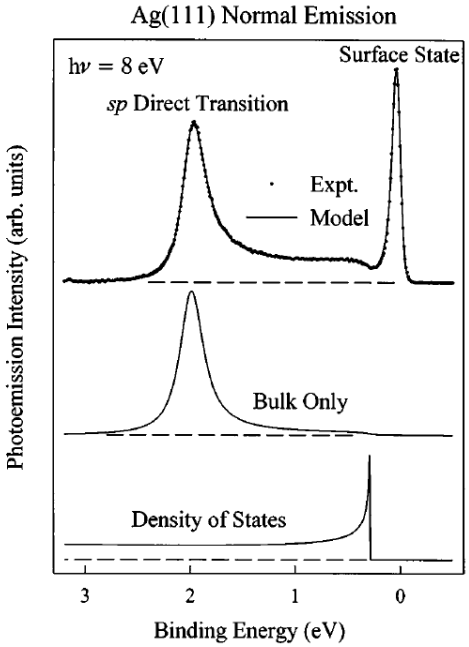

Figure 3.8. Surface transition in Ag(111) [3]. Top: a model fit (curve) to the normal emission spectrum (circles) of Ag(111), taking into account both the dipole transition and surface transition. Middle: spectral contribution from the dipole transition term. Bottom: the density of valence states.

4 Theoretical Background

4.1 Introduction

This chapter provides the necessary theoretical background for understanding the works reported in this thesis. Surface states, quantum well, Rashba effect and topological order are the key concepts in the discussion of topological thin films and the Bi/Ag surface alloy with a giant spin splitting, and those concepts are introduced in Sec. 4.2-4.5. Sec. 4.6 will present a brief introduction to the calculation method employed in this dissertation: density functional theory (DFT).

4.2 Surface states

The termination of a material with a surface not only gives rise to the surface relaxation and reconstruction, but also strongly modifies the electronic structure at the surface. Breaking of the lattice periodicity allows the existence of new states beyond the Bloch bulk states. The wavefunctions of those new states are localized near the surface, and thus they are accordingly termed surface states [1]. Their energy levels are found in the band gaps where bulk states are not allowed. Intuitively the surface states can be viewed as electronic states which are trapped by the band gap on one side of the surface and the surface barrier potential, which prevents electrons from escaping into the vacuum, on the other side.

Although the surface states are confined in the surface normal direction, they may well delocalized in the two dimensions parallel to the surface. This can lead to the formation of two-dimensional energy bands in the surface Brillouin zone (SBZ), $\boldsymbol{k}_{\parallel}$. In

order to examine the behavior of surface electrons, one needs to compare the surface bands with the bulk bands projected to the surface [2]. Fig. 4.1 gives such a comparison. Suppose the bulk band disperse along $\boldsymbol{k}_{\perp}$, the wavevector perpendicular to the surface, in the manner as shown in the left upper panel of Fig. 4.1. The width of this band then gives the continuum of allowed states in the surface reciprocal space, and the projected bulk bands are widened to have the shape of, say, the hatched area along a particular $\boldsymbol{k}_{\parallel}$ direction. Surface states may exist in the gap of the projected bulk bands as shown in the upper middle panel. In such a case, the states must be localized near the surface as they are not allowed in the bulk. Thus the wavefunctions of the surface states decay rapidly towards the interior of the solid as illustrated in the lower middle panel. If, however, a surface band stays in the band gap for only a limited range of $\boldsymbol{k}_{\parallel}$ and overlaps with the projected bulk bands for other $\boldsymbol{k}_{\parallel}$, as shown in the right upper panel, then the wavefunction will be gradually evanescent towards the bulk as shown in the right lower panel. These states inside the bulk band region are called surface resonance states. Both surface state and surface resonance are experimentally observable by photoemission spectroscopy, but a clear discrimination between the two is not always accessible. Fig. 4.2 shows projected bulk band structure (hatched area), surface states (solid curves) and surface resonances (dashed curves) for three ideal silicon surfaces [3]. The Ag(111) surface has a surface state at the zone center very close to the Fermi level, see the ARPES spectrum of the Ag (111) film in Fig. 3.6.

4.3 Quantum well states

If the film thickness is comparable to the coherence length of the electron, the electrons can bounce back and forth between the two boundaries of the film and form electronic standing waves, known as quantum well states (QWS). For thin films,

quantum well states are often the dominant features, giving rise to quantum size effects. The situation in the film normal direction is just like a 1D quantum box (Fig. 4.3(a)). The allowed momenta along the z direction are discrete and depend on the film thickness and boundary conditions (Fig. 4.3 (b)). As a consequence, the continuum of the valence band is quantized in the k_z direction (Fig. 4.3 (c)). Considering the dispersion along the k_x and k_y directions, say, free-electron like, the band structure of the thin film will consist of a set of parabolic quantum well subbands (Fig. 4.3(d)).

Calculating the QWSs in a rigorous manner requires solving the Schrődinger equation for the whole film-substrate system. This can be achieved by means of the modern first-principles method. The band structure of a 20 ML freestanding Ag(111) film is shown in Fig. 4.4. The parabolic quantum well subbands are derived from the *sp* valence orbitals of Ag while the densely packed flat bands are from the *d* orbitals of Ag. The quantum well states of thin films can be readily examined by ARPES as shown previously in Fig.3.6.

A much simpler way to interpret the QWS is given by the analogy between QWS and the Fabry-Pérot interferometer [4]. In this phenomenological picture, QWS is formed by multiple reflections of electron between the two confining boundaries (Fig. 4.5). Therefore, electron waves are modulated by an interference factor

$$\frac{1}{1 - r_s r_i \exp[i(2kNt + \Phi_s + \Phi_i)]\exp(-Nt / \lambda)}, \tag{4.1}$$

where r_s and r_i are the reflectivities at the surface and the interface, respectively, k is the electron wave vector, N is the film thickness in monolayers, t is the monolayer thickness, Φ_s and Φ_i are the phase shifts at the surface and interface, and λ is the quasiparticle mean free path. The photoemission intensity is proportional to the absolute square of the factor in Eqn. 4.1. Thus, the photoemission spectrum for a quantum well becomes

$$I \propto \frac{1}{1+\left(\frac{4f^2}{\pi^2}\right)\sin^2(kNt+\frac{\Phi_s+\Phi_i}{2})}, \tag{4.2}$$

where f is the Fabry-Pérot finesse (ratio of the peak separation to the peak width) given by [5]

$$f = \frac{\pi\sqrt{r_i r_s}\exp(-Nt/2\lambda)}{1-r_i r_s \exp(-Nt/\lambda)}. \tag{4.3}$$

Eqn. (4.2) yields a set of peaks at positions where the sine function in the denominator equals zero, and the resulting condition is just the Bohr-Sommerfeld quantization rule

$$2k(E)Nt + \Phi_i(E) + \Phi_s(E) = 2n\pi\,. \tag{4.4}$$

The quantization condition states that the accumulated phase shift after a round trip should be an integer of 2π. The peak width δE is

$$\delta E = \hbar\Gamma\eta\frac{1-r_s r_i \exp(-1/\eta)}{\sqrt{r_s r_i}\exp[-1/(2\eta)]}, \tag{4.5}$$

where Γ is the quasiparticle inverse lifetime which is related to the group velocity ν by Γ=ν/λ, and η= λ/(Nt). The quantities k and Γ (related to the real and imaginary parts of the electron self-energy) as well as r and Φ (related to the confinement potential) are of basic interest and completely determine the interferometer properties. While k and Φ determine the peak positions through Eq. (4.4), Γ and r control the peak width through Eq. (4.5). They all depend on the electron energy E, but not on the film thickness N. The Fabry-Pérot analysis of QWS has proven to be very successful for explaining many phenomena related to QWS. For example, the normal emission curves taken from Ag films on Fe(100) have been perfectly fitted using the Fabry-Pérot solutions.

Generally, the electron wave vector k and group velocity ν as a function of energy are derived from the bulk band structure. The reflectivity at the surface, r_s, should be unity. The reflectivity at the interface, r_i, depends on the interface potential and the

electron energy. The phase shifts, Φ_i and Φ_s, are related to the logarithmic derivatives of the wave functions at the boundaries. The electron mean free path is normally much larger than the film thickness (for *sp* electrons). Therefore, Eq. (4.5) can be simplified as

$$\delta E = \frac{\hbar v}{Nt} \frac{1 - r_i}{\sqrt{r_i}}. \tag{4.6}$$

The substrate modifies the QWS energy positions and the peak widths, through the reflectivity and phase shift at the interface (Eqns. (4.4) and (4.5)). When r_i is less than 1, the QWS becomes a quantum well resonance because the wave function penetrates into the substrate and forms a resonant state.

When the Fermi wave vector k_F is not at the zone boundary like the case shown in Fig. 4.3(c), the QWS crosses the Fermi level periodically as the film thickness N varies according to Eq. (4.4). The periodicity is simply

$$\Delta N = \pi / (k_F t). \tag{4.7}$$

This periodic crossing of QWS at the Fermi level brings about an oscillation of the density of states (DOS) at the Fermi level as a function of N. Since the DOS at the Fermi level is closely related to many physical properties such as resistivity, superconducting transition temperature, thermal stability, etc., these physical properties are expected to exhibit oscillating behavior when the film thickness varies [6].

4.4 Rashba effect

The Rashba effect is a momentum dependent spin splitting of electronic bands in two dimensional condensed matter systems (heterostructures and surface states) [7]. This spin splitting effect is a combined effect of atomic spin-orbit coupling and space inversion asymmetry (SIA) caused by the potential in the direction perpendicular to the two-dimensional plane. The essential physics can be easily seen in a simple model of an

ideal 2D electron gas propagating in the vertical electric field $\boldsymbol{E} = E_0\hat{z}$. Due to relativistic corrections an electron moving with velocity **v** in the electric field will experience an effective magnetic field **B,**

$$\boldsymbol{B} = \boldsymbol{v} \times \boldsymbol{E} / c^2, \tag{4.8}$$

where c is the speed of light. This magnetic field couples with the electron spin

$$H_{SO} = \frac{\mu_B}{2c^2}(\boldsymbol{v} \times \boldsymbol{E}) \cdot \boldsymbol{\sigma}, \tag{4.9}$$

where the factor 1/2 is a result of the Thomas precession and $\boldsymbol{\sigma}$ are Pauli matrices. Within this simple model, the Rashba Hamiltonian is given by

$$H_R = \alpha_R(\boldsymbol{\sigma} \times \boldsymbol{p}) \cdot \hat{z}, \tag{4.10}$$

where $\alpha_R = \frac{\mu_B E_0}{2mc^2}$.

The band structure of the ideal 2D electron gas with Rashba spin splitting around the $\bar{\Gamma}$ point ($\boldsymbol{k}_{\|}$=0) of the surface Brillouin zone is shown in Fig. 4.7 [8]. A cut along an arbitrary direction through $\bar{\Gamma}$ gives a characteristic dispersion of two split parabolas,

$$E_{\pm}(\boldsymbol{k}_{\|}) = E_0 + \frac{\hbar^2 k^2}{2m^*} \pm \alpha_B |k| = E_0' + \frac{\hbar^2}{2m^*}(k \pm k_0)^2, \tag{4.11}$$

where $k_0 = \alpha_R m^* / \hbar^2$ is the momentum offset of the band maximum and m^* is the effective mass which is negative in this case. The band dispersion can be divided in two qualitatively different region. If E lies below E_0, in region II, the constant energy contour consists of two circles of opposed spin helicities and the density of states (DOS) does not differ from that of the case without the SOC. If E is above E_0, in region I, the two circles have identical helicity and the DOS switches to a $1/\sqrt{E}$ behavior.

The Rashba model in solids can be derived in the framework of the $\boldsymbol{k} \cdot \boldsymbol{p}$ theory

[9] or from the point of view of a tight binding approximation [10]. However, the specific calculations are quite tedious. The intuitive model gives qualitatively the same physics given a good estimate of the Rashba parameter α_R. A more detailed discussion on the Rashba effect will be presented in Chapter 8.

4.5 Topological insulator and topological order

Topological insulator is a fundamentally new phase of electronic matter that has captured a lot of research interest over past several years. Topological insulators exhibit a rare type of behavior called topological order which describes the organized movement of the electrons in the crystal. There have been many excellent review articles on topological insulators [11,12]. Here we only present an intuitive physical picture which can be directly tested by ARPES measurements. A consequence of the topological order is that the surface electron spectrum of a topological insulator is qualitatively distinct from any ordinary material in such a way that it allows surface electrons flow without being scattered by impurities. In an ordinary insulator with spin-orbit coupling, there can be spin-polarized surface states that span the bulk energy gap as shown in Fig. 4.8. For ordinary insulators these surface states always disperse such that they form even number Fermi surface contours around time reversal invariant momenta (TRIM, $\mathbf{k}_1$ and $\mathbf{k}_4$ in Fig. 4.8). In topological insulator, however, the number of Fermi surface contours is odd. This even or odd count is a topological distinction and it's obvious that this method of counting relies on the fact that the material is a bulk insulator. Because of the opposite spin orientations in the two branches of the surface band, the backscattering of surface electrons is not allowed in the topological insulator and the overall gapless connection pattern of surface states to the bulk bands is protected as a subtle consequence of the time reversal symmetry.

Our group has successfully fabricated the topological insulator Bi_2Te_3 thin films of

high structural quality [13]. The ARPES spectra taken from those topological thin films are shown in Fig. 4.9 in which the quantum well states (QWS) and topological surface states (TSS) are clearly mapped out. The QWSs with energies between about –0.4 to –0.6 eV split into more and more subbands as the film thickness increases from 2 to 5 QLs. These layer-resolved QWSs provide a means to accurately calibrate the exact thickness of each film. The V-shaped TSS band spanning the whole bulk band gap and the single hexagonal constant energy contour around the zone center $\bar{\Gamma}$ point unambiguously demonstrate the nontrivial topological order of Bi_2Te_3. More discussion on topological insulator and topological order can be found in Ch. 5 and Ch. 6.

4.6 Density functional theory

The first-principles calculation employed in this thesis are based on density functional theory (DFT) which is a quantum mechanical modeling method used in physics and chemistry to investigate the electronic structure of many-body systems such as atoms, molecules, and the condensed matters. Within this theory, the properties of a many-electron system can be determined by a functional of the spatially dependent electron density [14,15]. The DFT approach is to replace the difficult interacting many-body system with an auxiliary non-interacting system that can be solved more easily [16]. This leads to independent-particle equations for the non-interacting system that can be considered soluble by numerical means with all the difficult many-body terms incorporated into an exchange-correlation functional of the density. The calculation accuracy is limited only by the approximations in the exchange-correlation functional.

For a non-interacting system, the ground state can be written in the form of a Slater determinant as,

$$\Psi(\boldsymbol{r}) = C\prod_{i=1}^{N}\psi_i(\boldsymbol{r}), \tag{4.12}$$

where ψ_i is the one-particle wavefunction and C is the operator that antisymmetrizes the wave function. The density of the auxiliary system is given by sums of squares of the orbitals for each particle

$$n(\boldsymbol{r}) = \sum_{i=1}^{N} n_i(\boldsymbol{r}) = \sum_{i=1}^{N} \left|\psi_i(\boldsymbol{r})\right|^2 . \tag{4.13}$$

The independent-particle kinetic energy is given by

$$T = -\frac{1}{2m}\sum_{i=1}^{N}\left\langle \psi_i \left| \nabla^2 \right| \psi_i \right\rangle = \frac{1}{2m}\sum_{i=1}^{N}\int d\boldsymbol{r}\left|\nabla\psi_i(\boldsymbol{r})\right|^2 , \tag{4.14}$$

and the classical Coulomb interaction energy of the electron density n(**r**) interacting with itself is defined as

$$E_{Hatree}[n] = \frac{1}{2}\int d\boldsymbol{r}d\boldsymbol{r}'\frac{n(\boldsymbol{r})n(\boldsymbol{r}')}{\left|\boldsymbol{r}-\boldsymbol{r}'\right|} . \tag{4.15}$$

The ground state energy functional for the auxiliary non-interacting system can be expressed in the form

$$E_{DFT} = T[n] + \int d\boldsymbol{r} V_{ext}(\boldsymbol{r})n(\boldsymbol{r}) + E_{Hatree}[n] + E_{II} + E_{XC}[n], \tag{4.12}$$

where V_{ext} ($\boldsymbol{r}$) is the external potential due to the nuclei and any other external fields, E_{II} is the interaction between the nuclei and E_{XC} is the exchange-correlation functional of the density. Solution of the auxiliary system for the ground state can be considered as the problem of minimization with respect to the density n(**r**). The Schrödinger-like equation for each particle can be derived by varying the ground state energy functional E_{DFT},

$$(H_{DFT} - \varepsilon_i)\psi_i(\boldsymbol{r}) = 0, \tag{4.13}$$

where ε_i are the eigenvalues, and H_{DFT} is the effective Hamiltonian,

$$H_{DFT}(\boldsymbol{r}) = -\frac{1}{2}\nabla^2 + V_{DFT}(\boldsymbol{r}), \tag{4.14}$$

with

$$V_{DFT}(\boldsymbol{r}) = V_{ext}(\boldsymbol{r}) + \frac{\delta E_{Hatree}}{\delta n(\boldsymbol{r})} + \frac{\delta E_{XC}}{\delta n(\boldsymbol{r})} = V_{ext}(\boldsymbol{r}) + V_{Hatree}(\boldsymbol{r}) + V_{XC}(\boldsymbol{r}). \tag{4.15}$$

The solution of the independent-particle equations, Eqn. (4.13), must be found self-consistently with the resulting density as shown in the diagram of Fig. 4.10. These equations are independent of any approximation to the functional $E_{XC}[n]$, and would lead to the exact ground state density and energy for the interacting system, if the exact functional $E_{XC}[n]$ were known.

The major problem with DFT is that the exact exchange and correlation functionals are unknown except for the free electron gas. However, approximations have been found which permit the calculation of physical quantities in many cases quite accurately. In physics the most widely used approximation is the local-density approximation (LDA), where the functional depends only on the density at the coordinate where the functional is evaluated,

$$E_{XC}^{LDA}[n] = \int d\boldsymbol{r}\varepsilon_{XC}(n)n(\boldsymbol{r}), \tag{4.16}$$

where $\varepsilon(n)$ is a function, rather than a functional, of the density n. Another popular approximation is the generalized gradient approximation (GGA). GGA is still local like LDA but also take into account the gradient of the density at the same coordinate,

$$E_{XC}^{GGA}[n] = \int d\boldsymbol{r}\varepsilon_{XC}(n,\nabla n)n(\boldsymbol{r}). \tag{4.17}$$

In this thesis, LDA is mostly employed for the first-principles calculations while there are situations where GGA is used to test the robustness of the calculation results.

The density functional theory could not have been so successful without the development of modern pseudopotentials. The pseudopotential theory is based on the fact

that many properties like conductivity and chemical bondings are governed only by valence electrons, with core electrons being inert. Pseudopotentials replace the strong Coulomb potential of the nucleus and the effects of the inert core electrons by an effective ionic potential acting on the valence electrons. This reduces, sometimes drastically, the number of electrons needed to solve. Even more importantly, this results in much smoother wave functions for the remaining valence electrons, making the problem much easier to solve numerically. The pseudopotential approach reduces greatly the computational power required for DFT calculations, making considerably complex tasks manageable even on desktop computers. A description of the software and pseudopotentials employed for our first-principles calculations will be given in Appendix A.

References:

[1] S. G. Davison and M. Steslicka, *Basic Theory of Surface States* (Clarendon Press,1992).

[2] X. Ding, X. Yang and X. Wang, *Surface Physics and Surface Analysis* (Fudan University Press, 2004).

[3] A. Zangwill, *Physics at Surfaces* (Cambridge University Press, 1988).

[4] J. J. Paggel, T. Miller, and T.-C. Chiang, Science **283**, 1709 (1999).

[5] M. Born, and E. Wolf, *Principles of Optics* (Pergamon, New York, ed. 6, 1980).

[6] T.-C. Chiang, Science **306**, 1900 (2004).

[7] Y. A. Bychkov and E. I. Rashba, J. Phys. C **17**, 6039 (1984).

[8] L. Moreschini et al., Phys. Rev. B **80**, 035438 (2009).

[9] R. Winkler, *Spin-orbit Coupling Effects in Two-Dimensional Electron and Hole Systems* (Springer, New York, 2003).

[10] L. Petersen and P. Hedegård, Surface Science **459**, 49 (2000).

[11] M. Z. Hasan and C. L. Kane, Rev. Mod. Phys. **82**, 3045 (2010).

[12] X. L. Qi and S. C. Zhang, Rev. Mod. Phys. **83**, 1057 (2011).

[13] Y. Liu, G. Bian, T. Miller, M. Bissen and T.-C. Chiang, Phys. Rev. B **85**, 195442 (2012).

[14] P. Hohenberg and W. Kohn, *Phys. Rev.* **136**, B864 (1964).

[15] W. Kohn and L. J. Sham, *Phys. Rev.* **140**, A1133 (1965).

[16] R. Martin, *Electronic Structure: Basic Theory and Practical Methods* (Cambridge University Press, 2008).

Figures:

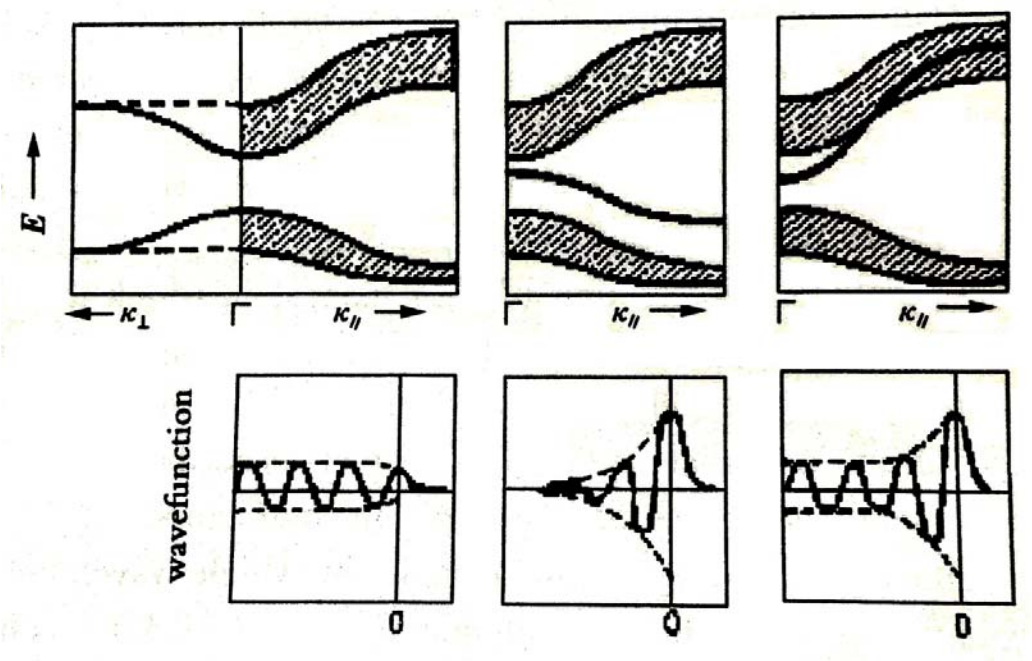

Figure 4.1. Schematic illustration of the surface states as compared with the projected bulk bands (the hatched area) [2]. Left: projected bulk bands and a bulk state. Middle: a surface band (the solid line) and a surface state. Right: a surface resonance. The "0" denotes the surface position.

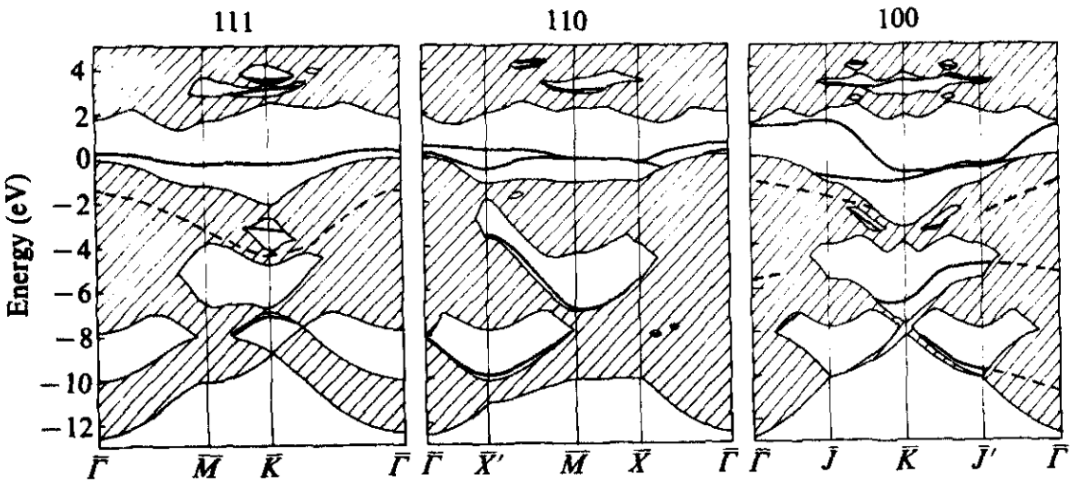

Figure 4.2. Projected bulk band structure (hatched area), surface states (solid curves) and surface resonances (dashed curves) for three ideal silicon surfaces (111), (110) and (100) [3].

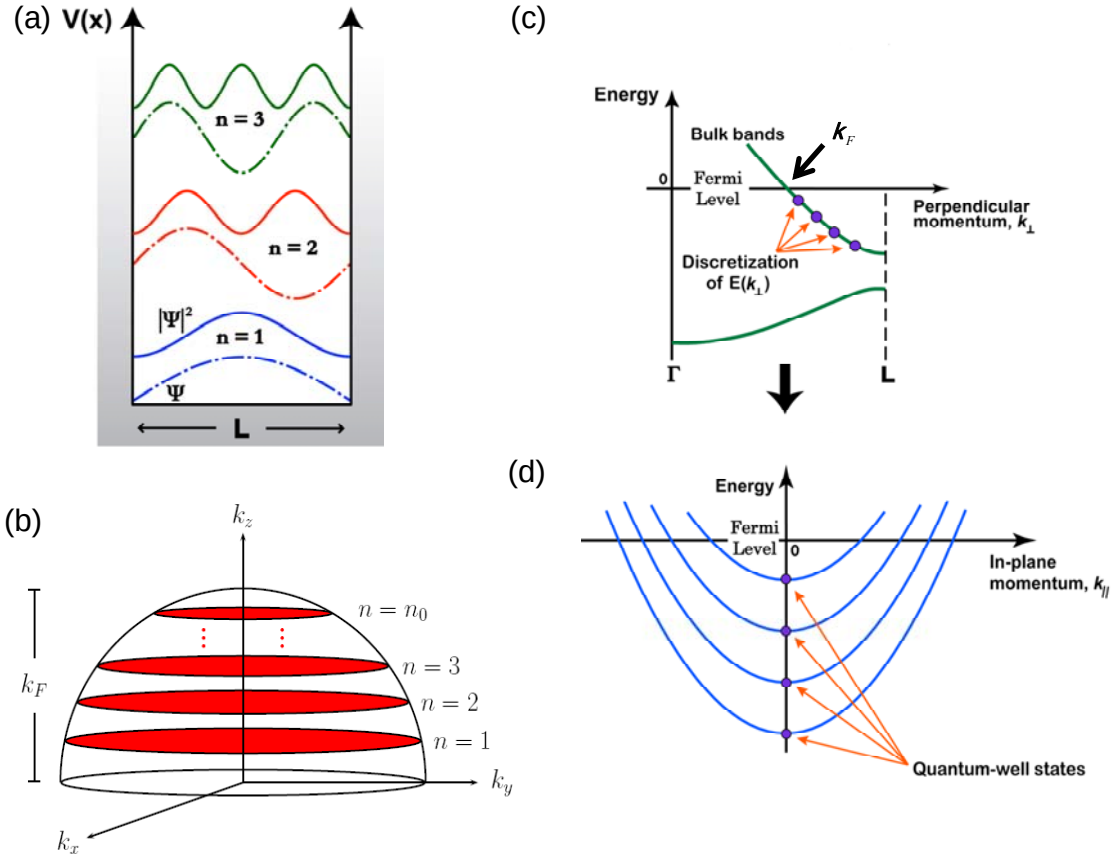

Figure 4.3. (a) quantum well states in a 1D quantum box. (b) Allowed electronic states in momentum space for a free-electron-like thin metal film. (c) Discretization of the continuum of the valence band. (d) Band dispersion relations of free-electron like quantum well subbands.

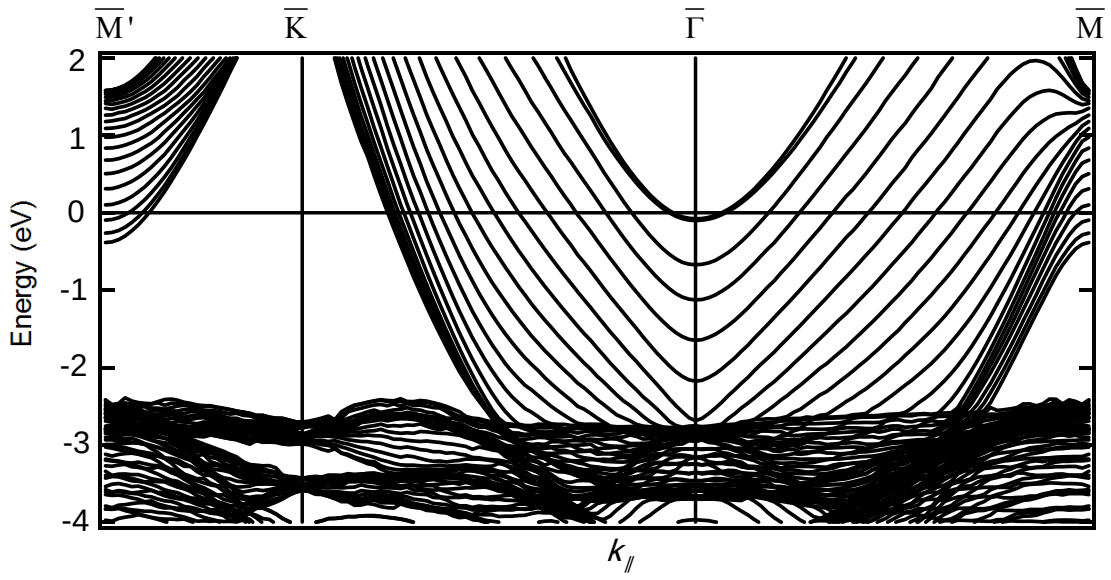

Figure 4.4. Band structure of a 20 ML freestanding Ag(111) film calculated by first-principles methods.

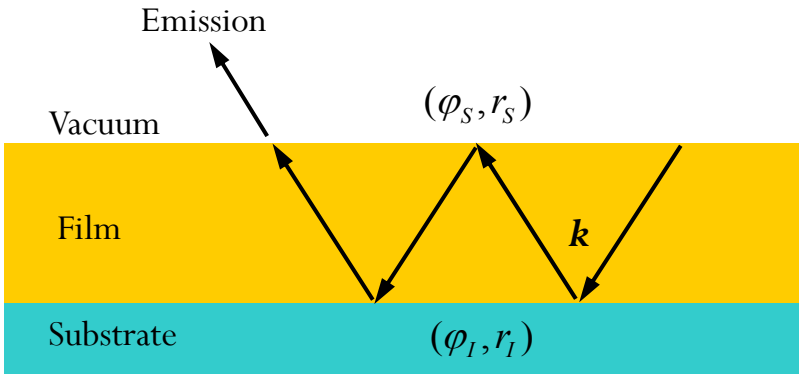

Figure 4.5. Schematic of a thin film as a Fabry-Pérot interferometer. The initial state undergoes multiple reflections to form QWS. After photoexcitation, the electron is emitted from the film as a time-reversed LEED state.

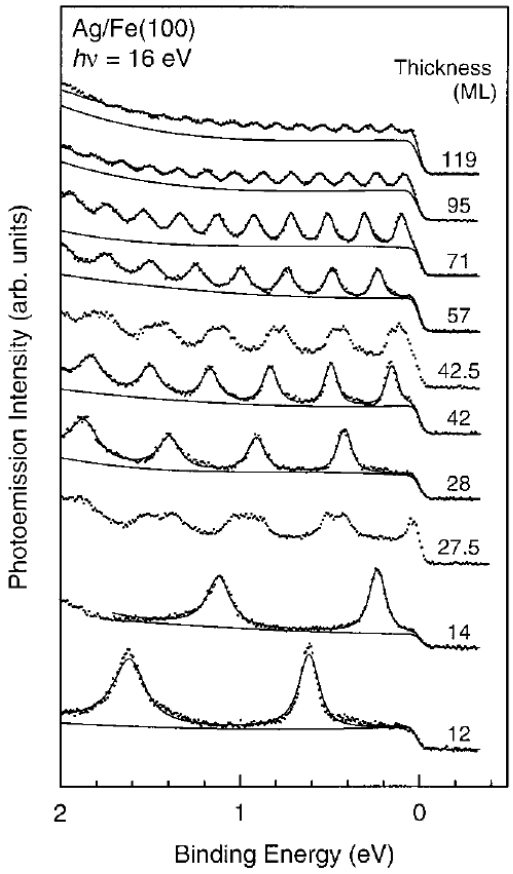

Figure 4.6. Experimental quantum well states for Ag films on Fe(100) taken with $h\nu = 16$ eV radiation [4].

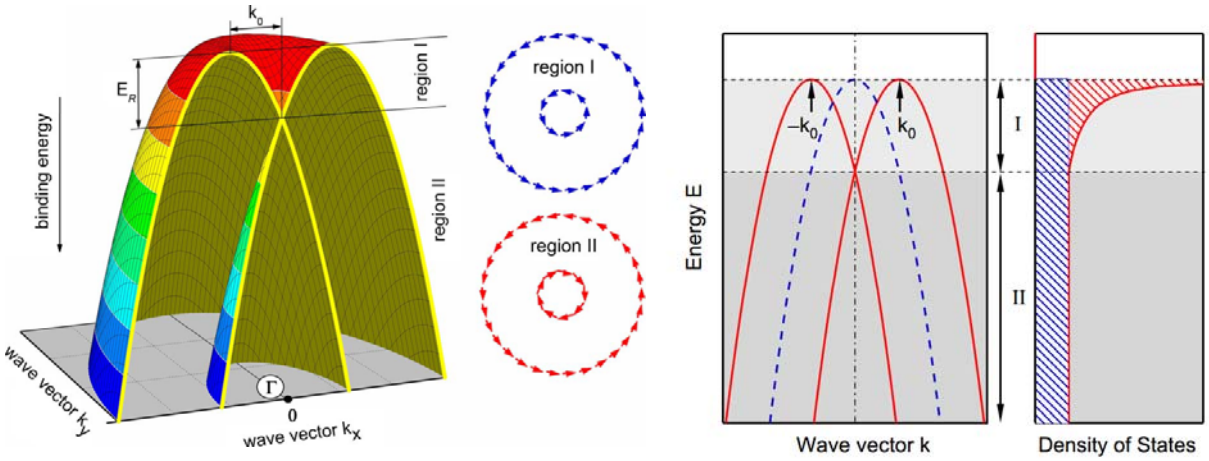

Figure 4.7. Schematic of the band dispersion with Rashba splitting [8]. The crossing point at $\overline{\Gamma}$ defines two different regions: region I, where the constant contours have the same helicity and the DOS follows a $1/\sqrt{E}$ behavior, and region II, where the two contours have opposite helicities and the Dos is constant as in a conventional 2D electron gas.

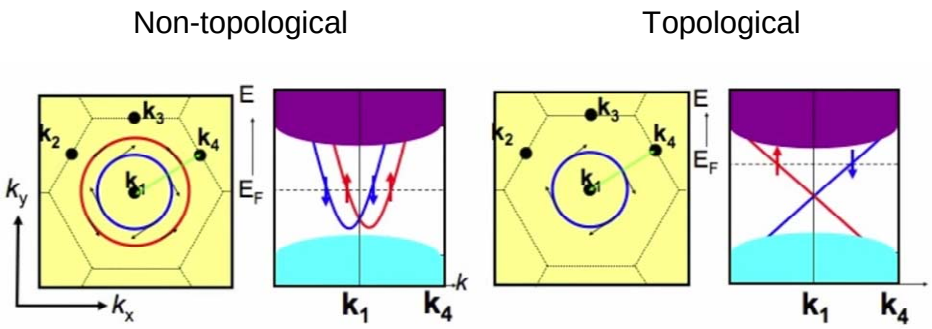

Figure 4.8. Schematic of Fermi surface contours and surface bands of an ordinary insulator (Left) and a topological insulator (Right).

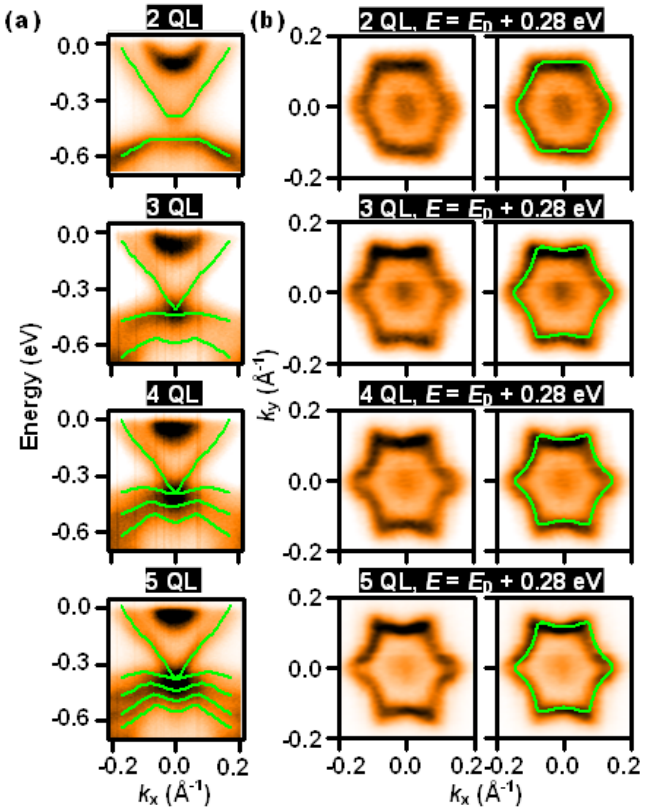

Figure 4.9. (a) Photoemission spectra of 2- through 5-QL Bi_2Te_3 films measured along the $\bar{\Gamma}\bar{M}$ direction, using 31-eV photons. Green curves are band dispersions extracted from data. (b) Constant energy contours at 0.28 eV above the Dirac point for the same set of films, taken with 26-eV photons. Green curves are best fits to the experimental data. [13]

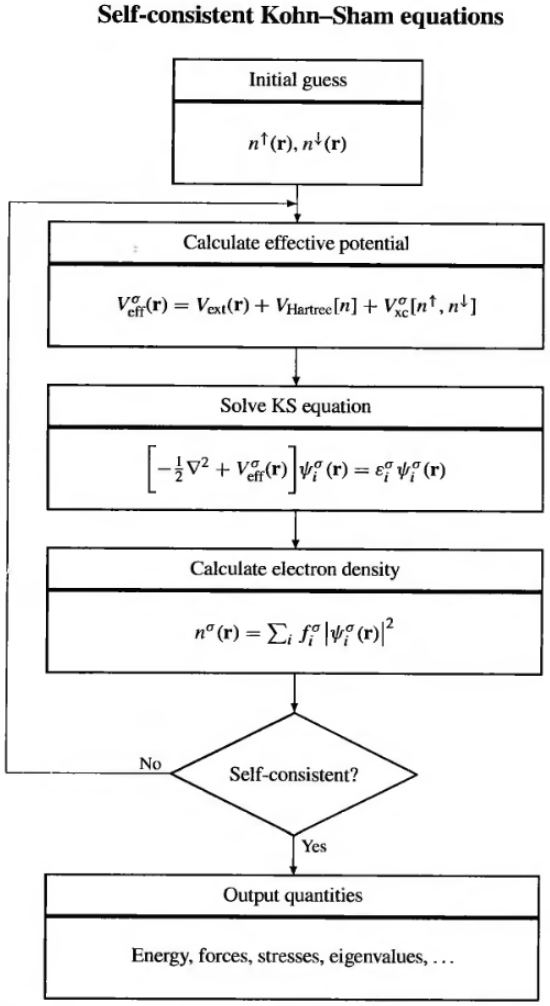

Figure 4.10. Schematic representation of the self-consistent loop for solution of Kohn-Sham equations [16].

5 Topological Sb Thin Films

5.1 Introduction

Topological insulators are characterized by a strong spin-orbit coupling that leads to a set of spin-split surface states with special connections to bulk states [1,2,3,4,5,6,7,8]. In the simplest case where just one pair of spin-split surface states exist in the gap, one of them must disperse into the bulk conduction band, and the other must disperse into the bulk valence band. The bulk gap is thus completely spanned by metallic surface states that carry a net spin current. Whereas the surfaces of bulk topological insulators provide a promising basis for spintronics applications for this reason, thin films are more relevant to actual device architecture. In this chaper we examine the mesoscopic regime where the film thickness is sufficiently large to retain the characters of the spin-polarized surface states, while the bulk continua are replaced by densely populated, but experimentally resolvable, quantum well states that are spin-unpolarized in centrosymmetric cases [9]. The surface states now must disperse and connect to the quantum well states and therefore lose their spin polarization in the process by bulk symmetry requirements. The nature of this passage, relevant to spin transport and relaxation in the ballistic regime, is the focus of this Chapter.

When topological films become ultrathin, the surface states on the two faces of the film can overlap and interact by quantum tunneling of the surface electrons between the two faces. The coupling breaks the degeneracy at the Dirac point, resulting in a gap [10,11]. This gap precludes electrical transport and can be detrimental to device performance, but it is a subject of great interest in connection with the search for Majorana states and other exotic emerging properties [12]. The size of the gap and the

underlying interaction are issues of central importance in the physics and applications of topological films, which are the subject matters of the second part of this chapter.

5.2 Experimental preparation of Sb films

We choose a simple model system, Sb films, for two reasons. Firstly, the semimetal Sb shares the same topological order as $Bi_{1-x}Sb_x$ ($0.07 < x < 0.2$) [5,13], the first material identified as a three-dimensional topological insulator [14]. Sb possesses a pair of Rashba-type spin split surface bands within its bulk band gap. Unlike other Rashba systems such as Au films [13], the two surface bands in Sb are connected to the conduction band and the valence band separately. The resulting gapless configuration of the surface bands gives rise to a single Dirac cone, which is the signature of nontrivial topological order. Secondly, recent studies of Bi films [15] also show entanglement between the surface states and quantum well states and merit a comparison. However, Bi is topologically trivial; it has a more complicated band structure involving mixing of surface and bulk bands near the zone center [16,17]. The complexity impedes a straightforward demonstration of the passage from the spin polarized surface states to quantum well states. Sb films present a much simpler case.

The spin-split surface states of bulk Sb samples have been studied by angle-resolved photoemission (ARPES) before, but these states are observable only near the surface zone center [18,19,20,21]. From the fabrication standpoint, making smooth thin films that preserve the surface spin properties presents a technical challenge. Through experimentation, we have found that Sb films grown on the usual Si(111) substrates are rough. Instead, we first prepared a Bi buffer layer (or a Bi-terminated Si(111)-$\sqrt{3}\times\sqrt{3}-R30^\circ$ surface) on the Si(111) substrate to support the growth of ultrasmooth Sb films. An n-type Si(111) wafer (Sb-doped with a resistivity of ~0.01

$\Omega \cdot \mathrm{cm}$) was cleaned by direct current heating to yield a (7×7) reconstructed surface. It was cooled to 60 K, and about 60 Å of Bi was deposited on top. The sample was then annealed at 400 K to smoothen the Bi film. This Bi covered substrate was used as the substrate for Sb film growth. The deposition of Sb was performed at 60 K; subsequently, the film was annealed to 450 K to form a well ordered Sb film. Bulk Sb has the rhombohedral A7 crystal structure, which is essentially a distorted fcc NaCl structure [22,23]. Films of Sb studied here are (111)-oriented and consist of a stack of bilayers (BL), each of which resembles a buckled graphene sheet. The surface Brillouin zone is a simple hexagon [19]. Fig. 5.1 shows the configuration of the sample, the atomic structure of the Sb films, and the surface Brillouin zone.

5.3 Bulk band structure of Sb

The relationship between the bulk Brillouin zone of Sb and the surface Brillouin zone along the [111] direction is shown in Fig. 5.2(a). The calculated bulk band structure of Sb along the Γ-T and L-X directions are shown in Figs. 5.2(b) and 5.2(c), respectively. Results from similar calculations, but with the spin-orbit coupling excluded, are shown in Figs. 5.2(d) and 5.2(e), respectively. The nearly parabolic quantum well subbands around the $\overline{\mathrm{M}}$ point observed in ARPES from the Sb film can be attributed to quantization of the nearly linear bulk bands along the X-L direction near the Fermi level. The bundle of subbands that converge toward 0.5 eV near normal emission from the film can be attributed to the nearly flat portion of the top valence band near the T point. The main effect of turning off the spin-orbit coupling is to shift the band energies. A more subtle effect is the introduction of nonzero Z_2 topological numbers to the system. Calculations show that Sb belongs to the nontrivial Z_2 class of (1;111)[5].

5.4 Passage from spin polarized TSS to spin degenerate QWS

ARPES mapping along the $\overline{\Gamma}-\overline{\mathrm{M}}$ direction of the band structure of a 20 BL (~79 Å) Sb film reveals a rich structure of subbands as a function of the in-plane wave vector k_x, as seen in Fig. 5.3(a). Figure 5.3(b) shows the same data differentiated twice along the energy axis. This differentiation effectively removes a background and enhances the contrast for a better visualization of the band dispersions. For comparison, Fig. 5.3(c) shows the results from a first-principles calculation; the film is assumed to be freestanding for simplicity. Substrate effects including the modification of the surface states at the interface (not observable by photoemission) and a possibly tiny splitting of the quantum well subbands [24] are thus ignored here, but these do not affect our main conclusions as discussed in [19].

Two bands that have been identified as surface states near the zone center in bulk Sb are labeled *A* and *B* in Fig. 5.3(c). They are degenerate at the surface zone center $\overline{\Gamma}$, but separate in energy elsewhere by spin-orbit coupling because of the surface potential gradient (Rashba effect). The shading in the figure indicates the bulk band continua (thick-film limit). A gap separates the valence and conduction bands throughout the entire zone, which makes Sb a semimetal. The calculated gap is somewhat smaller than the experimental results [14]. For bulk Sb, the upper and lower surface states merge with the conduction and valence bands, respectively, and are observable only near $\overline{\Gamma}$. In the film, the bulk continuum is replaced by quantum-well states, and calculation shows these two states remaining distinct all the way to the zone boundary at $\overline{\mathrm{M}}$. The solid curves in Fig. 5.3(e) indicate schematically the portions of the two states above the Fermi level based on a comparison between theory and experiment. The dashed curve *Q* indicates the topmost quantum well subband below states *A* and *B*. It serves as a reference for connecting the

two visible pieces of state *B*, which lie next above *Q*. Likewise, the two visible pieces of state *A* in Fig. 5.3(e) are connected as they lie next above *B*. In bulk Sb, the states *A* and *B* are not observed near the zone boundary by photoemission, but in the film they are seen and should correspond to quantum well states, as verified by calculation (see below). The $\bar{M}$ point is a special "time-reversal invariant" point in reciprocal space. The two states remain separate in energy at $\bar{M}$, which is a necessary, but not a sufficient, condition for nontrivial topological order [4,14,19,25].

Quantum well states in freestanding Sb films are, however, spin-unpolarized, because they are derived from bulk states that are invariant under time-reversal (**T**) and space-inversion (or parity, **P**) operations. Thus, each quantum well state is doubly degenerate relative to spin. The question is: how do the two spin-split surface states get connected to spin-degenerate pairs of quantum well states across the band edges? An important clue is revealed by turning off the spin-orbit coupling in the calculation (Fig. 5.3(d)), thus rendering the system topologically trivial. The subband structure and the bulk gap remain largely unaffected, but the two surface states *A* and *B* become degenerate within the gap. Each state *A* and *B* is additionally doubly degenerate because of the two surfaces; the total degeneracy is thus four-fold. Outside the gap, the two connecting quantum well states remain separate. Thus, the energy separation of the two quantum well states is not a consequence of spin interaction. It must arise from differences in the spatial parts of the wave functions that lead to different charge density patterns.

An explanation is offered by the schematic diagram in Fig. 5.4 that shows the charge and spin characters of the surface states of a 20 BL Sb film. At the zone center, there are four degenerate surface states; each of the two surfaces (left *L* and right *R*) of the film contains two spin degenerate surface states. For each surface, the spin degeneracy is lifted away from $\bar{\Gamma}$ (Fig. 5.4(a)). Consider the four points on the

dispersion relations, A, A', B, and B', with $k_x = \pm 0.1\left|\bar{\Gamma}\bar{\mathrm{M}}\right|$. Each surface state is characterized by a decay length (Fig. 5.4(b)). The two states on the right surface, A_R and B_R, are spin polarized in opposite directions, along $-y$ and $+y$, respectively. They are related to the two states on the left surface, A_L and B_L, by $A_L = \mathbf{TP}A_R$ and $B_L = \mathbf{TP}B_R$. For the two states on the same surface but with negative k_x, the relationships are $A_R' = \mathbf{T}A_R$ and $B_R' = \mathbf{T}B_R$. The actual charge and spin distributions of the four states from the calculation are presented in Fig. 5.4(c).

As k_x increases, the surface states move toward the bulk band continua. Their decay lengths increase as illustrated by the calculated plane-averaged charge densities for a 20 BL Sb film (Fig. 5.5). Near the edges of the band gap, each pair of degenerate surface states associated with the two surfaces (e.g., A_L and A_R) begin to overlap across the central plane of the film. They remain degenerate because of their opposite spin orientations. However, the spatial overlap leads to a cancellation of the spin polarizations. Eventually, they combine into a quantum well state pair, doubly degenerate with respect to spin, and with a charge density distribution resembling a standing wave bounded within the film. This manner of passage from surface states to quantum well states allows the spin polarization to switch smoothly across the band edges. The degeneracy of the two surface states associated with spatial separation (left and right surfaces) evolves into spin degeneracy for the two quantum well states with identical spatial wave functions.

With the spin-orbit coupling turned off in the calculation, the four states A_R, A_L, B_R, and B_L are degenerate within the gap (Fig. 5.3(d)). They split into two spin-degenerate pairs of quantum well states across the band edges, one pair derived from a mixture of A_R and A_L, and the other from a mixture of B_R and B_L. The splitting can be understood in

terms of how the two surface states from the two surfaces interact in real space when their decay lengths are long enough for them to overlap. The interaction leads to a mixing that can be either in phase or out of phase, resulting in an antinode or node at the midpoint of the film. The energy splitting is the usual even-odd splitting familiar from surface state calculations for films that are sufficiently thin for the states associated with the two surfaces to couple, and this mechanism applies only to states having the same spin. The calculated charge density functions in Fig. 5.5 reveal the differences in the nodal structures of the quantum well states.

The passage from surface states to quantum well states, with very different charge distributions, can be characterized by the charge separation function defined below for each of the two states *A* and *B*:

$$\Delta C(k_x) = \frac{2}{D} \sum_{i=L,R} \left\langle \Psi_i(k_x) \middle| (\rho \,|\, z \,|) \middle| \Psi_i(k_x) \right\rangle - 1, \tag{5.1}$$

where D is the film thickness, ρ is the normalized charge density operator, $z = 0$ is at the midpoint of the film, and the summation is for the two degenerate states associated with the two surfaces. It ranges from 0 (uniform charge distribution) to 1 (charge concentrated at the surfaces at $z = \pm D/2$). The results from the calculation, presented in Fig. 5.6, show a smooth transition across the band edges. Likewise, a spin separation function can be defined:

$$\Delta S(k_x) = \frac{2}{\hbar D} \sum_{i=L,R} \left\langle \Psi_i(k_x) \middle| s_y z \middle| \Psi_i(k_x) \right\rangle, \tag{5.2}$$

where s_y is the spin operator along y, the only direction yielding a nonzero value based on the Rashba effect [26]. This quantity is normalized to ±1 for a fully spin-polarized **TP** pair concentrated at the two film surfaces, and its sign indicates the spin orientation of the

state on the right (positive z) surface. The calculated results in Fig. 5.6 show a transition from oppositely polarized surface states at the two surfaces to unpolarized quantum well states, with a trend of transition very similar to that of the charge separation.

For the ten quantum well states of a 20 BL Sb film at the surface zone boundary $\overline{\mathrm{M}}$ point indicated by circles in Fig. 5.7(a), we have computed the corresponding plane-averaged charge densities; the results are shown in Fig. 5.7(b). For symmetry reasons, the charge distribution for each state must be symmetric about the midpoint of the film. It is either a minimum or a maximum there, and successive states derived from a single band should alternate between the two cases. All of the ten states follow this rule, except that there is a phase slip between the top two states; also, the top three states show envelope functions that do not follow a simple pattern. These variations are caused by the involvement of additional bulk bands within this energy range (Fig. 5.2).

We also mapped out the band structure of a 20 BL Sb film grown on a Bi-terminated Si(111)-$\sqrt{3}\times\sqrt{3}-R30^{\circ}$ surface, and the result is shown in Fig. 5.8. The role played by the Bi buffer layer and the Bi-terminated Si(111)-$\sqrt{3}\times\sqrt{3}-R30^{\circ}$ surface in the epitaxial growth of Sb films is to smoothen the Si(111)-7×7 surface.

5.5 Quantum tunneling effect in ultrathin Sb films

As the Sb films become thinner, the semimetallic gap widens. Our first-principles calculations show that the gap at a film thickness of 4 BL becomes slightly positive as shown in Fig. 5.9, making the system insulating in the bulk. The green band bordered by dashed lines indicates a +40 meV absolute band gap, defined as the gap between the top valence quantum well subband and the bottom conduction quantum well subband. Within this gap, there is a single crossing along $\overline{\Gamma}-\overline{\mathrm{M}}$ by the spin-polarized surface states.

Unlike the surface states, all quantum well subbands are spin unpolarized. The same calculation shows a tunneling-induced gap of 36 meV at the Dirac point of the surface states, an undesirable result. Surprisingly, angle-resolved photoemission spectroscopy (ARPES) measurements of a 4-BL film grown on Si(111) reveal no such gap at the Dirac point, even though the rest of the experimental band structure appears very similar to the calculated one. The observed robust gapless Dirac cone is very promising for applications. The puzzling difference between experiment and calculation is explained by additional model calculations taking into account of the substrate.

Figure 5.10(a) presents calculated band structures of freestanding Sb films at various thicknesses in the range of 1-10 BL along the $\bar{\Gamma}-\bar{M}$ direction. The shaded areas indicate the projected bulk band regions, and states within the bulk gap are of surface character. The spin-split surface states begin to appear at a thickness of 2 BL, but there is a fairly large tunneling-induced gap of 86 meV at $\bar{\Gamma}$. This gap diminishes as the film thickness increases and essentially vanishes at ~8 BL when the gap becomes smaller than thermal broadening. The calculated gap *E* as a function of thickness is shown in Figs. 5.10(b) and 5.10(c) using linear and logarithmic scales, respectively. The decay of the gap beyond above about 6 BL is exponential; a fit to the asymptotic behavior yields a decay length of about 1.1 BL, which characterizes the spatial extent of the surface state wave function. The calculated plane-averaged charge densities of the lower surface state at the zone center for a thick Sb(111) film and a 4-BL film are shown in Figs. 5.10(d) and 5.10(e), respectively. The surface state is mostly localized within the top BL. The small tail allows the surface states associated with the two faces of the 4-BL film to overlap, giving rise to the gap. The other bands in Fig. 5.10(a) are quantum well states in the film. Unlike the surface states, the quantum-well states are spin degenerate. Another important distinction is that the quantum-well bands become more numerous as the film becomes thicker.

ARPES mapping of the band structure of a 4-BL Sb film is presented in Fig. 5.11(a). The band dispersions are in fairly good accord with calculated ones presented in Fig. 5.11(b) for a freestanding 4-BL film. The data confirm the atomic-level uniformity of the film; any significant admixture of 3- or 5-BL patches would give rise to additional quantum-well bands. Similar comparison between experiment and theory for a 20-BL film is presented in Figs. 5.11(c) and 5.11(d). The surface states are well resolved, but not for the dense set of quantum well states at low energies. Despite the overall similarity, the experiment and theory do differ in some details. Shown in Fig. 5.11(e) is a close-up view of the experimental spin-split surface bands near the zone center for the 4-BL film; the data contrast has been enhanced by taking the second derivative in energy. The corresponding theoretical bands are shown in Fig. 5.11(f), with the bands suitably broadened to simulate the data. The gap at the zone center, 36 meV in the calculation, is absent in the data. The theoretical dispersion relations have noticeably higher energies.

It is interesting to note that prior studies of related systems such as Bi_2Se_3 thin films have shown convincingly the presence of tunneling-induced gaps at small film thicknesses [27]. Our observation here represents the first clear-cut case of a zero gap at a film thickness where a sizeable gap is predicted. The difference can be attributed to the boundary conditions specific to the interface bonding for each case. In our system, the bottom face of the Sb film forms chemical bonds with the substrate surface. Since the film and the substrate are incommensurate, an accurate theoretical modeling including the substrate is not feasible. Instead, we simulate the effect of interfacial bonding by terminating the bottom face of a 4-BL Sb film with H. The results of the calculation, shown in Fig. 5.11(g), are in much better agreement with the experiment than the freestanding case. Specifically, the gap becomes zero, and the energy positions of the two surface bands are much closer to the experimental results. Thus, H-termination is a good approximation for the interfacial bonding in our case. A similar case can be made for

Bi-termination. For comparison, data from the 20-BL film, presented in Fig. 5.11(h), shows no gap, just as expected. The surface states have somewhat lower energies, in agreement with the calculation shown in Fig. 5.11(d).

The absence of a gap at 4 BL can be understood as a result of the suppression of the tunneling-induced coupling. The chemical bonding at the interface introduces a large asymmetry in the film. The topological surface states at the interface undergo a large energy shift and are no longer degenerate with the surface states at the top surface. Quantum tunneling is thus turned off for lack of energy conservation, and the gap disappears correspondingly. This effect should become more pronounced at smaller film thicknesses. However, we have not been able to prepare atomically smooth films in the 1-3 BL range despite repeated attempts. Those films were rough probably due to an inherent critical thickness of 4 BL for smooth growth.

To explore the nature of the tunneling interaction and interfacial coupling in detail, we show in Figs. 5.12(a) and 5.12(c), respectively, the calculated band dispersion relations for a freestanding 6-BL Sb film and for the same film with its bottom face terminated by H. For an intermediate case involving a weak interfacial bonding, we choose a model in which the bottom layer of the film is replaced by a mixture of Sb and Bi, represented in the calculation using the average pseudopotential of Sb and Bi. The rationale is that Sb and Bi are isoelectronic and chemically similar. The mixing is a good approximation for a somewhat perturbed bottom layer caused by a weak interfacial bonding. The results of the calculation are shown in Fig. 5.12(b). In Fig. 5.12(a), the two surface bands show a tunneling-induced gap. In Fig. 5.12(b), the surface states on the bottom face of the film are shifted slightly downward in energy by the interfacial perturbation, resulting in two separate Dirac cones at the zone center. In Fig. 5.12(c), the downward energy shift for the bottom surface states is so large that these states merge into the quantum-well manifold, and only the pair of top surface states remains in the gap

with a zero gap at the Dirac point. The surface bands in Fig. 5.12(a) are doubly degenerate because of the two surfaces of the film, while those in Fig. 5.12(c) are non-degenerate.

The essential physics of the system can be further elaborated in terms of a four-band Rashba model with the basis set $\{|\Psi_T^{\uparrow}>,|\Psi_T^{\downarrow}>,|\Psi_B^{\uparrow}>,|\Psi_B^{\downarrow}>\}$, where Ψ is a surface state, and T and B denote the top and bottom surfaces, respectively. The effective Hamiltonian is

$$H(k)=\left(E_0+\frac{k^2}{2m}\right)\mathbf{I}_4+\alpha(k_x\sigma_y-k_y\sigma_x)\otimes\mathbf{I}_2+\beta\,\mathbf{I}_2\otimes\tau_x+V\mathbf{I}_2\otimes\tau_z, \tag{5.3}$$

where $\mathbf{I}_n$ is an $n \times n$ identity matrix, $\boldsymbol{\sigma}$ and $\boldsymbol{\tau}$ are the Pauli matrices associated with the electron spin and position (top or bottom), respectively, α is the Rashba coupling constant, β is a (thickness-dependent) tunneling matrix element, and V is a potential bias exerted by interfacial bonding. A more general form of Eq. (5.3) might include a warping factor and higher-order band structure shape factors [28], but these are irrelevant to the present discussion. The calculated band structures with m = 0.03, α = 0.6, β = 0.004, and V = 0, 0.05, and 2 in appropriate units (with energy in eV and momentum in $Å^{-1}$) are shown in Figs. 5.12(d)-5.12(f), respectively. The qualitative features of our findings thus far are well reproduced by the model. In particular, the tunneling-induced gap at V = 0, corresponding to a symmetric freestanding film, is eliminated at a large V, corresponding to a strong interfacial bonding.

The spin polarization of the surface states is a key property of concern for applications. It can be evaluated straightforwardly within the above model. The surface band dispersions for a fixed α= 0.6 are shown in Fig. 5.13 for (a) β = 0 and V = 0 (thick Sb sample with no tunneling), (d) β = 0.004 and V = 0 (6 BL freestanding film with

quantum tunneling), and (g) β = 0.004 and V = 2 (6 BL film with strong interfacial bonding). Along $\bar{\Gamma}-\bar{\mathrm{M}}$, the only nonzero component of the spin (in terms of the Pauli matrices) is σ_y. The values of σ_y and $|\sigma_y|$ for the lower surface band are shown in Fig. 5.13 for the three cases. In case (a), the system consists of a pair of chiral fermion bands and the electrons are fully spin-polarized in accordance with the Rashba interaction. Each band undergoes a spin reversal as k_x crosses $\bar{\Gamma}$. In case (d), tunneling causes a gap to open up at the Dirac point. The magnitude of the spin is suppressed near $\bar{\Gamma}$, and the spin reversal becomes gradual. Thus, not only the insulating gap can cause problems for electrical transport, the suppression of the spin near the gap can be detrimental to spin transport. In case (g), the strong bonding at the interface restores the surface states and their spin properties to the thick-film limit, and the results appear identical to case (a). It should be noted that the 100% spin polarization based on this simple model is generally not realized in real materials because of the complex coupling of the spin and orbital degrees of freedom [29].

Near the zone center the effective Hamiltonian [Eq. 5.3] with V = 0 (freestanding films) yields the energy dispersion relations

$$E = E_0 + \frac{k^2}{2m} \pm \sqrt{\beta^2 + \alpha^2 k^2} \simeq E_0 \pm \beta + \left(\frac{1}{2m} \pm \frac{\alpha^2}{2\beta} \right) k^2 , \tag{5.4}$$

where the + and – signs correspond to the upper and lower bands, respectively. The energy gap at k = 0 equals 2β. The effective masses at the zone center for the two bands are

$$m^* = \frac{m}{1 \pm \frac{m\alpha^2}{\beta}} \tag{5.5}$$

The effective mass of the upper band is always positive. The effective mass of the lower band is positive if $\beta > m\alpha^2$, and negative otherwise. A negative effective mass means that the lower band is hole-like near the zone center. Since the tunneling matrix element β depends on the film thickness, a sign reversal is expected at a critical film thickness determined by $\beta = m\alpha^2$ below which the effective mass is positive. Figure 5.14 shows the calculated band structures for freestanding 4- and 6-BL films based on first-principles methods and the four-band Rashba model. The effective mass of the lower surface band is negative at 6 BL and positive at 4 BL.

The four-band Rashba Hamiltonian without the $k^2/2m$ term is a good model for describing Dirac fermions associated with topological surface states. The system now possesses particle-hole symmetry, and the effective masses at the zone center with $V = 0$ are given by $\pm\beta/\alpha^2$, which vanishes at $\beta = 0$. Thus, tunneling gives rise to a finite effective mass. With a finite potential bias V, the double degeneracy associated with the two faces of the freestanding film is lifted. Some model calculations are presented in Fig. 5.15 to illustrate the qualitative features of the band structure under various conditions. Figure 5.15(d), with the addition of a $k^2/2m$ term, resembles Fig. 5.12(e).

An alternative way to simulate the substrate effect in our case is to terminate the bottom face of a freestanding Sb film with Bi atoms. For a 4-BL Sb film, the energetically optimized Bi-Sb bond length is 2.87 Å with each Bi atom bonded directly below an Sb atom on the bottom face. The resulting band structure is shown in Fig. 5.16. The overall band structure below the Fermi level is similar to the one for H-terminated film [Fig. 5.12(c)]. The surface bands associated with the top face are protected from band gap opening. The surface bands associated with the Bi-terminated bottom face are located above the Fermi level as indicated in the figure.

The mechanism of interfacial protection of the gap should be quite general. We have performed similar first-principles calculations for other topological insulator systems including Bi_2Se_3 and Bi_2Te_3. The results show the lack of a gap for a strong bonding at the bottom face of the film, just as expected.

5.6 Conclusion

Topological materials are of interest in that the surface states pinned at opposite surfaces possess opposite transverse spin orientations. Such spatial separation of spin and associated charge, without an applied magnetic field, is an essential ingredient for realizing the quantum spin-Hall effect [30,31]. Thin films of these materials offer flexibility for device design and integration. We employ a special Bi interface layer to prepare topologically nontrivial Sb films of excellent structural quality on standard Si substrates. A comparison between theory and experiment allows us to explore the interplay between quantum confinement and spin separation, which offers a path forward for utilizing topological materials for thin film applications.

In addition, our ARPES mapping of the surface band structure of an ultrathin, atomically smooth, 4-BL Sb film prepared on a Bi-terminated Si(111)-$\sqrt{3}\times\sqrt{3}-R30^{\circ}$ surface reveals no tunneling-induced energy gap at the Dirac point, despite a theoretically predicted one for a freestanding film. The observed robust Dirac cone, of interest to spintronic applications, is shown to be the result of a strong interfacial bonding between the film and the substrate, which suppresses quantum tunneling. Similar calculations performed for Bi_2Se_3 and Bi_2Te_3 films yield the same conclusions. Our work suggests that quantum tunneling, an intrinsic property dependent on the film thickness, and substrate bonding, an extrinsic factor amenable to interfacial engineering, can be effectively manipulated to achieve desired electronic and spintronic properties of topological thin films.

References:

[1] M. Z. Hasan and C. L. Kane, Rev. Mod. Phys. **82**, 3045 (2010).

[2] X.-L. Qi and S.-C. Zhang, Rev. Mod. Phys. **83**, 1057 (2011).

[3] B. A. Bernevig, T. L. Hughes, and S.-C. Zhang, Science **314,** 1757 (2006).

[4] L. Fu, C. L. Kane, and E. J. Mele, Phys. Rev. Lett. **98**, 106803 (2007).

[5] L. Fu and C. L. Kane, Phys. Rev. B **76**, 045302 (2007).

[6] D. Hsieh, D. Qian, L. Wray, Y. Xia, Y. S. Hor, R. J. Cava, and M. Z. Hasan, Nature **452**, 970 (2008).

[7] Y. Xia, D. Qian, D. Hsieh, L. Wray, A. Pal, H. Lin, A. Bansil, D. Grauer, Y. S. Hor, R. J. Cava, and M. Z. Hasan, Nature phys. **5**, 398 (2009).

[8] Y. L. Chen, J. G. Analytis, J.-H. Chu, Z. K. Liu, S.-K. Mo, X. L. Qi, H. J. Zhang, D. H. Lu, X. Dai, Z. Fang, S. C. Zhang, I. R. Fisher, Z. Hussain, and Z.-X. Shen, Science **325**, 178 (2009).

[9] T.-C. Chiang, Surf. Sci. Rep. **39**, 181 (2000).

[10] Y. Li, et al., Adv. Mater. **22**, 4002 (2010).

[11] O. V. Yazyev, J. E. Moore, S. G. Louie, Phys. Rev. Lett. **105**, 266806 (2010).

[12] A. Potter and P. Lee, Phys. Rev. Lett. **105**, 227003 (2010).

[13] D. Hsieh, Y. Xia, L. Wray, D. Qian, A. Pal, J. H. Dil, J. Osterwalder, F. Meier, G. Bihlmayer, C. L. Kane, Y. S. Hor, R. J. Cava, and M. Z. Hasan, Science **323**, 919 (2009).

[14] D. Hsieh, L. A. Wray, D. Qian, Y. Xia, Y. S. Hor, R. J. Cava, and M. Z. Hasan, New J. Phys. **12,** 125001 (2010).

[15] T. Hirahara, T. Nagao, I. Matsuda, G. Bihlmayer, E. V. Chulkov, Yu. M. Koroteev, P. M. Echenique, M. Saito, and S. Hasegawa, Phys. Rev. Lett. **97**, 146803 (2006).

[16] G. Bian, T. Miller, and T.-C. Chiang, Phys. Rev. B **80**, 245407 (2009).

[17] Yu. M. Koroteev, G. Bihlmayer, E. V. Chulkov, and S. Blügel, Phys. Rev. B **77**, 045428 (2008).

[18] L. M. Falicov and P. J. Lin, Phys. Rev. **141** 562 (1966).

[19] T. Kadono, K. Miyamoto, R. Nishimura, K. Kanomaru, S. Qiao, K. Shimada, H. Namatame, A. Kimura, and M. Taniguchi, Appl. Phys. Lett. **93**, 252107 (2008).

[20] K. Sugawara, T. Sato, S. Souma, T. Takahashi, M. Arai, and T. Sasaki, Phys. Rev. Lett. **96**, 046411 (2006).

[21] H. Höchst and C. R. Ast, J. Electron Spectrosc. Rel. Phenom. **137–140,** 441 (2004).

[22] Y. Liu and R. E. Allen, Phys. Rev. B **52**, 1566 (1995).

[23] H.-J. Zhang, C.-X. Liu, X.-L. Qi, X.-Y. Deng, X. Dai, S.-C. Zhang, and Z. Fang, Phys. Rev. B **80**, 085307 (2009).

[24] J. Hugo Dil, F. Meier, J. Lobo-Checa, L. Patthey, G. Bihlmayer, and J. Osterwalder, Phys. Rev. Lett. **101**, 266802 (2008).

[25] K. K. Gomes, W. Ko, W. Mar, Y. Chen, Z.-X. Shen, and H. C. Manoharan, arXiv:0909.0921v2 (2009).

[26] Y. A. Bychkov and E. I. Rashba, J. Phys. C **17,** 6039 (1984).

[27] Y. Zhang, et al., Nat. Phys. **6**, 584 (2010).

[28] L. Fu, Phys. Rev. Lett. **103**, 266801 (2009).

[29] G. Bian, X. Wang, Y. Liu, T. Miller, and T.-C. Chiang, Phys. Rev. B **84**, 235414 (2011).

[30] C. L. Kane and E. J. Mele, Phys. Rev. Lett. **95**, 226801 (2005).

[31] X.-L. Qi and S.-C. Zhang, Physics Today **63**, 33 (2010).

Figures:

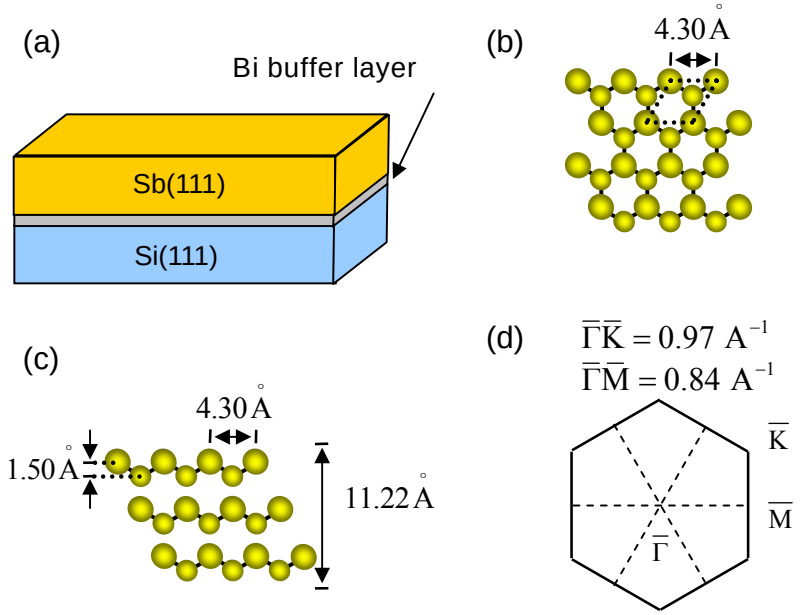

Figure 5.1. (a) Schematic of the sample configuration. (b) Top view of the atomic structure of Sb(111). Larger balls indicate atoms closer to the viewer. (c) Side view along $[11\bar{2}]$. (d) Surface Brillouin zone.

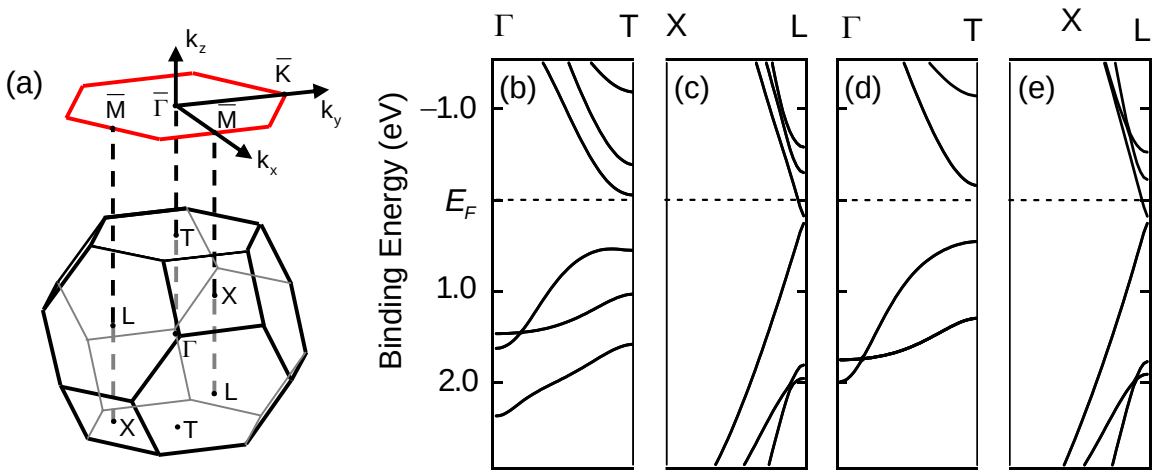

Figure 5.2. (a) Relationship between the bulk Brillouin zone and the (111) surface zone of Sb. (b,c) Calculated bulk band structure of Sb along $\Gamma - T$ and $X - L$. (d,e) Bulk band structure along the same two directions but calculated without spin-orbit coupling.

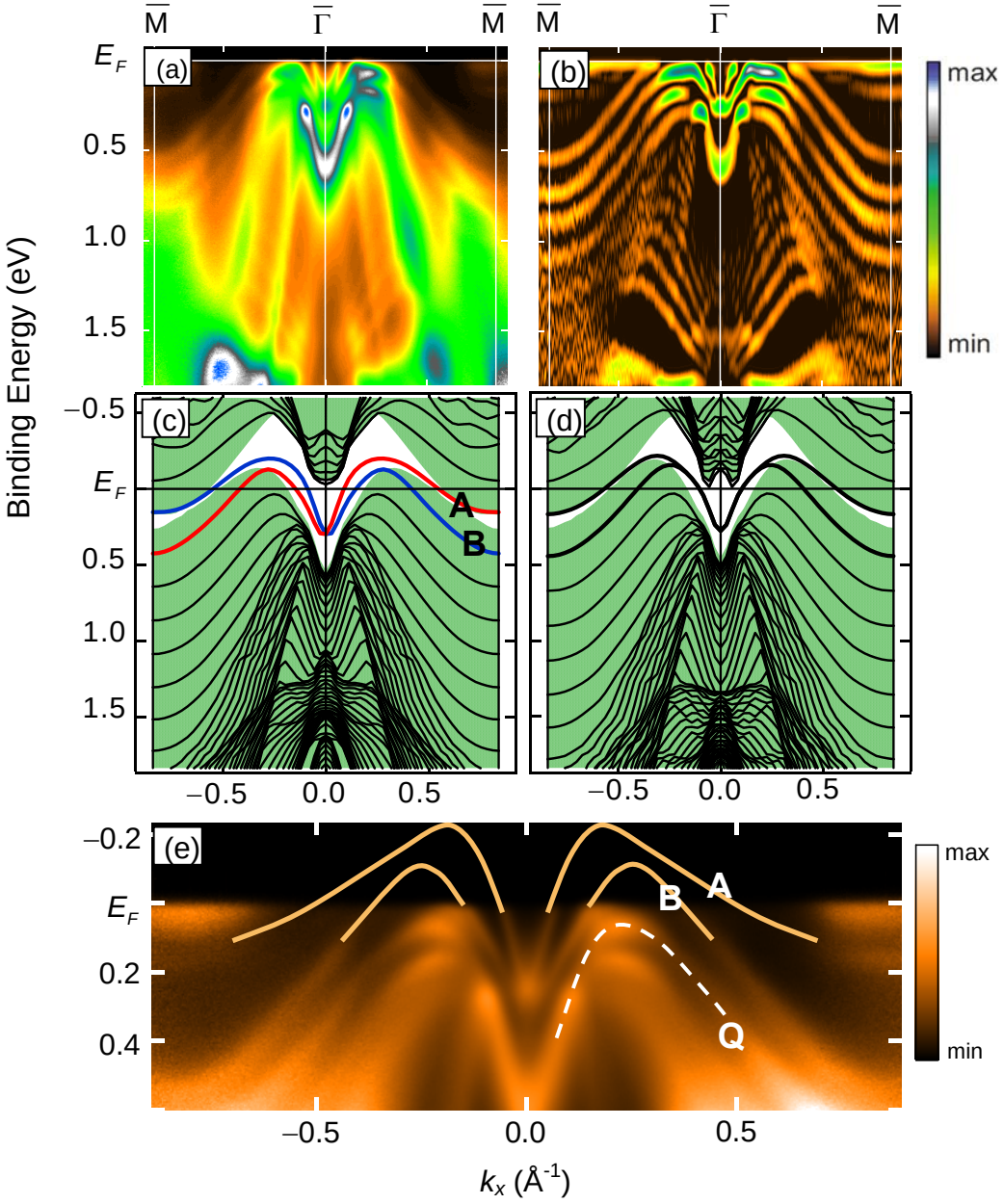

Figure 5.3. (a) ARPES data taken at 22 eV from a 20 BL Sb film grown on a Bi buffer layer. (b) Second derivatives of the data along the energy axis. (c,d) Calculated band structure for a freestanding 20 BL Sb film with and without spin-orbit coupling, respectively. (e) Data near the Fermi level, where the solid curves indicate schematically the surface bands *A* and *B* above the Fermi level by comparison with theory. The curve *Q* indicates the topmost quantum well subband below the states *A* and *B*.

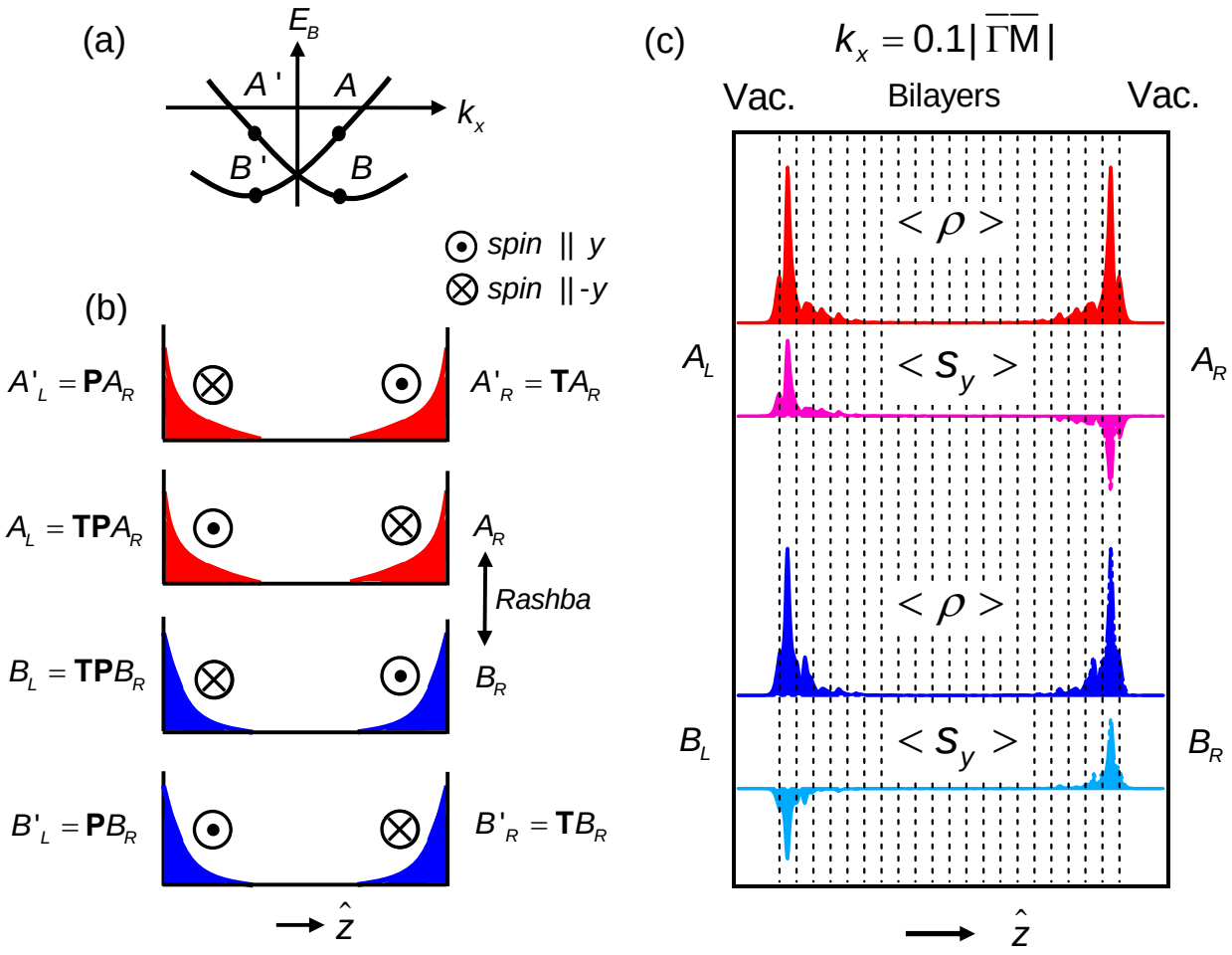

Figure 5.4. Charge and spin distributions of surface states of a 20 BL Sb film. (a) Surface band structures near the zone center with four points A, A', B, and B' marked at $k_x = \pm 0.1|\bar{\Gamma}\bar{\mathrm{M}}|$. Each point corresponds to two degenerate surface states located at the opposite surfaces of the film. (b) Schematic charge densities and spin orientations for states A, A', B, and B' on the two surfaces. The spin orientations are indicated. (c) Calculated charge density $\langle \rho \rangle$ and spin density $\langle s_y \rangle$ along z for the four surface states at $k_x = +0.1|\bar{\Gamma}\bar{\mathrm{M}}|$.

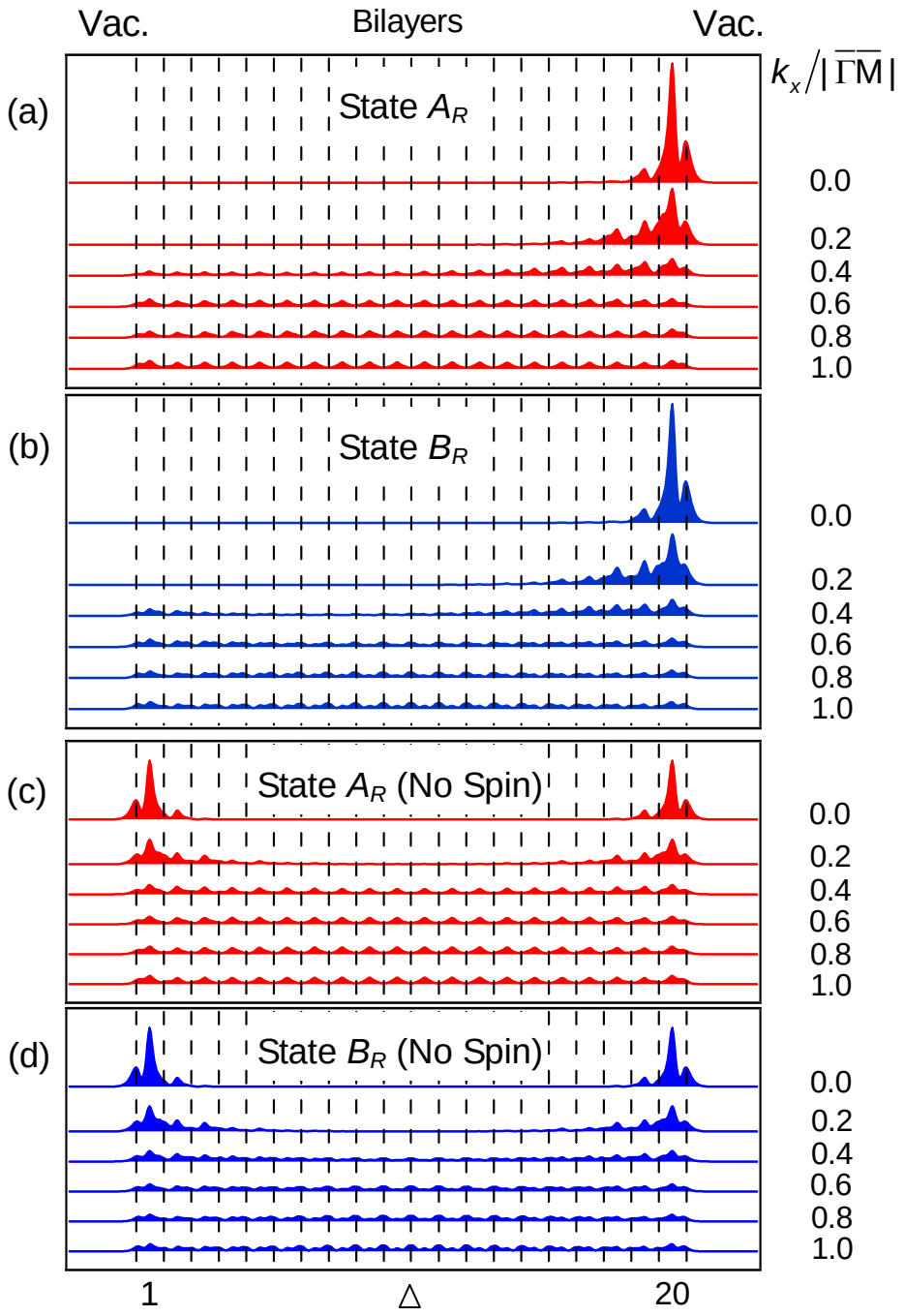

Figure 5.5. Calculated plane-averaged electronic charge densities in a 20 BL Sb film for (a) state A_R and (b) state B_R. The central plane of the slab is marked by a triangle. (c,d) Corresponding results computed without spin-orbit coupling.

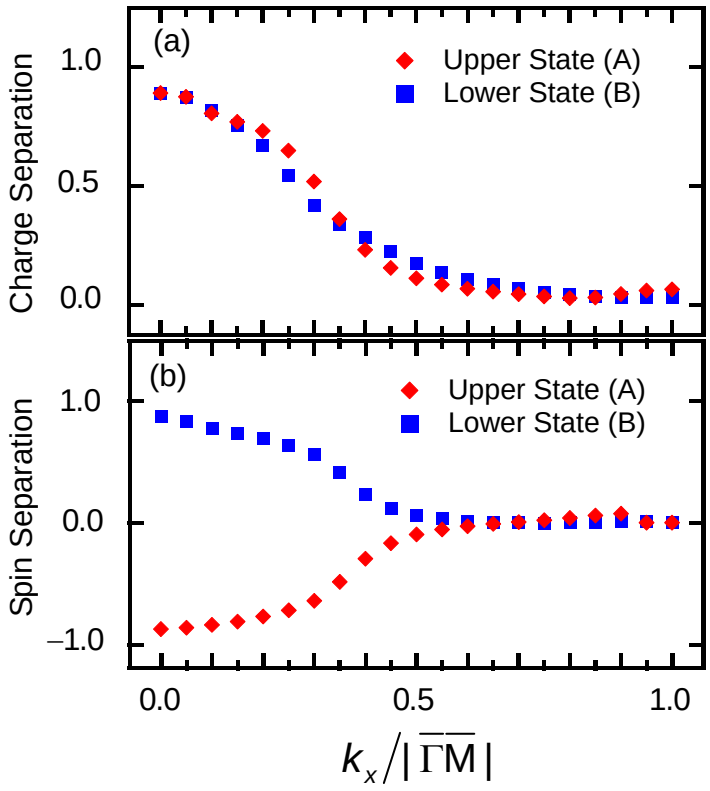

Figure 5.6. (a) Calculated charge separation function, or the normalized absolute charge moment, as a function of k_x for a 20 BL Sb film. (b) The corresponding spin separation function, or the normalized spin moment, along y.

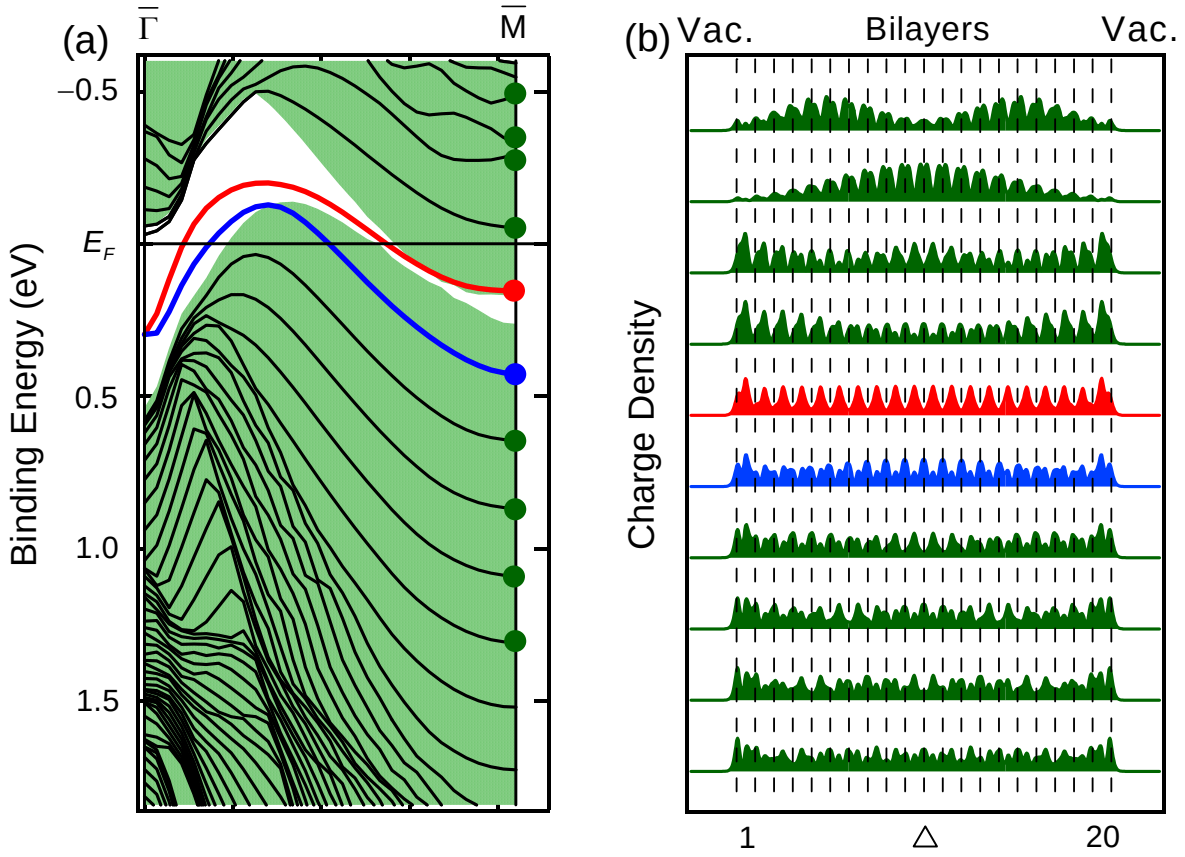

Figure 5.7. (a) Calculated band structure for a 20 BL Sb film. Ten states at the zone boundary are indicated by circles. (b) The corresponding charge density distributions in the film for the ten states. The midpoint of the film is indicated by a triangle.

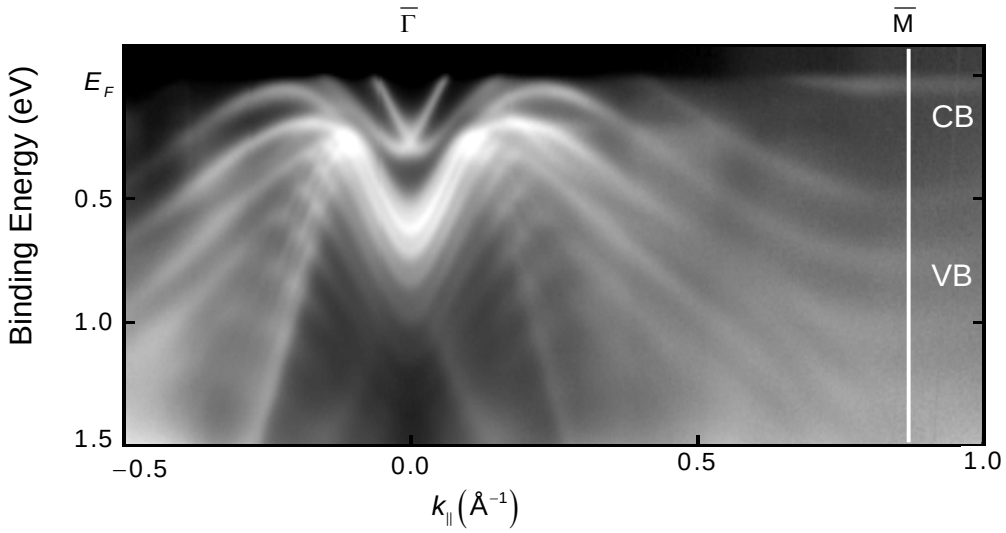

Figure 5.8. ARPES mapping of a 20 BL Sb film grown on the Bi-terminated Si(111)-$\sqrt{3}\times\sqrt{3}-R30^{\circ}$ surface.

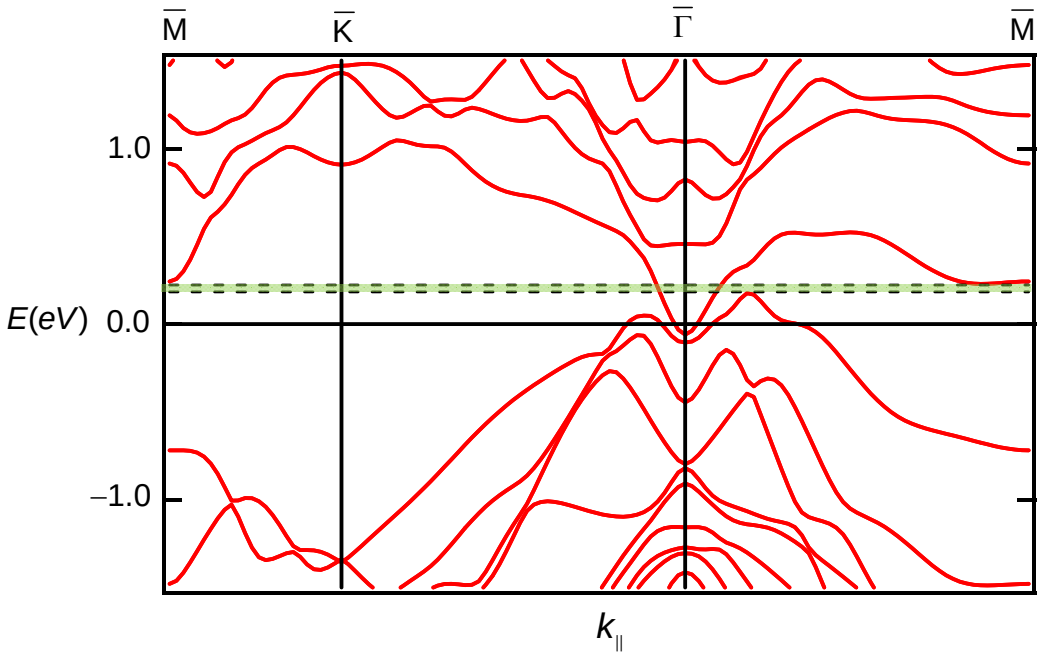

Figure 5.9. Calculated band structure of a freestanding 4-BL Sb film. The green band bordered by dashed lines indicates a positive band gap, within which there is a single crossing along $\bar{\Gamma}-\bar{\mathrm{M}}$ by the spin-polarized surface states.

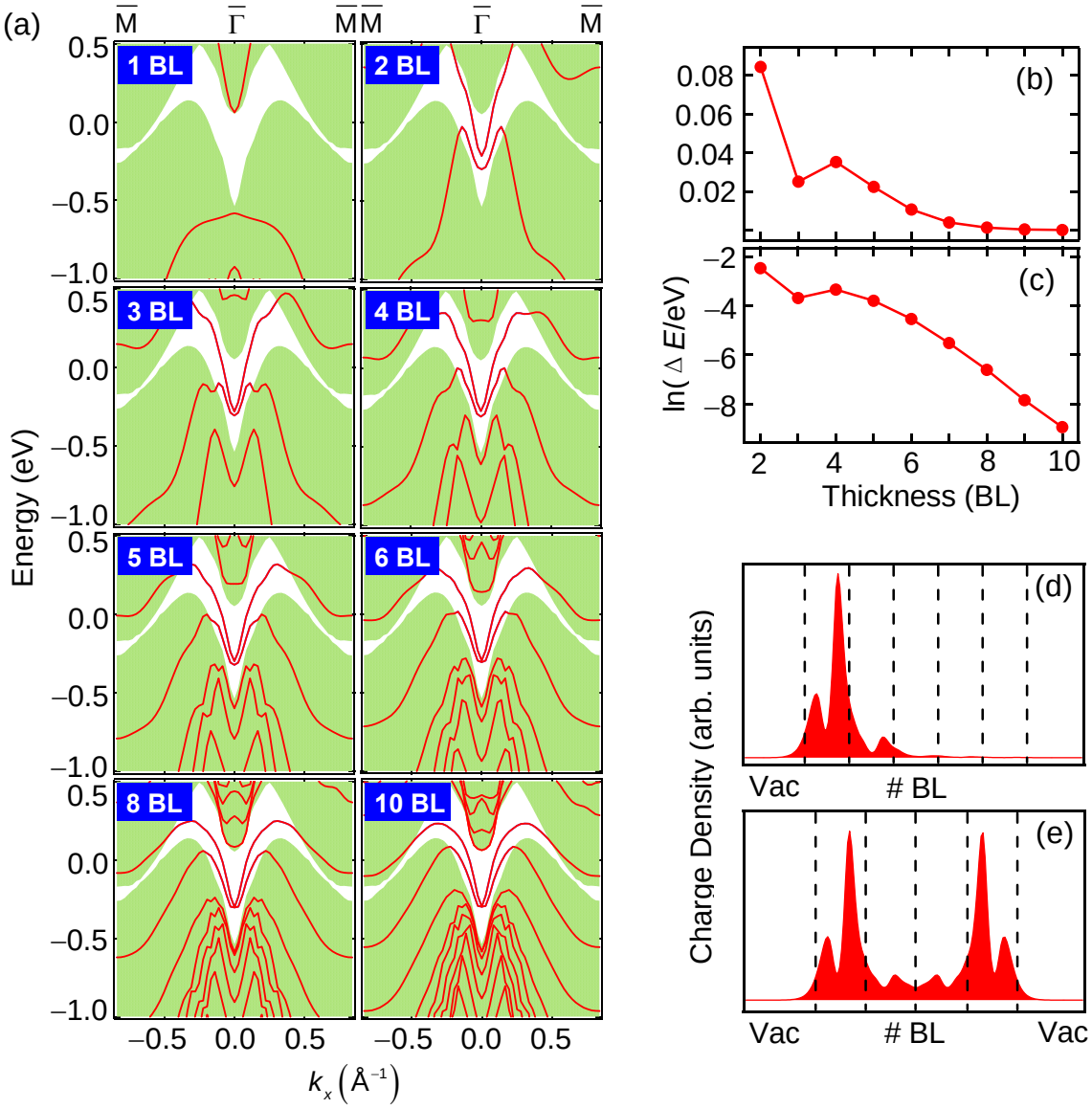

Figure 5.10. (a) Band structure of Sb(111) films of various thicknesses. The shaded areas indicate projected bulk band regions. (b) Calculated energy gap ΔE and (c) logarithmic gap $\ln(\Delta E)$ at $\bar{\Gamma}$ as a function of film thickness. (d) Plane-averaged charge density of the lower surface state at $\bar{\Gamma}$ as a function of distance from the surface for a thick film. The vertical dashed lines indicate the bilayers. (e) Same for a 4-BL film.

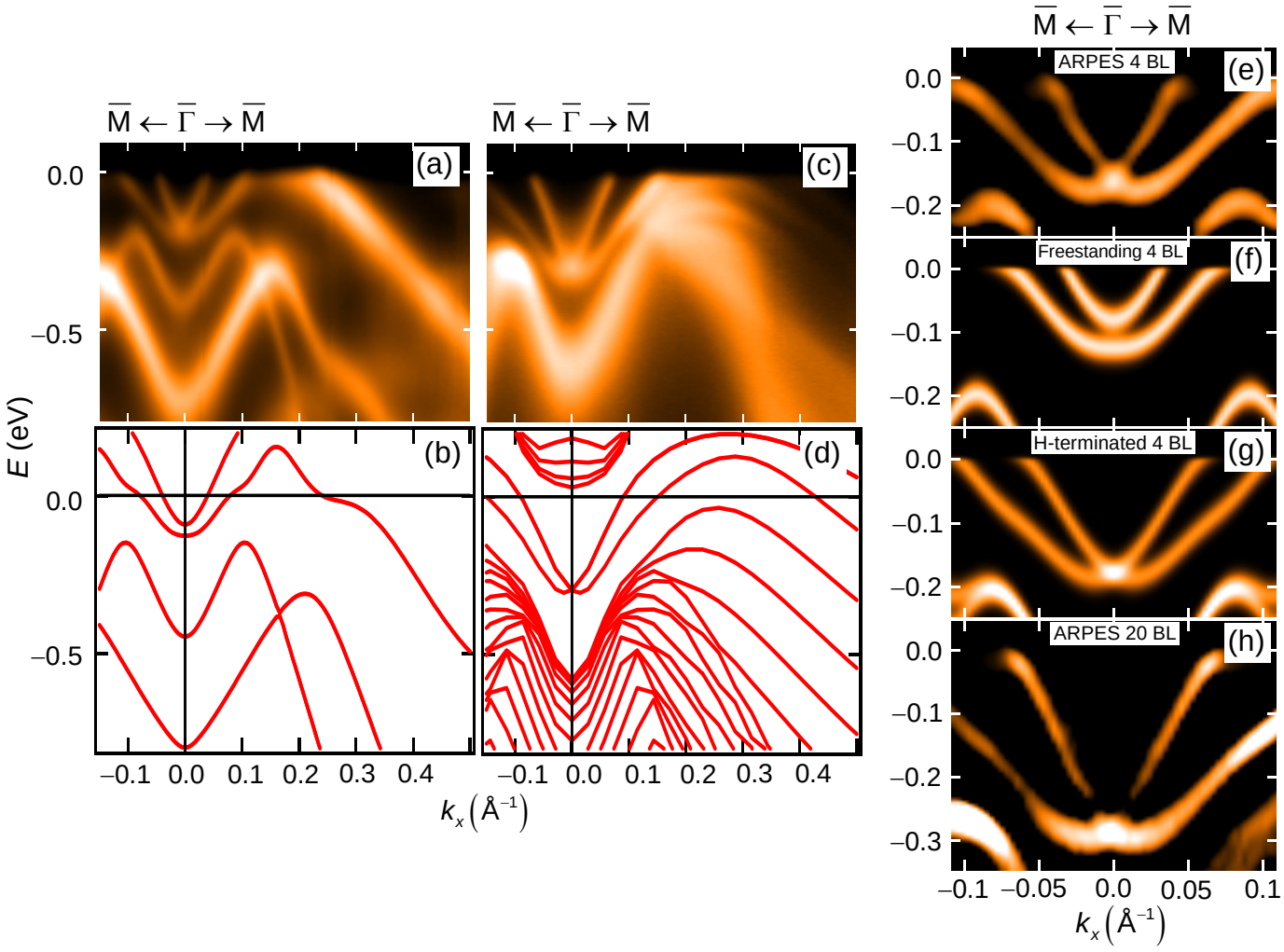

Figure 5.11. (a) ARPES map for a 4-BL Sb film taken along the $\overline{\Gamma}-\overline{\mathrm{M}}$ direction. (b) Calculated band structure of a 4-BL freestanding Sb film. (c) ARPES map for a 20-BL film. (d) Calculated band structure of a 20-BL freestanding Sb film. (e) Close-up view of the experimental surface band structure of a 4-BL film. The contrast has been enhanced by taking the second derivative along the energy axis. (f) Calculated band structure of a 4-BL film suitably broadened to simulate the data. (g) Same as (f) except that the bottom face of the film is terminated by H. (h) Close-up view of the experimental surface band structure of a 20-BL film.

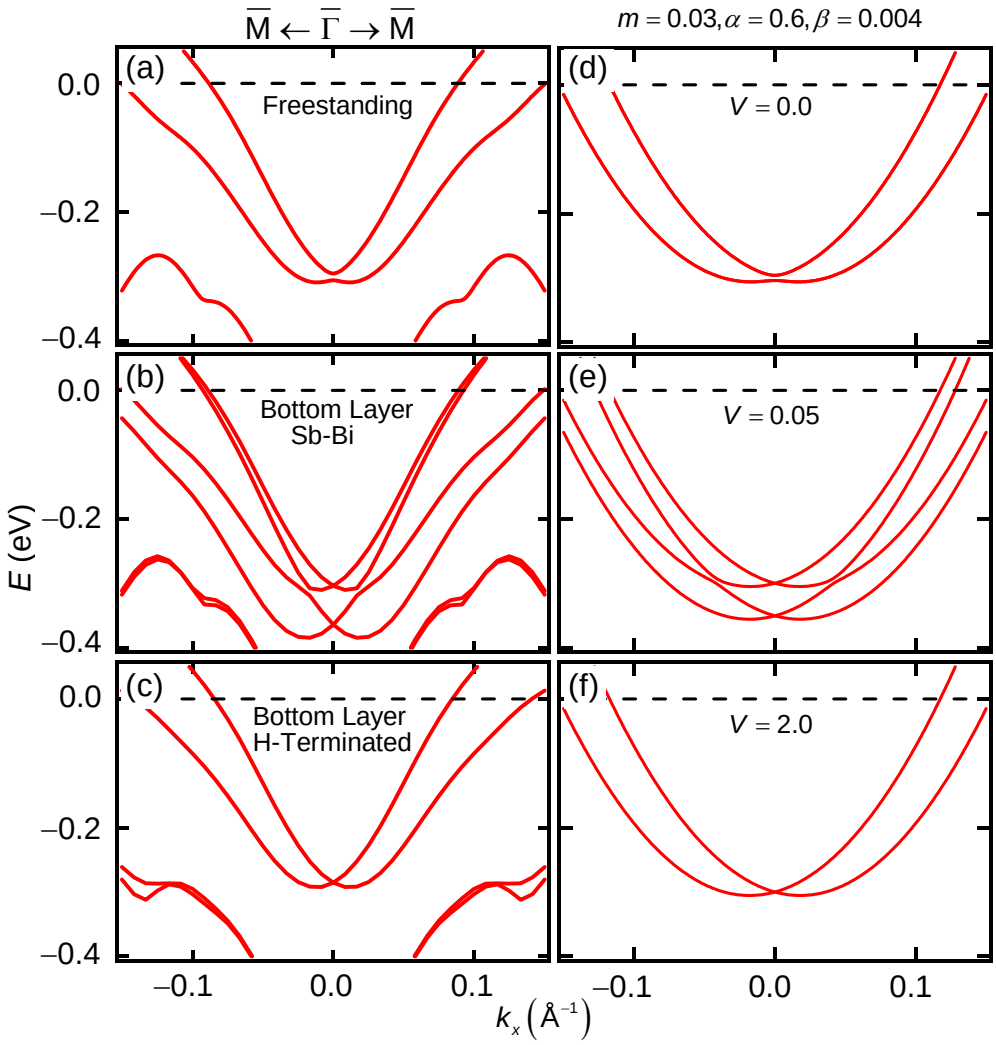

Figure 5.12. Calculated band structure of a 6-BL Sb film with different bottom surface conditions: (a) freestanding, (b) bottom layer of Sb atoms replaced with Sb-Bi averaged pseudo-atoms to simulate a weak interfacial bonding, and (c) bottom face terminated by H atoms. Also shown side-by-side for comparison are results of the four-band Rashba model with different surface biases: (d) $V = 0$, (e) $V = 0.05$, and (f) $V = 2.0$.

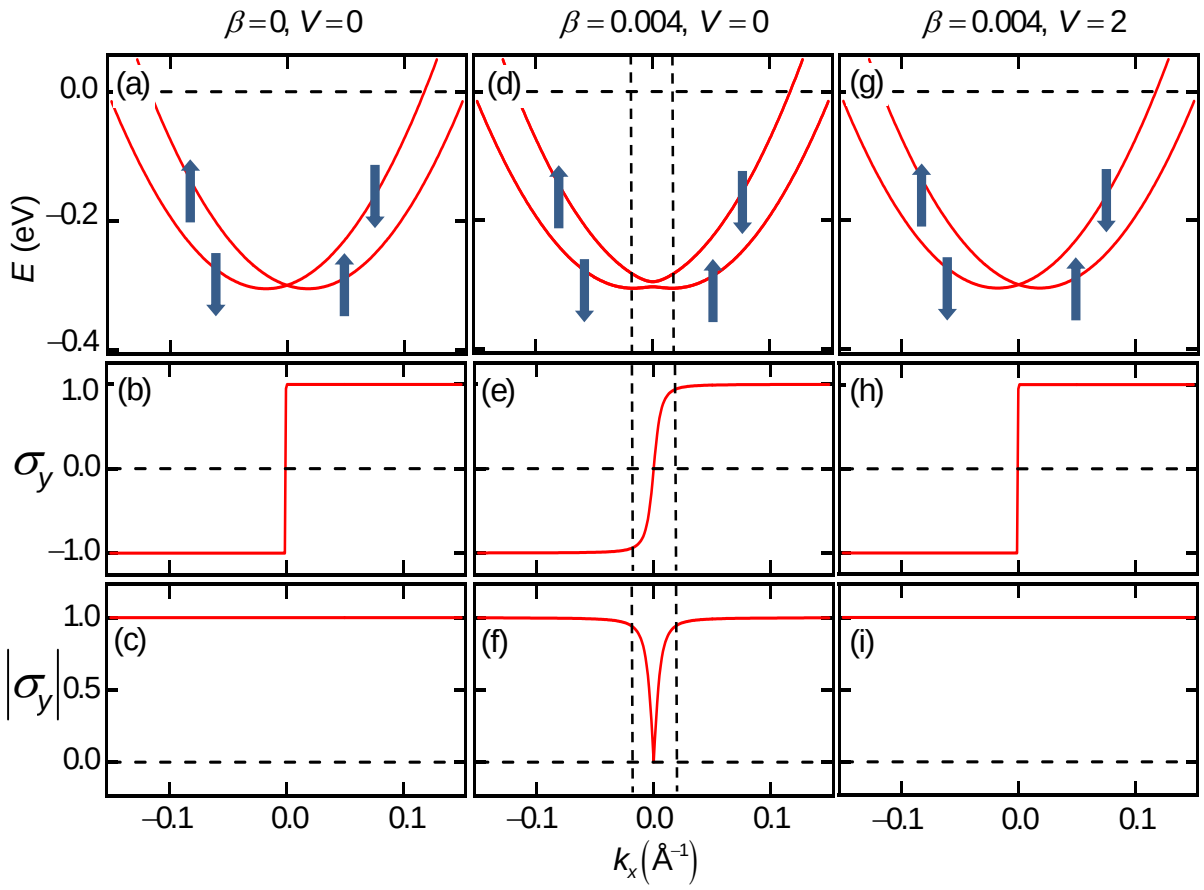

Figure 5.13. (a) Band structure along k_x of the four-band Rashba model (m = 0.03 and α= 0.6) with no tunneling (β = 0) and no surface bias (V = 0). (b) and (c) Normalized spin polarization and magnitude σ_y and $|\sigma_y|$, respectively, for the lower surface band. (d)-(f) Corresponding results for β = 0.004 and V = 0. (g)-(i) Corresponding results for β = 0.004 and V = 2.

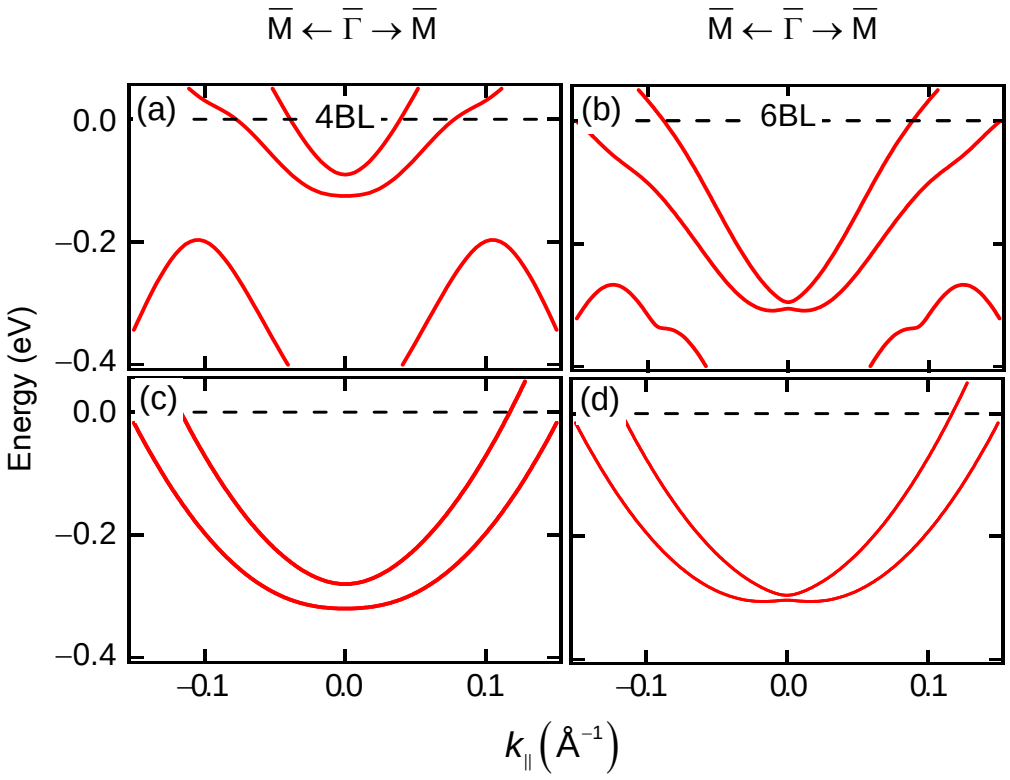

Figure 5.14. Calculated band structures for (a) a 4-BL and (b) a 6-BL freestanding film. Corresponding results based on the four-band Rashba model (m = 0.03, α = 0.6, V = 0) are shown for tunneling matrix element β = (c) 0.02 and (d) 0.004.

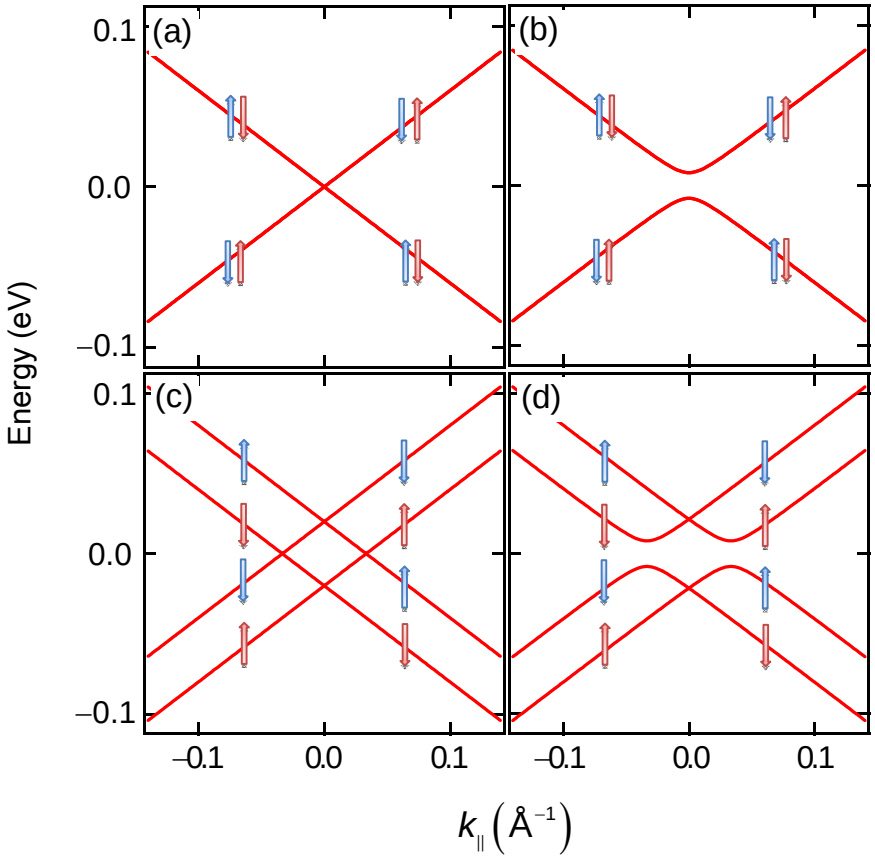

Figure 5.15. Band structures based on the four-band Rashba model with α = 0.6 and various values for the tunneling matrix element and potential bias: (a) β = 0 and V = 0, (b) β = 0.008 and V = 0, (c) β = 0 and V = 0.04, and (d) β = 0.008 and V = 0.04. The direction of each arrow indicates the spin orientation and the color (red or blue) of the arrow indicates the surface (top or bottom) at which the electron is localized.

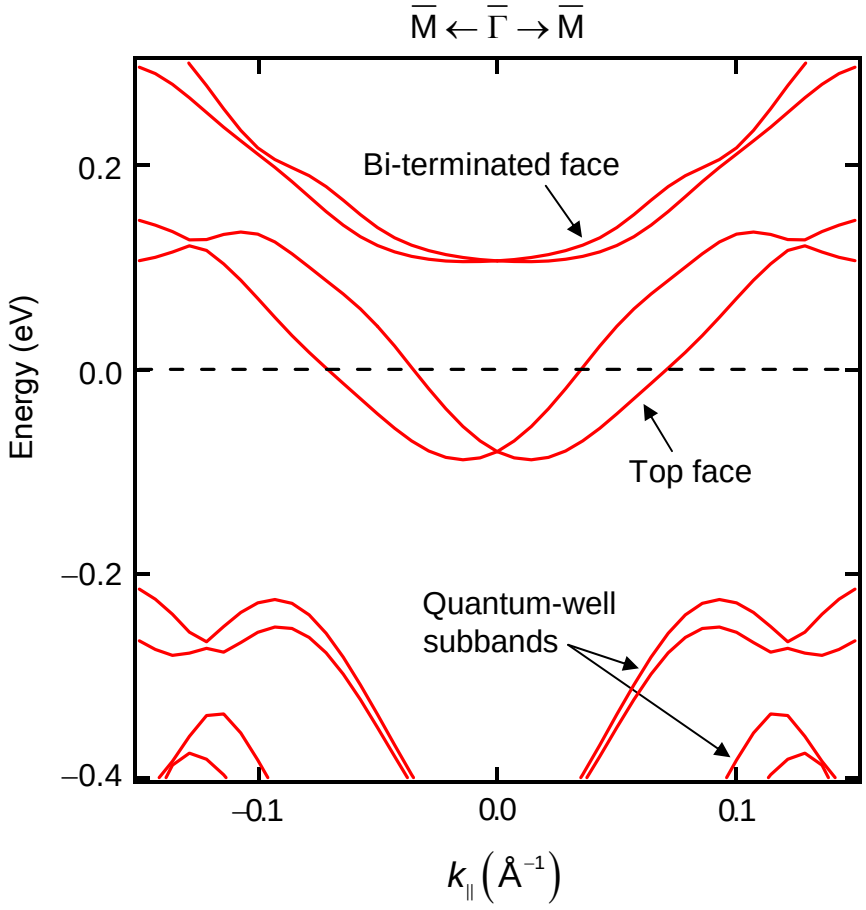

Figure 5.16. Calculated band structure for a 4-BL Sb film terminated by Bi atoms on its bottom face.

6 Topological Thin Films: Bi_2Se_3 and Bi_2Te_3

6.1 Introduction

Topological insulators are a new class of materials characterized by a bulk band gap, a strong spin-orbit coupling, and a conducting surface [1,2]. In these materials, an odd number of spin-polarized surface states span the bulk gap, giving rise to a net surface spin current at the Fermi level [3,4,5]. This spin current, protected by bulk symmetry, is of great interest for applications involving spin information processing [6,7]. While the topological order is a robust quantity, the topological surface states themselves giving rise to the spin current are not necessarily robust and can be highly sensitive to the boundary conditions [8,9]. This is a concern, as actual utilization of these materials requires a stable structure, and surface passivation, capping, or interface formation is generally required for device architecture. How this topological invariance manifests itself upon surface modification is an issue of importance to the basic physics of this class of material and the actual implementation for application. In this chapter there is a demonstration of a drastic transformation of the topological surface states in a model system under the constraint of topological-order invariance. Specifically, the surface states of Bi_2Se_3 and Bi_2Te_3 form a single Dirac cone at the zone center [10,11,12]. First-principles calculations based on a slab geometry show that, upon hydrogen termination of either face of the slab, the Dirac cone associated with this face is replaced by three Dirac cones centered at the time-reversal-invariant $\overline{M}$ points at the zone boundary, yet the topological order remains the same as evidenced by detailed calculations of the wave functions. Furthermore, the topological surface states on the two faces of the slab, with or without hydrogen termination, are quantum-mechanically entangled, and the overall

topological order of the system must be analyzed within this context.

We also studied the critical behavior of the TI film near the quantum critical point. It will be shown in the second part of this chapter that the topological surface states, while protected by symmetry in the bulk limit, can be missing completely in topological films even at large film thicknesses. This anomalous behavior occurs near the transition from topological to nontopological phases when the strength of the SOC is tuned across the critical point. The result is a substantial dead zone where the material is topological but without surface states, as demonstrated by first-principles simulations for freestanding Bi_2Se_3 films. This dead zone is suppressed in an asymmetric film of Bi_2Se_3 with one face terminated by H; the nontopological-to-topological transition is signified by a spatial transfer of a set of Dirac Fermion states from the H-terminated face to the pristine face of the film to form topological surface states.

6.2 Reorganization of Dirac cones in topological insulators by hydrogen termination

An often-invoked argument for the robustness of the surface spin current in topological insulators is that the spin-polarized surface states have a vanishing back scattering probability by surface perturbations because of time-reversal symmetry; indeed, experiments have demonstrated the insensitivity of the surface state Dirac cones to adsorption or gas exposure [13,14]. More generally, though, the surface spin texture can be affected by spin-orbit coupling through altered electronic orbital motions upon surface modification, and it is not necessarily an invariant quantity. Specifically, hydrogen termination leads to surface passivation by saturation of surface dangling bonds. Both the orbital and spin degrees of freedom of the surface electrons can be substantially altered, as demonstrated herein for Bi_2Se_3 and Bi_2Te_3. The results suggest interesting possibilities for optimizing material properties or device performance.

The band dispersion relations for 6 QL freestanding Bi_2Se_3 and Bi_2Te_3 slabs are presented as solid curves in Figs. 6.1(a) and 6.1(b), respectively. The shaded areas represent the projected bulk band regions; these results are in good agreement with previous calculations where available [15,16]. The dashed horizontal lines indicate the midgap positions, or the bulk Fermi levels. The fundamental band gaps are 0.35 and 0.16 eV, respectively. In each case near the zone center $\overline{\Gamma}$ are two surface bands that span the gap and cross each other at $\overline{\Gamma}$ to form a Dirac cone. The Dirac cone has a left-handed helical spin texture, and the two surface bands have opposite spin polarizations. Each point on the surface bands, except the Dirac point, is doubly degenerate corresponding to the surface states located on the two opposite faces of the slab, which are related by space inversion and time reversal. The two surface bands are shown in red and blue color to highlight their different spin orientations. They disperse into the bulk continuum a short distance away from $\overline{\Gamma}$, where they lose their surface character and become quantum well states [17]. Each band remains doubly degenerate; the two surface states associated with the two faces of the slab now fully penetrate the film and combine to form a spin-degenerate pair of quantum well states [18]. Each quantum well subband is spin degenerate as required by space inversion symmetry.

Results from calculations for the same slab with the bottom face of the slab terminated by hydrogen are presented in Figs. 6.1(c) and 6.1(d). While the surface bands near the zone center remain unchanged, a new Dirac cone emerges at $\overline{M}$, and these two cones are smoothly connected throughout the surface zone. With the newly emerged Dirac cone, the total number of surface band crossings of the bulk Fermi level between $\overline{\Gamma}$ and $\overline{M}$ becomes an even number (two or four). This is contrasted by a single crossing for the case without the hydrogen. As is well established, topological insulators must have an odd number of such crossings. At first glance, our results would seem to

violate the topological order of the system, which is a bulk property and cannot be altered by hydrogen termination.

This puzzling behavior is clarified by considering slabs with both faces terminated by hydrogen. The results, shown in Figs. 6.1(e) and 6.1(f), reveal the same surface bands associated with the Dirac cone at $\overline{\mathrm{M}}$, while the surface bands associated with the Dirac cone at $\overline{\Gamma}$ are eliminated. The number of Fermi level crossings is again odd. Evidently, the Dirac cone at $\overline{\mathrm{M}}$ is associated with the hydrogen-terminated face, while the Dirac cone at $\overline{\Gamma}$ is associated with the bare face. For the slab with just one face terminated, both sets of surface bands appear in the calculation. The counting of the Fermi level crossing for each face of the slab is still consistent with the topological order. There are three symmetry-equivalent $\overline{\mathrm{M}}$ points in the first zone, thus, hydrogen-termination results in a trifurcation of the Dirac cone. Hydrogen-termination also breaks the inversion symmetry of the system. The spin degeneracy of each quantum well subband is lifted [19], resulting in a small energy splitting, which diminishes with increasing slab thickness. This splitting is evident for some of the bands in Figs. 6.1(c) and 6.1(d), but not seen in the symmetrical cases.

The plane-averaged charge densities of the two surface bands are presented in Figs. 6.2(b) and 6.2(c) for a 12-QL Bi_2Se_3 slab with its bottom face terminated by hydrogen; the results are presented for 11 equally spaced points between $\overline{\Gamma}$ and $\overline{\mathrm{M}}$ as indicated by the triangles in Fig. 6.2(a). The vertical dashed lines in Figs. 6.2(b) and 6.2(c) indicate the QLs. The two surface states, labeled α and β, are degenerate at $\overline{\Gamma}$ and pinned at the top face of the slab. Near $k_x = 0.1\left|\overline{\Gamma}\overline{\mathrm{M}}\right|$, state β grazes the bulk valence band edge and develops a charge density more akin to a bulk state. It then evolves, at larger k_x, back

into the band gap, and the associated charge density becomes pinned at the bottom face all the way to $\overline{\mathrm{M}}$. State α shows a similar migration of charge density from the top face to the bottom face, but the transition occurs in a different range in *k* space. The directions of the triangles in Fig. 6.2(b), up- and down-pointing, indicate charge localization near the top and bottom faces of the slab, respectively.

This migration of charge density for each state can be described quantitatively by the charge localization function

$$C(k_x) = \frac{2}{D}\langle \psi(k_x) | z | \psi(k_x) \rangle, \tag{6.1}$$

where *D* is the film thickness, and *z* is the normal coordinate of the slab with its origin at the midpoint of the slab. This quantity ranges from –1 to +1, corresponding to a charge distribution fully concentrated at the bottom and top faces, respectively. The results, presented in Fig. 6.3(a), show a rapid passage around the places where the two states graze the bulk band edges.

The spin polarization of the two surface states α and β are characterized by the expectation values of the spin operators. Presented in Fig. 6.3(b) is $\langle S_y \rangle$ normalized to $\hbar/2$. Our calculations yield $\langle S_x \rangle = \langle S_z \rangle = 0$ (*x* points along $\overline{\Gamma}\overline{\mathrm{M}}$, and *z* points along the surface normal). The two states are thus strictly polarized along –*y* and +*y*, respectively, in accordance with the Rashba interaction [20], and the directions of spin polarization are maintained throughout the charge migration from the top to the bottom faces. These spin-locked channels allow the two faces of the slab to communicate. The magnitude of the spin polarization, normalized to $\hbar/2$, is less than 100% because of the coupling of the spin and orbital degrees of freedom. It is about 50%~60% near $\overline{\Gamma}$ where these states are associated with the bare top face of the slab, and it increases to almost 80% near $\overline{\mathrm{M}}$,

where they become surface states associated with the hydrogen-terminated bottom face. Evidently, hydrogen termination enhances the spin polarization of the surface states by partly disentangling the spin and orbital degrees of freedom.

The hydrogen-induced reorganization of the Dirac cones, from one cone at $\bar{\Gamma}$ to three cones at $\overline{M}$, as well as the formation of the spin-locked (or quantum-mechanically entangled) channels, can be understood qualitatively using the schematic diagram in Fig. 6.4(a). To first order, surface adsorption shifts the overall crystal potential for the surface states. With increasingly stronger interaction, the Dirac cone is shifted out of the band gap (middle panel), and eventually the displaced surface bands can intersect again in the gap at the zone boundary $\overline{M}$ point, resulting in a new Dirac cone there (bottom panel). If the band movement can be adjusted, the system could potentially adopt a configuration with gapless surface states but no Dirac cones in the bulk gap, as indicated in the middle panel of Fig. 6.4(a). With just one face of the slab terminated by hydrogen, the surface states on the two faces must connect via avoided crossings through bulk-like states that are located just at the bulk band edges, as indicated in Fig. 6.4(b). The quantization of the bulk states into quantum-well-state pairs in films helps isolate the spin-locked surface bands from the bulk-derived states.

6.3 Evolution of the band structure upon varying the hydrogen atom position

If the hydrogen atoms are gradually moved from a large distance away to their final equilibrium adsorption positions on both faces of a Bi_2Se_3 slab, the band structure should evolve smoothly from one configuration to the other. The results for several selected

H-Se bond lengths for symmetric H adsorption on a 6 QL Bi_2Se_3 slab are shown in Fig. 6.5.

When the bond length is large, the band structure of the slab is not affected by the hydrogen as shown in Fig. 6.5(a). With the hydrogen atoms approaching the surfaces, the original Dirac point at the zone center moves downwards in energy, and eventually merges into the valence band region. Band α, however, remains pinned within the bulk band gap because of anticrossing. The portion of the band near $\overline{\Gamma}$ begins to graze the valence band edge, and the portion of the band near the $\overline{\mathrm{M}}$ point, originally grazing the conduction band edge, now moves down into midgap. Time-reversal symmetry (Kramers theorem) requires double degeneracy at the $\overline{\mathrm{M}}$ point, and this requirement is satisfied by state α dragging its companion quantum well subband into the band gap to form a new surface band β'. The pair α and β' forms a Dirac cone at $\overline{\mathrm{M}}$ for the hydrogen-terminated surface.

6.4 Hydrogen-induced bonding states below the *p* valence bands

In addition to modifying the gapless surface states, hydrogen adsorption gives rise to new surface states within bulk band gaps. A prominent example is seen in Fig. 6.5 where two H-induced surface bands, α_H and β_H, arise within the *s*-*p* gap (the lower *s* bands are not shown). This pair shows the usual Rashba splitting and is topologically trivial. Presented in Fig. 6.6 are the charge distributions of states α_H and β_H at $\overline{\Gamma}$ for a 12 QL Bi_2Se_3 slab with its bottom face terminated by H. The charges are strongly localized

near the H-Se bonds. The calculated spin polarizations of these states are nearly 100%.

6.5 Robustness of the first-principles results

The calculations described in the main text were performed using LDA. To test the robustness of the results, we show in Figs. 6.7(a) and 6.7(b) the calculated dispersion relations for a 6 QL slab of Bi_2Se_3 with its bottom face terminated by hydrogen using two different exchange-correlation functionals: LDA and Perdew-Burke-Ernzerhof GGA, respectively. In each case, the H atom position is optimized energetically. The results are nearly identical; the main difference is that the Dirac point is at a slightly different energy. We have also explored the issue of atomic relaxation by allowing the positions of the surface layer of Bi_2Se_3 and the H atoms to relax in the LDA calculation. We find that the Se atom adjacent to each H atom moves outwards by 0.01 Å and the length of the H-Se bond is elongated by 0.05 Å. These slight atomic movements are not expected to cause significant changes in the calculated band structure. Indeed, the results, presented in Fig. 6.7(c), are very close to those in Figs. 6.7(a) and 6.7(b). Specifically, the topological properties of the system remain the same. Thus, our conclusions are independent of the details of the calculation.

6.6 Bulk band structures and parity eigenvalues of Bi_2Se_3 with/without SOC

Bi_2Se_3 has a rhombohedral crystal structure with nine occupied valence bands. There are eight time-reversal-invariant momenta (TRIMs) in the first Brillouin zone: Γ(0, 0, 0), Z(0.5, 0.5, 0.5), three equivalent F(0.5, 0.5, 0), and three equivalent L(0.5, 0, 0). We define ξ_{in} to be the parity eigenvalue of the n-th valence state at the i-th TRIM, where n = 1-9 and i = 1-8. We also define Pd^{TRIM} as the product of the parity eigenvalues of the

nine valence states at each TRIM and Pd^{band} as the product of the parity eigenvalues at the eight TRIMs for each band. The topological invariant ν is given by

$$(-1)^{\nu} = \prod_{i=1}^{8}\prod_{n=1}^{9}\xi_{in} = \prod_{i=1}^{8} Pd_i^{TRIM} = \prod_{n=1}^{9} Pd_n^{band} . \tag{6.2}$$

If the total product of the parity eigenvalues is -1, $\nu = 1$ and the material is topological. Otherwise, it is nontopological. The bulk band structures of Bi_2Se_3 without and with SOC are shown in Figs. 6.8(a) and 6.8(b), respectively. The corresponding parity eigenvalues are listed in Table 6.1. The calculated topological invariant reveals that Bi_2Se_3 without SOC is nontopological and vice versa. The crucial differences between the two cases, with or without SOC, happen at the zone center for the top valence band V1 and the bottom conduction band C1. The two states exchange their opposite parities across the transition, resulting in gap inversion.

6.7 Topological phase transition and Dirac fermion transfer in Bi_2Se_3 films

Device applications of topological materials must involve thin films for large-scale integration; how thin the films can be without losing their desirable characters is a key question. This issue is tied to the strength of the SOC. Changing the effective SOC strength can be realized experimentally by alloy substitution with elements in the same columns in the period table, such as substituting Sb for Bi and/or S for Se in Bi_2Se_3 [21 , 22]. The phenomenon of missing topological surface states near the topological-to-nontopological transition is a much more severe issue than a tunneling gap in the surface states that can open up as a result of the interaction between the two faces of the film. The tunneling gap does not preclude spin-polarized surface states and can be avoided by Fermi level tuning. Without surface states altogether, the system is insulating and useless for transport applications.

For bulk topological insulators with space-inversion symmetry, such as Bi_2Se_3, the Z_2 topological order ν is determined by the parity product of the valence states at time-reversal-invariant momenta (TRIMs) in the first Brillouin zone [23]. Calculations of the band structure at various levels of SOC strength (Fig. 6.9(b)) ranging from 0 to 100% confirm that Bi_2Se_3 is naturally topological, but becomes nontopological as the SOC is reduced to below 31.2%. At this quantum critical point (QCP), the conduction and valence band edges cross each other at Γ, resulting in a parity exchange and a gap reversal, which causes the system to undergo a topological-to-nontopological transition. The calculated fundamental gap (Fig. 6.9(c)) crosses zero at the QCP, which separates the nontopological phase ($\nu = 0$) from the topological phases ($\nu = 1$).

Surface properties are not available from bulk calculations. Instead, we perform a slab calculation for a Bi_2Se_3 freestanding film of a thickness of 6 quintuple layers (QLs). Prior theoretical and experimental work has shown that the surface states at this thickness are essentially in the bulk limit with a negligible tunneling gap [24]. The calculated band dispersion relations with different SOCs are shown in Figs. 6.10(a)-6.10(d). The shaded areas indicate the projected bulk band regions. At 100% SOC, the system shows a pair of surface states forming a Dirac cone at $\bar{\Gamma}$ and bridging the bulk gap. At 0% and 20% SOCs, the system is an ordinary insulator with no surface states. The case of 40% SOC is peculiar. The system is beyond the QCP and should be topological, but all of the states correspond to quantum well states. The apparent gap between the lowest conduction band and the highest valence band is induced by the tunneling effect between the topological surface states on the opposite surface. The coupling of surface states is roughly one half of the size of the apparent tunneling gap. In other words, without the tunneling effect this gap should vanish and a gapless Dirac cone should form within the bulk band gap. The topological surface states do not emerge until SOC becomes greater than 48%. Thus, there is a wide dead zone between the QCP of 31.2% and the onset point (OSP) of

surface states at 48%. The results are summarized in Fig. 6.10(e), where the absolute bulk gap is indicated by hatching, and the apparent gap between the lowest conduction band and the highest valence band is indicated by a curve. This curve crosses the QCP with an apparent gap of 0.18 eV, where the bulk gap vanishes; it crosses the OSP where the apparent gap equals the bulk gap of 0.11 eV. Beyond the OSP, the apparent gap becomes smaller than the bulk gap and the relevant states transform from quantum well states into surface states. The apparent gap does not vanish until SOC reaches about 80%, the saturation point (SP).

Calculations for a 10-QL Bi_2Se_3 film reveal a similar pattern (Fig. 6.10(e)). The dead zone, ranging from QCP = 31.2% to OSP = 42%, is smaller but still quite significant. The SP is reduced to about 70%. For the ∞-QL case (Fig. 6.10(e)), or the bulk limit, there are no surface states in the bulk gap below the QCP, and the system is an ordinary insulator. The topological surface states emerge beyond the QCP and form a Dirac cone at $\bar{\Gamma}$ with zero apparent gap.

A crude argument for the dead zone is a tunneling gap so large that the surface states are pushed out of the bulk gap. Rigorously speaking, this argument is incorrect because it assumes that surface states exist to begin with, an assumption not supported by the results. One way to suppress the tunneling gap effect is to make the film asymmetric, thus removing the degeneracy coupling of the surface states associated with the two faces of the film [25,26]. We consider here a 6-QL Bi_2Se_3 film terminated by hydrogen on the top face; energy-minimization calculations show a hydrogen atom on top of each surface selenium atom at a H-Se bond length of 1.46 Å. The calculated band dispersion relations (Figs. 6.11(a)) with the SOC set to 0, in comparison with the case without H (Fig. 6.10(a)), reveal a H-induced surface band within the bulk gap. The associated charge density is localized near the H-terminated face except at the $\bar{\Gamma}$ point, where the surface

band grazes the tip of the valence band region to yield a diffuse wave function in the film. The pristine face at the bottom of the film has no topological surface states in agreement with the results for the freestanding film (Fig. 6.10(a)).

With the SOC turned on to 20% (Fig. 6.11(b)), the H surface band becomes spin split due to the Rashba interaction and develops two chiral Dirac cones, one at $\bar{\Gamma}$ and the other at $\bar{M}$. The appearance of a pair of Dirac cones is in agreement with the chiral Fermion doubling rule [27]. Both Dirac cones are still localized near the H-terminated face. The system remains topologically trivial based on the usual rule of counting Fermi level crossings for each face. With the SOC raised to 40% (beyond the QCP), the material becomes topological, but the band structure (Fig. 6.11(c)) appears similar to the 20% case albeit with a larger spin splitting. However, expanded views of the band structure near $\bar{\Gamma}$ (Figs. 6.11(e) and 6.11(f)) show that the Dirac cone does not span the bulk gap at SOC = 20% but does so at 40%. Bulk gap spanning is a necessary, but not a sufficient, condition for "partner switching" and a nontrivial surface topological order [28].

The calculated three-dimensional charge distributions of the H-terminated 6-QL Bi_2Se_3 film at various levels of SOC reveal that the Dirac surface states at $\bar{M}$ remain localized at the H-terminated (top) face throughout the entire range of SOC variation (Fig. 6.12(b)). The main change in the dispersion relation (Fig. 6.11(a-d)) is the magnitude of the spin-orbit splitting. By contrast, the Dirac Fermion states near $\bar{\Gamma}$ (Fig. 6.12(a)) undergo a charge transfer from the H-terminated (top) face to the pristine (bottom) face with the SOC increasing through the QCP. For this calculation, we pick the upper surface band at a point slightly offset from $\bar{\Gamma}$ (at 0.025 $Å^{-1}$ or ~3% $\bar{\Gamma}\bar{M}$) to avoid the degeneracy with the bulk valence band edge at SOC below the QCP. Thus, with the SOC below the QCP, both Dirac cones at $\bar{\Gamma}$ and $\bar{M}$ are associated with the H-terminated

surface, and the two surface bands remain within the bulk gap. With the SOC crossing the QCP, the Dirac cone Fermions at $\bar{\Gamma}$ transfer to the pristine face, and simultaneously the surface bands touch both the conduction and valence band edges to bridge the bulk gap. Each Dirac cone yields just one Fermi level crossing per face of the film, and the system is topological based on the counting of Fermi level crossings.

The spatial transfer of the Dirac cone Fermions near $\bar{\Gamma}$ can be quantified by the charge moment

$$P = \frac{< \Psi_{SS} \mid \rho z \mid \Psi_{SS} >}{D} \tag{6.3}$$

where D is the film thickness, ρ is the normalized charge density operator and $z = 0$ is at the midpoint of the Bi_2Se_3 film. Its absolute value ranges from 0 (symmetric bulk states) to 0.5 (tightly bound surface states) and its sign indicates the charge bias (+ toward the H-terminated face, and – toward the pristine face). The calculated results (Fig. 6.12(c)) show a spatial transfer of the Dirac cone states at $\bar{\Gamma}$ across the QCP. With H-termination, there is an ambiguity about the "midpoint" of the film, and this accounts for the slight offset of the zero crossing of the curve.

6.8 Band structures of a 6-QL Bi_2Se_3 film with the top face terminated by F or Cl

We have computed the effects of F and Cl termination of a 6-QL Bi_2Se_3 film to simulate the effects of interfacial bonding to highly electronegative surfaces. The results for the two cases are very similar. Without SOC, there is a surface band induced by the adsorbate (Fig. 6.13). The band shapes are similar to the case of H-termination, but the surface band sticks to the bottom point of the conduction band region instead of the top

point of the valence band region. The atomic orbitals involved in the surface states are the 1s orbital of H, the 2p orbital of F, and the 3p orbital of Cl. The s and p orbitals have different parities, and the corresponding surface states must connect to either the conduction or valence band edge with a compatible parity.

6.9 Conclusion

In this chapter we demonstrates that the surface states of topological insulators as well as their associated spin structure and degree of spin polarization can be substantially modified by surface and/or interface engineering. The reconfigured surface states still satisfy the requirements of topological order and time-reversal symmetry. Robustness of the surface states against surface perturbation because of a vanishing back scattering probability does not prevent these states from transforming into drastically different configurations. These conclusions are independent of the details of the model as demonstrated by additional calculations using the GGA approximation or allowing surface atomic layer relaxation. Our findings suggest opportunities for optimization of the spin current and spin texture. For thin films in the ballistic transport regime, the spin currents of the two opposite faces of the film could be connected with locked spin directions through bulk-like states without going through the side faces. This connection is a unique feature of topological insulators.

Moreover, the phenomenon of the dead zone, where topological insulator films exhibit no topological surface states and behave like band insulators, sets a lower limit on the film thickness suitable for device applications. This limiting thickness can be quite large in "marginal" topological insulators with a relatively weak SOC. This dead zone effect can be suppressed in an asymmetric film configuration, which can be readily realized in experiments or actual device configurations by growing the film on a substrate with a strong interfacial bonding to break the degeneracy coupling underlying the

tunneling effect. The restoration of the topological surface states on the pristine face in the dead zone is via spatial transfer of Dirac Fermion states from the other face; thus, the evolution of the system remains analytically continuous.

References:

[1] M. Z. Hasan and C. L. Kane, Rev. Mod. Phys. **82**, 3045 (2010).

[2] X. L. Qi and S. C. Zhang, Rev. Mod. Phys. **83**, 1057 (2011).

[3] D. Hsieh *et al.*, Nature **452**, 970 (2008).

[4] L. Fu and C. L. Kane, Phys. Rev. B **76**, 045302 (2007).

[5] R. Roy, Phys. Rev. B **79**, 195322 (2009).

[6] I. Garate and M. Franz, Phys. Rev. Lett. **104**, 146802 (2010).

[7] L. Fu and C. L. Kane, Phys. Rev. Lett. **100**, 096407 (2008).

[8] Y. L. Chen *et al.*, Science **329**, 659 (2010).

[9] O. V. Yazyev, J. E. Moore and S. G. Louie, Phys. Rev. Lett. **105**, 266806 (2010).

[10] Y. Xia *et al.*, Nat Phys **5**, 398 (2009).

[11] Y. L. Chen *et al.*, Science **325**, 178 (2009).

[12] Y. Zhang *et al.*, Nat Phys **6**, 584 (2010).

[13] H. M. Benia, C. Lin, K. Kern and C. R. Ast, arXiv:1105.2664v1 (2011)

[14] Z.-H. Pan, D. R. Gardner, S. Chu, Y. S. Lee and T. Valla, arXiv:1104.0966v1 (2011)

[15] Z. Wei *et al*., New J. Phys. **12**, 065013 (2010).

[16] H. Zhang *et al.*, Nat Phys **5**, 438 (2009).

[17] T. C. Chiang, Surf. Sci. Rep. **39**, 181 (2000).

[18] G. Bian, T. Miller and T.-C. Chiang, Phys. Rev. Lett. **107**, 036802 (2011)

[19] J. H. Dil *et al.*, Phys. Rev. Lett. **101**, 266802 (2008).

[20] Y. A. Bychkov and J. Rashba, Phys. C: Solid State Phys. **17**, 6039 (1984).

[21] S. Xu, et al., Science **332**, 560 (2011).

[22] T. Sato, et al., Nat. Phys. **7**, 840 (2011).

[23] Z. Wei, et al., New J. Phys. **12**, 065013 (2010).

[24] G. Bian, et al., Phys. Rev. Lett. **108**, 176401 (2012).

[25] G. Bian, et al., Phys. Rev. B **84**, 235414 (2011).

[26] X. Wang, et al., Phys. Rev. Lett. **108,** 096404 (2012).

[27] N. B. Nielsen and M. A. Ninomiya, Phys. Lett. B **105**, 219 (1981).

[28] D. Hsieh, et al., New J. Phys. **12**, 125001 (2010).

Figures and tables:

0% SOC	V1	V2	V3	V4	V5	V6	V7	V8	V9		Pd^{TRIM}		C1
Γ	+1	-1	-1	-1	+1	+1	-1	-1	-1		+1		+1
L (3)	-1	-1	-1	-1	-1	-1	+1	+1	+1		+1		+1
F (3)	-1	+1	-1	-1	-1	+1	+1	-1	-1		+1		+1
Z	-1	-1	+1	-1	+1	+1	-1	-1	-1		+1		+1
Pd^{band}	-1	-1	-1	+1	+1	-1	+1	-1	-1		+1		+1

100% SOC	V1	V2	V3	V4	V5	V6	V7	V8	V9		Pd^{TRIM}		C1
Γ	-1	+1	-1	+1	-1	+1	-1	-1	+1		-1		-1
L (3)	-1	-1	+1	-1	-1	-1	-1	+1	+1		+1		+1
F (3)	-1	+1	-1	-1	+1	-1	-1	+1	-1		+1		+1
Z	-1	-1	+1	-1	+1	+1	-1	-1	-1		+1		+1
Pd^{band}	+1	+1	+1	-1	+1	+1	+1	+1	+1		-1		-1

Table 6.1. Parity eigenvalues at the eight TRIMs of the nine valence bands and the lowest conduction band of Bi_2Se_3 calculated without/with spin-orbit coupling.

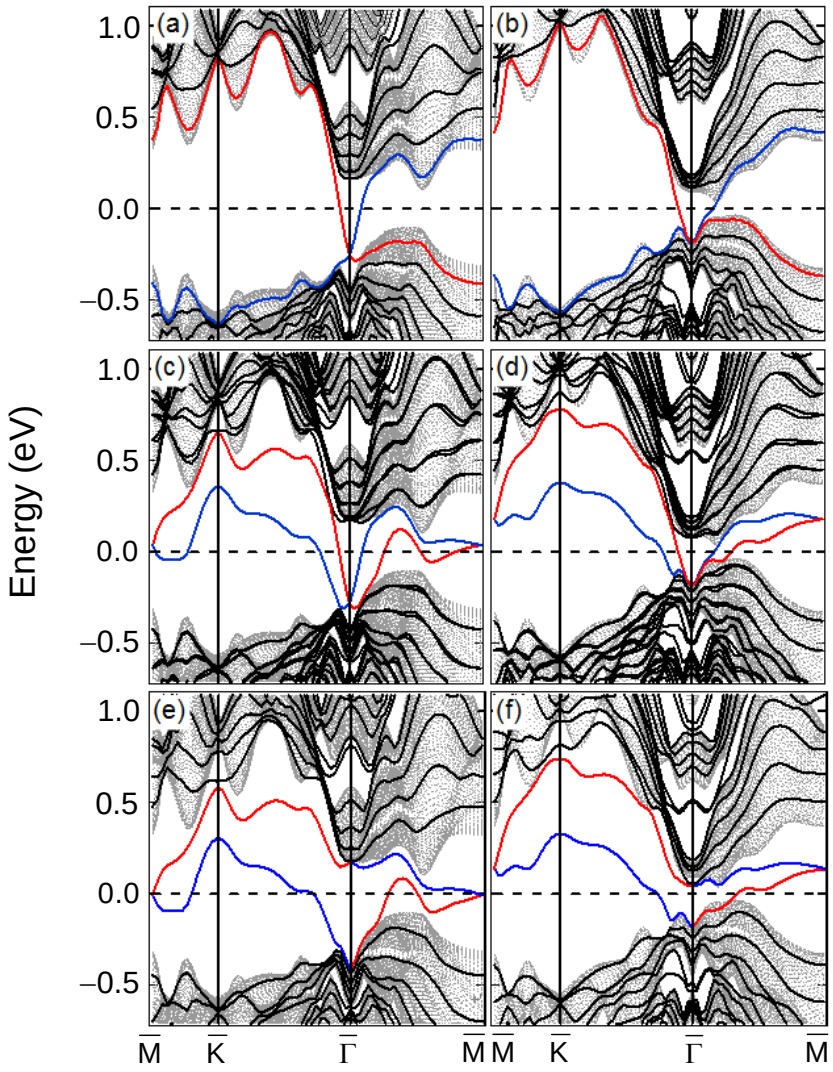

Figure 6.1. (a and b) Calculated dispersion relations (solid curves) for 6 QL slabs of Bi_2Se_3 and Bi_2Te_3, respectively. The shaded areas are projected bulk band regions. The horizontal dashed lines indicate the bulk Fermi levels. The red and blue curves represent surface states and their continuations into the bulk regions. (c and d) Results after the bottom faces of the slabs are terminated by hydrogen. (e and f) Results after both faces are terminated by hydrogen.

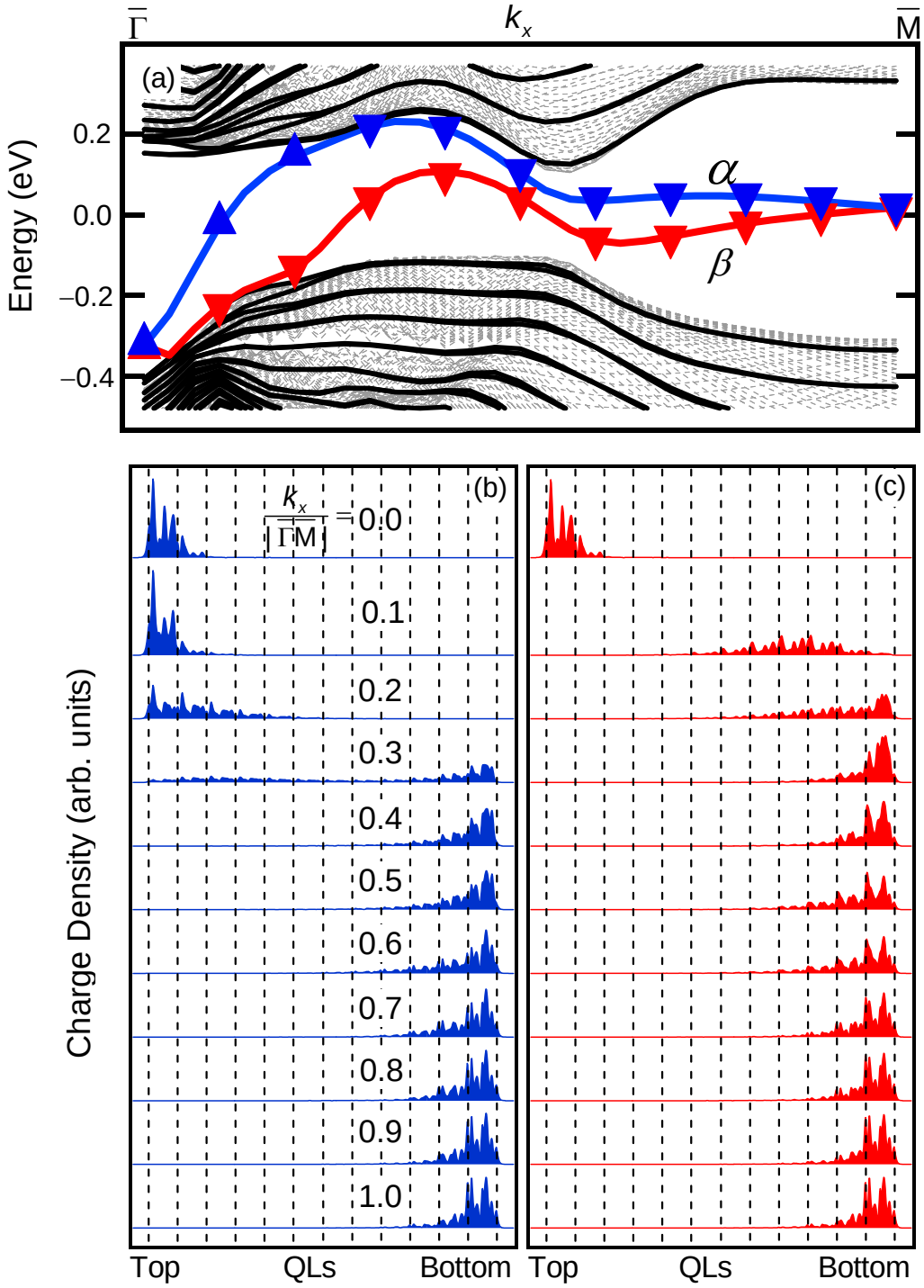

Figure 6.2. (a) Surface bands, α and β, of a 12 QL slab of Bi_2Se_3 with its bottom face terminated by hydrogen. (b and c) Plane-averaged electronic charge densities for the two states.

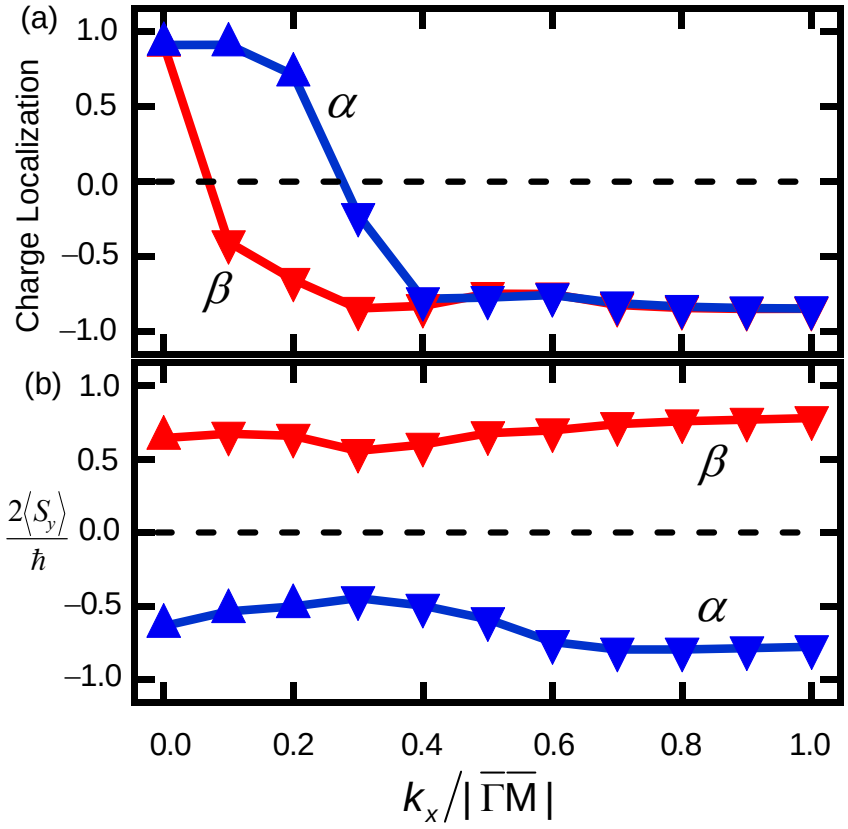

Figure 6.3. (a) Charge localization as a function of k_x (along $\bar{\Gamma}\bar{\mathrm{M}}$) for the two states α and β in a 12 QL slab of Bi_2Se_3 with its bottom face terminated by hydrogen. It equals +1 and –1 for charge fully localized at the top and bottom faces of the slab, respectively. (b) Calculated spin polarization $2\langle S_y \rangle / \hbar$.

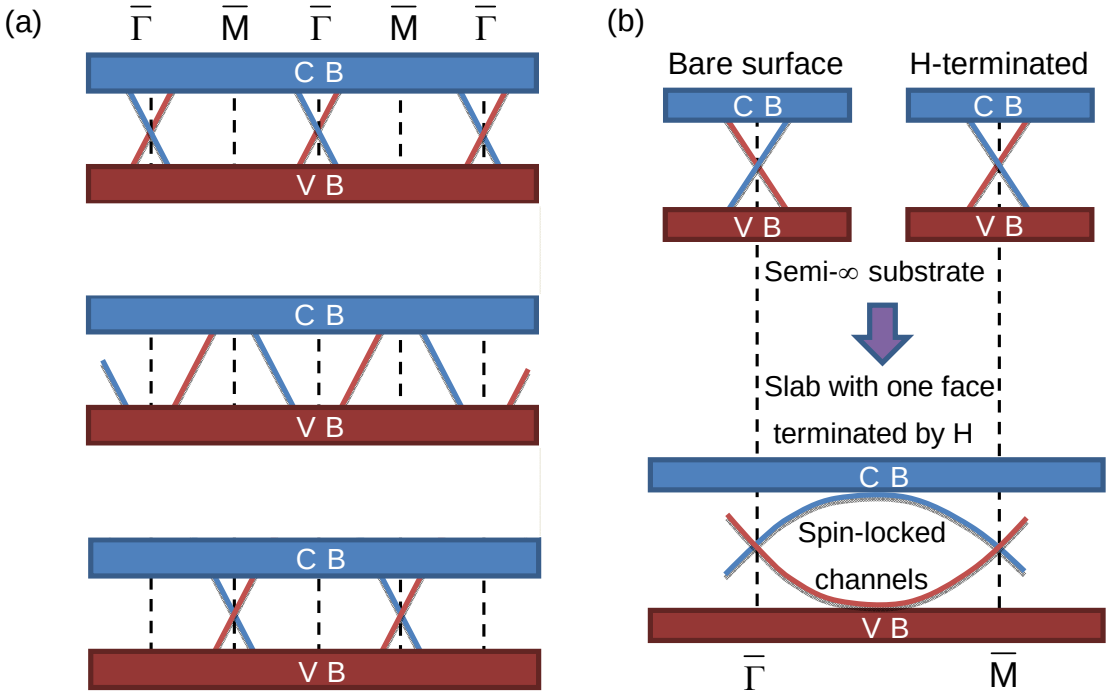

Figure 6.4. (a) Displacement of Dirac cones in the vertical direction relative to the bulk conduction band (CB) and valence band (VB) as the surface potential changes. (b) The top two diagrams correspond to semi-infinite substrates, one without and the other with hydrogen termination; the Dirac cones are located at $\overline{\Gamma}$ and $\overline{\mathrm{M}}$, respectively. For a finite slab with just the bottom face terminated by hydrogen, the Dirac cones associated with the two faces must connect by analytic continuation (or anti-crossing), resulting in spin-locked channels as shown in the bottom diagram.

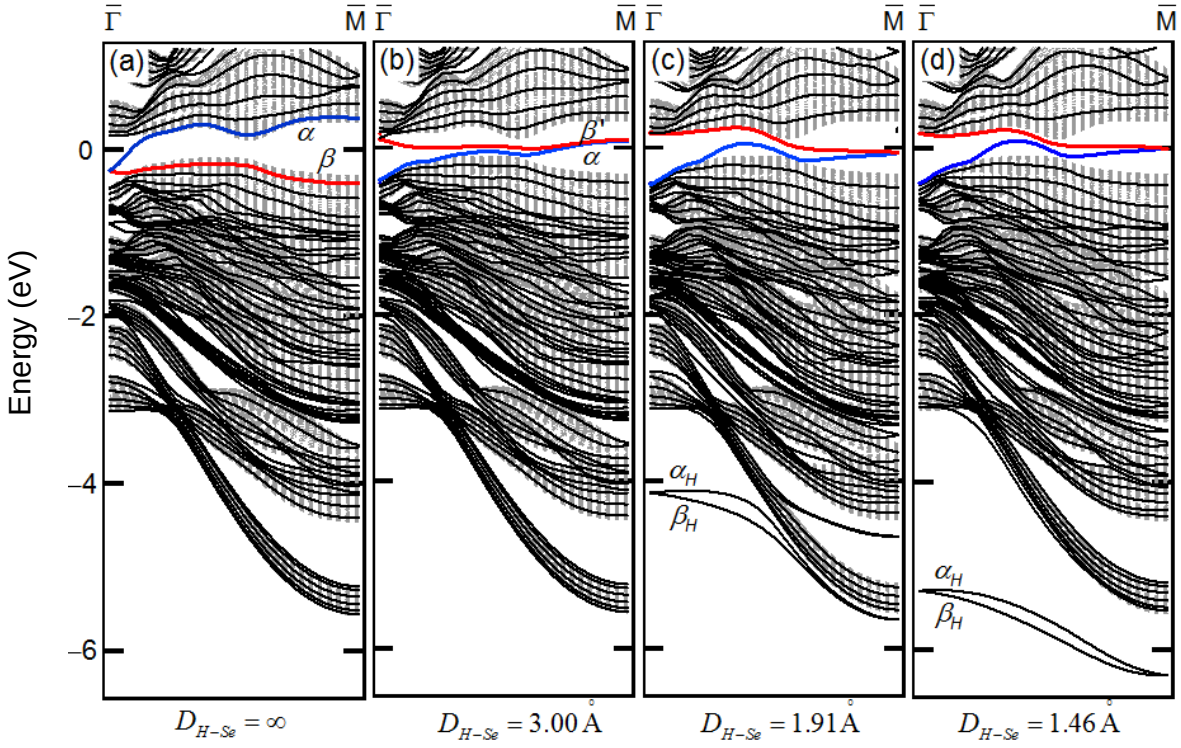

Figure 6.5. Evolution of band structure as hydrogen adatoms approach both faces of a 6 QL Bi_2Se_3 slab. The H-Se bond length is (a) ∞, (b) 3.00, (c) 1.91, and (d) 1.46 Å (equilibrium bond length).

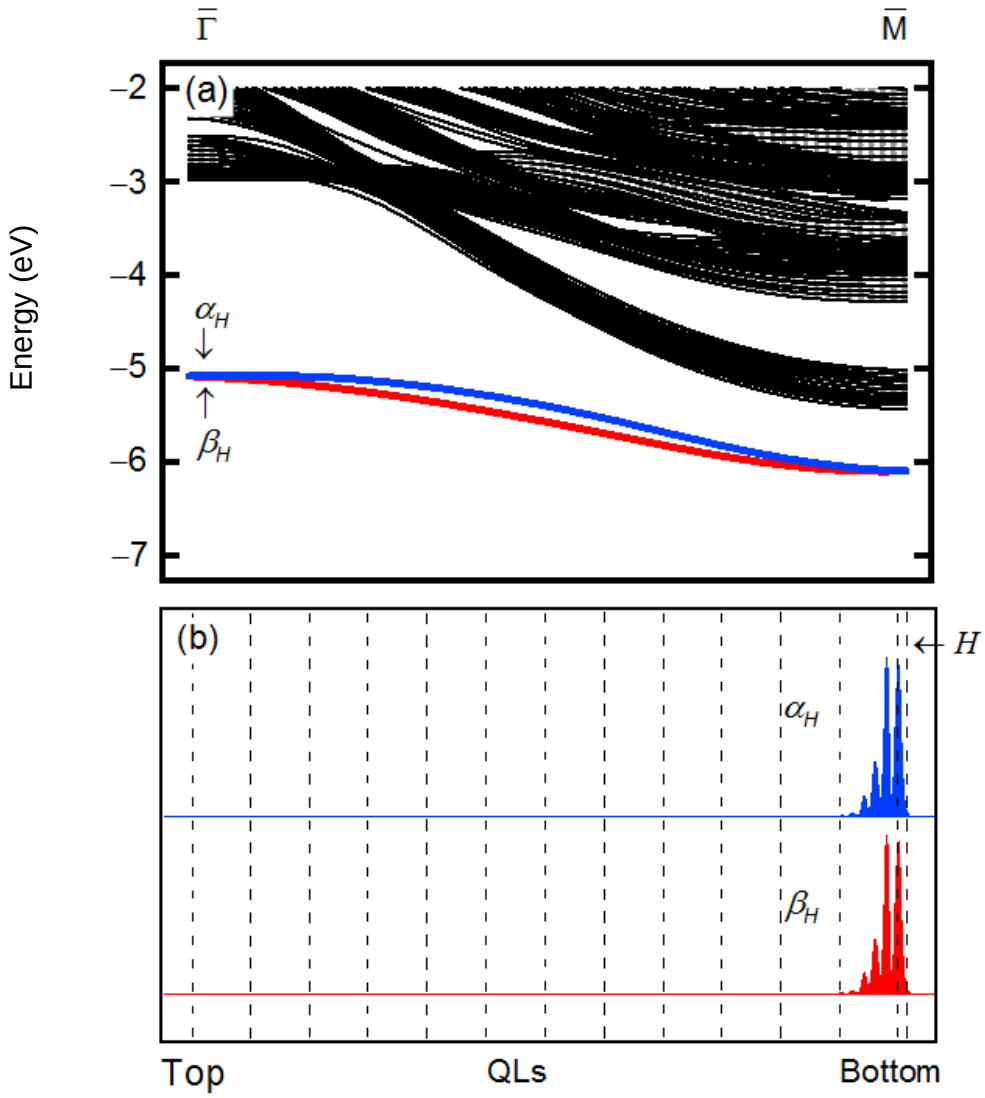

Figure 6.6. (a) Hydrogen-termination-induced bands α_H and β_H for a 12 QL Bi_2Se_3 slab with its bottom face terminated by H. (b) Charge distributions of states α_H and β_H at the zone center $\bar{\Gamma}$.

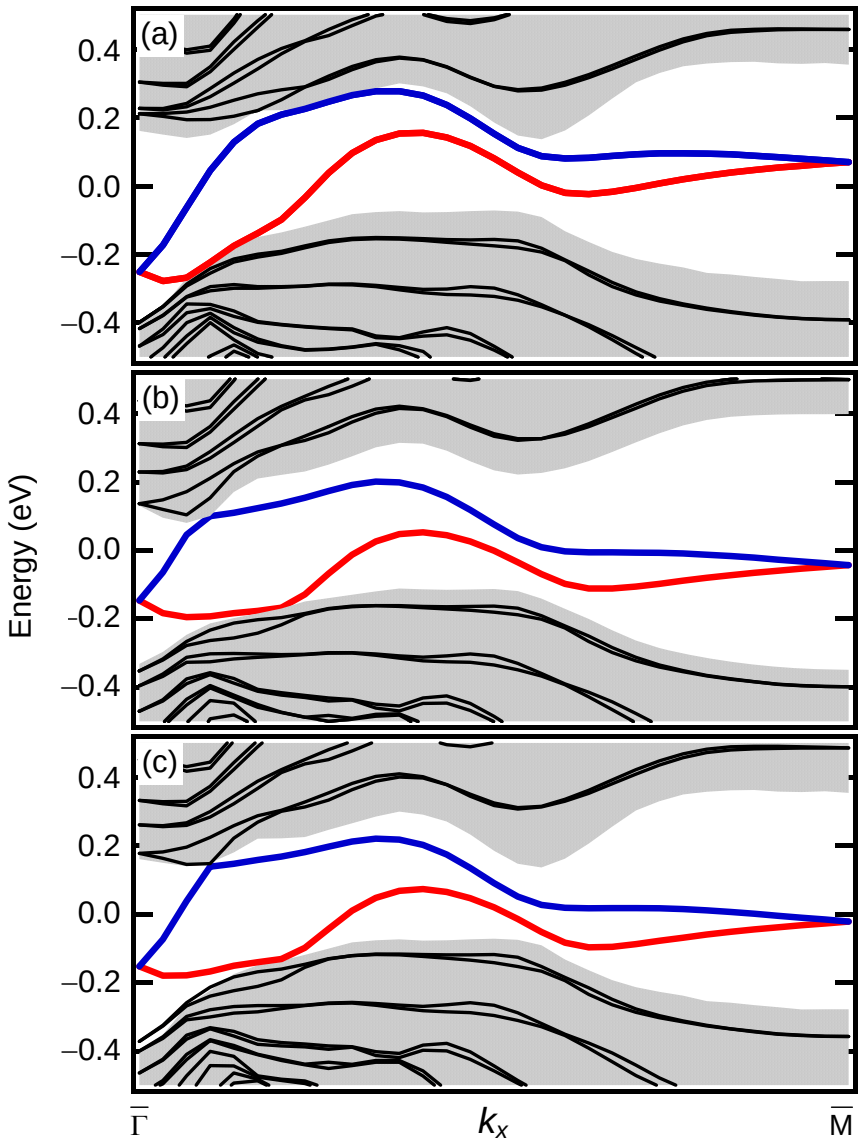

Figure 6.7. Calculated dispersion relations for a 6 QL slab of Bi_2Se_3 with its bottom face terminated by hydrogen. Only the position of the H atom is optimized using (a) LDA and (b) GGA for the exchange-correlation functional. (c) The surface Se atomic layer of Bi_2Se_3 and the H atoms are relaxed using LDA.

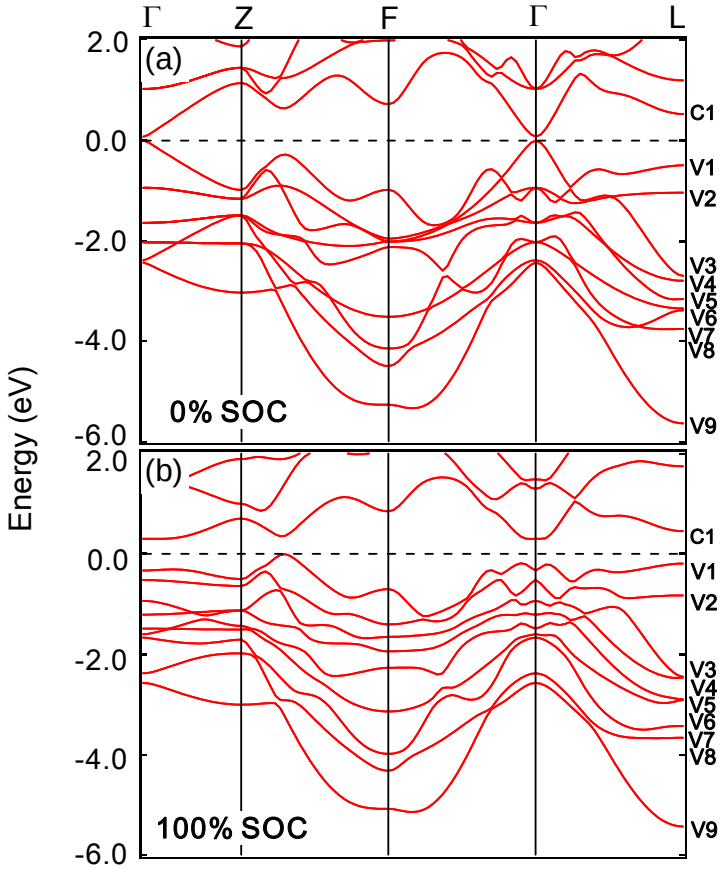

Figure 6.8. Bulk band structure of Bi_2Se_3 without/with SOC.

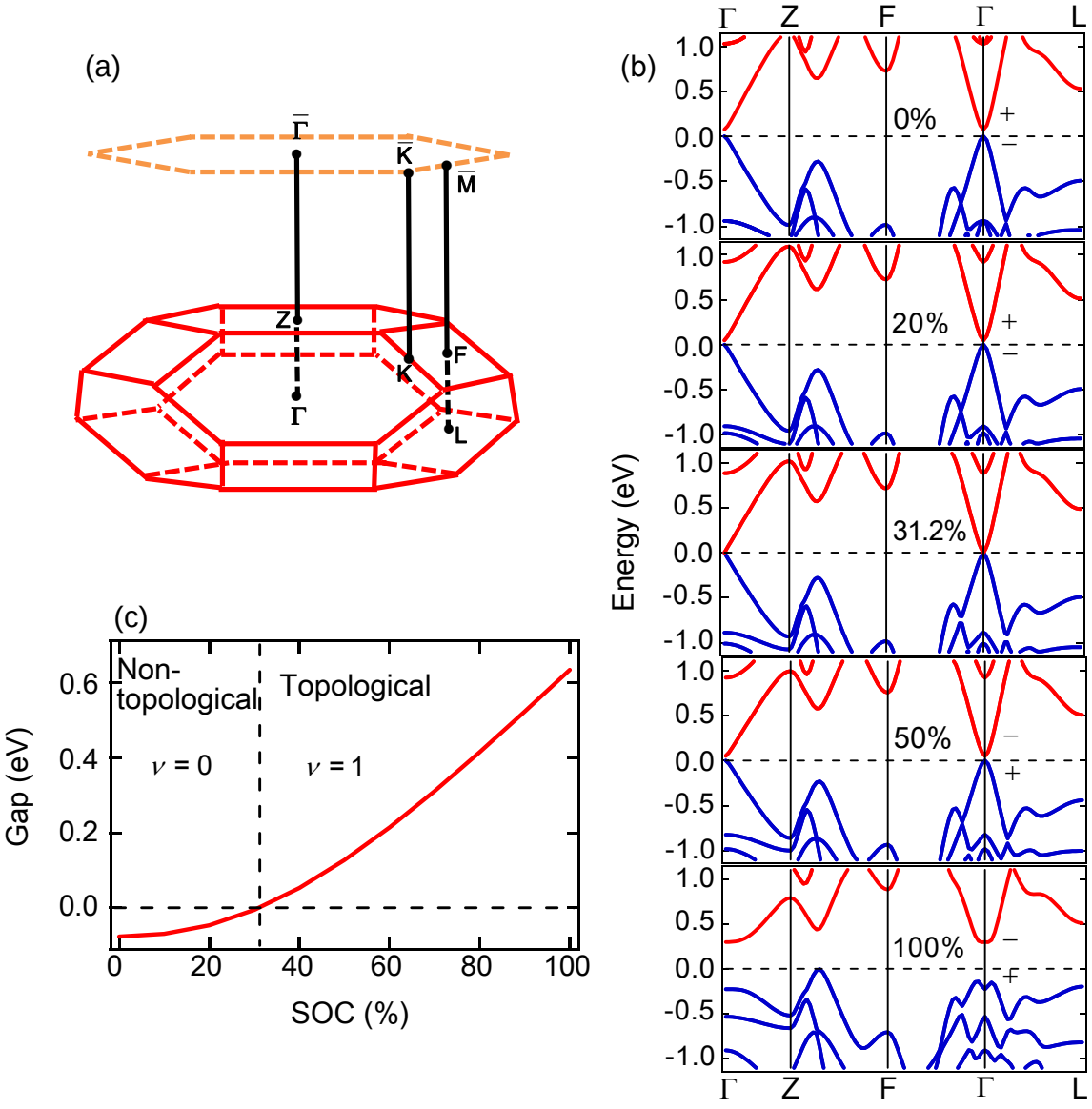

Figure 6.9. (a) Bulk and surface Brillouin zones of Bi_2Se_3 with the special points indicated. (b) Calculated bulk band structure of Bi_2Se_3 at various strengths of the SOC. (c) The bulk band gap at Γ as function of SOC. The gap is positive when the state with odd parity is above the state with even parity.

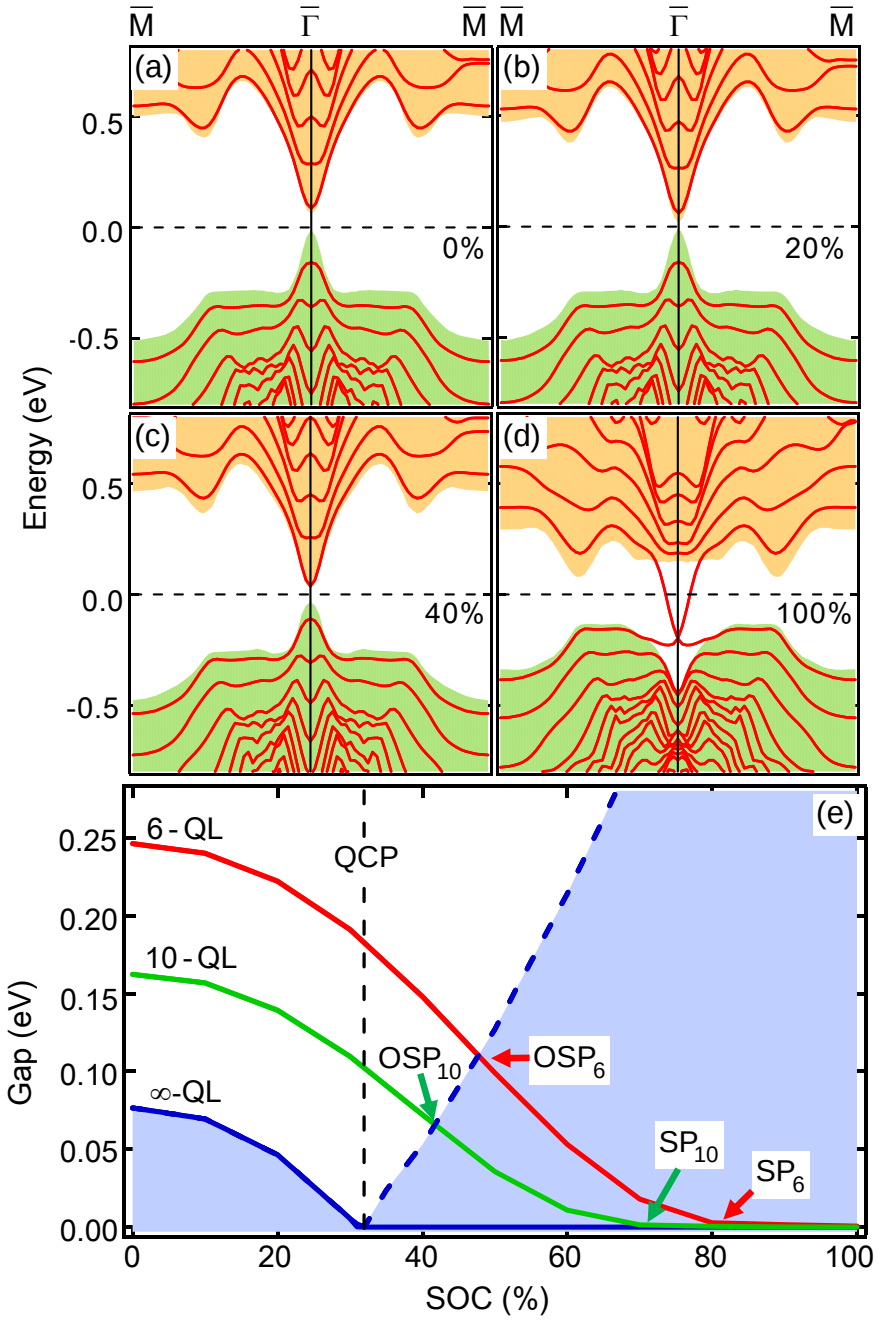

Figure 6.10. (a)-(d) Band structures of a freestanding 6-QL Bi_2Se_3 film with the SOC at 0%, 20%, 40% and 100%, respectively. (e) The apparent gap at $\bar{\Gamma}$ as a function of SOC for 6-, 10-, and ∞-QL films. The hatched area indicates the absolute bulk gap.

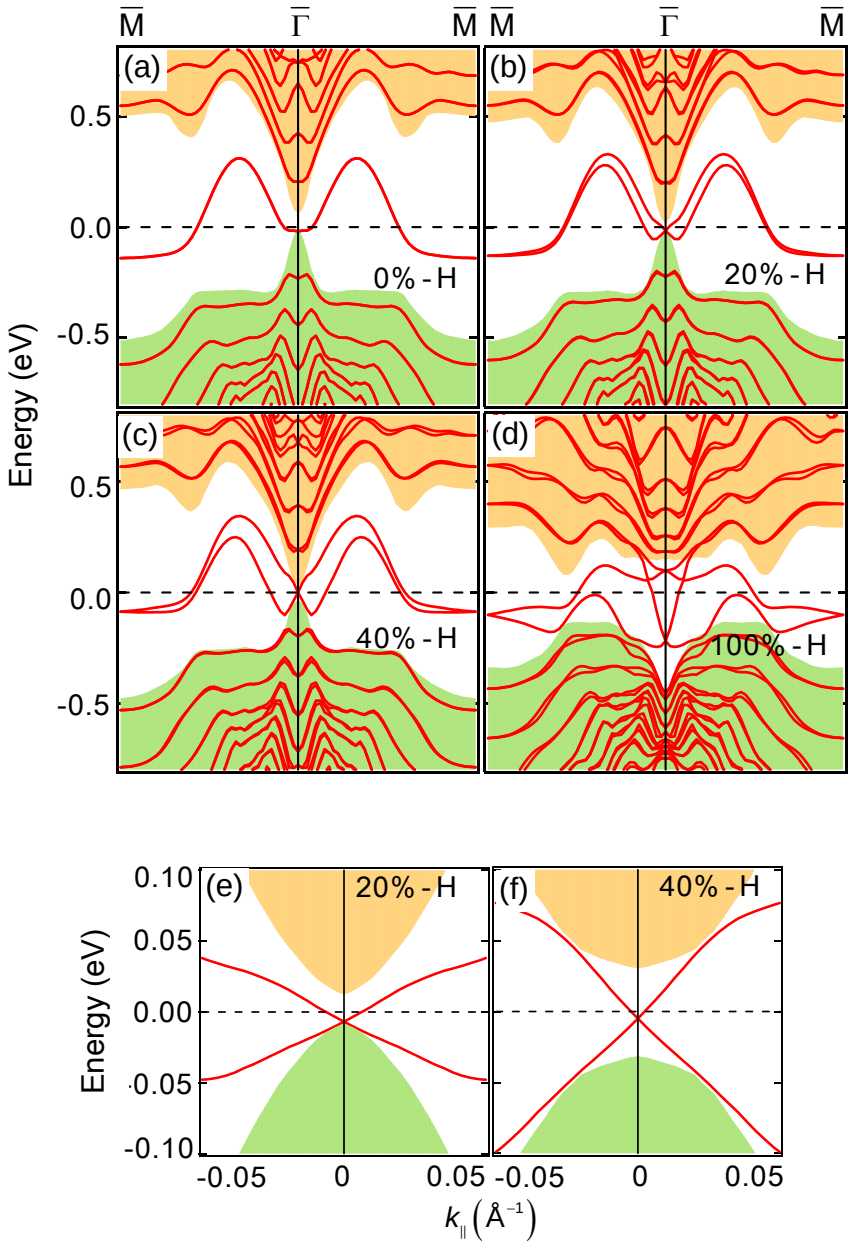

Figure 6.11. (a)-(d) Band structures of a 6-QL Bi_2Se_3 film with the top face terminated by H with the SOC at 0%, 20%, 40% and 100%, respectively. The shaded regions indicate projected bulk band regions. (e) and (f) Close-up views of the band structures near $\bar{\Gamma}$ with the SOC at 20% and 40%, respectively.

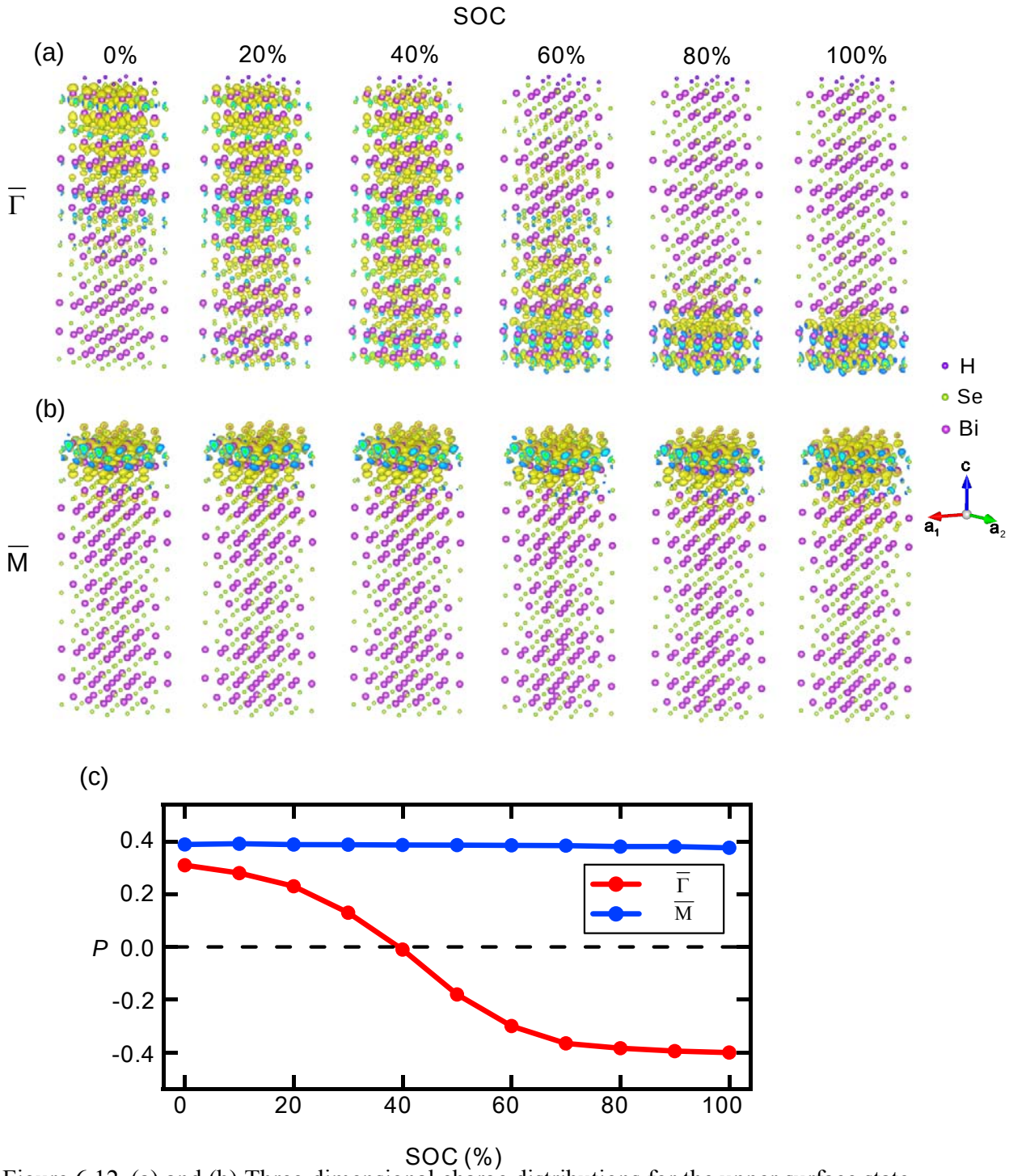

Figure 6.12. (a) and (b) Three-dimensional charge distributions for the upper surface state near $\overline{\Gamma}$ and the surface state at $\overline{M}$, respectively, at various SOC strengths. (c) The corresponding charge moments *P* for the two cases.

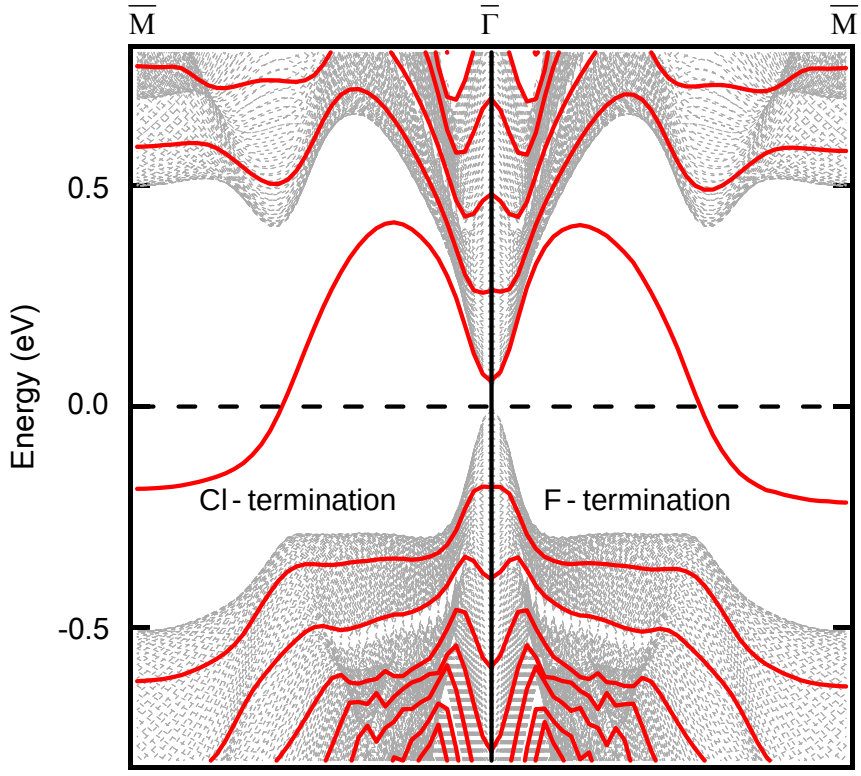

Figure 6.13. Band structures of a 6-QL Bi_2Se_3 film with its top face terminated by F (right panel) or Cl (left panel). The shaded areas indicate the projected bulk band regions. The spin-orbit coupling is turned off

7 Epitaxial Bi Films on Si(111): Surface-Mediated Metastability

7.1 Introduction

Semi-metallic Bi has attracted intense interest because of its unique combination of physical properties including a strong spin-orbit coupling, a large Fermi wavelength, and a small Fermi surface with Dirac-like band features that are tunable by doping or alloying [1,2,3,4,5]. These attributes make Bi a promising candidate for electronic and spintronic applications [6]. In this chapter, we report the observation of a metastable pseudocubic (PC) phase of Bi films made by annealing initially disordered films of thicknesses 20 to ~100 Å deposited on Si(111)-(7×7) at low temperatures. The metastability of the PC phase is demonstrated by the transformation, upon annealing to higher temperatures, to the stable rhombohedral (RH) bulk phase. The two phases are easily distinguished by angle-resolved photoemission as they exhibit different surface states and quantum-well subbands [7]. While the electronic structure of the RH phase has been well characterized in prior studies [8,9,10], the present work provides the first detailed experimental mapping of the surface states and the quantum-well subbands in the metastable PC phase. It is interesting to note that the two phases have nearly the same atomic volume, but the measured band topologies are very different. Specifically, the curvatures of the subbands at the zone center $\bar{\Gamma}$ have opposite signs. The RH phase shows a Dirac-like subband around $\bar{M}$ along $\bar{K}-\bar{M}-\bar{K}$ [11,12], which is absent in the PC phase. A bundle of surface states in the RH phase below the Fermi level is replaced by a concave surface band in the PC phase that moves slightly upward and pokes through the Fermi level with increasing film thicknesses. These observations are in generally

good accord with first-principles slab calculations.

The metastable behavior is observed over a film thickness range from 20 to ~100 Å. Below 20 Å, the film's structure after annealing is always the PC phase; above ~100 Å, the only stable phase is RH. For comparison, previous scanning tunneling microscopy (STM) work on Bi films reported a surface structure identified as that of the PC phase for film thicknesses equal to or less than 4 bilayers (BL) (13 Å; see below for an explanation of the bilayer); thicker films showed a surface structure consistent with the RH phase [13,14]. The critical thickness of 4 BL was attributed to a crossover of the relative importance of the surface and bulk energies of the films, with the PC phase having a lower surface energy. Evidently, the previous STM study did not look specifically for metastable structures, and our study shows that the critical thickness is 6 BL instead. At the upper thickness limit of metastability (~100 Å), the surface bilayer constitutes just ~4% of the system; this has strong implications regarding the energetics of the metastable-to-stable phase transformation.

7.2 Sample preparation and computational methods

In our experiment, an n-type Si(111) wafer (Sb-doped with a resistivity ~0.01 $\Omega \cdot \mathrm{cm}$) was used as the substrate. It was cleaned by direct current heating to yield a (7×7) reconstructed surface. Bi was deposited onto the substrate maintained at 60 K. The amount of deposition was measured by a quartz thickness monitor. The film after deposition was disordered based on *in-situ* electron diffraction. Annealing was performed by passing a current through the sample.

For comparison with the experimental results, we performed first-principles slab calculations of the electronic structure of the films using HGH-type pseudopotentials and a plane-wave basis set [15]; the main program employed was developed by the ABINIT

group [16,17]. Appropriate surface relaxation parameters were included in the structural model [18]. Spin-orbit coupling, which is crucial for the description of the electronic structures of heavy elements such as Bi, was included in the calculation.

7.3 Metastability of epitaxial Bi films

Figure 7.1 shows model drawings of the PC and RH structures [8,18]; each can be described in terms of a stack of BLs, where each BL contains two closely spaced atomic layers. The RH films are oriented along [111]. Currently there are two proposed structural models for the PC phase: one is a black-phosphorus-like structure and the other is a slightly expanded (by ~1%) bulk-like structure oriented along [110]. The differences between the two models are fairly minor [19], but the latter matches our data slightly better and is shown in Fig. 7.1. Within this model, the PC and RH films have similar bulk structures but different crystallographic orientations. The atomic density of 1 BL is 1.12 $\times$ 10^{15} atoms/cm^2 for the RH phase and 9.27 $\times$ 10^{14} atoms/cm^2 for the PC phase; thus, 1 BL of RH is equivalent to 1.21 BL of PC. The nominal thickness of each BL is 3.93 Å for the RH phase and 3.28 Å for the PC phase. The PC to RH transformation thus involves a rather unusual rearrangement of the incommensurate layer structures. In the following, we will refer to the film thickness in terms of either the PC BL or the RH BL, where appropriate. The surface Brillouin zones for the two phases are shown in Fig. 7.1; the direction mapped by the photoemission measurements corresponds to the $\bar{\Gamma}\bar{M}$ and $\bar{\Gamma}\bar{K}$ directions of the PC and RH phases, respectively.

Figure 7.2(a) shows photoemission results for a 6 BL PC film obtained by annealing to 350 K; this thickness is the upper limit of stability for PC. Figure 7.2(b) shows the same data differentiated twice along the energy axis. This differentiation effectively removes a background and enhances the contrast for a better visualization of

the band dispersions. Figure 7.2(c) is the results of our first-principles slab calculation for comparison. Overall, there is a good agreement between the present calculation, a previous calculation [18], and the experiment. Experimentally, the top subband (marked by small circles) has a concave shape near $\bar{\Gamma}$ and nearly grazes the Fermi level. A comparison of the calculated slab band structure to a calculated projected bulk band structure reveals that this band has a surface character near $\bar{\Gamma}$ (see below for further evidence). While this band is fully occupied based on the experiment, the calculation puts it slightly higher, resulting in a hole pocket at $\bar{\Gamma}$. The experiment and calculation agree that the next few subbands below are nearly flat near $\bar{\Gamma}$, and the ones further below become convex.

Figure 7.3(a) presents the photoemission results from a film of thickness equivalent to 20 BL in the PC phase or 17 BL in the RH phase. After deposition, the film was annealed to 280 K and cooled back to 60 K; its structure is PC. The second derivative of the data is present in Fig. 7.3(b). The results are similar to those seen in Fig. 7.2, but with more densely packed quantum well subbands as expected. The top subband near $\bar{\Gamma}$, indicated by circles, is distinctly separated from the others because of its surface character. Compared to the 6 BL case, it has moved slightly upward to create a small hole pocket at $\bar{\Gamma}$. These features are generally consistent with the theoretical results shown in Fig. 7.3(c). The calculation shows pairs of subbands near $\bar{\Gamma}$, which arise from a pair of closely spaced bulk bands of Bi along the $\Gamma - X$ direction [12]. The energy difference in each pair is too small to be resolved experimentally; thus, each pair appears in the experiment as a single broadened subband.

Figure 7.4 presents theoretical evidence for the surface and bulk characters of the

various states. The upper panel shows a detailed view of the band structure near the Fermi level for a 20 BL Bi film in the PC phase; several states A-E are marked. The corresponding plane-averaged charge densities for these states are shown in the lower panel. Evidently, states A and B are derived from bulk states, while states C-E are surface states as they decay away from the surfaces. The decay lengths of the surface states are quite long; at small film thicknesses, the charge distributions localized near the two surfaces join, and a charge density plot alone is insufficient to make a positive identification of the surface character.

The photoemission spectra from the same film change dramatically after annealing to 350 K, as seen in Fig. 7.3(d) and its second derivative in Fig. 7.3(e). The set of convex quantum well subbands near $\bar{\Gamma}$ at binding energies 1-2 eV for the PC phase have disappeared. Instead, one observes a bundle of closely packed concave bands with complex structures near $\bar{\Gamma}$. For comparison, Fig. 7.3(f) presents the results of our slab calculations for the RH structure, with the surface states indicated by small circles. The similarities between the experiment and theory are apparent, thus confirming the RH structure of the film. Our results also agree with a previous photoemission mapping of the bands for the RH phase [8,9]. The calculated results in Fig. 7.3(f) show a bunch of surface states at low binding energies near $\bar{\Gamma}$. This is seen in photoemission as an intense peak at ~0.4 eV.

Of special interest are the bands near $\bar{M}$, where there is an excellent agreement between the calculation and experiment. Near the Fermi level, a small gap, marked by D, separates a Λ-shaped lower band and a V-shaped upper band. These dispersion relations are nearly-Dirac-like along $\bar{K}-\bar{M}-\bar{K}$. In the bulk limit, the region under the Λ-shaped band is completely filled with bulk states. Quantum size effects lead to

discretization of the bulk band continuum and bring about the Dirac-like dispersion. The present work suggests that quantum size effects could be an additional mechanism for modifying the band structure and realizing Dirac physics in low-dimensional systems.

Experimentation with various film thicknesses has established the PC-RH metastability regime to range from 20 to ~100 Å (6 BL PC phase to ~27 BL RH phase). The transformation from PC to RH is illustrated by the results presented in Fig. 7.5. The top row displays photoemission data from a 14 BL (referred to the RH phase) Bi film recorded at various sample temperatures while the sample temperature was raised slowly. The corresponding second derivatives are shown in the bottom row. The spectra taken before annealing are featureless because of structural disorder. Features associated with the PC phase emerge around 250 K and become fully developed at ~300 K. Further annealing to 315-335 K results in a mixture of the PC and RH phases, as one can detect the characteristic subband dispersions of both phases in the data. Annealing to 350 K fully converts the film to the RH phase. Annealing to even higher temperatures leads to broadening and fading of the subbands, which can be attributed to thermal roughening of the film.

An inspection of the data in Fig. 7.5 reveals that the quantum-well subbands for the PC phase remain at the same energy positions throughout the gradual transition to the RH phase. If the phase transformation begins at the surface or interface of the film and propagates thickness-wise, one would expect the quantum-well subband structure of the PC phase to evolve in accordance with a gradual reduction in film thickness. This is clearly not the case based on the experiment. We conclude that the transformation mainly involves the formation of lateral domains that expand laterally as the annealing progresses.

Previous studies have proposed that the PC structure is stable at lower thicknesses

because it has a lower surface energy (but a higher bulk energy) [13,14]. As the film thickness increases, the surface contribution diminishes relative to the bulk contribution, and the total energy of PC becomes higher than that of RH at thicknesses greater than 6 BL (or 4 BL based on the previous STM study). But why does the PC phase persist as a metastable phase to a rather large film thickness of ~100 Å? A physical picture is as follows. As an initially disordered film is annealed, it is likely that the atoms at the surface become mobile first because of the reduced coordination. The surface atoms tend to adopt the PC structure locally for its lower energy, and the ordering then propagates throughout the film resulting in a metastable PC film. Thus, the metastable phase formation is likely a kinetic effect associated with surface nucleation. Annealing to higher temperatures causes the system to make a transformation to the stable phase. The annealing temperature needed for this transformation, ~350 K, corresponds to just 30 meV, a very small thermal energy. This suggests that the barrier for the phase transformation is very low. Furthermore, the metastable phase persists to a large thickness (~100 Å) at which the surface bilayer constitutes just ~4% of the film. This suggests that the difference in bulk energies between the two phases is very small; otherwise thermal fluctuations could readily bring the system over the barrier and down a steep energy slope, thus severely restricting the range of metastability. The near degeneracy of the bulk energy is consistent with the observation that the two phases have nearly the same bulk structure, the main difference being a slight expansion by ~1% of the PC phase. It is interesting to note a somewhat analogous behavior of another group V element, P, which exhibits a PC-RH transition upon compression under pressure [20,21].

7.4 Conclusion

In this chapter, the study based on photoemission demonstrates the existence of a metastable PC phase and a stable RH phase of Bi films over a wide range of film

thickness from 20 to ~100 Å. Below 20 Å, PC is the only ordered phase observed; above ~100 Å, RH is the only one. The quantum well subband structures for the two phases have very different topologies, which make a positive identification of the phases straightforward. This is a much more robust identification of the internal film structure than STM or electron diffraction observation of the (near) surface atomic geometry. The complex electronic structures of the two phases as determined by photoemission are confirmed by first-principles slab calculations. Among the many interesting electronic features, the PC phase has a surface band at $\bar{\Gamma}$ that grazes the Fermi level, while the RH phase has a Dirac-like subband at $\bar{M}$ along $\bar{K}-\bar{M}-\bar{K}$. The PC-RH metastability range of 20 to ~100 Å is unusually wide, but it can be understood in terms of a near degeneracy of the bulk energies of the two phases and a surface-nucleation process that facilitates the formation of the metastable phase. Subbands in thin films can be tuned by changing the film thickness; together with metastability, the results suggest opportunities for fine tuning the electronic structure of Bi films, a system of interest for spintronic applications.

References:

[1] Y. M. Koroteev et al., Phys. Rev. Lett. **93**, 046403 (2004).

[2] C. R. Ast and H. Höchst, Phys. Rev. Lett. **87**, 177602 (2001).

[3] C. R. Ast and H. Höchst, Phys. Rev. B **67**, 113102 (2003).

[4] J. Fan and J. Eom, Appl. Phys. Lett. **92**,142101 (2008).

[5] D. Hsieh et al., Nature **452**, 970 (2008).

[6] I. Žutić, J. Fabian, and S. Das Sarma, Rev. Mod. Phys. **76**, 323 (2004).

[7] T.-C. Chiang, Surf. Sci. Rep. **39**, 181 (2000).

[8] T. Hirahara et al., Phys. Rev. Lett. **97**, 146803 (2006).

[9] T. Hirahara et al., Phys. Rev. B **76**, 153305 (2007).

[10] T. Hirahara et al., Phys. Rev. B **75**, 035422 (2007).

[11] P. A. Wolff, J. Phys. Chem. Solids 25, 1057 (1964).

[12] Y. Liu and R. E. Allen, Phys. Rev. B **52**, 1566 (1995).

[13] T. Nagao et al. Phys. Rev. Lett. **93** 105501 (2004).

[14] S. Yaginuma et al. J. phys. Soc. Jpn. **77**, 014701 (2008).

[15] C. Hartwigsen et al. Phys. Rev. B **58**, 3641 (1998).

[16] X. Gonze et al., Comp. Mater. Sci. **25**, 478 (2002).

[17] X. Gonze et al, Zeit. Krist. **220**, 558 (2005).

[18] Y. M. Koroteev et al., Phys. Rev. B **77**, 045428 (2008).

[19] S.Yaginuma et al. Surf. Sci. **601** 3593 (2007).

[20] H. Iwasaki and T. Kikegawa, Acta Cryst. B **53**, 353 (1997).

[21] J. C. Jamieson, Science **139**, 1291 (1963).

Figures:

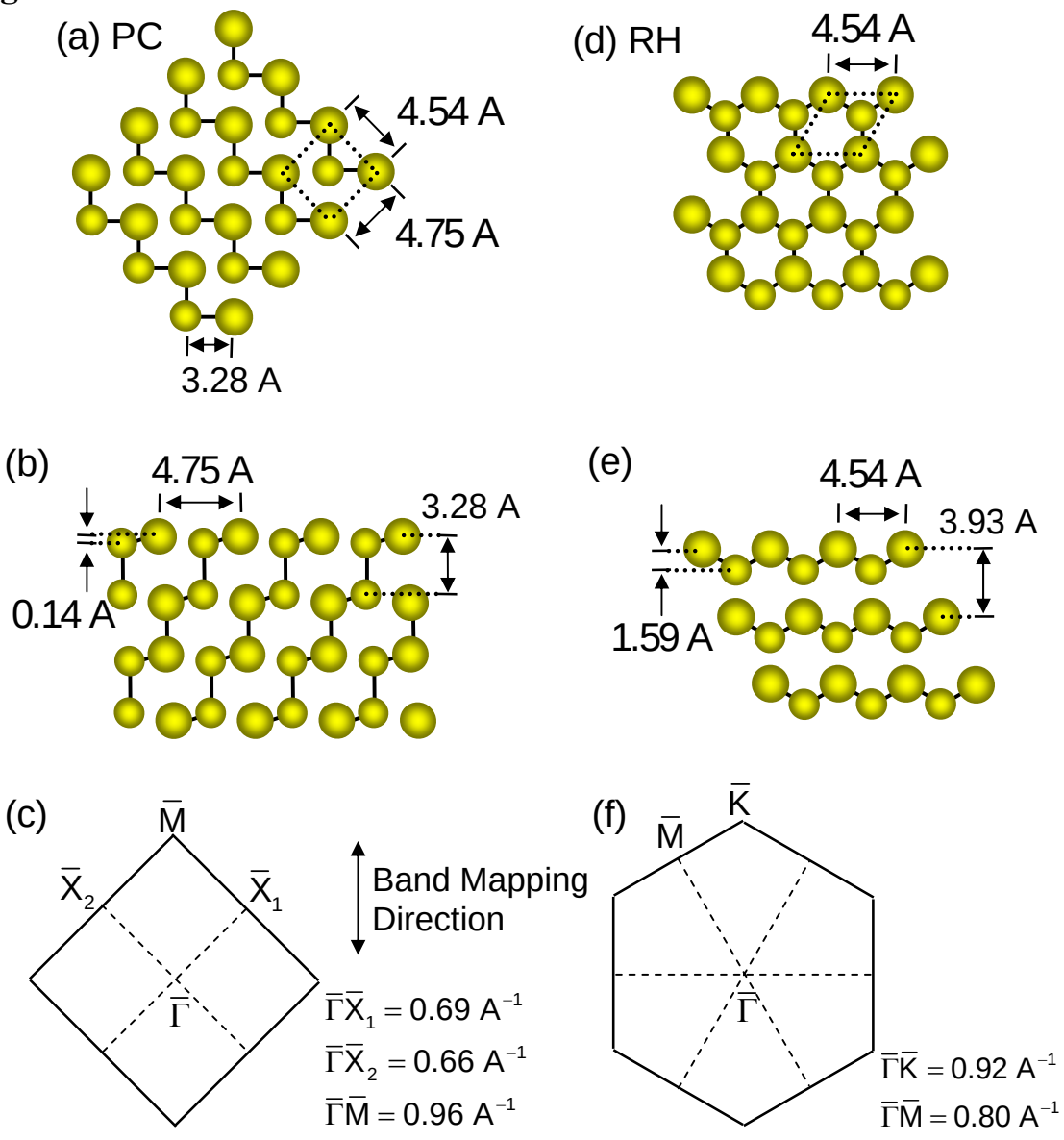

Figure 7.1. (a) Top view of (110), (b) side view along $[1\bar{1}0]$, and (c) surface Brillouin zone of the PC structure. (d) Top view of (111), (e) side view along $[11\bar{2}]$, and (f) surface Brillouin zone of the RH structure. Larger balls indicate atoms closer to the viewer. The direction of photoemission band mapping is indicated.

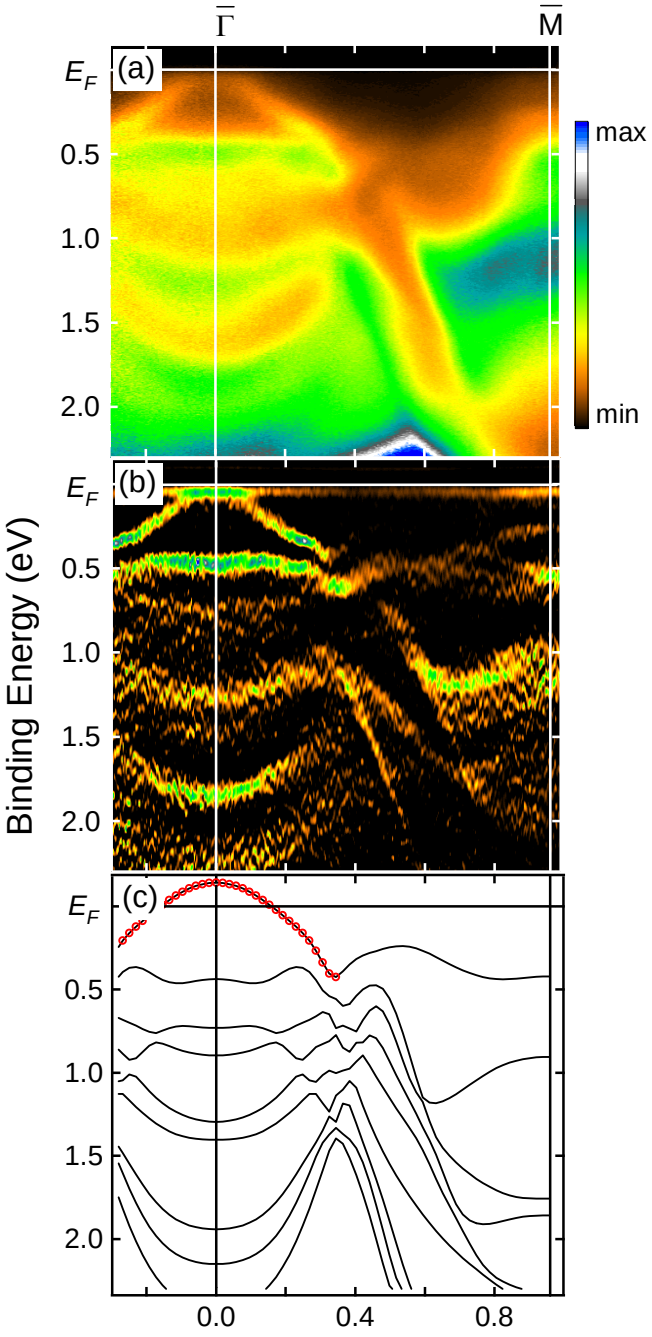

Figure 7.2. (a) Photoemission results from a 6 BL Bi film in the PC phase. (b) Second derivative along the energy axis of the photoemission data to enhance the contrast. (c) Calculated band structure. The top band, marked by small circles, has a surface character.

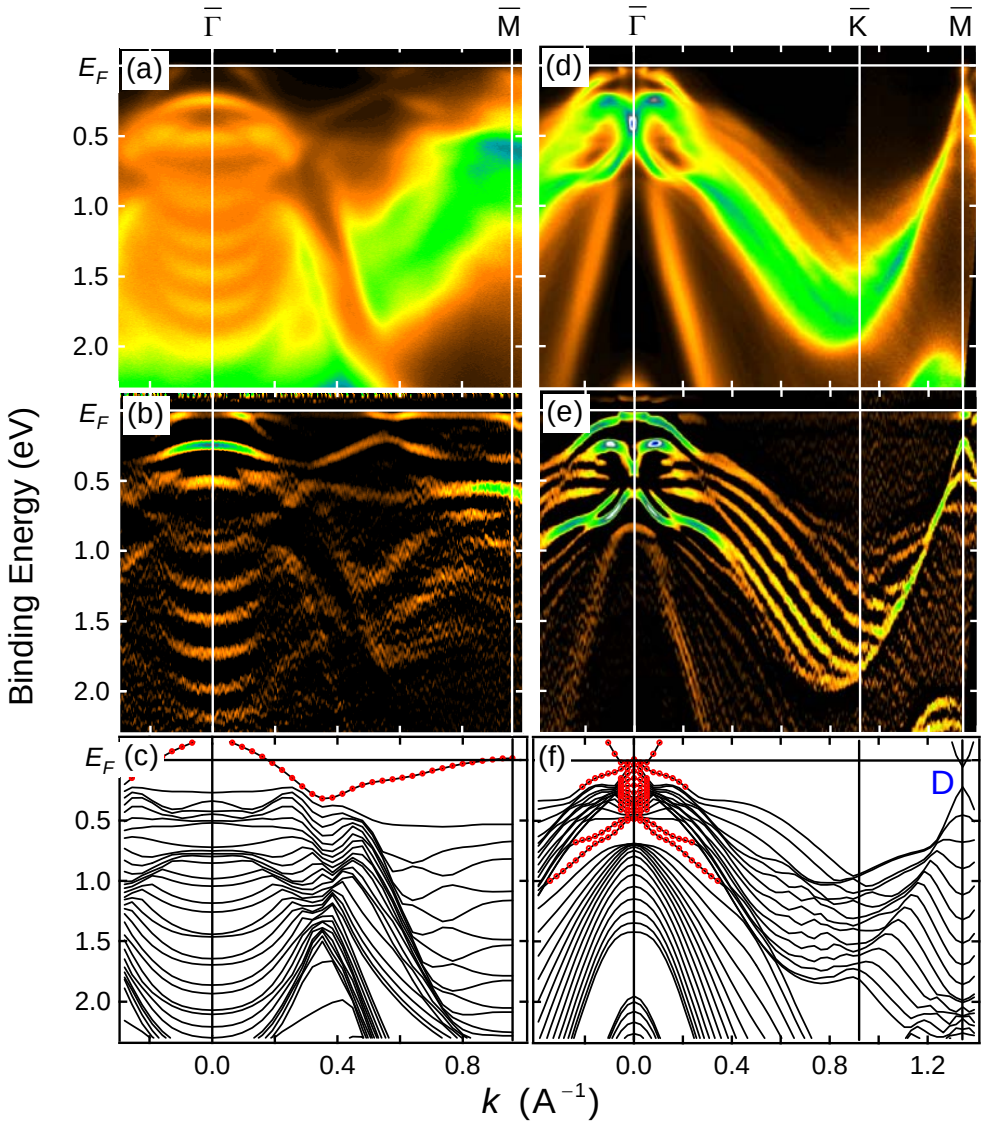

Figure 7.3. (a) Photoemission data and (b) second derivative taken from a Bi film of thickness equivalent to 20 BL in the PC phase or 17 BL in the RH phase after annealing to 280 K. The structure of the film is PC. (c) Calculated band structure for the PC phase. (d) Photoemission data and (e) second derivative taken from the same film after annealing to 350 K. The structure of the film is RH. (f) Calculated band structure for the RH phase; the label "D" marks a Dirac-like feature. Surface states are indicated by small circles in (c) and (f).

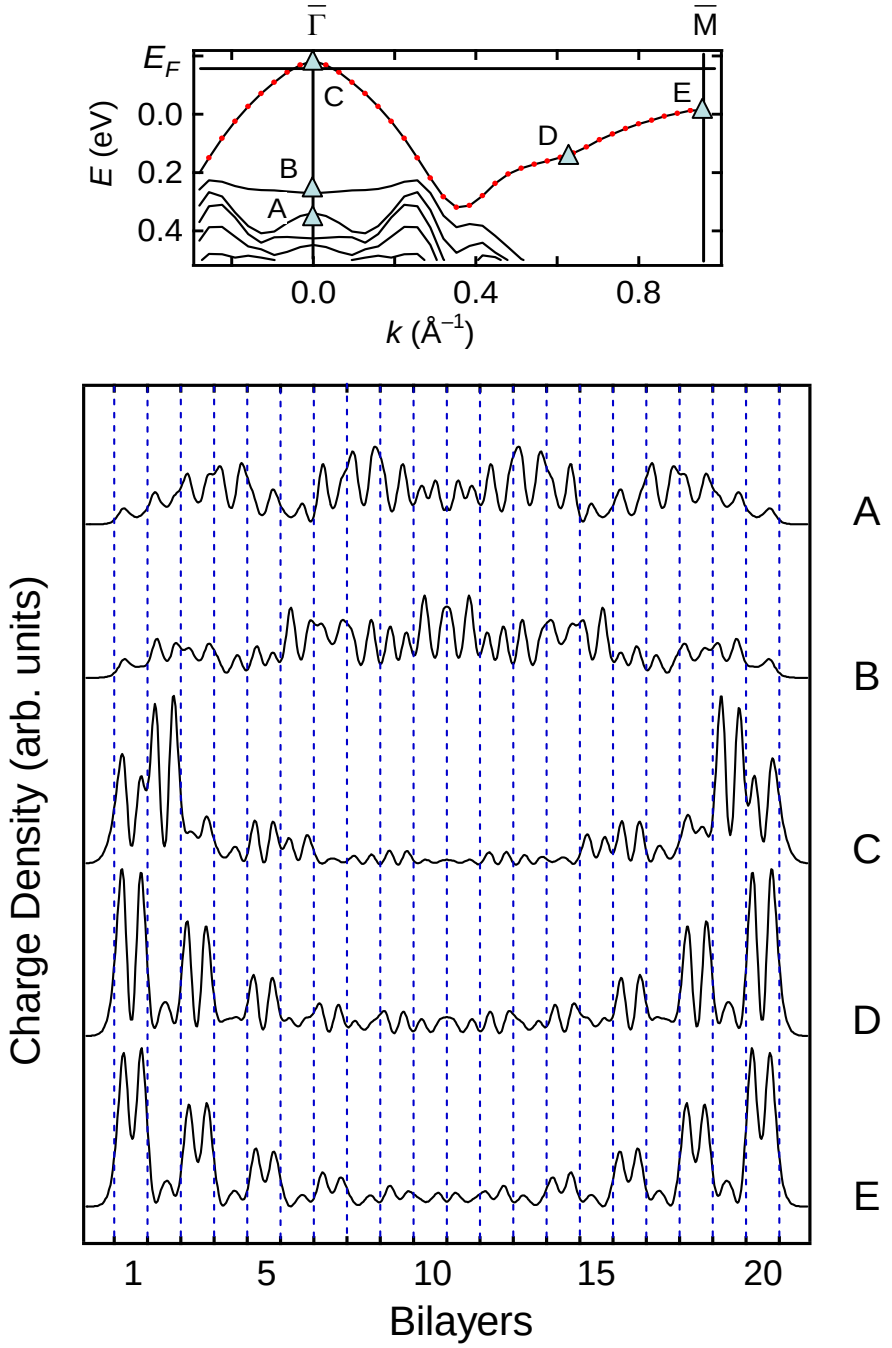

Figure 7.4. Upper panel: calculated electronic structure of a 20 BL film in the PC phase. Five states A-E are marked. Lower panel: the plane-averaged electronic charge densities within the film for the five states.

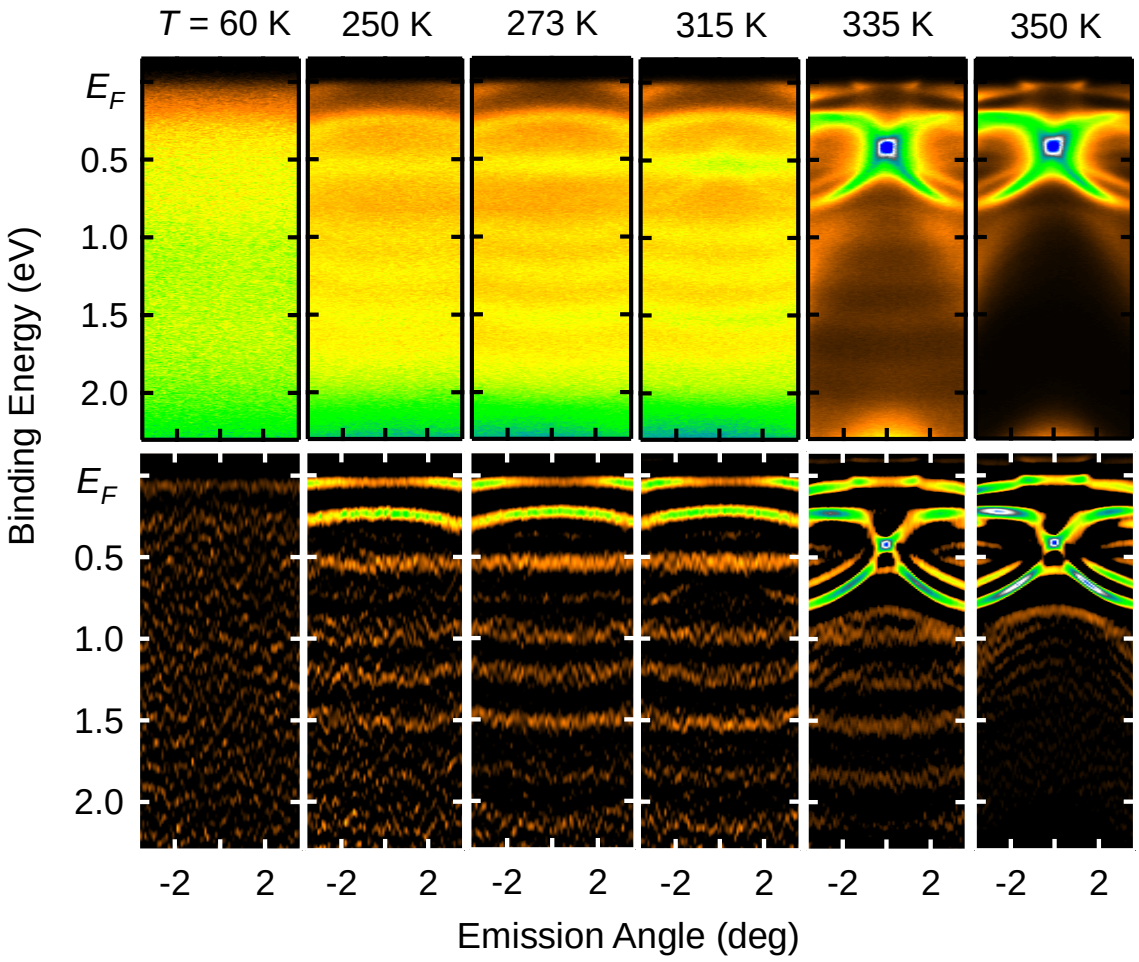

Figure 7.5. (a) Photoemission results from a Bi film of thickness 14 BL (referred to the RH structure) after annealing to various temperatures as indicated. The structure of the film changes from a disordered phase to the PC phase first, then to a mixed phase, and finally to the RH phase. (b) Second derivative of the data in (a).

8 Giant-Rashba System: Bi/Ag(111) Surface Alloy

8.1 Introduction

One third of a monolayer (ML) of Bi alloyed into a Ag(111) surface yields a free-electron-like surface state with the largest known Rashba spin splitting [1,2], a property of great interest in connection with the search for exotic phases including two-dimensional superconductors and Majorana states [3]. We show how the complex spin texture [4,5] resulting from the entanglement of this surface state with the quantum well states in a thin Ag(111)-film substrate can be unraveled by circularly-polarized angle-resolved photoemission spectroscopy (CARPES). CARPES has emerged as a powerful method for probing spin, pseudospin, and correlated electron structures [6,7,8,9], but a comprehensive theoretical basis has been lacking. We show that the strong dichroic pattern in Bi/Ag arises from the interference between two surface photoemission contributions, the Rashba interaction [7] and an often-neglected nonzero $\nabla \cdot \mathbf{A}$ [10,11,12], as demonstrated by excellent agreement between a parameter-free calculation and experiment.

The Rashba-Bychkov (RB) model has been very successful in describing two-dimensional (2D) electron systems with a structural inversion asymmetry (SIA). An electric field perpendicular to the 2D electron system lifts the spin degeneracy resulting in a characteristic band dispersion [13]. The spin splitting of 2D electron systems depends on several physical factors such as the atomic spin-orbit coupling and structural inversion asymmetry. The RB model is only a qualitative model accounting for an effective electric field acting on a 2D free electron gas since it combines all these factors into one single parameter. The detailed contributions from the atomic spin-orbit coupling and the

structural inversion asymmetry are completely neglected in the framework of the RB model. Both the atomic spin-orbit coupling and the surface corrugation (giving rise to SIA) are essential for generating large spin splitting in the Bi/Ag surface alloy. We present a systematic first principles study to address the issue how the local atomic spin-orbit coupling and the surface corrugation affect the spin splitting respectively. The results are discussed in the second part of this chapter.

8.2 Preparation of Bi/Ag(111) surface alloy and CAPRES measurement

Our ARPES measurements were performed at the Synchrotron Radiation Center (SRC), University of Wisconsin-Madison, using the U9 VLS-PGM beam line with a tunable output polarization. The polarization purity is better than 99% for HP and VP, and better than 80% for LCP and RCP. An n-type Si (111) wafer was used as the substrate. It was cleaned by heating to ~1200°C to create a Si(111)-(7x7) surface. Ag(111) films were grown on Si(111)-(7x7) at 60 K followed by annealing to near room temperature to create smooth well-ordered films. Subsequently, 1/3 ML of Bi was deposited and annealed to 500 K to form a well-orded $\sqrt{3}\times\sqrt{3}$ alloy surface as verified by reflection high-energy electron diffraction. All spectra were taken with the sample temperature at 60 K. The photon energy used was 22 eV for all data shown.

8.3 The Surface Spin Texture of the Bi/Ag(111) Surface Alloy Studied by Circularly-Polarized Photoemission

The giant Rashba spin splitting in surface alloys is also of great interest for spintronic applications, but the metallic substrate can act as an electrical short and a source of scattering. Surface alloys based on ultrathin films are much more promising for applications, as the reduced bulk part of the system limits the number of bulk conduction

channels near the Fermi level, resulting in an enhanced surface contribution to the net system response. Ultrathin films are furthermore amenable to gate tuning. We have chosen to focus on Bi deposited on nanometer-scale Ag(111) films as a prototypical system. Ag films of atomic layer uniformity can be readily grown on Si(111), the most common semiconductor substrate material. The quantization of the electronic states in the film results in discrete quantum well states that can be adjusted by varying the film thickness [14]. The entanglement of the alloy surface state and the quantum well states leads to a complex surface spin texture in Bi/Ag, which is an ideal test ground for the basic physics of dichroism based on CARPES in terms of electromagnetic interactions with surface charge and spin. The method should be of general utility for probing novel states of matter.

The sample configuration and lattice structure of Bi/Ag(111) are indicated in Figs. 8.1(a)-8.1(c). The 1/3 ML of Bi organizes into a $\sqrt{3}\times\sqrt{3}$ structure in the top atomic layer. For comparison, we also examine a similar surface alloy system Sb/Ag(111), which exhibits a much smaller spin splitting. The Bi and Sb atoms are located higher than the top Ag atomic plane by d = 0.65 and 0.10 Å, respectively [15]. The surface Brillouin zones of the surface alloy and the Ag(111) film are shown in Fig. 8.1(d); they are related by a 30° rotation and a length ratio of $\sqrt{3}$. We use the labels $\overline{\Gamma}$, $\overline{\mathrm{M}}$, and $\overline{\mathrm{K}}$ for the special points in the Brillouin zone of the $\sqrt{3}\times\sqrt{3}$ surface alloy, and the corresponding primed quantities for the Ag film surface.

A typical photoemission spectral map taken from Bi/Ag prepared on a 20 ML Ag film is presented in Fig. 8.1(e). The map is taken along $\overline{\mathrm{M}}-\overline{\Gamma}-\overline{\mathrm{M}}$ and reaches the $\overline{\Gamma}$ point of the second Brillouin zone of the surface alloy, which coincides with the $\overline{\mathrm{K}'}$ point of the first Brillouin zone of the Ag(111) film. The pair of intense concave parabolic

bands symmetric about the first $\overline{\Gamma}$ point is the Bi-induced surface states with the characteristic Rashba splitting [16]. In the background centered around $\overline{\Gamma}$ is a set of convex parabolic subbands associated with the quantum well states in the Ag film. They become more densely packed as the Ag(111) film thickness increases, while the surface state bands remain unchanged. Anticrossing or hybridization gaps arise where the surface bands cross the quantum-well subbands [17,18], giving rise to the strong modulations of the surface band intensities. Similar patterns are seen around the second $\overline{\Gamma}$ point, where umklapp scattering by the $\sqrt{3}\times\sqrt{3}$ reconstructed surface potential yields the weaker replica emission from the quantum well subbands [19].

The experimental geometry is present in Fig. 8.2(a). We take the normal of the sample to be along $\hat{\mathbf{z}}$ and the $\overline{\Gamma}\overline{\mathrm{M}}$ direction to be along $\hat{\mathbf{x}}$. The photon beam incidents in the *xz* plane at an angle of $\theta \approx 60^{\circ}$. The polarization vector of vertically-polarized (VP) light is along $\hat{\mathbf{y}}$, and that of the horizontally polarized (HP) light lies within the *xz* plane; here, "vertical" and "horizontal" refer to the plane of the electron storage ring used as the photon source. A schematic band diagram for the surface alloy (without the underlying quantum well states), assuming a large spin splitting appropriate for Bi/Ag, is presented in Fig. 8.2(b) with the red and blue colors indicate opposite Rashba spin directions $\pm\boldsymbol{k}\times\hat{\mathbf{z}}$. For Sb/Ag, the red and blue bands in each pair nearly coincide and cannot be resolved experimentally. Spectra of Sb/Ag prepared on a 22-ML Ag(111) film taken along $\overline{\mathrm{K}}-\overline{\Gamma}-\overline{\mathrm{K}}$ and $\overline{\mathrm{M}}-\overline{\Gamma}-\overline{\mathrm{M}}$ with HP light are shown in Figs. 8.2(c) and 8.2(d), respectively. The intense concave surface band at binding energies larger than 0.4 eV originates from the Sb *s*-p_z orbitals. The other weaker surface band poking through the Fermi level is derived from the Sb p_x-p_y orbitals [20,21]. The

underlying quantum well subbands are weak but evident. The corresponding spectrum taken along $\overline{\mathrm{M}}-\overline{\Gamma}-\overline{\mathrm{M}}$ form Bi/Ag prepared on a 20-ML Ag(111) film (Fig. 8.2(e)) shows a large Rashba splitting. Since the p_x-p_y bands have weak intensities, especially along the $\overline{\Gamma}-\overline{\mathrm{M}}$ direction, we shall focus on the s-p_z bands only.

The Rashba-split s-p_z bands can be described by the dispersion relations

$$E(k) = E_0 - \frac{(k \pm k_0)^2}{2m^*} \tag{8.1}$$

where m^* is the effective mass of each hole-like band. The momentum offset k_0 is determined by the strength of the Rashba interaction and equals 0.005 Å^{-1} for Sb/Ag and 0.13 Å^{-1} for Bi/Ag; the latter is much larger partly because of the larger atomic mass of Bi but mostly because of the larger outward relaxation d of the Bi atoms relative to the surface Ag atomic plane resulting in a stronger surface potential gradient. The two spin-split s-p_z bands in Bi/Ag show very different intensities in Fig 8.2(e), implying a strong spin-dependent photoemission process.

Photoemission is governed by the interaction Hamiltonian

$$\Delta H \propto \mathbf{A}\cdot\nabla + \frac{1}{2}\nabla\cdot\mathbf{A} + \alpha\mathbf{s}\cdot\mathbf{A}\times\nabla V \tag{8.2}$$

where **A** is the vector potential of the incident light. The first term corresponds to dipole transition and is the dominant contribution for bulk direct transitions governed by momentum conservation in all three dimensions. It is generally negligible for surface and quantum well states away from direct transitions. The second term, known as the surface-photoemission term, is important only at the surface where the dielectric function ε and hence the vector potential **A** are discontinuous [10,11,12]. The discontinuity results

in a $\nabla \cdot \mathbf{A}$ peaked around the surface. The third term depends on the spin **s** explicitly and stems from the Rashba interaction [7], where the canonical momentum depends on **A**. It also peaks around the surface because of the gradient of the surface potential ∇V.

With the first term in Eq. (8.2) ignored, the photoemission matrix element becomes

$$\left\langle \Psi_f \left| \Delta H \right| \Psi_i \right\rangle \propto \left[\frac{\hbar e}{2m_e} \left(1 - \frac{1}{\varepsilon} \right) A_z + \frac{d\beta e}{\hbar} \mathbf{A} \times \boldsymbol{\sigma} \cdot \hat{\mathbf{z}} \right] \Psi_f^*(0) \Psi_i(0) \tag{8.3}$$

where $\Psi_f^*(0)\Psi_i(0)$ is the product of the initial and final state wave functions at the surface, $\varepsilon = 1.26 + 2.03i$ for Ag at 22 eV [22], $d = 0.65$ Å is the outward relaxation of the Bi atoms, $\boldsymbol{\sigma}$ is the normalized spin polarization of the initial state, and the Rashba parameter β = 3.05 eV-Å is determined from the measured k_0. The product $\Psi_f^*(0)\Psi_i(0)$ is a smooth function of energy and momentum and is taken to be a constant in our calculation over the limited data range. Thus, apart from an overall proportional constant, Eq. (8.3) contains no arbitrary or unknown parameters. To calculate the photoemission spectral map, we set up a Hamiltonian containing the spin-split bands (Eq. (8.1)) and a set of parabolic quantum well subbands positioned to correspond to the experiment. A spin-independent coupling term is included to generate the anticrossing gaps as seen in the experiment. Diagonalization of the Hamiltonian yields $\boldsymbol{\sigma}$, from which the photoemission spectral maps are computed for various polarization configurations including HP, VP, left circular polarization (LCP), and right circular polarization (RCP) by taking the absolute square of the matrix element. Here, "left" and "right" refer to an observer viewing along the incident beam at the sample. A small constant lifetime broadening is included in the calculation.

Data taken along $\overline{\mathrm{M}} - \overline{\Gamma} - \overline{\mathrm{M}}$ at 22 eV with HP, LCP, and RCP from Bi/Ag based

on a 20-ML Ag film are presented in Figs. 8.3(a)-8.3(c). The calculated band dispersions (Fig. 8.3(d)) show the surface bands, the quantum well bands, and the anticrossing gaps. Remaining in the gaps are the quantum well states with the opposite spin orientation than the crossing surface bands. With k_x pointing along $\overline{\Gamma} - \overline{\mathrm{M}}$, the only nonzero spin component is σ_y. The *xz* plane, which contains the incident photon beam, is a mirror plane of the sample. As a result of the overall symmetry of the system, LCP is equivalent to RCP, and there should not be any circular dichroism. Indeed, the LCP and RCP data appear to be identical, and the surface band with spin polarization along $+\hat{\mathbf{y}}$ is much more intense than the other surface band with spin polarization along $-\hat{\mathbf{y}}$. The same intensity imbalance is evident in the HP data. A calculated photoemission map (Fig. 8.3(e)) for HP shows indeed an intensity imbalance in agreement with the data. By contrast, the same calculation, assuming no spin-orbit coupling by setting β to zero, yields a map with equal intensities for the two bands (Fig. 8.3(f)). The results indicate that the intensity imbalance between the two bands is a spin effect, despite the lack of circular dichroism.

Circular dichroism becomes apparent for measurements along $\overline{\mathrm{K}} - \overline{\Gamma} - \overline{\mathrm{K}}$, for which the system no longer possesses mirror symmetry about the *xz* plane. While the HP map (Fig. 8.4(a)) shows equal intensities for the two spin-split bands, the LCP and RCP maps (Figs. 8.4(b-c)) show different intensities. In fact, the LCP and RCP maps appear to be left-right mirror images of each other about $\overline{\Gamma}$. To quantify this difference, we define a dichroic function

$$\xi = \frac{I_L - I_R}{I_L + I_R} \tag{8.4}$$

where $I_{L,R}$ are the photoemission intensities for LCP and RCP, respectively. The

experimental results are presented in Fig. 8.4(d), where red and blue colors indicate positive and negative values of ξ, respectively. The maximum value of ξ is about ±30% at the top of each surface band and the sign of ξ is opposite for the two bands. Fig. 8.4(e) shows the theoretical spin polarization inherited from the Rashba split surface states. States with spin polarization along $+\hat{\mathbf{x}}$ and $-\hat{\mathbf{x}}$ directions are colored in red and blue, respectively. Near the hybridization gaps, the states transform smoothly from surface-like to bulk-like and the hybrid states are partially spin polarized. The calculated dichroic function (Fig. 8.4(f)) is in excellent agreement with the experimental pattern. The maximum value of ξ is ±38.9% from the calculation. It is somewhat higher than the experimental value; the difference can be attributed to the less than perfect polarization state of the LCP and RCP light and possibly to sample imperfections.

8.4 Transition matrix elements for surface photoemission

Derivation of the coefficients of the two terms in Eq. (8.3) is sketched here. In the classical limit, the product of the dielectric function and the *z*-component of the vector potential εA_z is continuous across the surface, while the in-plane components of the vector potential $A_{x,y}$ are continuous. Because ε is discontinuous at the surface, A_z must be discontinuous. As a result, $\nabla \cdot \mathbf{A}$ is proportional to $\delta(z)$ with the surface located at z = 0. The matrix element involves an integration over all space. The result contains the product of the initial and final state wave functions at the surface, $\Psi_f^*(0)\Psi_i(0)$. Quantum mechanically, the delta function $\delta(z)$ is somewhat broadened with a width of about the screening length. For the second term in Eq. (8.3) arising from the Rashba interaction, the surface potential V has a finite jump at the surface over a distance of about the outward relaxation of the Bi atoms (d = 0.65 Å for Bi/Ag). Its gradient, ∇V, is also a somewhat broadened delta function. After integration, it, too, contains the same

$\Psi_f^*(0)\Psi_i(0)$ factor. This factor can be taken to be part of the normalization factor and does not enter into the final calculations. The dichroic behavior is entirely determined by the relative strengths of the two terms. The photocurrent is given by

$$I \propto |C|^2 A_z^2 + |D|^2 \left| A_y \langle \sigma_x \rangle - A_x \langle \sigma_y \rangle \right|^2 + \left(C^* D A_z^* \left(A_y \sigma_x - A_x \sigma_y \right) + c.c. \right) \qquad (8.5)$$

where $C = \hbar e(\varepsilon - 1)/2m_e \varepsilon$, $D = e\beta d/\hbar$, and $A_{x,y,z}$ are the components of the vector potential. The Rashba parameter β equals 3.05 eV-Å for Bi/Ag. Under typical conditions with the usual lifetime broadening of the states, circular dichroic effects become difficult to detect with the Rashba coefficient smaller than about 0.5 eV-Å.

8. 5 CARPES spectra of Ag quantum well states

For comparison, we have performed similar measurements of a 20-ML Ag film prepared on Si(111)-(7x7) without Bi. Photoemission maps taken along $\overline{\mathrm{M}} - \overline{\Gamma} - \overline{\mathrm{M}}$ at 22 eV with HP, VP, LCP, and RCP are presented in Fig. 8.5. The parabolic bands are derived from quantum well states; the emission feature right around the Fermi level near $\overline{\Gamma}$ is derived from a Ag(111) Shockley surface state. The photoemission intensities of the surface state and the quantum well states are close to zero for VP. The reason is that the surface-photoemission term related to $\nabla \cdot \mathbf{A}$ vanishes with $A_z = 0$. The Rashba term is negligible because of a very weak spin-orbit coupling in Ag. The dipole term is negligible. The HP, LCP, and RCP maps look the same; the quantum-well bands appear symmetric in intensity. As expected, there is no circular dichroism.

8.6 First-principles study of a single Bi/Ag layer

The Rasha-Bychkov model is a successful phenomenological theory describing the spin splitting induced by the structural inversion asymmetry (SIA) in 2D electron systems.

The model was originally developed for semiconductor heterostructures. At interfaces, inversion symmetry is naturally broken and the bound states there experience an effective electric field normal to the interface. The RB model can be described by an effective Hamiltonian:

$$H_{RB} = \alpha_R \boldsymbol{\sigma} \cdot (\boldsymbol{k}_{\parallel} \times \boldsymbol{e}_z) = \alpha_R (k_y \sigma_x - k_x \sigma_y) \tag{8.6}$$

where α_R is the Rashba parameter. The resulting energy dispersion of a nearly free electron gas is

$$E(\boldsymbol{k}_{\parallel}) = \frac{\hbar^2}{2m^*}(k_{\parallel} \pm \Delta k)^2 + E_0, \tag{8.7}$$

where m^* is the effective mass, $\Delta k = m^* \alpha_R / \hbar^2$ is the offset by which the parabola is shifted away from the high symmetry point, and E_0 is an offset in energy. The energy dispersion of a Rashba split nearly free electron gas is schematically shown in Fig. 8.6.

The same argument can be applied to the surface states too. A noted example for a Rashba spin split 2D electron gas is the surface states at the Au(111) surface [23,24,25]. The SIA is due to the confinement of the surface states on one side by the surface barrier and on the other side by the bulk band gap of Au. The momentum offset Δk for Au(111) surface is 0.012 Å^{-1} [26], which is considerably larger than the 0.0007 Å^{-1} momentum offset of Ag (111) surface. The larger spin splitting of Au (111) can be attributed to the fact that Au is heavier than Ag and thus has much stronger atomic spin-orbit coupling. The surface alloy Bi/Ag(111) have been identified with an unexpectedly large spin splitting in its surface band structure ($\Delta k \approx 0.13\ \text{Å}^{-1}$). Considering the similar atomic weights of Au and Bi, the enhanced spin splitting in the Bi/Ag(111) surface alloy is a consequence of the prominent corrugation in the surface structure. Therefore, both atomic

spin-orbit coupling and the surface corrugation are essential for realizing huge spin splitting in the surface states. The prominent outward relaxation of Bi atoms relative to the Ag atomic plane produces not only a large vertical potential gradient, the key ingredient for Rashba splitting, but also an anisotropic in-plane SIA [27]. This additional SIA within the confinement plane leads to a hexagonal warping in the surface band dispersion [28] as well as out-of-plane spin polarization. Extending the RB model to include the in-plane potential gradient results in a strong enhancement of the spin splitting. Previous study [29] pointed out that the wavefunctions of surface states are strongly localized in the topmost layer, i.e., in the alloy layer while the supporting substrate carries at most 22% of the spectral weight. Therefore, the substrate atoms have a negligible effect on the spin splitting of the surface states. For the sake of simplicity, we perform a systematic first-principles study of the alloy layer without considering the substrate Ag layers.

The band structure of a Bi/Ag surface alloy layer is shown in Fig. 8.7. In the calculation each Bi atom sits in a 3-fold hollow site above the Ag atomic plane at 0.64 Å, a value experimentally determined by IV-LEED [15]. Around the zone center $\bar{\Gamma}$ there are two sets of Rashba split surface bands near the Fermi level. The state slightly below the Fermi energy has mainly sp_z character at the Bi site. The band above the Fermi level dispersing downward along the $\overline{\Gamma M}$ and $\overline{\Gamma K}$ directions has almost purely Bi $p_{x,y}$ character [30]. The Rashba momentum offset in the sp_z band is 0.144 $Å^{-1}$ which is very close to the experimental value 0.13 $Å^{-1}$ and this justifies the negligible effect of the substrate layers on the Rashba splitting in the surface bands.

The buckling geometry of the surface alloy layer is essential for the spin splitting in the surface bands. Without the surface corrugation, the Bi atoms sits within the Ag atomic plane and the overall structure is space-inversion symmetric with respect to each Bi atom.

There will be no spin splitting in this case due to the simultaneous presence of the space inversion symmetry and the time reversal symmetry. When the Bi atoms get relaxed out of the Ag plane, the alloy layer loses the space inversion symmetry and as a consequence the spin splitting shows up in the surface bands. On the other hand, if the Bi atoms are pulled too far away from the Ag plane, the effective coupling between Bi orbitals and Ag orbitals vanishes. The system is equivalent to two isolated layers of Bi and Ag atoms and each atomic layer (Bi or Ag) is space-inversion symmetric. Under this isolation limit the spin degeneracy gets recovered. Therefore, there must be an optimal buckling parameter d to yield the largest spin splitting. The calculated band dispersion of the surface alloy layer with different buckling parameters is plotted in Fig. 8.8. The spin splitting in the $p_{x,y}$ bands grows gradually from zero as the Bi atoms moves out of the Ag plane and it reaches the maximum value ~ 0.9 $Å^{-1}$ when the Bi atoms are 0.8 Å above the Ag planes. As Bi moves even further away, the Rashba splitting decreases as a result of the diminishing coupling of Bi with Ag. The dependence of the spin splitting on the buckling parameter d is shown in Fig. 8.9 (b). The response of the spin splitting in the sp_z bands to the displacement of Bi atoms is much more complicated due to the hybridizing effect of the sp_z bands with their neighboring bands. In addition, the surface alloy layer with $d \approx 0.6$ Å has the lowest surface energy as shown in Fig. 8.9 (a). The calculated stable relaxation of Bi atoms is very close to the experimental value 0.64 Å for the Bi/ AG surface alloy on the Ag(111) surface indicating again that the Ag substrate has little effect on the electronic structure of the surface alloy layer.

The other important parameter determining the Rashba splitting of the surface alloy layer is the atomic spin-orbit coupling (SOC). There are two components of the surface alloy: Bi and Ag. It's instructive to learn how the SOCs of Bi and Ag affect the band structure of the surface alloy individually. Fig. 8.10 presents the band structures of a single layer Bi/Ag surface alloy with the SOCs of Ag and Bi atoms turned on and off

alternately. The band dispersion with only Ag SOC (Fig. 8.10 (c)) is very similar to that without any atomic SOC (Fig. 8.10(a)) except the small energy gap ~0.1 eV between the top two bands near the zone center $\bar{\Gamma}$. The Bi SOC alone, by contract, can induce the giant Rashba splitting of the Bi/Ag surface alloy, which is demonstrated by comparison of Fig. 8.10(b) and Fig. 8.10(d). Therefore, the strong atomic SOC of the heavy element Bi is crucial for achieving the giant Rashba splitting in the Bi/Ag surface alloy while the Ag atoms act as a messenger to transfer the Bi SOC to the surface states of the alloy systems by coupling to the Bi atoms. Calculations of the band structure at various levels of SOC strength (Fig. 8.11(a)) ranging from 0 to 100% confirm the key role played by the atomic SOC in the Rashba splitting of the surface alloy. The linear dependence of the Rashba momentum shift Δk in the sp_z bands as shown in Fig. 8.11(b) is in good accordance with Petersen and Hedegard's tight-binding description of Rashba splitting of *sp*-derived surface states [31]. The tight bind model gives the Rashba coupling (α_R in Eqn. 8.6) is proportional to the atomic spin-orbit interaction as well as the surface potential gradient which breaks the space inversion symmetry.

Previous electronic structure calculation [1] has shown that the Bi/Ag surface states are much more tightly localized in the topmost layer than the Ag(111) or Au(111) Shockley surface states. Therefore, the giant Rashba splitting and the Bi/Ag surface band dispersion are not directly affected by the thickness of the Ag supporting film. That's why our calculation for only the surface alloy layer can yield the essential physics in this prototypical Rashba system. We also performed calculation for the surface alloy system with the Ag supporting layers included to demonstrate the substrate effect of Ag films. The results for the Bi/Ag surface alloy sitting on a 1ML Ag film and a 9ML Ag film are shown in Fig. 8. 12(a) and (b), respectively. Apparently the Ag substrate doesn't affect the magnitude of the Rashba splitting in the surface band dispersion, but it introduces to the system the Ag *sp* quantum well states which are hybridized with the spin split surface

states. Through this hybridization mechanism, the Ag quantum well states gain finite spin polarization [4,18].

Isostructural surface alloy systems Sb/Ag(111) and Pb/Ag(111) have been experimentally realized [20,30]. The SOC induced spin splitting ($\Delta k_{sp_z} \approx 0.005$ Å^{-1}) in the Sb/Ag(111) surface alloy is strongly reduced compared with the Bi case because of the much weaker atomic SOC and the less outward relaxation of Sb atoms ($d \approx 0.11$ Å) [15]. The Pb/Ag(111) surface states, on the other hand, show up a considerably large Rashba splitting ($\Delta k_{sp_z} \approx 0.03$ Å^{-1}). This is because Pb is a high-Z element and the surface buckling ($d \approx 0.46$ Å) is more prominent than the Sb case. We calculated the band dispersion relation of the surface alloy layer with different adatoms (Sb, Pb and Bi) under the same structural geometry. When the surface corrugation is small, all three surface alloy layers have little spin splitting in their surface bands as shown in Figs. 8. 13 (a-c). For a larger surface buckling d=0.64 Å, the Rashba momentum shift in the sp_z surface bands is 0.035, 0.087 and 0.144 Å^{-1} for Sb/Ag, Pb/Ag and Bi/Ag, respectively. The atomic SOCs in Sb 5*p* orbitals (ζ_{5p}(Sb)), Pb 6*p* orbitals (ζ_{6p}(Pb)) and Bi 6*p* orbitals (ζ_{6p}(Bi)) are 0.4, 0.91 and 1.25 eV, respectively. The ratio of Rashba splitting in three systems is 0.24:0.60:1 and the ratio of the atomic SOCs is 0.32:0.73:1. Therefore, the Rashba splitting in the three cases roughly reflects the relative strength of the atomic SOC of the three adatoms. Comparing to the ratio of the atomic SOCs, the ratio of the Rashba splitting of Sb/Ag (Pb/Ag) to the Bi/Ag case is slightly smaller, which can be attributed to the smaller atomic radius of Sb (Pb) and thus the weaker coupling between the Sb and Ag atoms within the surface alloy layer.

8.7 Conclusion

The Bi/Ag surface alloy possesses giant Rashba spin splitting in its surface bands,

which makes it a potential platform for future applications of spintronics and quantum computation. We performed a systematic first-principles calculation for the surface alloy layer to investigate the dependence of the Rashba spin splitting on the atomic spin-orbit coupling and the surface corrugation. The results shows that the Rashba splitting is proportional to the atomic SOC, and it saturates at certain surface buckling parameter due to the trade-off between the breaking of space inversion symmetry and the interatomic coupling strength within the surface alloy layer. In the case of Bi/Ag, the optimal relaxation length is $d \approx 0.8$ Å. Our work offers a guideline for searching two dimensional systems with large Rashba spin splitting.

We also did a circular ARPES measurement on the Bi/Ag surface alloy. The good agreement between experiment and our calculation under various experimental conditions is a strong testimony of the theoretical treatment. The results confirm the strong spin texture of Bi/Ag including the complex pattern of interference between the spin-polarized surface states and the unpolarized quantum well states. A key finding is that the surface-photoemission term derived from a nonzero $\nabla \cdot \mathbf{A}$ and the **A**-dependent part of the Rashba interaction can interfere with each other and are both important for understanding our results. The $\nabla \cdot \mathbf{A}$ term has been largely ignored in prior publications, and our analysis here is the first quantitative study of spin-orbit coupling effects taking both terms into account. The methodology developed here should be valuable for unraveling the electronic structure of complex systems including topological insulators, heavy-element compounds, superconductors, and strongly correlated systems in general [32,33,34,35].

References:

[1] C. Ast et al., Phys. Rev. Lett. **98**, 186807 (2007).

[2] H. Bentmann et al., Europhys. Lett. **87,** 37003 (2009).

[3] A. C. Potter and P. A. Lee, Phys. Rev. Lett. **105**, 227003 (2010).

[4] K. He et al., Phys. Rev. Lett. **104**, 156805 (2010).

[5] F. Meier et al., Phys. Rev. B **77**, 165431 (2008).

[6] V. B. Zabolotnyy et al., Phys. Rev. B **76**, 024502 (2007).

[7] Y. H. Wang et al., Phys. Rev. Lett. **107**, 207602 (2011).

[8] Y. Liu et al., Phys. Rev. Lett. **107**, 166803 (2011).

[9] Y. Ishida et al., Phys. Rev. Lett. **107**, 077601 (2011).

[10] T. Miller, W. E. McMahon and T.-C. Chiang, Phys. Rev. Lett. **77**, 1167 (1996).

[11] T. Miller, E. D. Hansen, W. E. McMahon and T.-C. Chiang, Surf. Sci. **376**, 32 (1997).

[12] E. D. Hansen, T. Miller and T.-C. Chiang, Phys. Rev. Lett. **78**, 2807 (1997).

[13] Y. A. Bychkov and E. I. Rashba, Sov. Phys. JETP Lett. **39**, 78 (1984).

[14] T.-C. Chiang, Surf. Sci. Rep. **39**, 181 (2000).

[15] I. Gierz et al., Phys. Rev. B **81**, 245430 (2010).

[16] Y. A. Bychkov and E. I. Rashba, J. Phys. C **17**, 6039 (1984).

[17] E. Frantzeskakis et al., Phys. Rev. Lett. **101**, 196805 (2008).

[18] K. He et al., Phys. Rev. Lett. **101**, 107604 (2008).

[19] S.-J. Tang et al., Phys. Rev. Lett. **96**, 216803 (2006).

[20] L. Moreschini et al., Phys. Rev. B **79**, 075424 (2009).

[21] G. Bihlmayer, S. Blügel and E. V. Chulkov, Phys. Rev. B **75**, 195414 (2007).

[22] H. J. Hagemann, W. Gudat and C. Kunz, J. Opt. Soc. Am. **65**, 742 (1975).

[23] S. Lashell, B. A. McDougall, and E. Jensen, Phys. Rev. Lett. **77**, 3419 (1996).

[24] F. Reinert, J. Phys: Condens. Matter **15**, S693 (2003).

[25] J. Henk, A. Ernst and P. Bruno, Phys. Rev. B **68**, 165416 (2003).

[26] H. Cercellier et al., Phys. Rev. B **73**, 195413 (2006).

[27] J. Premper et al., Phys. Rev. B **76**, 073310 (2007).

[28] L. Fu, Phys. Rev. Lett. **103**, 266801 (2009).

[29] L. Moreschini et al., Phys. Rev. B **80**, 035438 (2009).

[30] D. Pacile et al., Phys. Rev. B **73**, 245429 (2006).

[31] L. Petersen and P. Hedegård, Surface Science **459**, 49 (2000).

[32] M. Z. Hasan and C. L. Kane, Rev. Mod. Phys. **82**, 3045 (2010).

[33] X.-L. Qi and S.-C. Zhang, Rev. Mod. Phys. **83**, 1057 (2011).

[34] I. Gierz et al., Phys. Rev. Lett. **103**, 046803 (2009).

[35] K. Yaji et al., Nat. Commun. **1**:17 (2010).

Figures:

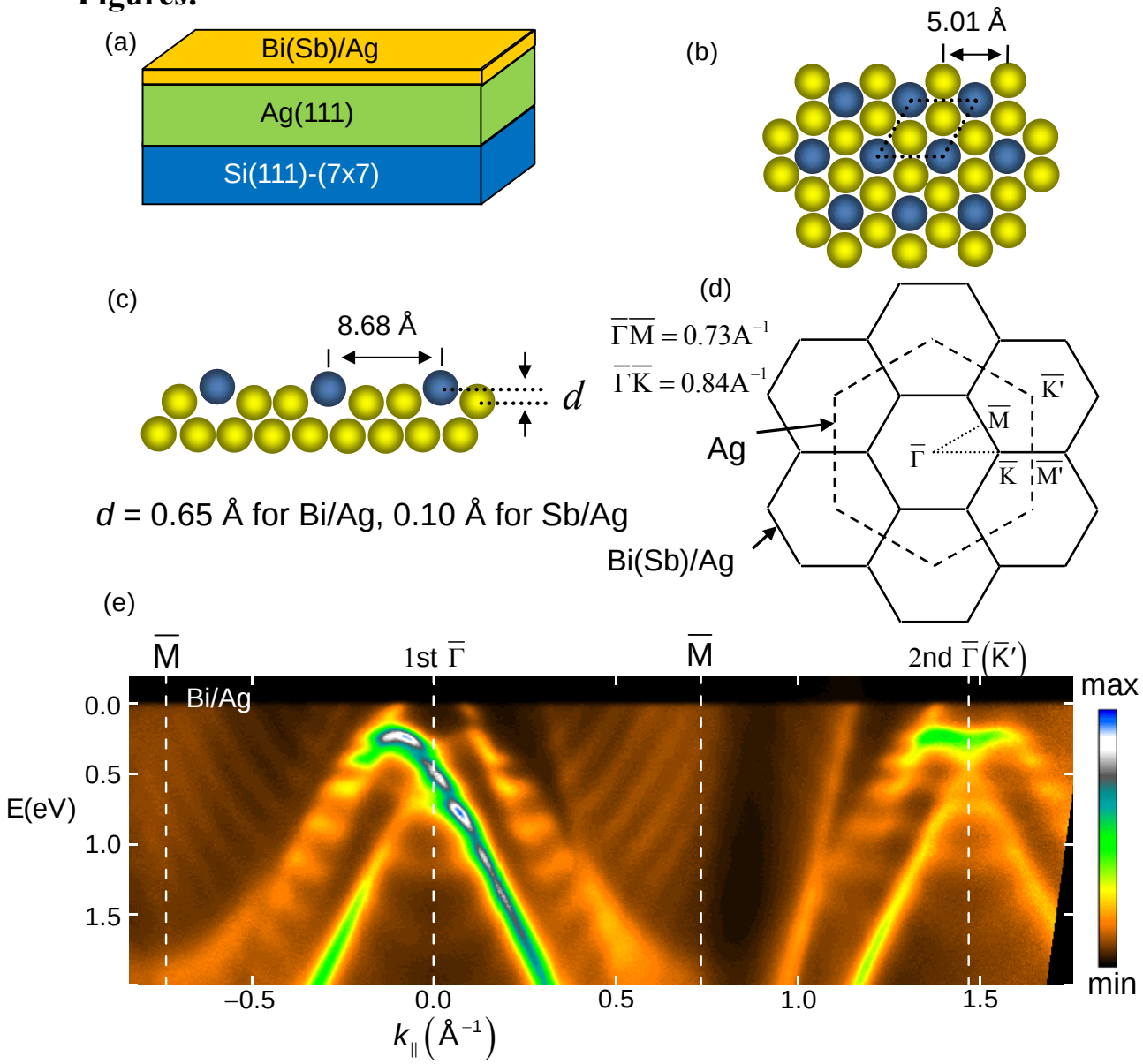

Figure 8.1. (a) Structures of Bi(Sb)/Ag Surface Alloys and photoemission data from Bi/Ag. (a) Sample configuration. (b) and (c) Top and side views of the lattice structures of the surface alloys. Blue balls indicate Bi or Sb atoms and yellow balls stand for silver atoms. (d) Surface Brillouin zones of the surface alloy and Ag(111) films. (e) A map taken from Bi/Ag based on a 20-ML Ag film. The spectrum is mapped using 22 eV horizontally polarized photons.

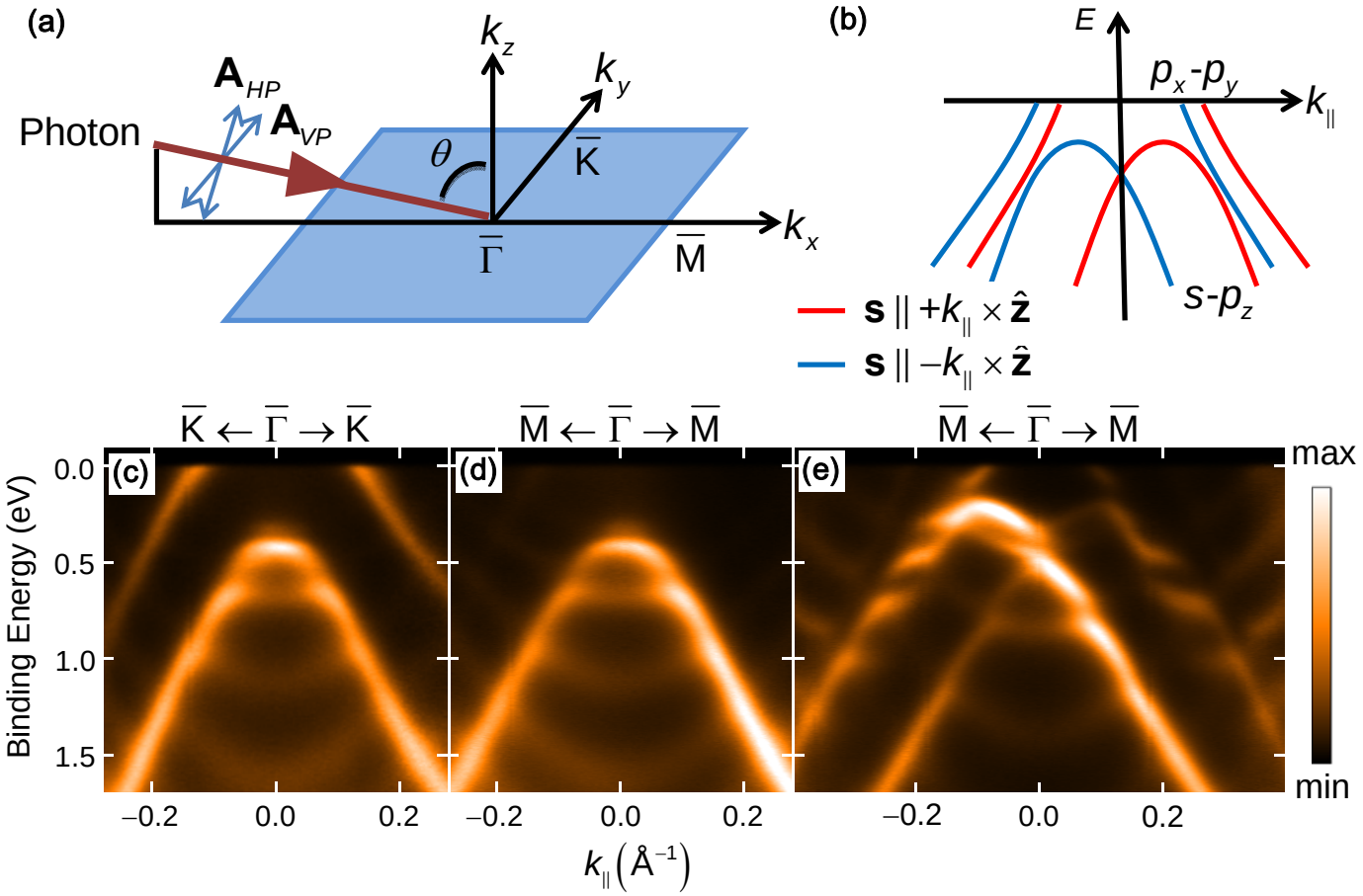

Figure 8.2. Experimental geometry and ARPES maps from Bi(Sb)/Ag(111) surface alloys taken with HP light at 22 eV. (a) Experimental geometry. The normal of the sample surface is along $\hat{\mathbf{z}}$ and the vertical direction is along $\hat{\mathbf{y}}$ in the laboratory frame of reference. (b) Schematic band dispersion relations and spin textures of Bi/Ag; Sb/Ag has similar band dispersion relations but the spin splittings are much smaller and not apparent in the data. (c) and d) Photoemission results taken along $\bar{\mathrm{K}} - \bar{\Gamma} - \bar{\mathrm{K}}$ and $\bar{\mathrm{M}} - \bar{\Gamma} - \bar{\mathrm{M}}$ directions, respectively, from Sb/Ag based on a 22-ML Ag film. (e) Photoemission results taken along $\bar{\mathrm{M}} - \bar{\Gamma} - \bar{\mathrm{M}}$ from Bi/Ag based on a 20-ML Ag film.

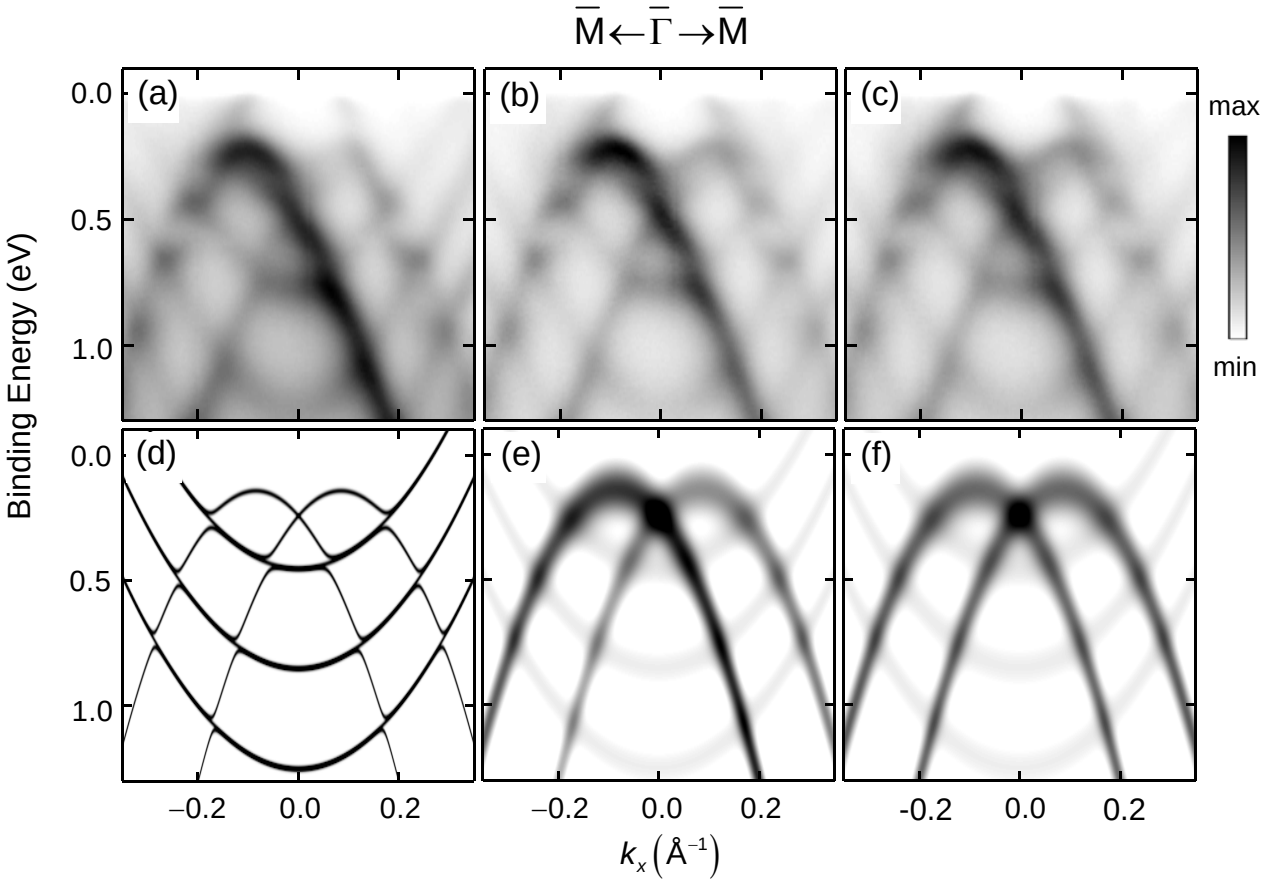

Figure 8.3. Photoemission results taken from Bi/Ag based on a 20-ML Ag film. The data were taken along $\overline{M}-\overline{\Gamma}-\overline{M}$ using 22-eV photons and (a) HP, (b) LCP, and (c) RCP polarization configurations. (d) Calculated band structure showing the hybridization of *s*-p_z surface bands with quantum well bands of the Ag film. (e) Calculated photoemission map for HP. (f) Calculated photoemission map for HP assuming that the spin-orbit-coupling contribution to surface photoemission is zero.

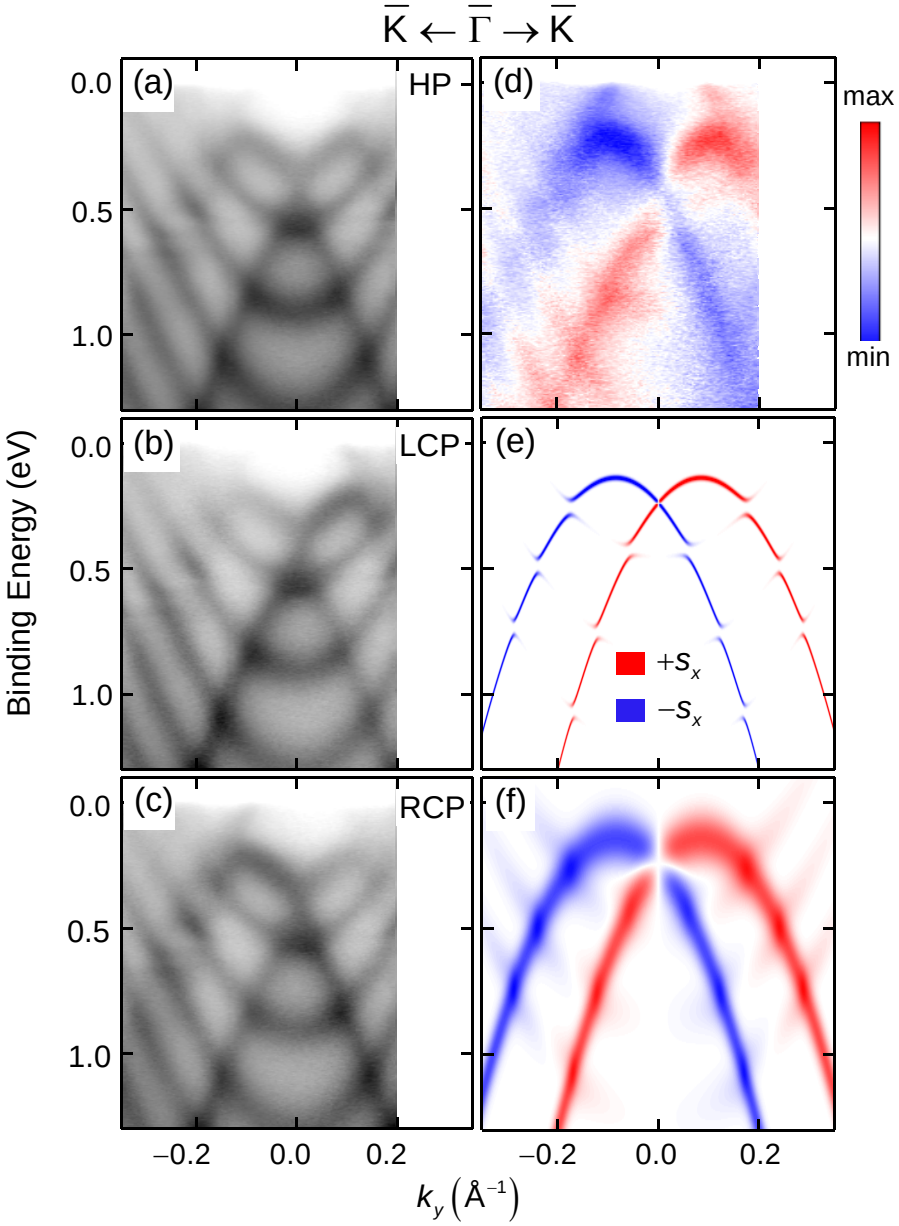

Figure 8.4. Photoemission results taken from Bi/Ag based on a 20 ML Ag film. The data were taken along $\bar{K}-\bar{\Gamma}-\bar{K}$ using 22-eV photons and (a) HP, (b) LCP, and (c) RCP polarization configurations. (d) Dichroic function extracted from the data. (e) Calculated band structure weighted by the spin polarization inherited from the Rashba split surface states using red and blue colors. (f) Calculated dichroic function.

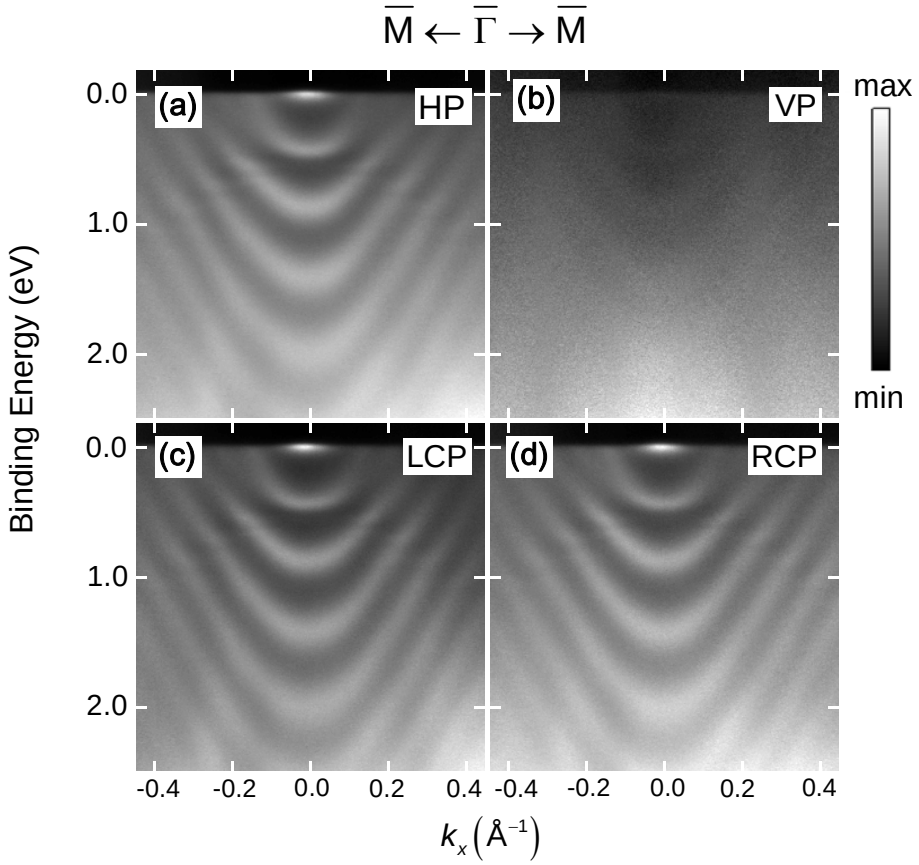

Figure 8.5. Photoemission results taken from a 20-ML Ag film along $\overline{M} - \overline{\Gamma} - \overline{M}$ using 22 eV photons. The data are for (a) HP, (b) VP, (c) LCP, and (d) RCP polarization configurations.

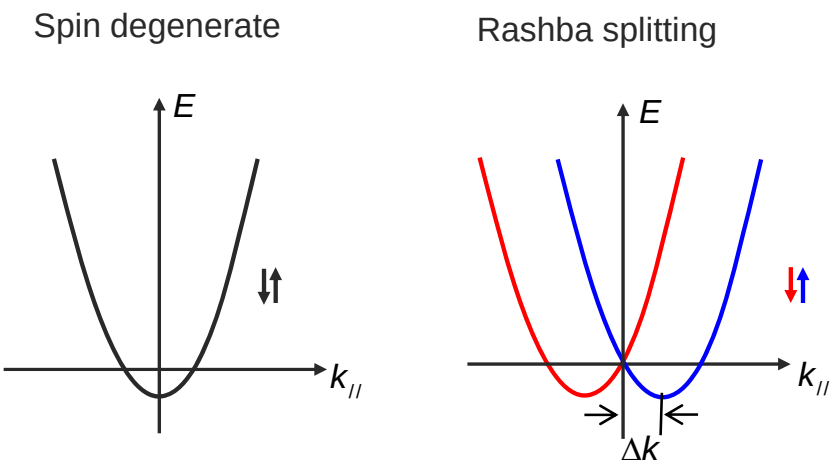

Figure 8.6. Schematic energy dispersion of a Rashba split nearly free electron gas.

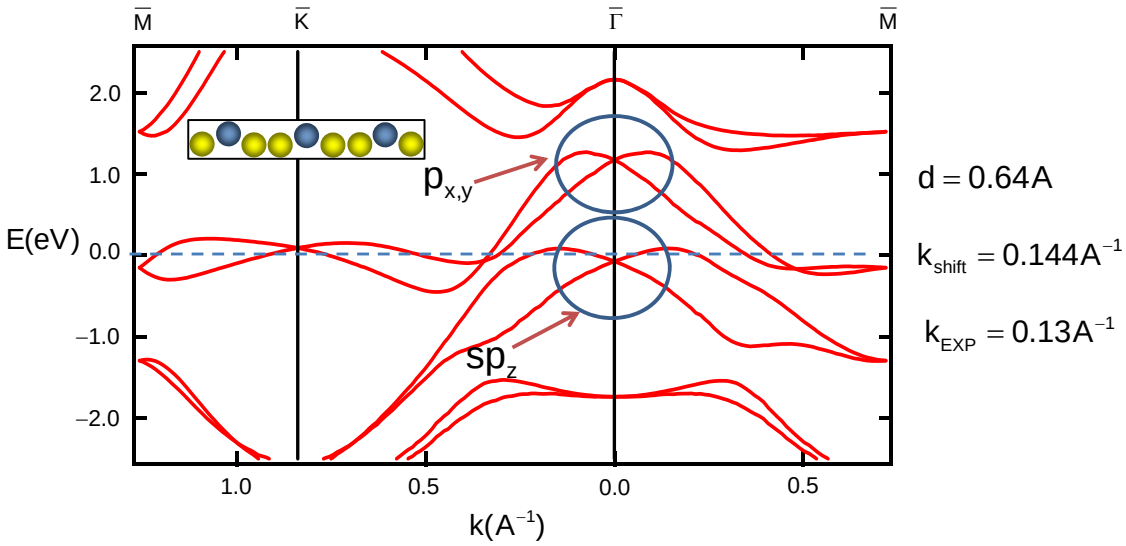

Figure 8.7. Band structure of a single layer Bi/Ag surface alloy without Ag supporting layers.

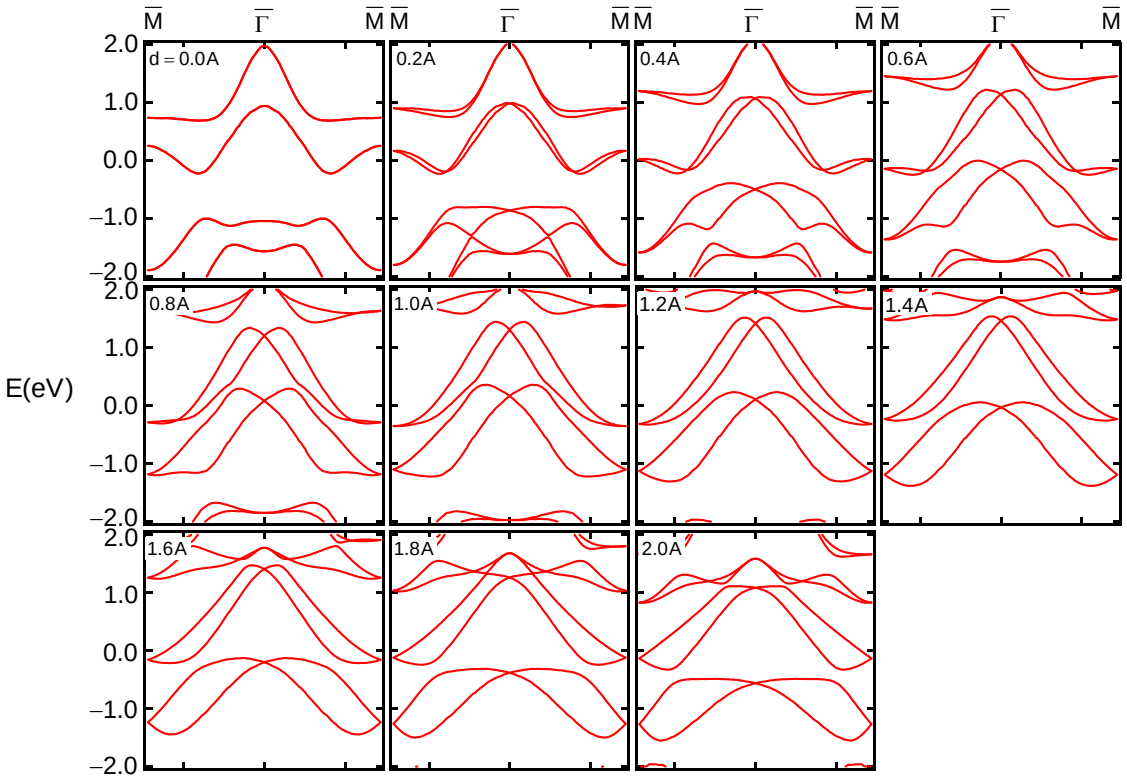

Figure 8.8. Band structure of a single layer Bi/Ag surface alloy with different buckling parameter *d*.

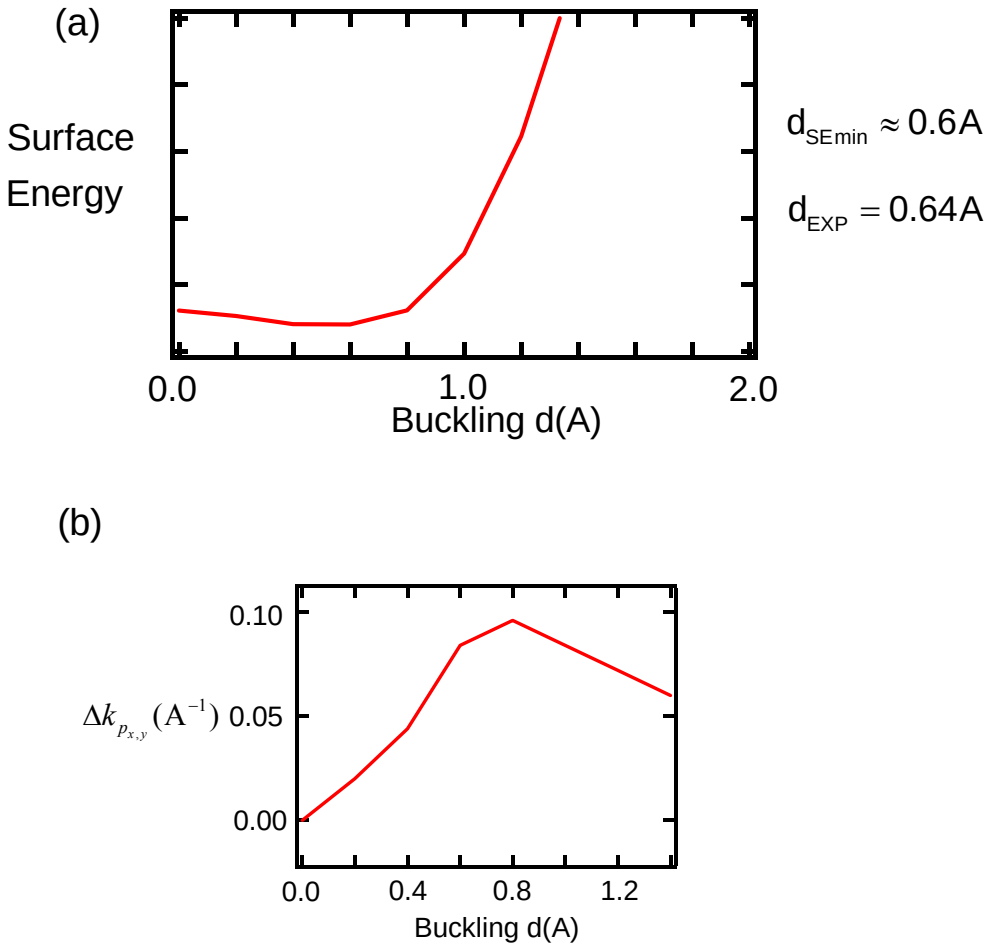

Figure 8.9. (a) Surface energy of a single layer Bi/Ag surface alloy as a function of the buckling parameter *d*. (b) The Rashba momentum shift in the $p_{x,y}$ bands as a function of *d*.

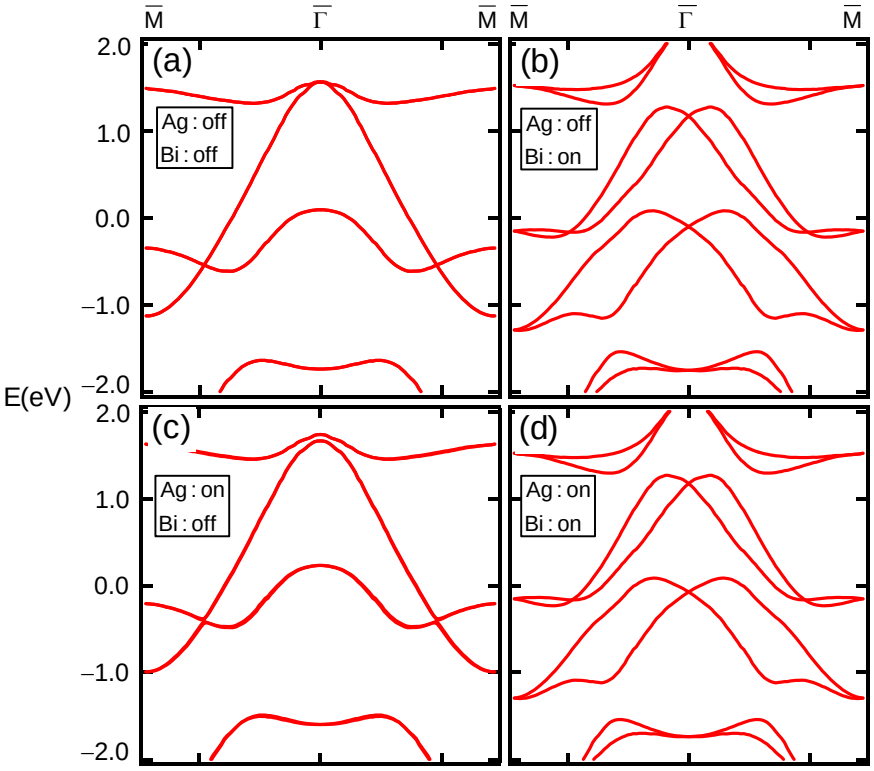

Figure 8.10. (a-d) Band structure of a single layer Bi/Ag surface alloy with the spin-orbit coupling of Ag and Bi atoms turned on/off.

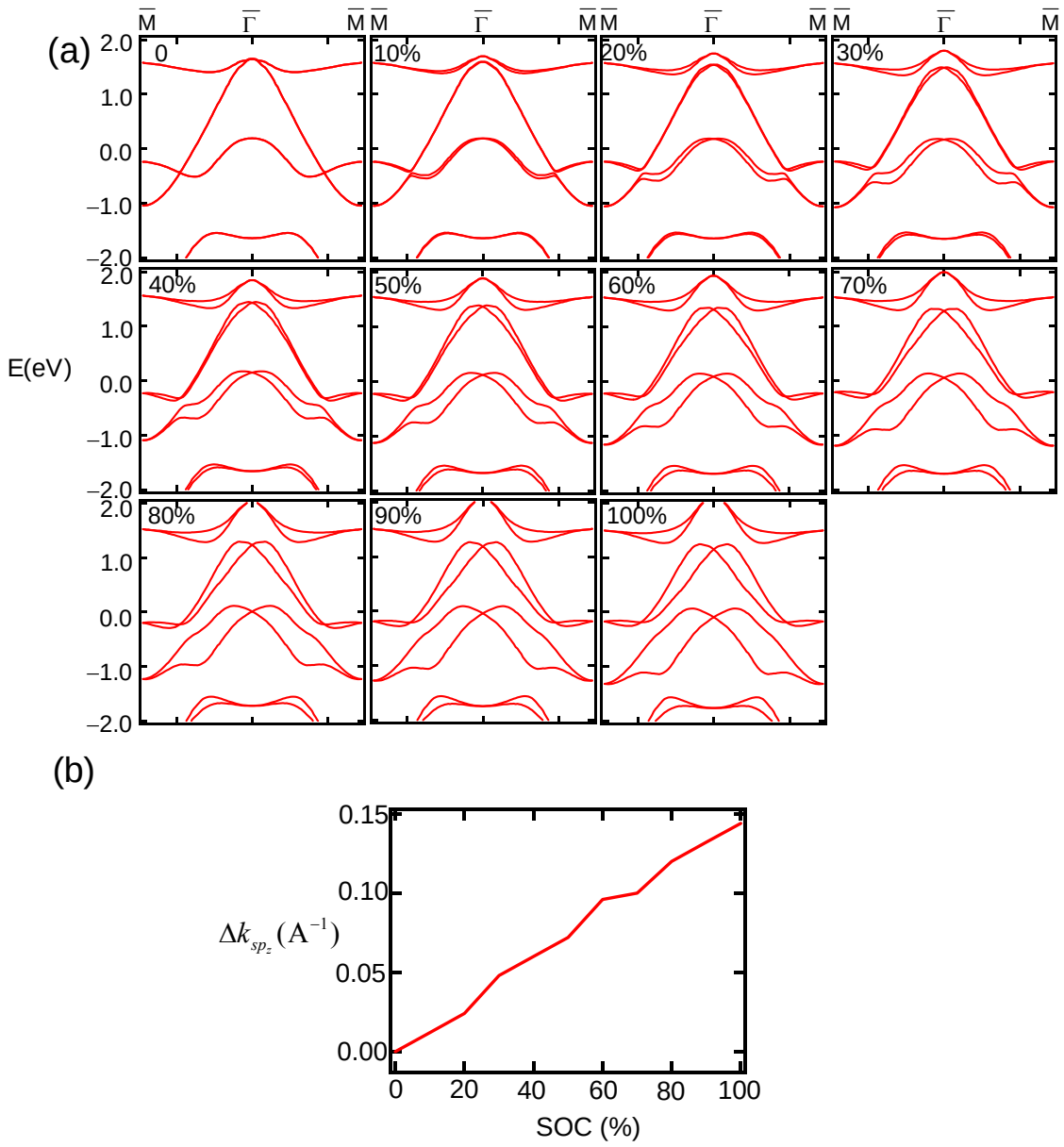

Figure 8.11. (a) Band structure of a single layer Bi/Ag surface alloy with different spin-orbit coupling. (b) Dependence of the Rashba momentum shift in the sp_z bands on spin-orbit coupling.

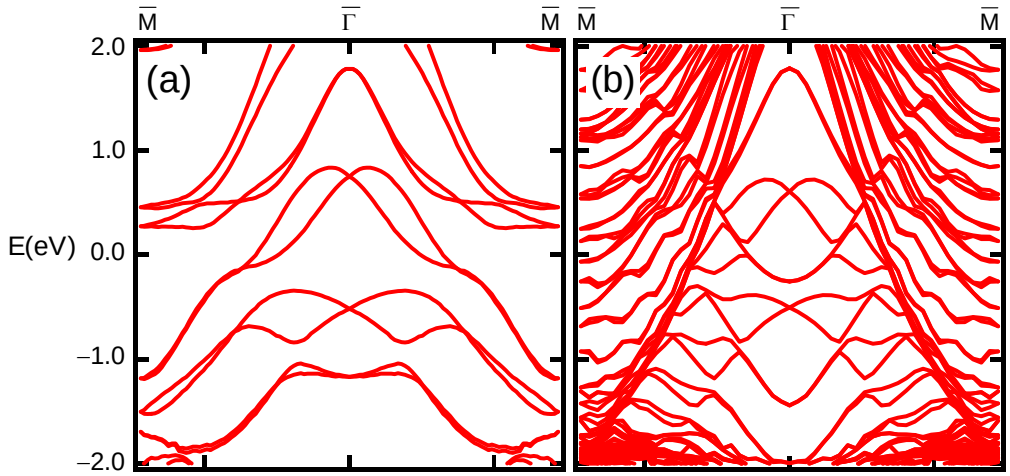

Figure 8.12. Band structure of the Bi/Ag surface alloy sitting on (a) 1 ML Ag(111) slab and (b) 9 ML Ag(111) slab.

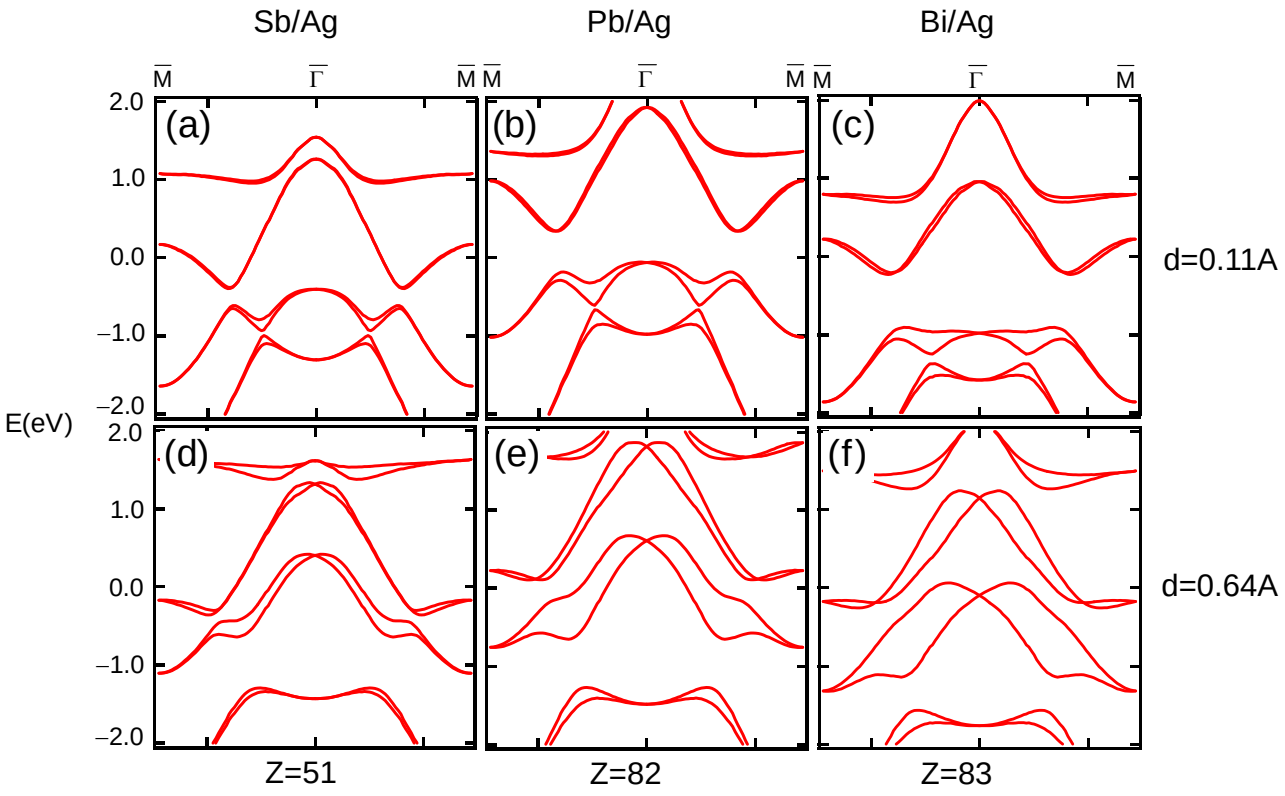

Figure 8.13. (a-f) Band structure of a single layer Sb/Ag, Pb/Ag and Bi/Ag surface alloy with different buckling parameters *d*.

9 Summary and Outlook

This thesis has focused primarily on ARPES and first-principles studies of the topological Sb, Bi_2Te_3 and Bi_2Se_3 thin films. In addition, two systems of technological importance, the Bi thin film and the Bi/Ag surface alloy, have been investigated. Many observed phenomena such as the metastability of Bi thin films and the quantum tunneling gap at the Dirac point of the topological surface bands are direct manifestations of quantum size effects, intrinsic to thin films.

Atomically uniform Sb films have been successfully fabricated on the Si(111) substrate. A Bi buffer layer or a a Bi-terminated Si(111)- $\sqrt{3}\times\sqrt{3}-R30^{\circ}$ surface reconstruction is essential for the smooth growth of the epitaxial Sb films. The ARPES spectra have shown clearly the nontrivial topological order of the Sb films as well as a smooth passage from spin-polarized surface states to spin-unpolarized quantum well states. Moreover, ARPES mapping of a 4-BL Sb film has shown no tunneling-induced energy gap at the Dirac point of the topological surface bands, contrary to a theoretically predicted one for a freestanding film. The observed robust Dirac cone is the result of a strong interfacial bonding between the film and the substrate. The interfacial interaction lifts the energy degeneracy of the surface states on the opposite faces of the film and thus suppresses quantum tunneling effect.

Topological order and topological surface states are the intriguing characteristics of topological materials. Even though the topological order is a robust quantity protected by time reversal symmetry, the detailed dispersion of topological surface states is be very sensitive to the boundary conditions. Our first-principles calculations for Bi_2Te_3 and Bi_2Se_3 thin films have shown, upon hydrogen termination of either face of the slab, the Dirac cone associated with this face is replaced by three Dirac cones centered at $\overline{\mathrm{M}}$

points at the zone boundary. In addition, we have shown by first-principles simulations for freestanding Bi_2Se_3 films that the topological surface states can disappear completely in topological films even at large film thicknesses. This anomalous behavior occurs when the effective SOC of the system is tuned close to the topological critical point and it can be suppressed in an asymmetric film of Bi_2Se_3 with one face terminated by H.

Our photoemission experiment on epitaxial Bi films has demonstrated the existence of a metastable PC phase and a stable RH phase of Bi films over a wide range of film thickness from 20 to ~100 Å. The PC-RH metastability range is unusually wide, which can be understood in terms of a near degeneracy of the bulk energies of the two phases and a surface-nucleation process that facilitates the formation of the metastable phase. We have also performed a circular ARPES measurement on the Bi/Ag surface alloy, a system with a giant Rashba spin splitting. A theoretical approach has been developed to build up a connection of the observed dichroic pattern with the spin texture of the surface alloy. The key finding is that the surface-photoemission term derived from a nonzero $\nabla \cdot \mathbf{A}$ and the **A**-dependent part of the Rashba interaction can interfere with each other and are both important for understanding our results. In addition, a systematic first-principles calculation for the surface alloy layer has been done to examine the dependence of the Rashba spin splitting on the atomic spin-orbit coupling and the surface corrugation. The results have indicated that the Rashba splitting is proportional to the atomic SOC and saturates at certain surface buckling parameter due to the trade-off between the breaking of space inversion symmetry and the interatomic coupling strength within the surface alloy layer. Our work will shed some light on the search of two dimensional systems with large Rashba spin splitting.

In this dissertation research, atomically uniform thin films of Sb, Bi, the topological insulator Bi_2Te_3 and the surface alloy Bi(Sb)/Ag(111) have been successfully fabricated on semiconductor substrates. Their structural qualities have been examined by

experimental tools such as RHEED and LEED, and their electronic structures have been thoroughly studied by ARPES and first-principles calculations. These thin films and surface alloys have great potential for practical device applications of spin-related electronics and quantum computation. To further test the electronic properties, detailed transport measurements are needed. Weak anti-localization and anomalous Hall effect stemming from topological order may have a profound impact on the transport properties of atomically thin materials and device structures.

Electronic chirality and Berry's phase are topics of central importance for understanding unique electronic and spin properties of topological materials. Our work on the Bi/Ag surface alloy has proven that the circular dichroic ARPES is a powerful probe of the spin texture. This novel experimental method can be straightforwardly utilized to examine electronic chirality and Berry's phase of topological materials. In addition, the Bi/Ag surface alloy is the key ingredient of Potter and Lee's proposal for realizing the elusive Majorana states. In their experimental scheme, a ferromagnetic insulating EuO thin film is used induce a Zeeman splitting to surface electrons of the Bi/Ag layer. A p_x+ip_y pairing can be induced by proximity to a conventional superconductor like Nb. A crucial condition for this junction is that the thickness of the Ag film cannot exceed the superconducting coherent length. We have obtained a well ordered Bi/Ag $\sqrt{3}\times\sqrt{3}$ surface on atomically uniform Ag thin films by MBE method. The thickness of epitaxial Ag films is several nanometers, which guarantees the effectiveness of the proximity effect. The deposition of ferromagnetic insulating EuO thin film can be achieved in an oxide MBE chamber. The major challenge will be to obtain well-ordered Ag films on the surface of a conventional superconductor, since a smooth Ag surface is the precondition for making the Bi/Ag surface alloy. Considerable experimental effort will be required to optimize the structural quality of the surface alloy as well as the superconducting proximity effect on the Bi/Ag surface states. The result

could provide an appealing possibility to realize Majorana fermions and a potential platform for future topological quantum computation.

Appendices

Appendix A: Computational software: ABINIT

The computational software employed for the first-principles calculations in this thesis is ABINIT [1,2]. Here is a brief introduction to this versatile software. ABINIT is a package whose main program allows one to find the total energy, charge density and electronic structure of systems made of electrons and nuclei (molecules and periodic solids) within Density Functional Theory (DFT), using pseudopotentials and a planewave or wavelet basis. ABINIT also includes options to optimize the geometry according to the DFT forces and stresses, or to perform molecular dynamics simulations using these forces, or to generate dynamical matrices, Born effective charges, and dielectric tensors, based on Density-Functional Perturbation Theory, and many more properties.

When heavy atoms like Bi are involved in the calculation, the spin-orbit coupling (SOC) has to be taken into account. It's very convenient to handle SOC in the framework of ABINIT. The incorporation of SOC is accomplished through the relativistic LDA approximation [3]. For atoms, the Dirac equation is solved and the $2(2l+1)$ l-channel degeneracy is lifted according to the eigenvalues of the $\boldsymbol{L}+\boldsymbol{S}$ operator ($l+1/2$ and $l-1/2$ of degeneracy $2l+2$ and $2l$). After pseudization, the associated wave functions can be recovered by adding to usual pseudo-potential projectors a spin-orbit term of the generic form $v(\boldsymbol{r})|l,s\rangle \boldsymbol{L}\cdot\boldsymbol{S}\langle l,s|$. Not all potentials include this additional term, but it turns out that it is the case for all the HGH type pseudopotentials [4]. In a plane-wave calculation, the wavefunctions will be two components spinors, that is will have a spin-up and a spin-down component but these components will be coupled. This means the size of the Hamiltonian matrix is quadrupled.

To run ABINIT, there are three types of files needed:

(1) A file specifying the names and directories of input and output files

(2) An input file providing detailed information about the calculation: the lattice structure, the exchange-correlation functional, etc.

(3) Pseudopotential files

An example of the main input file is given below: the meaning of input variables are indicated by the comments.

```
#########################################################################################
# A supercell of 4BL Sb(111) slab plus 4BL vacuum
# Computation of the band structure.
# First, a SCF density computation, then a non-SCF band structure calculation.

#Global setting
ndtset        2              # gives the number of data sets to be treated
ixc           1              # type of exchange-correlation functional
nspinor       2              # spin-orbit coupling switch
so_psp        2              # spinor of each atom
occopt        7              # occupation option
tsmear        0.01           # temperature of smearing
enunit        1              # energy units print in eV
prtwf         0              # option for printing wavefunction
chksymbreak   0              # check symmetry breaking

#Dataset 1 : usual self-consistent calculation
iscf1         7              # option for self-consistent field (SCF) cysles
kptopt1       1              # option for the automatic generation of k points,
ngkpt1        8 8 2          # k point grid taking into account the symmetry
nshiftk1      1              # number of shifts for k point grid
shiftk1       0.0 0.0 0.5    # shift of k points
prtden1       1              # Print the density, for use by dataset 2
toldfe1       1.0d-9         # tolerance on the difference of total energy, criterion for convergence

#Dataset 2 : the band structure
iscf2         -2             # non-self-consistent calculaiton
getden2       -1             # read the density from previous self-consistent part
```

```
kptopt2       -2
nband2        50                    # number of bands to calculate
ndivk2        75    50              # number of divisions of the k lines
kptbounds2     1.0   0.5   0.0     # M'-bar point, boundaries of k points
               0.0   0.0   0.0      # Gamma-bar point
               0.5   0.0   0.0      # M-bar point
tolwfr2    1.0d-12

#Definition of the unit cell
acell 3*8.127145312                  # scaling of unit cell lattice vectors, in Bohr
rprim      1.0          0.0          0.0       # film primitive vectors (to be scaled by acell)
           0.5          sqrt(0.75)   0.0
           0.0          0.0          6.9583    # thickness: 4BL Sb(111)+4BL vacuum

#Definition of the atom types
ntypat    1                # There is only one type of atom
znucl     51               # The keyword "znucl" refers to the atomic number of the
                           # possible type(s) of atom. Here, the only type is Antimony (Sb)

#Definition of the atomic coordinates
natom    8                           # number of atoms in unit cell
typat    8*1                         # All possible atoms are type 1.
xred      0.0     0.0     0.00       #1   Sb, reduced coordinates of atom
          1/3     1/3     0.0502     #2   Sb
          2/3     2/3     0.125      #3   Sb
          0.0     0.0     0.1752     #4   Sb
          1/3     1/3     0.250      #5   Sb
          2/3     2/3     0.3002     #6   Sb
          0.0     0.0     0.375      #7   Sb
          1/3     1/3     0.4252     #8   Sb

nstep     200     # Maximal number of SCF circles
ecut      15      # Maximal kinetic energy cut-off, in Hartree
#################################################################################
```

Appendix B: Rhombohedral lattices of Bi, Sb, Bi_2Te_3 and Bi_2Se_3

Bulk Bi, Sb, Bi_2Te_3 and Bi_2Se_3 have the rhomohedral structure. The three primitive vectors of the lattice are

$$\begin{aligned} \boldsymbol{a}_1 &= (-a/2, -\sqrt{3}a/6, c/3), \\ \boldsymbol{a}_2 &= (a/2, -\sqrt{3}a/6, c/3), \\ \boldsymbol{a}_3 &= (0, \sqrt{3}a/3, c/3). \end{aligned} \tag{B1}$$

Here a and c are the lattice constants in the hexagonal unit cell. The corresponding reciprocal lattice vectors, defined by $\boldsymbol{a}_i \cdot \boldsymbol{b}_j = 2\pi\delta_{ij}$, are given as

$$\begin{aligned} \boldsymbol{b}_1 &= (-1, -\sqrt{3}/3, b)g, \\ \boldsymbol{b}_2 &= (1, -\sqrt{3}/3, b)g, \\ \boldsymbol{b}_3 &= (0, 2\sqrt{3}/3, b)g, \end{aligned} \tag{B2}$$

with

$$\begin{aligned} b &= a/c \\ g &= 2\pi/a. \end{aligned} \tag{B3}$$

The lattice structure of Bi and Sb is composed of two interpenetrating, diagonally distorted face-centered-cubic lattices with two atoms per unit cell. The relative position of the two basis atoms is given by

$$d = (0, 0, 2\mu)c. \tag{B4}$$

The lattice parameters for Bi and Sb are listed in Table B1 [5,6], and the unit cell for Bi and Sb is shown in Fig. B1 [7].

The Bi_2Se_3 family of compounds has a layered structure with five atomic layers as a basic unit, namely a quintuple layer (QL) [8]. As shown in Fig. B2(a), Se2 is taken to be the origin (0, 0, 0) of the unit cell; then two Bi atoms are at $(\pm\mu, \pm\mu, \pm\mu)$ and two Se1

are at $(\pm v, \pm v, \pm v)$, defined in the unit of primitive vectors. All the experimental lattice constants for the Bi_2Se_3 family of compounds are listed in Table B2 [9]. Fig. B2(c) shows the 3D Brillouin zone (BZ) and the 2D surface BZ of Bi_2Se_3. Γ (0, 0, 0), L(π, 0, 0) ($\times 3$), F(π, π, 0) ($\times 3$) and Z(π, π, π) are eight time-reversal invariant momentum (TRIM) points in the 3D BZ. Γ and Z are projected onto $\overline{\Gamma}$, and L and F are projected onto $\overline{\mathrm{M}}$ in the surface BZ. $\overline{\Gamma}$ and $\overline{\mathrm{M}}$ ($\times 3$) are four TRIM points in the surface BZ.

Appendix C: Surface States, Quantum Well States and Excited States of Ag(111) films

We will revisit several key electronic properties of Ag(111) thin films in this section. As discussed in Chapter 4, the spatial confinement results in quantization of the bulk bands as shown in Fig. C1. The band structure of a 20 ML freestanding Ag(111) film is replotted in Fig. C1(b). The energy of the calculated *d* bands is too high by ~ 2 eV compared to the experimental data [10]. This is because LDA (or GGA) functionals tend to over-delocalize electrons and as a consequence the one-site Coulomb repulsion is not well accounted for. This problem is more severe for highly localized *d* and *f* electrons, and it can be corrected by more sophisticated methods like DFT+U [11]. The band edge of Ag along (111) direction is at ~ -0.3 eV, which allows the existence of surface states in this narrow energy gap. The two bands grazing the Fermi level at $\bar{\Gamma}$ in Fig. C1(b) are of surface nature. The plane-averaged charge densities of the two surface states at $\bar{\Gamma}$ are shown in Fig. C2. Due to the finite thickness of the Ag film, the two surface states on the opposite faces can couple with each other and form two hybridized states. One of the hybridized states shows node at the film center in the charge density while the other shows anti-node. There exists a tiny energy difference between two hybridized states due to the hybridization. The top five waves plotted in Fig. C3(a) are the *sp* quantum well states at $\bar{\Gamma}$ starting from the one right below the surface states. The envelope functions of those quantum wells states arise from the crystal potential. It can be explained as a beating pattern involving two plane waves with wave vectors *k* and *G*-*k*, where *G* is the primitive reciprocal lattice vector along [111]. The beating number ν can be derived from the Bohr-Sommerfeld quantization rule,

$$2kNt + \Phi = 2n\pi \qquad \text{(C1)}$$

where k is measured from the zone center, N is the number of atomic layers, t is the monolayer thickness and Φ is the total phase shift at surface and interface. Since the momentum k ($k_\perp$) of those QWSs are very close to the zone boundary at $k_L = \pi / t = \sqrt{3}\pi / a$ (a is the lattice constant of Ag), it's more convenient to write the quantization condition in terms of k' ($k' = \pi / t - k$) measured from the zone boundary.

$$2k'Nt - \Phi = 2(N - n)\pi = 2\nu\pi \qquad \text{(C2)}$$

The quantum number ν ($\nu = N - n$) are small values near the band edge. Specifically, $\nu = 1$ corresponds to the quantum well state closest to the band edge. ν also gives the number of peaks in the envelope function of quantum well states.

The other waves in Fig. C3(a) correspond to the *d* states adjacent to the *sp* quantum well states. Those charge densities exhibit fine structure which can be seen in those of *sp* states. In Fig. C3(a) there are excited states with energy larger than 4 eV around the zone center. Those excited states form discrete parabolic subbands as a result of the finite vacuum thickness (d_{vac}=10 ML) adopted in our DFT calculation. The eigenvalues and wavefunctions of excited states in DFT have no clear physical meaning because DFT refers only to the calculation of the total energy and charge density of the ground states. Nevertheless DFT offers a qualitatively reliable estimate of excited states of the system. The charge densities of excited states at $\bar{\Gamma}$ are shown in Fig. C3(b). The wave at bottom corresponds to the excited state with the lowest energy. The charge of this states lies mostly within the Ag film except a tiny tail in vacuum. As the excitation energy increases, the charge gradually leaks into the vacuum and eventually it forms standing wave in the vacuum layer with a minor part left in the Ag film. For infinite vacuum, the excited states have plane-wave form outside the film, and their wavefunctions are determined by the boundary condition at the interface. This is consistent with the time-reversed-LEED-state description of the final states in the theory of ARPES.

Appendix D: Topological Phase Transition in the Kane-Mele Model

In this section we will examine the Kane-Mele model of graphene [12,13]. At sufficiently low temperature a single layer of graphene exhibits a quantum spin Hall (QSH) effect with an energy gap generated by the intrinsic spin-orbit interaction. The key idea is that the spin-orbit coupling (SOC) serves as an effective magnetic field in a way such that spin-up and spin-down electrons feel opposite magnetic fields and as a consequence the Hall currents for spin-up and spin-down electrons propagate in opposite directions. In the QSH phase there exist a net spin current at the boundary without breaking the time reversal symmetry. The honeycomb lattice structure, the Brillouin zone and the band structure of graphene are shown in Fig. D1.

The tight-bind Hamiltonian of graphene is

$$H_{Kane-Mele} = t\sum_{\langle ij\rangle} c_i^{\dagger} c_j + i\lambda_{SO}\sum_{\langle\langle ij\rangle\rangle} \varepsilon_{ij} c_i^{\dagger} s^z c_j + \lambda_v \sum_i \xi_i c_i^{\dagger} c_i \,. \tag{D1}$$

The first term is a nearest neighbor hopping term on the honeycomb lattice. The second term is the mirror symmetric spin-orbit interaction which involves spin dependent second neighbor hopping. Here $\varepsilon_{ij} = (2/\sqrt{3})(\hat{\boldsymbol{d}}_1 \times \hat{\boldsymbol{d}}_2)_z = \pm 1$, where $\hat{\boldsymbol{d}}_1$ and $\hat{\boldsymbol{d}}_2$ are unit vectors along the two bonds the electron traverses going form site *j* to *i*. s^z is a Pauli matrix describing the electron's spin. The third term is a staggered sublattice potential ($\xi_i = \pm 1$). The projected 1D Brillouin zone along the zigzag direction can be found in Fig. D1(b). The band structure for a zigzag ribbon of width 50 atomic chains is shown in Fig. D2. In the case without SOC and the staggered potential, the quantum well subbands derived from the π band of graphene are stacked around $\overline{\mathrm{K}}$. In addition, there are two degenerate edge bands with zero energy connecting the bulk states at two $\overline{\mathrm{K}}$ points.

With nonzero staggered potential, an energy gap of size $|2\lambda_v|$ is opened and the two edge bands are no longer degenerate. The SOC term in Eqn. D1 can also open an energy gap at the Dirac point. The energy gap induced by SOC is equal to $|3\sqrt{3}\lambda_{SO}|$. When both SOC and the staggered potential are present, the energy gap is of magnitude $|3\sqrt{3}\lambda_{SO} - 2\lambda_v|$. For $\lambda_v > 3\sqrt{3}\lambda_{SO}/2$, the gap is dominated by λ_v, and the system is an ordinary insulator. $\lambda_v < 3\sqrt{3}\lambda_{SO}/2$ describes a topologically distinct phase, the QSH phase. Figs. D3(a-c) demonstrate those different topological phases. Both phases have a bulk energy gap and edge states, but only in the QSH phase the edge states traverse the energy gap in pairs. At the transition between the two phases, the energy gap closes, allowing the edges states to "switch partners". The band structure with solely SOC is shown in Fig. D3(d). The edge states on the opposite boundaries are degenerate, and they form "Dirac cones" centered at $\overline{\mathrm{M}}$. The phase diagram of the Kane-Mele model is present in Fig. D4.

The intrinsic SOC gap in graphene is about 10 mK~1 K. The small energy gap hinders the observation of the QHS effect. The Kane-Mele model has motivated great research interest in a single layer of silicon and germanium, namely, silicene and germanene. Those systems have stronger SOC, and therefore the QSH effect is easier to observe in those atomic sheets. The reported SOC band gap is 1.55 meV (~18 K) for silicene and 23.9 meV (277 K) for germanene [14].

To test the robustness of the topological order, a potential bias is put on the top atomic chain of the topological graphene ribbon as schematically shown in Fig. D5(a). The band structures with different edge potentials are plotted in Fig. D5(b). As the edge potential bias increases, the energy of the top edge band is gradually lifted. When the top edge band merges into the conduction band as illustrated in the third panel of Fig. D5(b),

the highest conduction subband is isolated from the bulk band region, and the states in this band are pretty much trapped in the top atomic chain due to the large potential bias. At the same time, the highest valence subband is pulled into bulk band gap and becomes localized near the top edge. With sufficiently large potential bias, the top atomic chain is essentially cut off from the ribbon, yielding a different atomic configuration at the top edge. The altered boundary condition makes the top-edge "Dirac cone" centered at $\overline{\Gamma}$ in contrast with the unperturbed one at $\overline{M}$.

This simple tight-binding model gives essentially the same physics discussed in Chapter 6. Below is the Matlab M-file for the calculation:

```
%%%%%%%%%%%%%%%%%%%%%%%%%%%%%%%%%%%%%%%%%%%%%%%%%%%%%%%%%%%%%%%%%%%%%%%%%%%%
% The code is done in collaboration with Ching-Kai Chiu
clear all
% Band Structure of Kane-Mele Model along ZigZag direction
t=1; %hopping coefficient
lso=0.0; %spin orbit coupling
lr=0.0;    %Rashba coefficient
lv=0.0;    %staggered potential
eb=0.0;    %edge potential bias
mf=0.0;      %vertical magnetic field
L=50; % width of graphene ribbon
N=4*L; %dimension of matrix

  % define unit cell, k space
a=1;
k=0;
count=1;
kmax=6.29;
kint=0.01;
M=zeros(N,N); % initializing matrix

while k < kmax
      pp=exp(i*a*k);
```

```
    ss=sin(a*k);
    for nn=1:L
        M(4*nn-3,4*nn-1)=(1+pp)*t;
        M(4*nn-2,4*nn)=(1+pp)*t;
        M(4*nn-3,4*nn-3)=lso*ss;
        M(4*nn-2,4*nn-2)=-lso*ss;
        M(4*nn-1,4*nn-1)=-lso*ss;
        M(4*nn,4*nn)=lso*ss;
        M(4*nn-3,4*nn)=i*lr*(0.25*(1+pp)+i*0.25*sqrt(3)*(1-pp));
        M(4*nn-2,4*nn-1)=i*lr*(0.25*(1+pp)-i*0.25*sqrt(3)*(1-pp));
        M(4*nn-3,4*nn-3)=M(4*nn-3,4*nn-3)+lv+mf;
        M(4*nn-2,4*nn-2)=M(4*nn-2,4*nn-2)+lv-mf;
        M(4*nn-1,4*nn-1)=M(4*nn-1,4*nn-1)-lv+mf;
        M(4*nn,4*nn)=M(4*nn,4*nn)-lv-mf;
        if (nn<L)
            M(4*nn-1,4*nn+1)=t;
            M(4*nn,4*nn+2)=t;
            M(4*nn-3,4*nn+1)=i*0.5*lso*(-1+pp);
            M(4*nn-2,4*nn+2)=i*0.5*lso*(1-pp);
            M(4*nn-1,4*nn+3)=i*0.5*lso*(1-pp);
            M(4*nn,4*nn+4)=i*0.5*lso*(-1+pp);
            M(4*nn-1,4*nn+2)=i*0.5*lr;
            M(4*nn,4*nn+1)=i*0.5*lr;
        end
     end

     for mm=1:N
        for nn=1:mm
            M(mm,nn)=conj(M(nn,mm));
        end
     end
     M(1,1)=M(1,1)+eb;
     M(2,2)=M(2,2)+eb;
    pict(count,:)=transpose(sort(eig(M)));
    count=count+1;
    k=k+kint;
end

figure(1)
plot(0:0.01:kmax,pict,'-k','linewidth',1.5)
```

```
axis([0, 6.29, -3, 3])
set(gca, 'XTick', [],'YTick', []);
line('XData',[0 6.29],'YData',[0 0],'color','r','LineStyle','-.','LineWidth',1.5)
line('XData',[pi*2/3 pi*2/3],'YData',[-3 3],'color','r','LineStyle','-.','LineWidth',1.5)
line('XData',[pi*4/3 pi*4/3],'YData',[-3 3],'color','r','LineStyle','-.','LineWidth',1.5)

%%%
```

Appendix E: Probing Berry's Phase in Graphene by Circular ARPES

Electronic chirality near the Dirac point is a key property of graphene systems [15]. The direction of the pseudospin vector in monolayer graphene tracks the rotation of the electronic crystal momentum, resulting in a Berry's phase of π [16,17]. Our group has observed the chiral property of graphene using circular ARPES [18]. The elegant ARPES experiment was performed by my labmate Dr. Yang Liu. In the section we will give an intuitive understanding of the experimental results.

The ARPES geometry is shown in Fig. E1(a). The sample is monolayer graphene prepared on SiC. 30-eV photons are incident nearly in the normal direction of sample surface. The vector potential of photon is

$$\mathbf{A}=\mathrm{A}_x\hat{\mathbf{x}}+\mathrm{A}_y\hat{\mathbf{y}}+\mathrm{A}_z\hat{\mathbf{z}}\,. \tag{E1}$$

Under the experimental conditions, A_z is negligibly small. Ignoring the contribution form surface transition, which is proportional to $\left|\mathrm{A}_z\right|^2$, the photoemission intensity is given by the dipole transition probability

$$I\propto\left|\left\langle\Psi_f^k\left|\mathbf{A}\cdot\mathbf{p}\right|\Psi_i^k\right\rangle\right|^2\,\delta(E_f-E_i-\hbar\omega)\,. \tag{E2}$$

Generally, the vector potential for elliptically polarized light is given by

$$\mathbf{A}=\mathrm{A}_0(\cos\varphi_A\hat{\mathbf{x}}+i\sin\varphi_A\hat{\mathbf{y}})\,, \tag{E3}$$

where $\tan\varphi_A$ is the ellipticity. $\varphi_A=0,\pi/4,\pi/2$ and $3\pi/4$ for HP, LCP, VP and RCP, respectively.

The two-component electron wavefunction of monolayer graphene, close to the K point, obeys the 2D Dirac equation,

$$-iv_F\boldsymbol{\sigma}\cdot\nabla\Psi(\boldsymbol{r})=E\Psi(\boldsymbol{r}). \tag{E4}$$

The wavefunction, in momentum space, for the momentum around the K point has the form

$$\Psi_{\pm,K}(\boldsymbol{k})=\frac{1}{\sqrt{2}}\begin{pmatrix} e^{-i\theta_k/2} \\ \pm e^{i\theta_k/2}\end{pmatrix} \tag{E5}$$

for $H_K=v_F\boldsymbol{\sigma}\cdot\mathbf{k}$, where the $\pm$ signs correspond to the eigenenergies $E=\pm v_F k$, that is, for the π^* and π bands (bands above and below the Dirac point), and θ_k is illustrated in Fig. E1(b). Note that if the phase angle θ_k is rotated by 2π, the wavefunction changes sign indicating a phase of π which, in the literature, is called a Berry's phase. This change of phase by π under rotation is characteristic of spinors.

Fig. E1(c) shows ARPES results around the K point measured along the *y* direction with LCP and RCP. Evidently, photons with different helicity selectively excite one of the two branches of the Dirac cone with opposite pseudospin directions. Fig. E2 presents typical constant energy maps of the π* and π bands of monolayer graphene, respectively, using the four polarization configurations. For each band, the semicircular pattern rotates counterclockwise in 90º steps in going from HP to LCP to VP and to RCP. Furthermore, the patterns of the π* and π bands are related by inversion. These ARPES patterns can be understood as the interference between the emissions from A and B sublattices shown in Fig. E1(d). Specifically, the initial states can be written in terms of the states on A and B sites,

$$\Psi_i^k=e^{-i\theta_k/2}\Psi_A(\boldsymbol{k})\pm e^{i\theta_k/2}\Psi_B(\boldsymbol{k}). \tag{E6}$$

Substituting Eqn. E6 into Eqn. E2, we'll have

$$I\propto\left|\left\langle A_x\xi_x(e^{-i\theta/2}\pm e^{i\theta/2})+A_y\xi_y(e^{-i\theta/2}\mp e^{i\theta/2})\right\rangle\right|^2, \tag{E7}$$

where

$$\xi_x = \left\langle \Psi_f^k \middle| p_x \middle| \Psi_A(\boldsymbol{k}) \right\rangle = \left\langle \Psi_f^k \middle| p_x \middle| \Psi_B(\boldsymbol{k}) \right\rangle,$$
$$\xi_y = \left\langle \Psi_f^k \middle| p_y \middle| \Psi_A(\boldsymbol{k}) \right\rangle = -\left\langle \Psi_f^k \middle| p_y \middle| \Psi_B(\boldsymbol{k}) \right\rangle. \quad \text{(E8)}$$

In deriving Eqn. (E7), we have made use of the facts:

(a) The xz plane is the mirror plane of graphene.

(b) Ψ_A and Ψ_B are all derived from the carbon $2p_z$ orbital. They are related to each other by the mirror symmetry as shown in Fig. E1(d).

(c) The allowed final state of photoemission Ψ_f^k near the K point must be of even parity with respect to reflection about the *xz* plane because the photoelectron detector lies in the mirror plane. (Note that for the final state with odd mirror parity, Eqn. E8 will become

$$\xi_x = \left\langle \Psi_f^k \middle| p_x \middle| \Psi_A(\boldsymbol{k}) \right\rangle = -\left\langle \Psi_f^k \middle| p_x \middle| \Psi_B(\boldsymbol{k}) \right\rangle,$$
$$\xi_y = \left\langle \Psi_f^k \middle| p_y \middle| \Psi_A(\boldsymbol{k}) \right\rangle = \left\langle \Psi_f^k \middle| p_y \middle| \Psi_B(\boldsymbol{k}) \right\rangle. \quad \text{(E9)}$$

The resulting ARPES pattern will be similar to those in Fig. E2 but with the π* and π bands switched.)

Assuming $\xi_y = e^{i\beta}\xi_x$, the photoemission intensity is

$$I \propto A_0^2 \left| \left\langle \cos\varphi_A (e^{-i\theta/2} \pm e^{i\theta/2}) + i \sin\varphi_A e^{i\beta} (e^{-i\theta/2} \mp e^{i\theta/2}) \right\rangle \right|^2 \quad \text{(E10)}$$

If $\beta = 0$ i.e. $\xi_y = \xi_x$, which is approximately the case at 30 eV, the photocurrent intensity is proportional to $I \propto \frac{1}{2}(1 \pm \cos(\theta - 2\varphi_A))$. The circular dichroism is

$$D = \left| \frac{I_{LCP} - I_{RCP}}{I_{LCP} + I_{RCP}} \right| = \left| \sin\theta \right|, \quad \text{(E11)}$$

which shows maximal value in k_y direction. Those features are in good accordance with the experimental data.

If $\beta = \pi/2$ i.e. $\xi_y = i\xi_x$, the photocurrent intensity is $I \propto \frac{1}{2}(1 \pm \cos\varphi \cos 2\varphi_A)$. In this case, $D = \left|I_{LCP} - I_{RCP}\right| / \left|I_{LCP} + I_{RCP}\right| = 0$. There is no circular dichroism. The simulated constant energy maps for $\beta = 0$ and $\pi/2$ are plotted in Figs. E3 and E4.

Interestingly, this method of ARPES with elliptically polarized light can distinguish electrons near the K and K′ points. The wavefunction near the K′ point has the form

$$\Psi_{\pm,K'}(\boldsymbol{k}) = \frac{1}{\sqrt{2}} \begin{pmatrix} e^{i\theta_k/2} \\ \pm e^{-i\theta_k/2} \end{pmatrix}, \tag{E12}$$

for $H_{K'} = v_F \boldsymbol{\sigma}^* \cdot \mathbf{k}$. The wavefunctions at K and K′ are related by time-reversal symmetry. Apparently, we can get the wavefunction at K′ by substituting $-\theta_k \to \theta_k$ in Eqn. E5. Therefore, the rotation of ARPES maps with respect to the photon ellipticity φ_A is reversed for electrons at K′.

Further discussion on photon-energy dependence and dichroic pattern of bilayer graphene can be found in [18].

References:

[1] X. Gonze et al. Computer Phys. Commun. **180**, 2582 (2009).

[2] X. Gonze et al, Zeit. Krist. **220**, 558 (2005).

[3] Spin lesson of the ABINIT tutorial, see

http://www.abinit.org/documentation/helpfiles/for-v6.12/tutorial/lesson_spin.html

[4] C. Hartwigsen et al. Phys. Rev. B **58**, 3641 (1998).

[5] L. M. Falicov and P. J. Lin, Phys. Rev. **141**, 562 (1966).

[6] S. Golin, Phys. Rev. **166**, 643 (1968).

[7] Y. Liu and R. E. Allen, Phys. Rev. B **52**, 1566 (1995).

[8] W. Zhang et al., New Journal of Physics **12**, 065013 (2010).

[9] R. Wyckoff, *Crystal Structures.* vol. 2 (Wiley, New York, 1964).

[10] N. J. Speer et al., EuroPhys. Lett. **88**, 67004 (2009).

[11] R. Martin, Electronic Structure: Basic Theory and Practical Methods (Cambridge University Press, 2008).

[12] C. L. Kane and E.J. Mele, Phys. Rev. Lett. **95**, 146802 (2005).

[13] C. L. Kane and E.J. Mele, Phys. Rev. Lett. **95**, 226801 (2005).

[14] C. Liu et al., Phys. Rev. Lett. **107**, 076802 (2011).

[15] A. H. Castro Neto et al., Rev. Mod. Phys. **81**, 109 (2009).

[16] K. S. Novoselov et al., Nature **438**, 197 (2005).

[17] Y. Zhang et al., Nature **438**, 201 (2005).

[18] L. Yang, G. Bian, T. Miller and T.-C. Chiang, Phys. Rev. Lett. **107**, 166803 (2011).

Figures and tables

		Bi	Sb
Lattice constants in hexagonal system	a (Å)	4.5332	4.3007
	c (Å)	11.7967	11.2221
Rhombohedral angle	α	57°19′	57°14′
Internal displacement parameter	μ	0.2341	0.2336
Reciprocal-lattice constant	g (Å^{-1})	1.3861	1.4610
Nearest-neighbor distance	d_1 (Å)	3.0624	2.9024
Next-nearest-neighbor distance	d_2 (Å)	3.5120	3.3427

Table B1. Crystal Structure parameters of Bi and Sb at 4.2K [5,6].

		Sb_2Te_3	Bi_2Te_3	Bi_2Se_3
Lattice constant	a (Å)	4.250	4.383	4.138
	c (Å)	30.35	30.487	28.64
Inner coordinates	μ	0.400	0.400	0.399
	ν	0.211	0.212	0.206

Table B2. Experimental lattice parameters of the Bi_2Se_3 family of compounds [9].

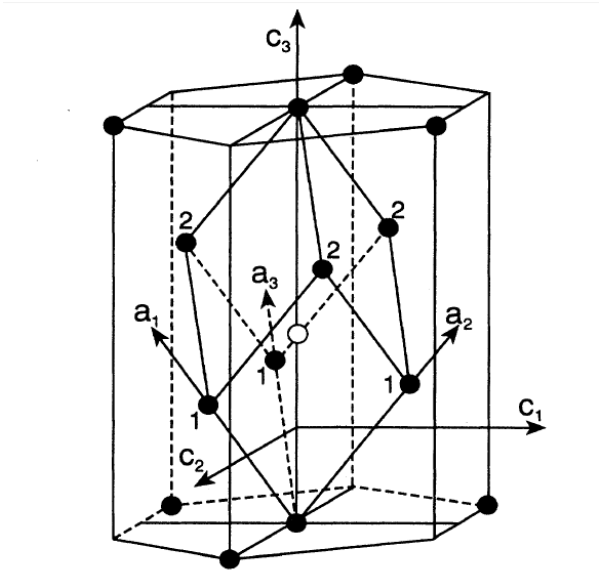

Figure B1. Crystal structure of Sb and Bi, showing first and second neighbors (labeled as 1 and 2) to the central atom represented by an open circle [7].

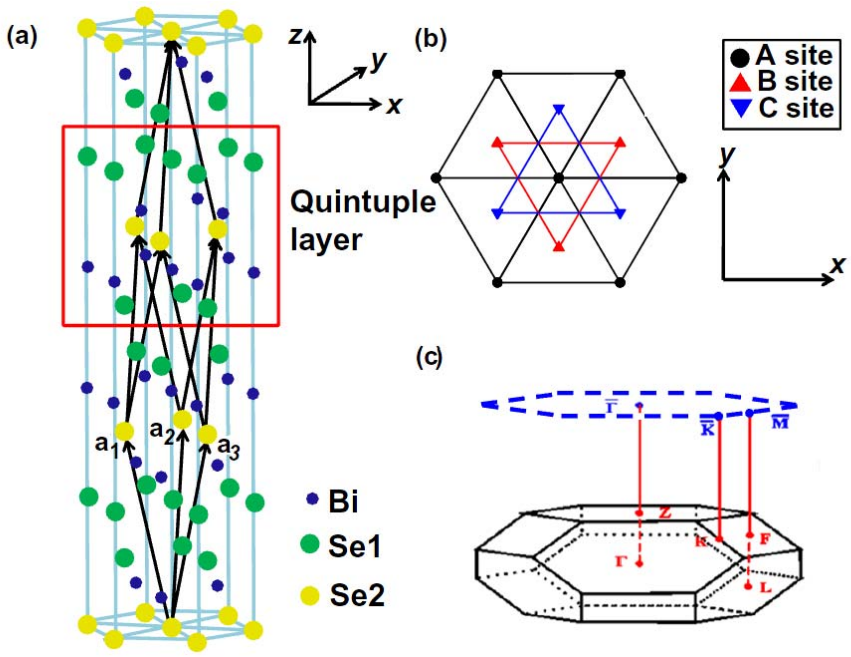

Figure B2. Crystal structure of the Bi_2Se_3 family of compounds [8]. (a) The hexagonal supercell containing 15 atomic layers and primitive vectors $\mathbf{a}_{1,2,3}$. (b) The top view of a QL in the triangle lattice. Three sets of hexagonal sublattices labeled as A, B and C are presented. The stacking of atomic layers along the *z*-direction is in the order of …-C(Se1)-A(Se1)-B(Bi)-C(Se2)-A(Bi)-B(Se1)-C(Se1)-…. (c) The 3D Brillouin zone (BZ). TRIM points Γ (0, 0, 0), L(π, 0, 0), F(π, π, 0) and Z(π, π, π) are denoted. The corresponding surface BZ is represented by the dashed hexagon. $\bar{\Gamma}$ and $\bar{M}$ are the TRIM points in the surface BZ.

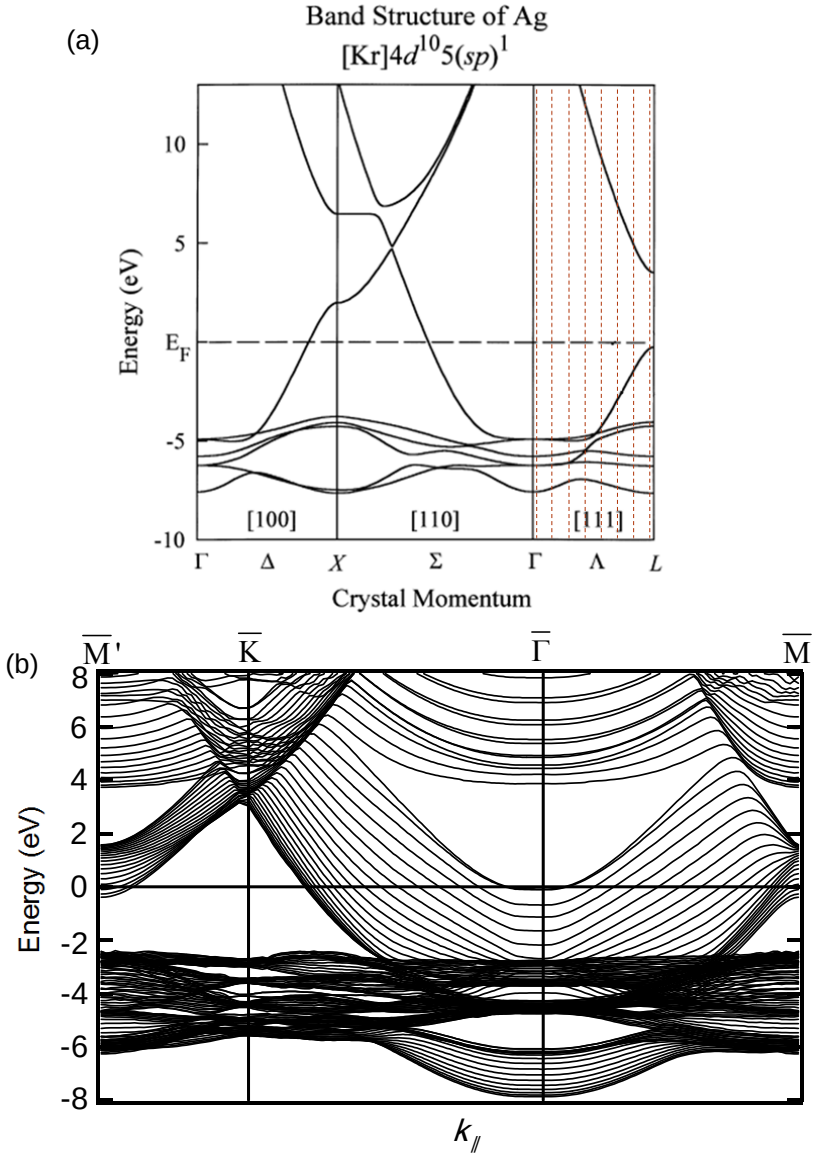

Figure C1. (a) Bulk band structure of Ag. (b) Band structure of a 20 ML Ag film.

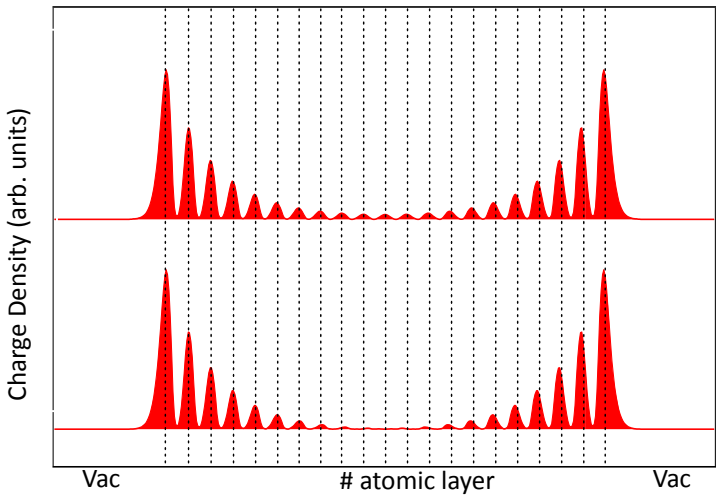

Figure C2. Plane-averaged charge densities of Ag(111) surface states at zone center $\bar{\Gamma}$.

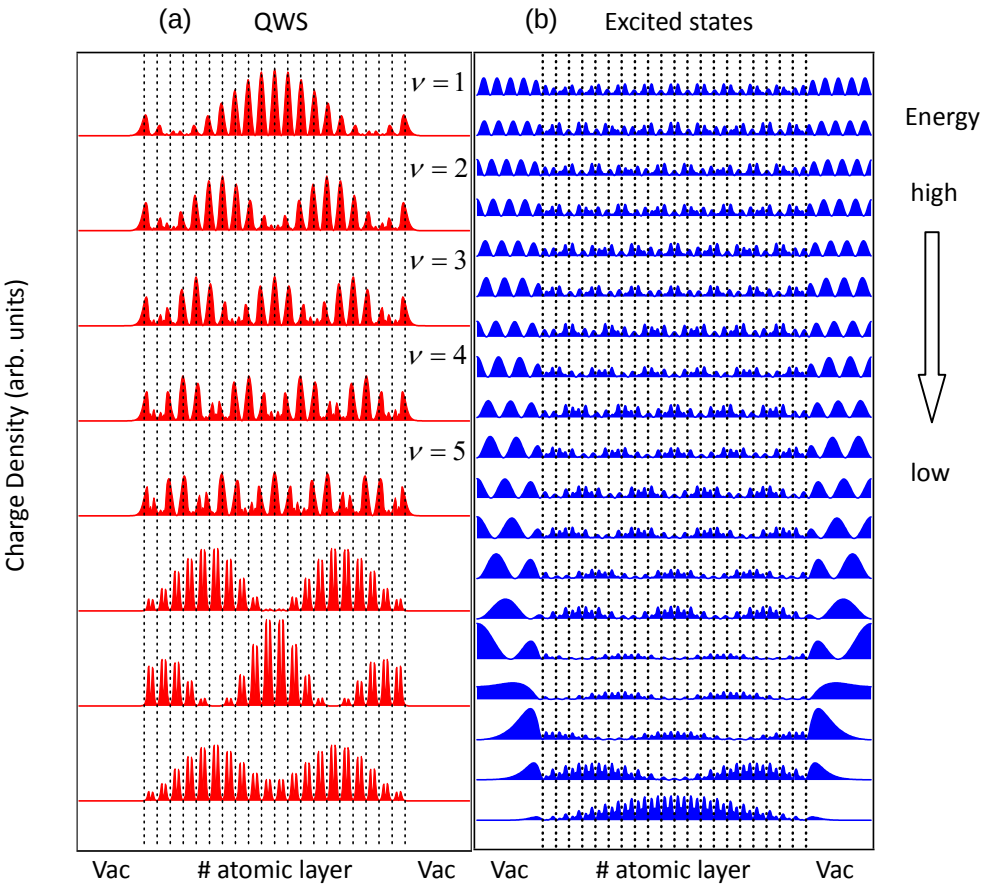

Figure C3. Plane-averaged charge densities in a 20 ML Ag(111) film for (a) quantum well bulk states and (b) excited states at zone center $\bar{\Gamma}$.

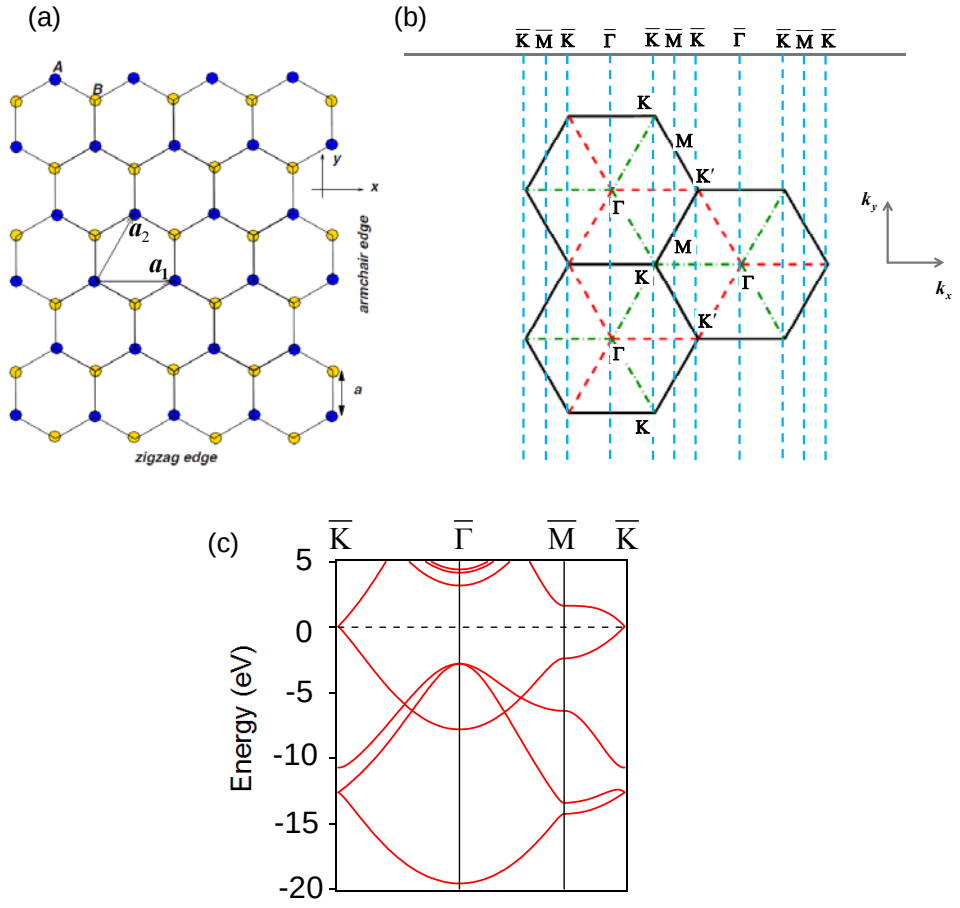

Figure D1. (a) Lattice structure of graphene. The lattice constant a=0.246 nm. (b) 2D Brillouin zone of graphene and projected 1D Brillouin zone of zigzag graphene ribbon. (c) Band structure of graphene.

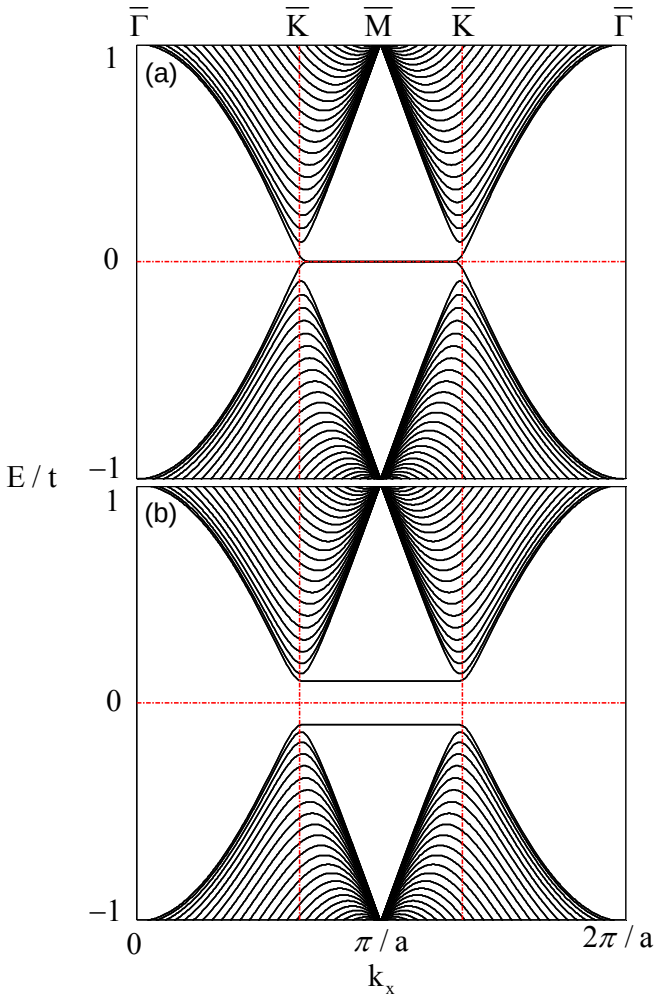

Figure D2. Tight-binding bands of a zigzag graphene ribbon (L=50). (a) $\lambda_{so} = 0$, $\lambda_v = 0$. (b) $\lambda_{so} = 0$, $\lambda_v = 0.1t$.

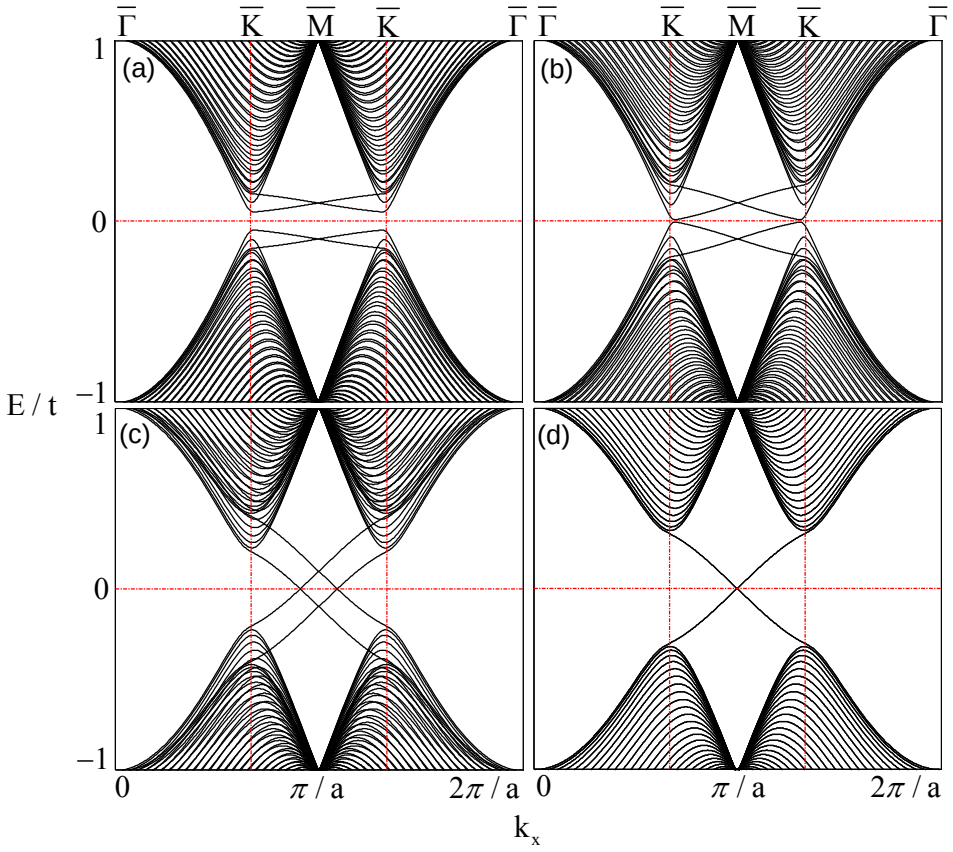

Figure D3. Tight-binding bands of a zigzag graphene ribbon (L=50). (a) $\lambda_{so} = 0.02t$, $\lambda_v = 0.1t$. (b) $\lambda_{so} = \sqrt{3}t/45$, $\lambda_v = 0.1t$. (c) $\lambda_{so} = 0.12t$, $\lambda_v = 0.1t$. (d) $\lambda_{so} = 0.12t$, $\lambda_v = 0$.

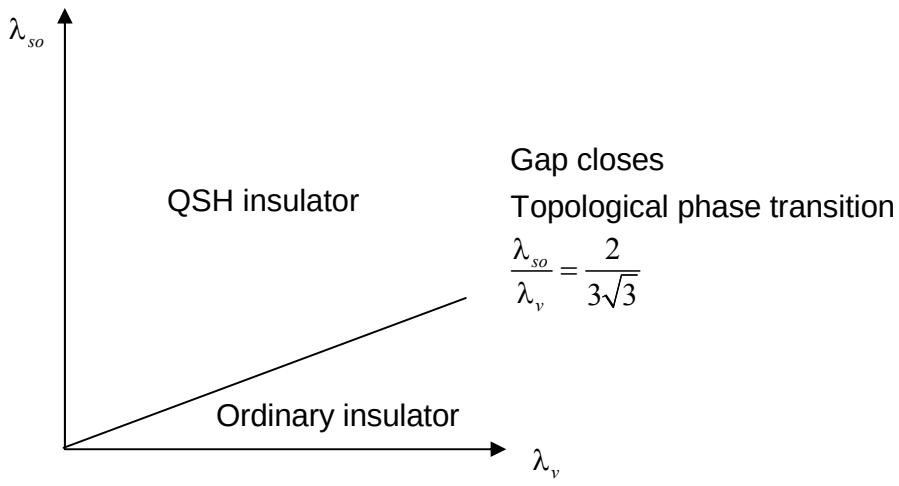

Figure D4. Phase diagram of the Kane-Mele model with SOC (λ_{so}) and a staggered sublattice potential (λ_v).

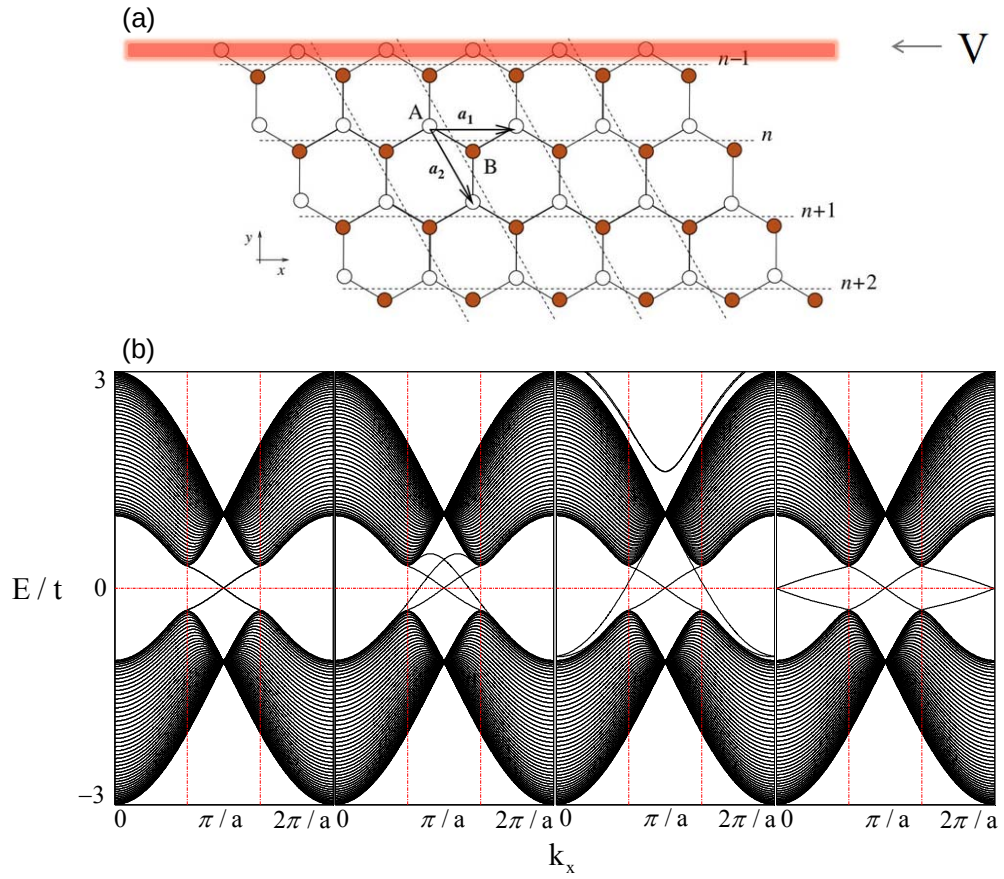

Figure D5. (a) Schematic of edge potential bias on the top atom chain of a zigzag graphene ribbon. (b) Tight binding bands of a zigzag graphene ribbon (L=50) with $\lambda_{so} = 0.12t$, $\lambda_v = 0$. The four panels (from left to right) correspond to the edge potential bias V=0, 0.4t, 1.6t and 400t.

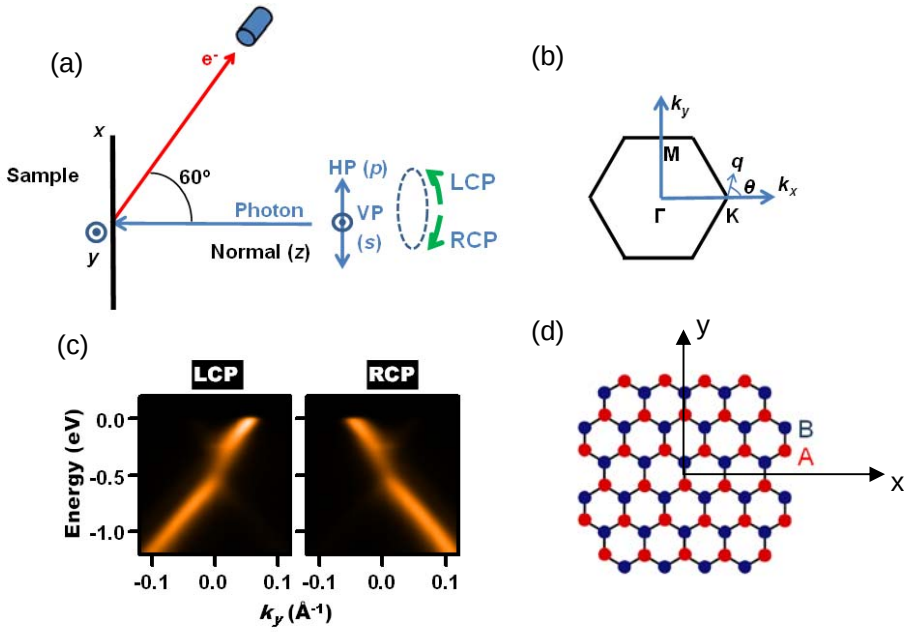

Figure E1. (a) Experimental geometry. (b) Brillouin zone of graphene. (c) ARPES spectra from graphene near the *K* point along using 30 eV LCP and RCP photons. (d) Sublattices of graphene.

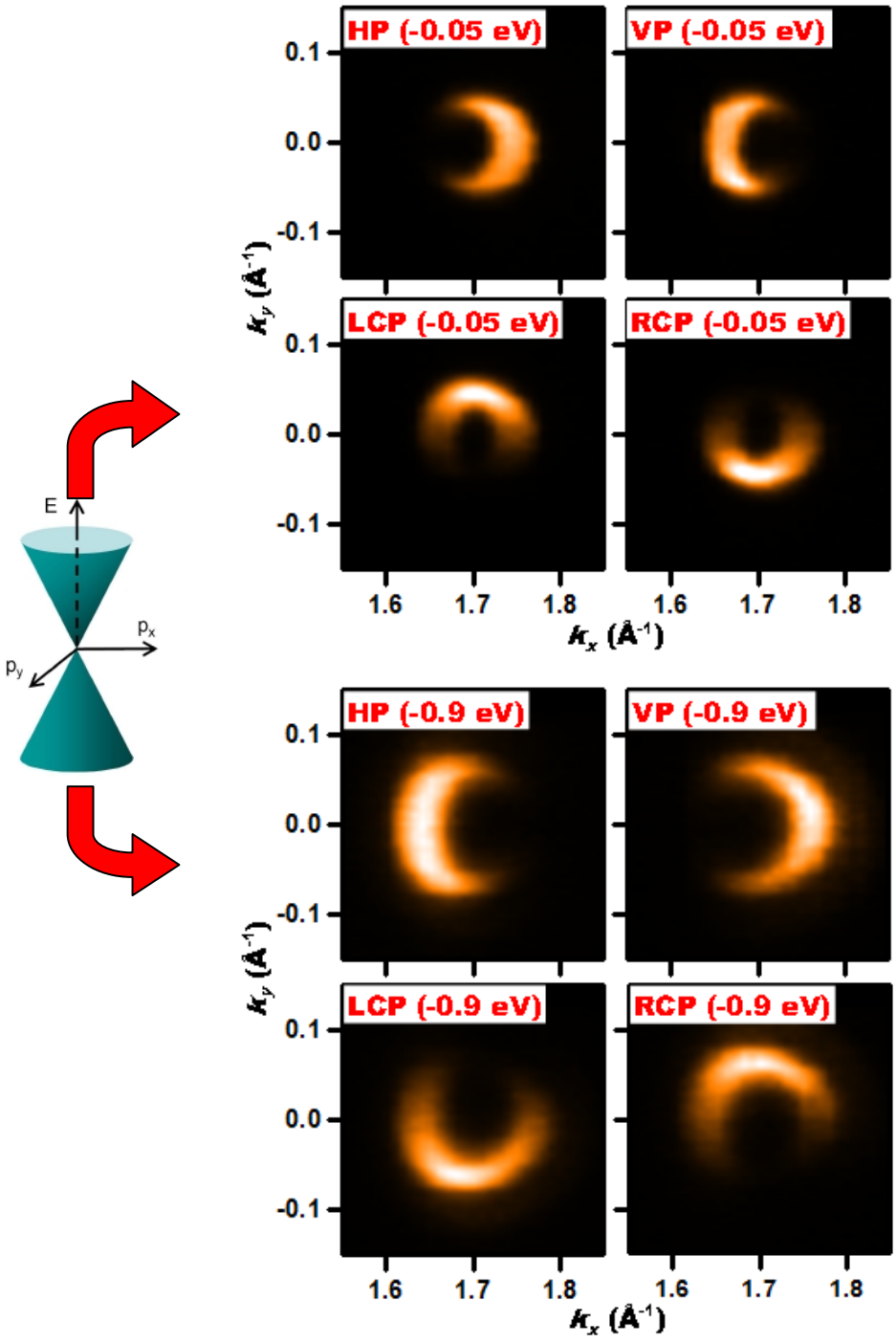

Figure E2. ARPES data from monolayer graphene taken with HP, VP, LCP, and RCP using 30 eV photons. The Dirac point is at -0.45 eV. (a) Constant energy maps at -0.05 eV. (b) Constant energy maps at -0.9 eV.

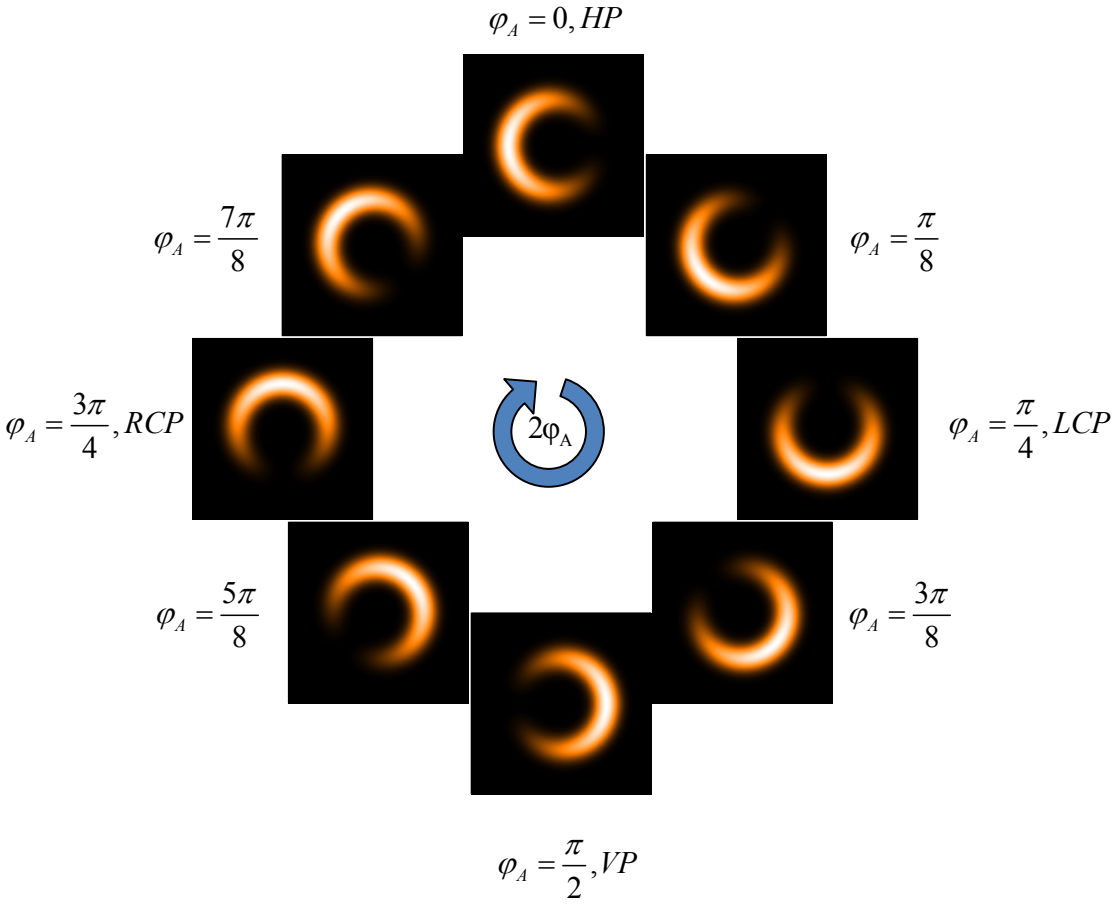

Figure E3. Simulated constant energy maps below the Dirac point with $\xi_x = \xi_y$.

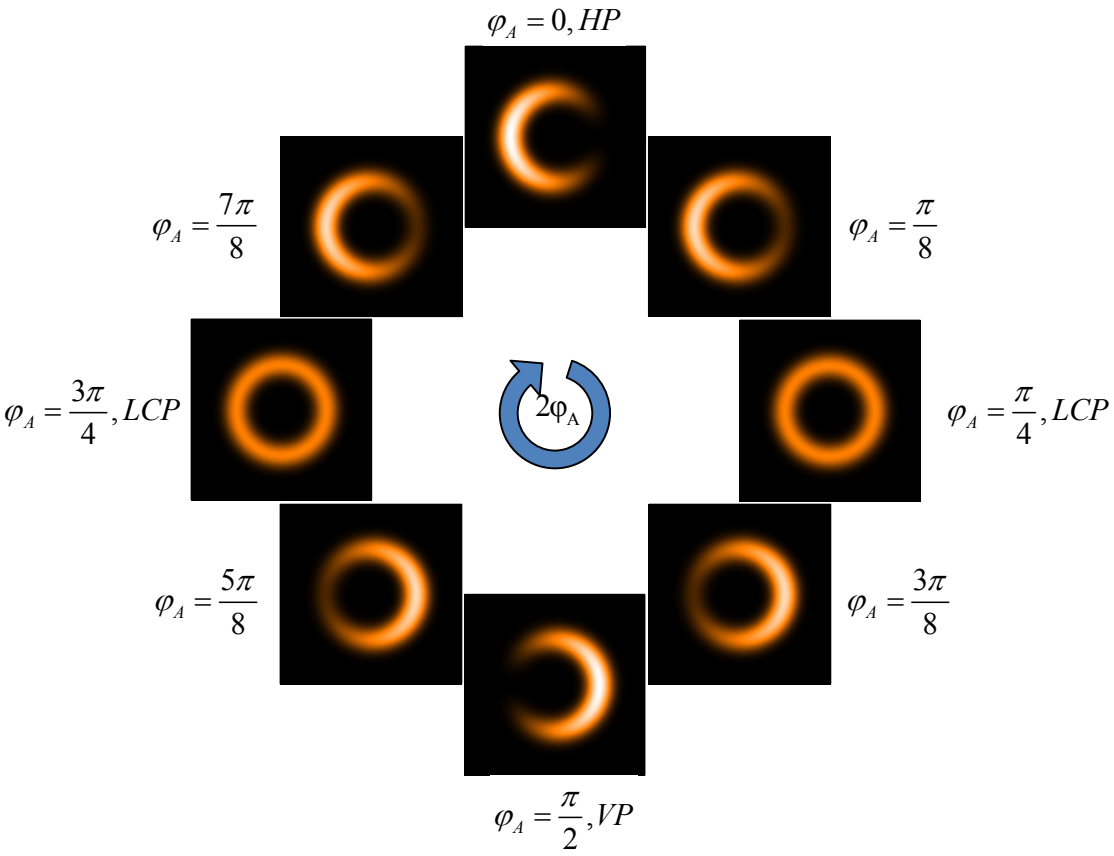

Figure E4. Simulated constant energy maps below the Dirac point with $\xi_x = i\xi_y$.